

**Storage of oil sand waste in sub-surface salt caverns: a feasibility
analysis based on experimental rock mechanics and geological
setting**

Sander Osinga

M.Sc. Thesis

July 2013

Supervisors:

Prof R.J. Chalaturnyk

University of Alberta, Geotechnical Engineering

3-070 Markin/CNRL Natural Resources Engineering Facility

Edmonton, Alberta, Canada T6G 2W2

Prof. C.J. Spiers

Utrecht University, Department of Earth Sciences

Budapestlaan 4, P.O. Box 80021, 3508 TA,

Utrecht, The Netherlands



Universiteit Utrecht

Far out in the uncharted backwaters of the unfashionable end of the Western Spiral arm of the Galaxy lies a small unregarded yellow sun.

Orbiting this at a distance of roughly ninety-eight million miles is an utterly insignificant little blue-green planet whose ape-descended life forms are so amazingly primitive that they still think digital watches are a pretty neat idea.

Douglas Adams

- The Hitchhikers Guide to the Galaxy

ABSTRACT

In order to reduce the environmental impact of heavy oil production operations in East-Central Alberta, hydrocarbon energy companies have been disposing production-related waste in solution mined sub-surface salt caverns. These caverns are situated in two bedded salt layers separated by approximately 150 m of mudstones and a thinner salt layer. In order to optimize well usage and improve project efficiency, two salt caverns per well are proposed, one in each salt formation. This study aims to provide a feasibility analysis for the proposed sub-surface storage based on a study of the geological setting combined with rock mechanical experiments. Analysis of the local and regional geology of the proposed cavern operation reveals a simple stratigraphy and tectonic stability. This implies that the project area is suitable for a salt cavern operation from a geological perspective. A total of 59 geomechanical laboratory experiments were performed on core samples to constrain the geomechanical properties of the formations involved in the salt cavern operation. These results were implemented in a FLAC^{3D} (Fast Lagrangian Analysis of Continua in three dimensions) numerical model to investigate cavern stability, creep rates and surface subsidence. The results from this model imply that surface subsidence will be minimal (<12.1 mm over 50 years), shear stresses around the cavern will be low (<5MPa) and that failure will not occur.

TABLE OF CONTENTS

	Page No.
1. INTRODUCTION	1
1.1 Background	1
1.2 Technical approach and scope of the present study	1
1.3 History of salt cavern use	3
1.4 Creep properties of rock salt	4
1.4.1 Dislocation creep	4
1.4.2 Fluid-assisted grain-boundary migration	6
1.4.3 Fluid-assisted grain-boundary diffusional creep (pressure solution)	7
1.4.4 Micro-cracking and crystal plasticity	8
1.5 Thesis organization	8
2. GEOLOGICAL SETTING	9
2.1 Western Canada Sedimentary Basin	9
2.1.1 Geological and depositional history	9
2.1.2 CNRL 8B WD LIND 08-13-57-5W4 well	18
3. GEOMECHANICAL TESTING PROGRAM	23
3.1 Core storage and specimen preparation	23
3.2 Sample Preparation	24
3.3 Laboratory assessment methodology	26
3.3.1 Water Content and Density	26
3.3.2 Particle Size Distribution	27
3.3.3 Insoluble Content of Salt Rocks	27
3.3.4 Pore Water Chemistry	27
3.3.5 XRD and SEM analysis	28
3.3.6 Ultrasonic Wave Velocity	28
3.3.7 Brazilian Indirect Tension Tests (BTS)	30

3.3.8	Unconfined Compressive Strength (UCS)	33
3.3.9	Standard Triaxial Compression Test (STC)	35
3.3.10	Constant Mean Stress Tests.....	38
3.3.11	Creep Testing	40
3.4	Laboratory Results	44
3.4.1	Watt Mountain Formation	44
3.4.2	Prairie Evaporite Formation.....	48
3.4.3	Keg River Formation	54
3.4.4	Cold Lake Formation.....	57
3.4.5	Ernestina Lake Formation.....	60
3.4.6	Lotsberg Formation	65
4.	NUMERICAL MODELLING	70
4.1	Aims and approach	70
4.2	Results.....	74
5.	DISCUSSION.....	81
5.1	Geological setting	81
5.1.1	Geological history and tectonic stability	81
5.1.2	Lateral continuity of formations.....	81
5.1.3	Vertical and lateral continuity of formation properties	82
5.2	Laboratory testing program.....	84
5.2.1	Watt Mountain Formation	84
5.2.2	Prairie Evaporite Formation.....	89
5.2.3	Keg River Formation	93
5.2.4	Cold Lake Formation.....	95
5.2.5	Ernestina Lake Formation.....	95
5.2.6	Lotsberg Formation	99

5.2.7	Sample preparation	100
5.2.8	Late failure in CMC compared to UCS	100
5.2.9	Dilatancy	102
5.2.10	Stress path influence on creep	104
5.3	Numerical modelling.....	106
5.3.1	Justification of Scenarios and density choices.....	106
5.3.2	Assumptions	106
5.3.3	Implications.....	107
5.4	General discussion	108
5.4.1	Comparison to other work.....	108
5.4.2	Dynamic and static elastic moduli	109
5.4.3	Salt creep: mechanism of flow	110
5.4.4	Scaling problems.....	110
5.4.5	Estimating properties away from the well	111
6.	CONCLUSIONS.....	113
6.1	Geological setting	113
6.2	Laboratory testing program.....	113
6.3	Modelling.....	116
	REFERENCES.....	118
	ACKNOWLEDGEMENTS.....	123
	Appendix A.....	1
	Appendix B.....	1
	Appendix C.....	1
	Appendix D.....	1
1.1	Watt Mountain Formation.....	2
1.1.1	Unconfined Compression Tests	2

1.1.2	Standard Triaxial Compression Tests.....	3
1.1.3	Index testing	5
1.2	Prairie Evaporite Formation.....	6
1.2.1	Unconfined Compression Tests	6
1.2.2	Constant Mean Compression Tests	7
1.2.3	Creep.....	9
1.2.4	Creep – flow law fitting.....	10
1.3	Keg River Formation	12
1.3.1	Unconfined Compression Test.....	12
1.3.2	Standard Triaxial Compression	13
1.4	Cold Lake Formation	15
1.4.1	Unconfined Compression Strength Test.....	15
1.5	Ernestina Lake Formation	17
1.5.1	Unconfined Compression Test.....	17
1.5.2	Standard Triaxial Compression	18
1.5.3	Creep.....	20
1.5.4	Index testing	21
1.6	Lotsberg Formation.....	22
1.6.1	Unconfined Compression Strength.....	22
1.6.2	Constant Mean Compression Tests	24
1.6.3	Constant Mean Extension Tests	26
1.6.4	Creep.....	27
1.6.5	Creep – flow law fitting.....	28
	Appendix E	1
	Appendix F	1

TABLE OF FIGURES**Page No.**

Figure 1. Schematic overview of the proposed salt cavern configuration.	2
Figure 2. An edge and screw dislocation and their relationship in a 3-D lattice.	5
Figure 3. A typical strain-time diagram for rock salt at low temperatures.....	6
Figure 4. Schematic representation of fluid-assisted grain-boundary migration.....	6
Figure 5. Schematic representation of fluid-assisted grain-boundary diffusional creep.	7
Figure 6. Depth to basement in the Western Canada Sedimentary Basin	10
Figure 7. Pre-Devonian topography of the Western Canada Sedimentary Basin.....	11
Figure 8. Location of the study area.	13
Figure 9. GR, V_p and density logs for well 10-15-604W4.	14
Figure 10. The four stages of the deep-water evaporite model.....	17
Figure 11. Field logs for CNRL 8B WD LIND 08-13-57-5W4 well.....	19
Figure 12. Thickness and distribution of the Prairie Evaporite Formation	20
Figure 13. Thickness and distribution of the Upper Lotsberg Formation	21
Figure 14. Thickness and distribution of the Lower Lotsberg Formation	22
Figure 15. Photograph of core storage at the University of Alberta	23
Figure 16. Cutting perpendicular ends.	25
Figure 17. Failure of core sample while lathing.	26
Figure 18. Ultrasonic wave velocity setup	29
Figure 19. Setup of the BTS test.....	31
Figure 20. Stress distribution in a BTS sample	33
Figure 21. Setup of the UCS test.	34
Figure 22. Schematic Set-Up Triaxial Testing.....	37
Figure 23. Creep Test Set Up.....	42
Figure 24. Typical weathered core material from the Watt Mountain Formation	45
Figure 25. Comparison between laboratory and wireline log values for density in the Watt Mountain Formation.....	45
Figure 26. Anhydrite layers in the Prairie Evaporite Formation	49
Figure 27. Comparison between laboratory and wireline log values for density in the Prairie Evaporite Formation	50
Figure 28. Comparison between laboratory and wireline log values for density in the Keg River Formation.....	54

Figure 29. Clay content of the Cold Lake Formation near the interface with the Ernestina Lake Formation.....	57
Figure 30. Comparison between laboratory and wireline log values for density in the Cold Lake Formation.....	59
Figure 31. Salt inclusions in the Ernestina Lake Formation	61
Figure 32. Red shale in the Ernestina Lake Formation	61
Figure 33. Comparison between laboratory and wireline log values for density in the Ernestina Lake Formation	64
Figure 34. Lotsberg Formation with white translucent character on the left and red colouring on the right.....	66
Figure 35. High clay content in the Lotsberg Formation, near the interface with the Ernestina Lake Formation	66
Figure 36. Comparison between laboratory and wireline log values for density in the Lotsberg Formation.....	69
Figure 37. Geometry used for the salt caverns in the FLAC ^{3D} model.....	72
Figure 38. Visual representation of the different contributions to internal pressure.....	73
Figure 39. Salt cavern configurations.....	74
Figure 40. Graphical representation of the maximum shear stress experienced over a 50 year period for a four cavern configuration	79
Figure 41. Graphical representation of the total vertical displacement experienced over a 50 year period for a four cavern configuration.	80
Figure 42. Three photographs of core material from the Ernestina Lake Formation.....	83
Figure 43. Mohr Coulomb Failure Circles – Watt Mountain Formation	85
Figure 44. A p-q diagram for the Watt Mountain Formation.	86
Figure 45. Comparison of Lab Measured Values with Field Logs - Watt Mountain	87
Figure 46. Differential Stress at failure versus Depth – Watt Mountain Formation	88
Figure 47. Power law fit – Entire Prairie Evaporite Formation.	90
Figure 48. Power law fit – Core 31, 1037 m, Prairie Evaporite	91
Figure 49. Comparison of Laboratory Measured Values with Geophysical Logs – Prairie Evaporite Formation.....	92
Figure 50. A p-q diagram – Keg River Formation	93
Figure 51. Comparison of Laboratory Measured and Geophysical Data – Keg River Formation ..	94

Figure 52. A p-q diagram – Ernestina Lake Formation..... 95

Figure 53. Correlation between differential stress at failure and Young’s Modulus for Ernestina Lake Formation 96

Figure 54. Vp and Poisson’s Ratio, Comparison of Laboratory Measured with Field Log (RokDoc) – Ernestina Lake 98

Figure 55. CMC extrapolation. 101

Figure 56. I1 vs J2^{0.5} Plot..... 103

Figure 57. Comparison of stress paths for conventional and radially unloading creep testing. . 105

1. INTRODUCTION

1.1 Background

Oil reserves in Canada were estimated at 175 billion barrels (28.2 billion tonnes) at the end of 2011 (BP Statistical Review of World Energy, Chapter 6, 2012), making Canada the country with the third largest oil reserves after Venezuela and Saudi Arabia. Approximately 98% of these reserves are found in the oil sand deposits in the province of Alberta (U.S. Energy Information Administration, 2012). The Northern Alberta oil sands resources are distributed over three deposits: Athabasca, Cold Lake and Peace River, which extend over 77,000 km² (Chalaturnyk et al., 2002). About 20% of the oil is surface mineable, the rest lies too deep below the surface and can only be extracted by in-situ techniques.

Canadian Natural Resources Limited (CNRL) is one of the largest independent crude oil and natural gas producers in the world, producing approximately 681.000 BOE (barrels of oil equivalent) per day (CNRL Press Release, 2013). It holds claims in the Athabasca and Cold Lake deposits and operates both open pit mining and in-situ operations. To reduce the environmental impact of a proposed in-situ operation in East-Central Alberta, CNRL has proposed to dispose of production-related waste in sub-surface salt caverns created by solution mining. These proposed caverns would be situated in two bedded salt formations that are separated by approximately 150 m of mudstones and a thinner salt layer. To optimize the project efficiency, two salt caverns per well are proposed, one in each major salt formation. This results in a vertical stacking of caverns, as illustrated in Figure 1.

1.2 Technical approach and scope of the present study

The use of natural rock salt deposits for storage facilities is becoming of increasing importance in the oil and gas industry, not only directly for the storage of oil field wastes, but also for temporary hydrocarbon storage and the sequestration of CO₂. Geomechanical properties of rock salt deposits vary significantly due to different origins, mineralogy, lithostratigraphic disposition, texture and diagenetic history. The overall stability of storage facility is not only governed by the properties of the rock salt, but must also consider the properties of overlying caprock formations.

This study aims to provide a feasibility analysis for the proposed sub-surface storage based on a study of the geological setting combined with experimental rock mechanics. More specifically, it focuses on the geomechanical implications and restrictions associated with multi-level solution mining and subsequent waste disposal in the resulting salt caverns.

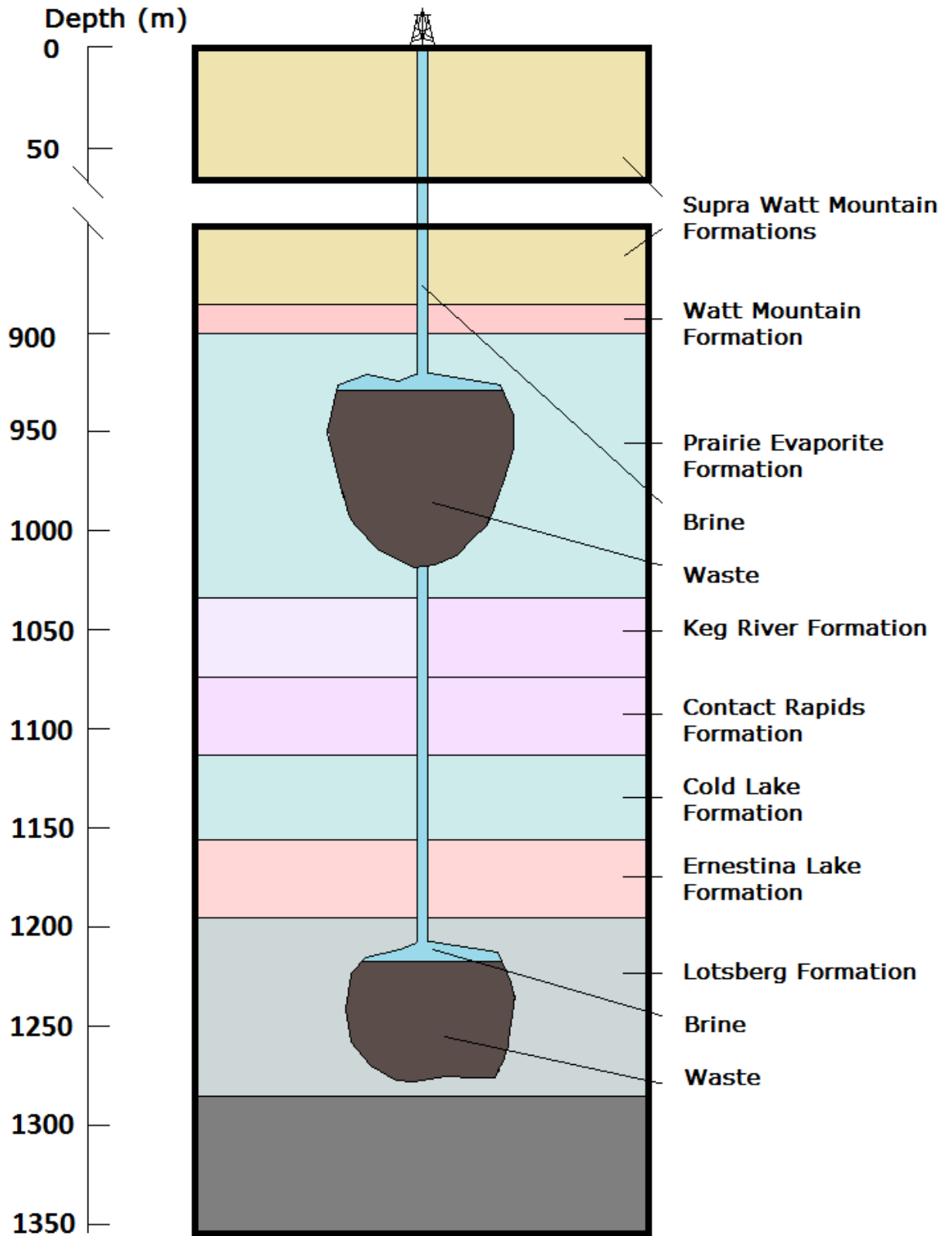


Figure 1. Schematic overview of the proposed salt cavern configuration.

A study of the geological setting was performed through the use of published academic and industrial research papers, the use of publically available geophysical wireline logs and the study of core from the CNRL 8B WD LIND 08-13-57-5W4 well. The main purpose of this geological study is to gain understanding of the geological history of the area and to investigate the different processes that have led to the current configuration of the different formations and their respective properties. This is essential to assess the potential to extrapolate geomechanical properties away from the wells, to evaluate the lateral and vertical continuity of properties and to assess the accuracy with which these properties can be extracted from geophysical wireline logs.

Experiments conducted on specimens obtained from the CNRL 8B WD LIND 08-13-57-5W4 well allowed geomechanical properties such as Young's Modulus (E), Poisson's Ratio (ν), peak strength under uniaxial compression, and creep parameters to be determined. These parameters are of extreme importance for numerical models of salt cavern behavior, and were compared to values calculated from geophysical wireline logs to assess the relation between static laboratory data and dynamic geophysical wireline data. For this research project, a total of 59 geomechanical tests were performed. A complete overview of the tests can be found in Section 3 of the thesis.

1.3 History of salt cavern use

Salt mining was among the first substances mined by man, and the history of salt mining goes back several millennia. Underground mining of salt may have begun more than 4000 years ago in Austria and Romania. However, the use of the underground caverns that are formed as a consequence of solution mining has occurred over only about the last sixty to seventy years (Thoms and Gehle, 2000). The idea of using salt caverns for liquid and gas storage was first patented in Canada in 1944 (Pattinson, 1944) and later in the United States of America (Pattinson, 1957). In the early 1950's, salt caverns were used in North America and Europe for the storage of liquid petroleum gas (LPG) and other light hydrocarbons as well as for crude oil in England. The storage of natural gas commenced in the early 1960's (Thoms and Gehle, 2000).

The current use of salt caverns can be divided into two categories; temporary storage and permanent storage (disposal). Temporary storage, mainly of hydrocarbons, is currently the main use of salt caverns worldwide, with thousands of caverns worldwide being used for this purpose (Bérest and Brouard, 2003). Underground storage is the safest way to store large amounts of hydrocarbons for several reasons. Underground, hydrocarbons are separated from oxygen by several hundred meters of

overlying strata. This makes combustion a virtual impossibility. The overlying strata also protect the hydrocarbons from wildfires, willful damage and aircraft impact. Apart from safety considerations, salt caverns also require very little land area for operation, which makes them an economically viable option for storage.

Increasingly, salt caverns are used for oil field waste disposal. In North America, this is mainly done in Texas and in Western Canada, both by oil field operators and by specialized companies. As environmental laws are becoming stricter with regards to waste disposal, salt caverns are becoming an increasingly attractive option because of their waste isolating properties.

1.4 Creep properties of rock salt

Understanding the way in which rock salt behaves under different conditions is imperative to our understanding of how salt caverns will evolve during their initial formation, during waste injection and after abandonment. When subjected to deviatoric stress, rock salt can deform by a number of different processes, mainly depending on the temperature and pressure under which deformation occurs, but also to a certain extent depending on the magnitude of the deviatoric stress (Urai et al., 2008). For temperatures below 200 °C, creep in rock salt occurs by dislocation creep, fluid-assisted grain-boundary migration, fluid-assisted grain-boundary diffusional creep (pressure solution), and micro-cracking combined with crystal plasticity (Urai et al., 2008). These mechanisms will briefly be discussed below.

1.4.1 Dislocation creep

Dislocation creep allows crystalline materials such a rock salt to deform plastically by glide of dislocations in the crystal planes. Dislocations occur in all crystalline materials and allow crystal plasticity to occur under much lower stresses than would be required if the crystal lattice was perfect. The two basic types of dislocations are screw and edge dislocations, both of which are schematically shown in Figure 2. At temperatures below 200 °C, dislocation creep has been found to be important in laboratory experiments (i.e. at high stresses/strain rates), able to accommodate large strains, even at confining pressures as low as 10 MPa (Urai et al., 2008).

Dislocation creep at relatively low temperatures (less than 30% of the melting temperature) generally shows three stages, known as transient (or primary) creep, steady-state (or secondary) creep, and accelerating (or tertiary) creep. The final creep stage may be absent, depending on the conditions at

which deformation occurs, such as temperature and strain rate. Figure 3 shows a typical creep graph for low temperatures.

Transient creep is characterized by a decrease in strain rate. This decrease is related to the low temperature, which decreases the frequency by which dislocations can pass obstacles by climb or cross-slip. The dislocations are therefore limited to movement within their glide plane, which becomes increasingly difficult as more and more dislocations encounter obstacles such as impurities and other dislocations. Each increment of strain makes further deformation more difficult, which leads to a steady decline in strain rate. This process is known as strain hardening (Fokker, 1995).

Steady-state creep is achieved when the decline in strain rate stops and the slope in strain-time space becomes constant. This occurs when at every increment of strain, work hardening processes are balanced by recovery processes which allow dislocations to pass an obstacle and continue movement along their glide plane. At low temperatures, recovery behaviour is governed by stress-assisted thermal vibration which allows dislocations to 'jump' past obstacles (Spiers, personal communication).

Accelerating creep is the final stage of dislocation creep which eventually leads to failure of the deforming material by means of a positive feedback mechanism. During accelerating creep, the strain rate starts increasing, causing (local) weakening of the material due to the formation of micro-cracks, which in turn causes the strain-rate to increase even more. This self-sustaining cycle continues until the micro-cracks start connecting to form macroscopic shear plane that causes failure. This final creep stage may be absent if healing of micro-cracks keeps pace with the creation of new micro-cracks, allowing steady-state creep to continue without resulting in catastrophic failure (Chan et al., 1996).

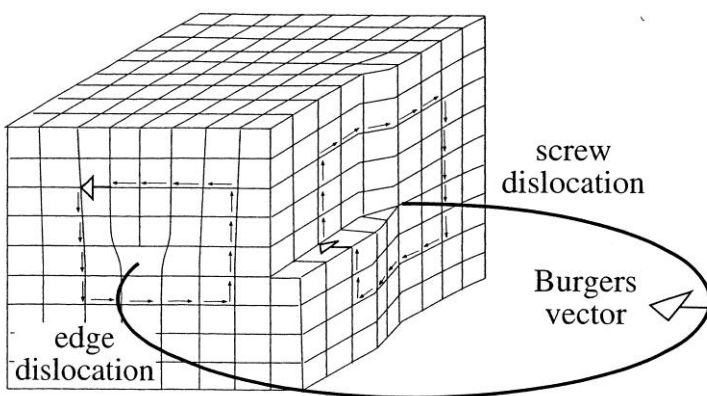


Figure 2. An edge and screw dislocation and their relationship in a 3-D lattice. (Passchier and Trouw, 2005, p. 33)

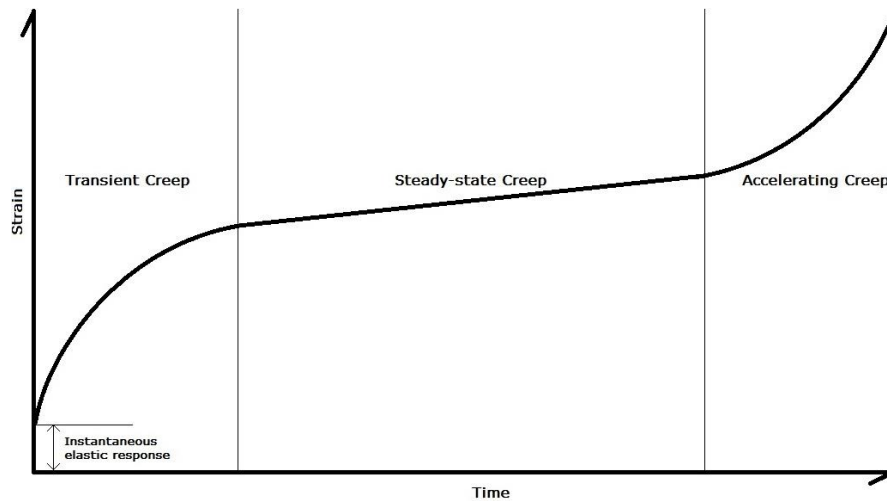


Figure 3. A typical strain-time diagram for rock salt at low temperatures

1.4.2 Fluid-assisted grain-boundary migration

During fluid-assisted grain-boundary migration, mass transfer occurs across a grain-boundary. This mass transfer is driven by a difference in potential energy between the two grains, caused by a difference in dislocation density (Urai et al., 2008). Dissolved mass moves from the high-energy grain to the low-energy grain. During this process, the dislocation density and potential energy of the high-energy grain is lowered and the grain boundary moves in the direction of the high-energy grain (Figure 4).

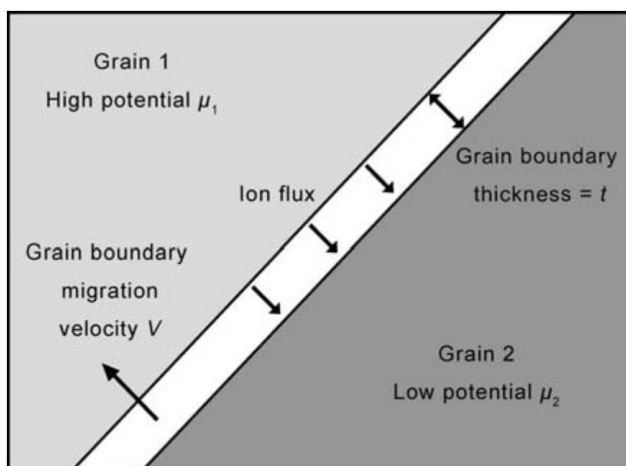


Figure 4. Schematic representation of fluid-assisted grain-boundary migration (Urai et al., 2008)

1.4.3 Fluid-assisted grain-boundary diffusional creep (pressure solution)

During fluid-assisted grain-boundary diffusional creep (also known as pressure solution), grains dissolve at highly stressed boundaries, and after diffusion of the dissolved material through the grain boundary fluid, the dissolved material precipitates at a low normal stress interface (Schutjens and Spiers, 1999). This process differs from fluid-assisted grain-boundary migration since mass is being transported *around* grain boundaries, and is not just transported *across*. (Figure 5)

Pressure solution creep is an important deformation mechanism in most wet rock systems in the Earth's crust, and it is especially fast in rock salt (Urai et al., 2008). However, because of the strong grain size dependence of the mechanisms and the relatively high stresses and short duration of laboratory tests, it is usually not observed in laboratory tests on natural rock salt. Laboratory testing on synthetic salt samples indicates that for rock salt with an average grain size of 10 mm, pressure solution accommodates creep at a strain rate of less than 10^{-12} s^{-1} . This implies that solution precipitation creep is only relevant for considerations on a geological time-scale (Spiers et al., 1990)

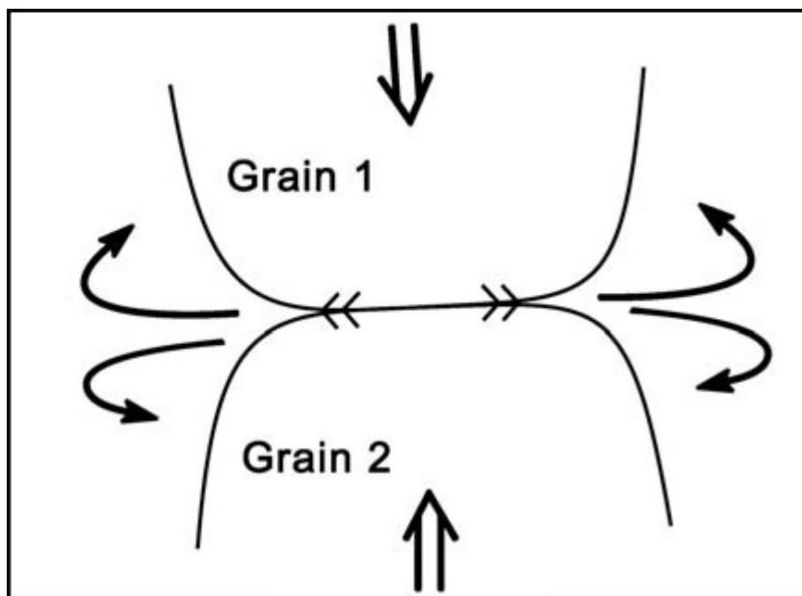


Figure 5. Schematic representation of fluid-assisted grain-boundary diffusional creep. Open arrows indicate the highest compressive principal stress, closed arrows indicate mass transport. (Adapted from Urai et al., (2008)

1.4.4 Micro-cracking and crystal plasticity

At confining stresses less than a few MPa and high (>15 MPa) differential stresses, crystal plasticity combined with micro-cracking, grain rotation and grain-boundary slip can accommodate strain (Urai et al., 2008). Under these circumstances, dilatancy and permeability increase rapidly. When mean stress increases, micro-cracking is suppressed (Peach and Spiers, 1996) and other creep mechanisms determine the creep behaviour.

1.5 Thesis organization

The remainder of the thesis is organized as follows.

- In Section 2, a study of the geological setting for this project is provided. This includes a short geological history and assessment of lateral continuity of formations based on geophysical wireline logs.
- In Section 3, the geomechanical laboratory testing program is described and results are summarized.
- In Section 4, FLAC^{3D} numerical modelling of the proposed salt caverns is presented.
- In Section 5, the geological setting, the laboratory testing program and the numerical modelling are discussed, both separately and in relation to one another.
- In Section 6, an overall summary and conclusions are provided.

This thesis includes six appendices.

- Appendix A: Well logs for geological setting
- Appendix B: Core Log Summary – CNRL 8B WD LIND 08-13-57-5W4
- Appendix C: Methodology – X-ray Diffraction
- Appendix D: Detailed Laboratory Test Results
- Appendix E: SEM Photographs
- Appendix F: Numerical Modelling Results

2. GEOLOGICAL SETTING

2.1 Western Canada Sedimentary Basin

2.1.1 Geological and depositional history

The salt formations of interest for this project are situated in the Elk Point Group, which is of Early to Middle Devonian age. The Elk Point Group is a succession of evaporite, carbonate and clastic rocks of Devonian age in the Western Canada Sedimentary Basin. The Elk Point Group was named by McGehee (1949) and assigned a type section by Crickmay (1954); Anglo Canadian Elk Point No. 11, which is situated at 53.9360N 110.6811W.

The Western Canada Sedimentary Basin is a vast wedge-shaped sedimentary basin, underlying 1.4 million square kilometers of western Canada, that consists of Phanerozoic sedimentary rocks and tapers in the north-easterly direction. Its south-west end exceeds 6 kilometers in thickness and is marked by the eastern boundary of the Rocky Mountains. The wedge tapers out on the Canadian Shield in north-eastern Alberta, northern Saskatchewan and western Manitoba (Figure 6). The evolution of the basin started over 1750 My ago with the deposition of the Sauk sequence and can roughly be divided in two fundamentally different stages and a transitional stage (Porter et al., 1982).

The first stage, lasting from early Proterozoic to Middle Ordovician times, is a platformal stage in which basement subsidence was mainly caused by cooling of the lithosphere and flexural response of the lithosphere to sediment loading. A subsequent transitional stage, from Middle Ordovician to Middle Jurassic, is characterized by differentiation into a network of arches and basins. Basin development during this stage is controlled by erosion and uplift of the arches and differential subsidence of the basins. The cause for the development of basins and arches during this period is poorly understood (Porter et al., 1982). During the final stage, the basin evolved into a foreland basin for the Rocky Mountains in the west. During this stage, the wedge was compressed and pushed towards the north-east by the overriding plate (Porter et al., 1982).

Deposition of the Elk Point Group starts in the Early Devonian on a surface of considerable relief (Figure 7). This surface relief is caused by differential basement subsidence and uplift of arches during the transition from a platformal basin to a foreland basin. Due to the paleotopography at the beginning of the Early Devonian, deposition of the Lower Elk Point Group is discontinuous throughout the Western Canada Sedimentary Basin, and limited to the Central Alberta Sub-basin, the Northern Alberta Sub-basin and the southern Mackenzie Sub-basin in the North-West Territories (Figure 7). The Peace River Arch

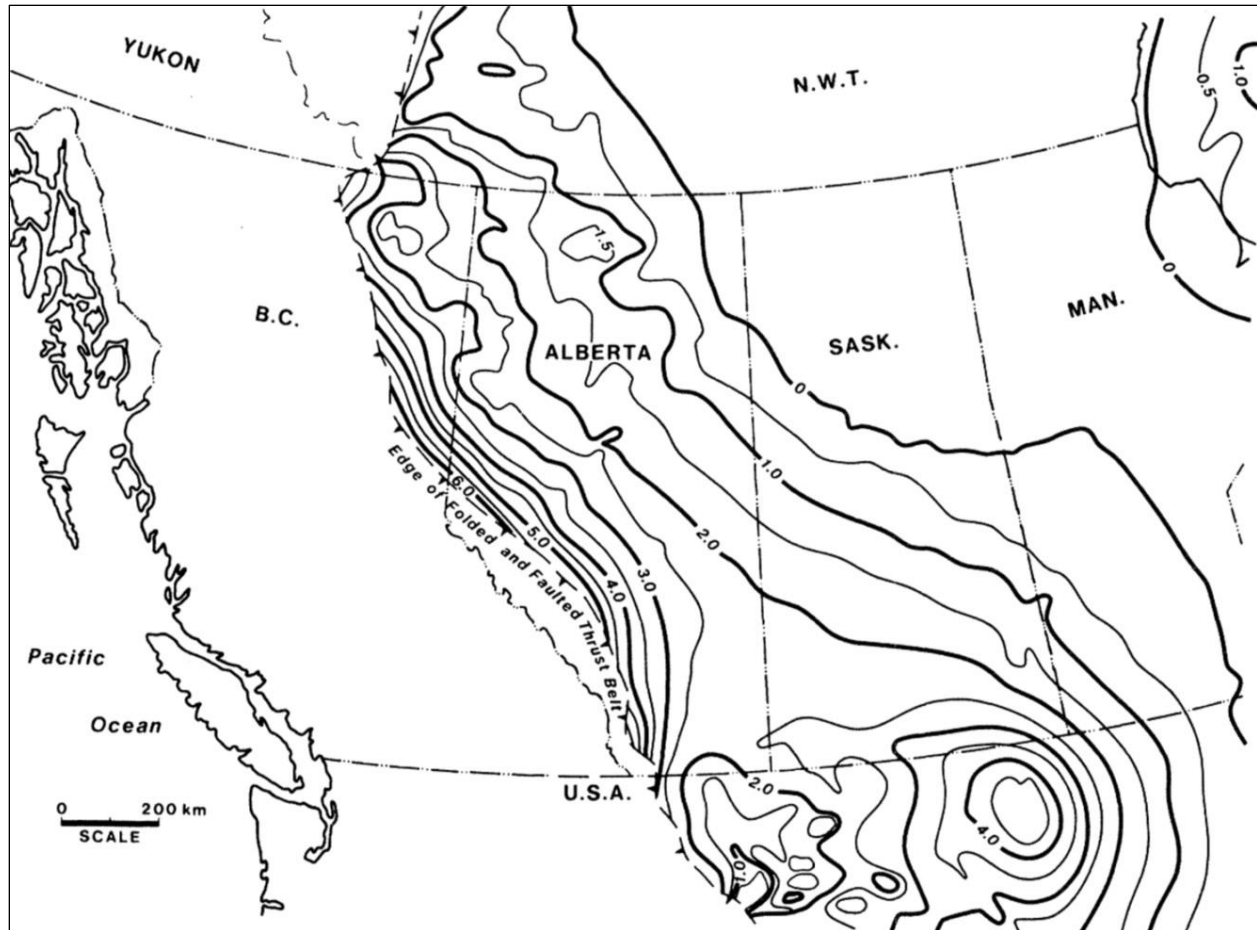


Figure 6. Depth to basement (in kilometers) in the Western Canada Sedimentary Basin (Porter et al. 1982)

separates the Central Alberta Sub-basin and the Northern Alberta Sub-basin, the southern Mackenzie Sub-basin and the Northern Alberta Sub-basin are separated by the Tathlina Uplift (Grobe, 2000).

In the depocentres of the sub-basins, the Lower Elk Point Group is dominated by evaporites and carbonates (in the Mackenzie Sub-basin), while towards the boundaries near-shore and clastic sediments prevail. The infill of the sub-basins with the formations of the Lower Elk Point Group levels out the surface topography, causing the basins to expand laterally, until they eventually merged into one basin (Grayston et al., 1964).

The first widespread correlatable formation is the Winnipegosis/Keg River carbonate (nomenclature depends on location, although the formations are essentially identical). It is considered to be the first formation of the Upper Elk Point Group. The Winnipegosis/ Keg River carbonate is composed of both reef and non-reef carbonates and is often highly dolomitized, although original limestone is preserved in some areas. The nature of the formation causes thickness to vary considerably

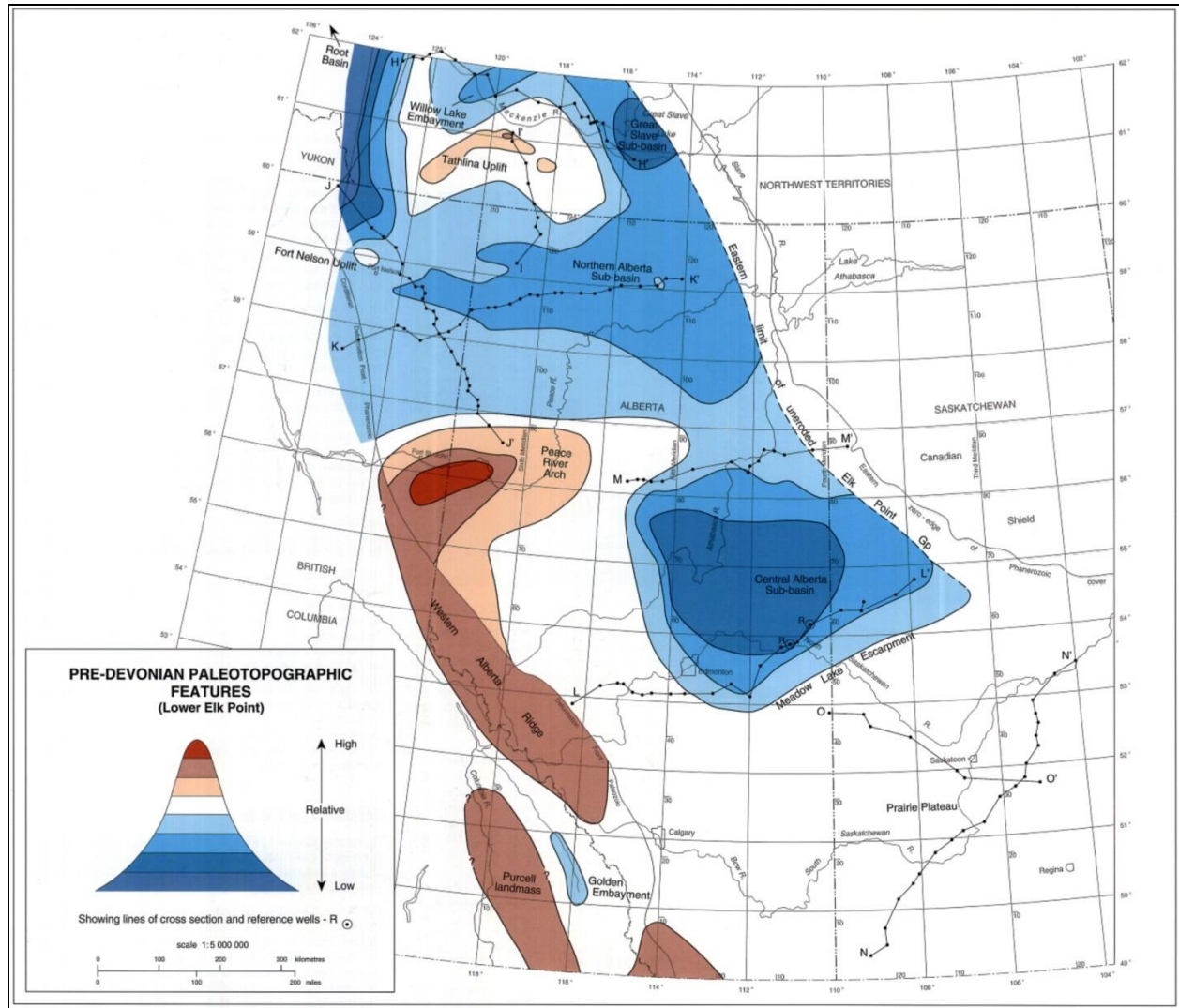


Figure 7. Pre-Devonian topography of the Western Canada Sedimentary Basin (Grobe, 2000)

within the formation. Non-reef carbonates may be as thin as 15 m while some reef carbonates are over 200 m thick (Grayston et al., 1964).

The Winnipegosis/Keg River carbonate sequence is overlain by the Prairie Evaporite Formation in Saskatchewan, Manitoba, North Dakota and Central Alberta and by the Muskeg Formation in Northern Alberta and Northern British Columbia. The Prairie Evaporite Formation is an interbedded sequence of halite and anhydrite, which grades into the interbedded anhydrite and dolostone of the Muskeg Formation. The varying thickness of the formations is almost completely due to the varying thickness of the underlying Winnipegosis/Keg River carbonate, which is reflected in the flat top of the formation. In sections where the underlying carbonates are thin, the evaporite thickness ranges up to

300 m, and the highest reefs are covered by approximately 75 m of Prairie Evaporite Formation or Muskeg Formation (Grayston et al., 1964).

The youngest formations present in the Elk Point Group are the Dawson Bay Formation and the Watt Mountain Formation. In East-Central Alberta, the Dawson Bay Formation is thin and not always present (Grayston et al., 1964).

The proposed salt cavern waste disposal project is situated in the centre of the Devonian Central Alberta Sub-basin, in the region where the Lotsberg Formation attains its maximum thickness of approximately 115 m, and where the Prairie Evaporite reaches up to 150 m in thickness. The samples used in the geomechanical assessment study, are all taken from core from the CNRL 8B WD LIND 08-13-57-5W4 well (the 8th well in section 13, Township 57, Range 5, West of the 4th meridian), situated at 53.9240N; 110.6039W, approximately 5.25 km from the Anglo Canadian Elk Point No. 11, the type well for the Elk Point group, in which both the Prairie Evaporite Formation and the Lotsberg Formation are situated. The study location is identified on Figure 8.

Based on well log data, this well penetrates the Prairie Evaporite Formation (which has a local thickness of approximately 140 meters) completely, but log data stops at 1240, about 30 meters into the Lotsberg Formation, before exiting the Lotsberg Formation, leaving the exact thickness of this formation undetermined at this location. Log data from CNRL 8B WD LIND 2-13-57-5W4, about 340 m away, reaches down to over 1600 m, confirming the thickness of the Prairie Evaporite Formation and showing the thickness of the Lotsberg Formation to be approximately 115 m at this location.

Ten well logs from vertical wells in the area are used to constrain the geological setting for the Elk Point Group in the area of the CNRL 8B WD LIND 08-13-57-5W4 well. The formations of interest are (from top to bottom): Watt Mountain Formation, Prairie Evaporite Formation, Keg River Formation, Contact Rapids formation, Cold Lake Formation, Ernestina Lake Formation and Lotsberg Formation. All formations have characteristics that make them easy to identify in the well logs. Figure 9 shows well 10-15-60-4W4 in which all formations of interest are present. Although the absolute values differ from well to well, the patterns for the Gamma Ray (GR), Compressive Wave Velocity (V_p) and density (Rho) log are virtually identical for each well log and recognizing the different formations is straightforward. The available geophysical wireline logs for all wells in the area can be found in Appendix A.

The deposition of the Elk Point Group started in the topographic lows of the pre-Devonian topography. One of these topographic lows is the Central Alberta Sub-basin. This section deals with the depositional setting in this specific sub-basin.



Figure 8. Location of the study area. (Adapted from Norman Einstein, Creative Commons)

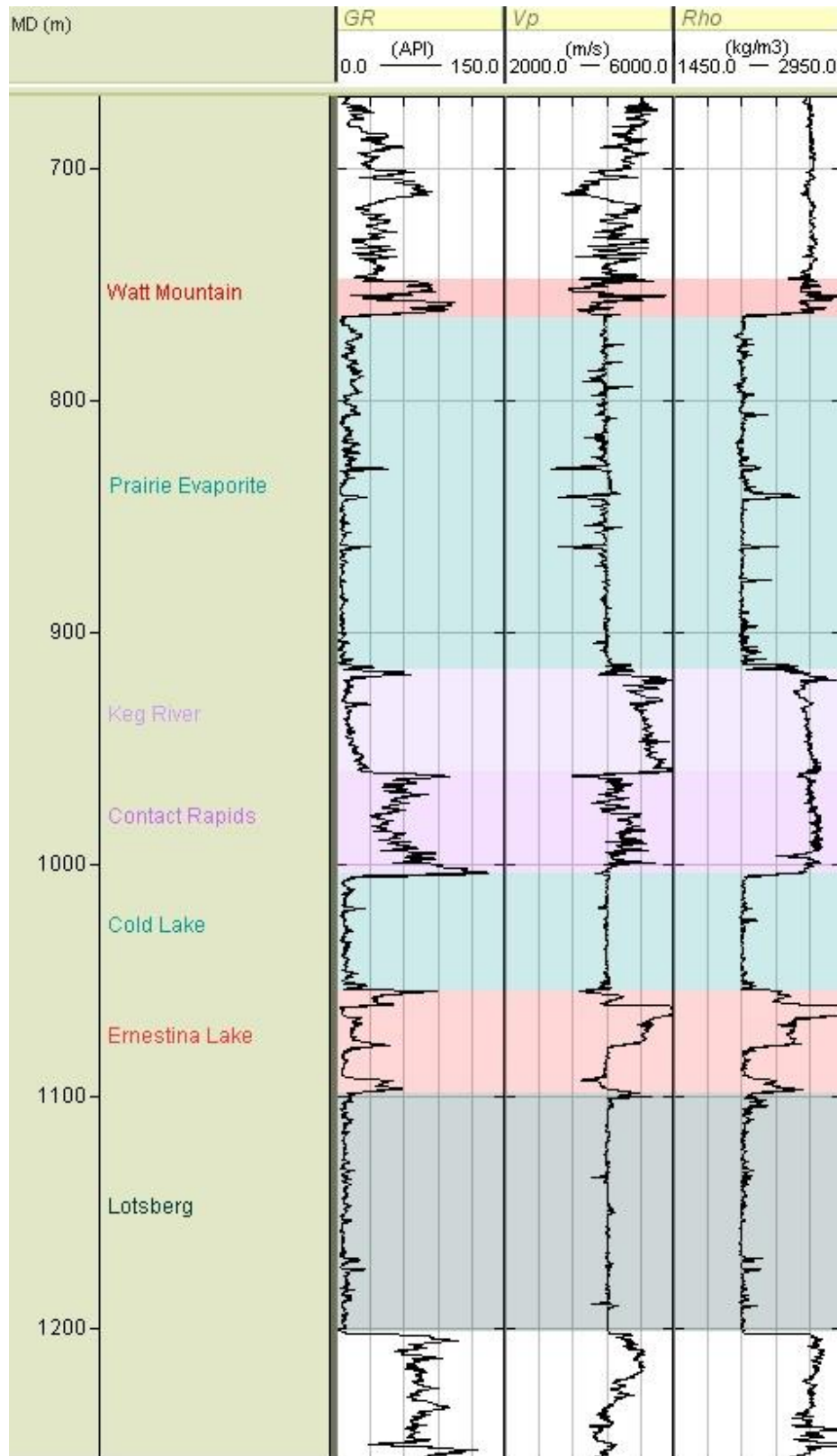


Figure 9. GR, V_p and density logs for well 10-15-604W4. (Created in RokDoc, Ikon Science)

The first formation to be deposited in the basin is the Basal Redbeds. The Basal Redbeds are composed of siltstones, sandstones and red dolomitic shales, representing a transgressive near-shore facies consisting of reworked regolith and surface debris (Grayston et al., 1964; Schmalz, 1969; Hamilton, 1971). The red colour of the deposit reflects the oxidizing conditions under which the deposit formed.

The Lotsberg Formation is deposited directly on top of the redbeds and is commonly divided into a Lower and Upper Lotsberg Formation, which are separated by a red dolomitic shale of up to 60 meters thick. This separation is reported to occur only near the centre of the basin (Grayston et al., 1964). Towards the edges of the basin, the Lower and Upper Lotsberg Formation are not separated and appear as one continuous salt formation. Chemical analysis shows that the Lotsberg Formation is greater than 95% pure halite. This is thought to be due to a history of repeated solution and redeposition of the formation (Grobe, 2000). The halite crystals are clear and very coarse (up to several centimeters in diameter) and clay/shale inclusions occur as structureless, beddingless inclusions, which supports this hypothesis. The continuous transition from redbeds to halite suggests that the Lotsberg formation was deposited in a well-oxygenated, shallow-water environment where surface evaporation exceeded precipitation and terrestrial run-off. The occurrence of the redbed and salt sequence as described above can be adequately explained by a depositional environment in which transgressive near-shore facies shales were deposited in a basin that slowly turned into an evaporitic environment (Schmalz, 1969).

The Ernestina Lake Formation - Cold Lake Formation sequence that follows the Lotsberg Formation is most probably the result of a similar history. The Ernestina Lake Formation consists of a lower red shale, a middle carbonate and an upper anhydrite (Grayston et al., 1964). Although the composition differs from the Basal Redbeds, the depositional environment is similar in nature; well-oxygenated bottom waters in a transgressive, near-shore environment. The anhydrite represents the transition to an evaporitic environment, which continues in the Cold Lake formation. In the Central Alberta Sub-basin, the Cold Lake Formation consists of halite and is very pure in composition. Once again, this is likely due to a history of repeated solution and redeposition (Grobe, 2000). Towards the western margins of the sub-basin, as well as in towards the Peace River Arch, the Cold Lake Formation grades into a red dolomitic shale. The Cold Lake Formation is the first formation to extend over the Peace River Arch and represents the onset of merging of the sub-basins.

The Winnipegosis/Keg River Formation extends over a much wider area than the older Lower Elk Point Group formations and continues the merging of the different sub-basins. It consists of carbonates

(often dolomitized) of both reefal and non-reefal nature. The fossilized pinnacle reefs and marine fauna suggests that the Winnipegosis/Keg River Formation was formed under conditions that are similar to the current conditions in the Mediterranean Sea, with normal marine surface waters and stagnant, anoxic, reducing conditions in the bottom waters (Schmalz, 1969).

The Contact Rapids Formation consists of basal redbeds which grade into grey, green and black argillites and carbonates towards the top of the formation. This formation represents a fundamentally different environment in which reducing conditions are widespread throughout the Elk Point Group basins (Schmalz, 1969).

The reducing conditions during the Contact Rapids and Winnipegosis/Keg River deposition are thought to be caused by a deepening basin, either due to sedimentation or increased basin subsidence. In the deepening basin, stagnant bottom water accumulated due to the presence of the Peace River Arch which prevented backflow towards the open ocean in the north-west. Due to a high evaporation rate at the surface, brines of increasing density collected at the bottom of the basin, until deep-water evaporite deposition commenced and the Prairie Evaporite Formation started to form.

The deep-water evaporite deposition model as proposed by Schmalz (1969) has become the widely accepted model to explain the occurrence of thick salt deposits such as the Prairie Evaporite in the Western Canada Sedimentary Basin and the Zechstein Salt in Europe. The model is comprised of four different stages, which are depicted in Figure 10. The first stage (formative stage) commences with a system in which evaporation exceeds runoff and precipitation combined. This results in slightly enriched brines that sink to the bottom of the basin due to their density. During the second (euxinic) stage, net evaporation continues and stagnant bottom waters form as the result of high brine density and the presence of a sill that prevents backflow to the open ocean. In the third (ephemeral) stage, salt starts to precipitate at the surface, but re-dissolves at depth, causing further enrichment in the stagnant bottom waters. When the whole water column is saturated with respect to a certain salt (anhydrite, halite, etc.), precipitation commences at the bottom of the basin. This fourth stage is called the permanent evaporite stage. This stage occurs at different brine densities for different salts, which means that the basin can be in an earlier stage with respect to halite, while anhydrite is already being precipitated at the bottom. For a more complete discussion of the deep-water evaporite model, the reader is referred to Schmalz (1969).

The Prairie Evaporite Formation consists mainly of evaporites (anhydrite and halite) although it is not as pure as the Lotsberg and Cold Lake formations. This is probably due to the fact that the Prairie

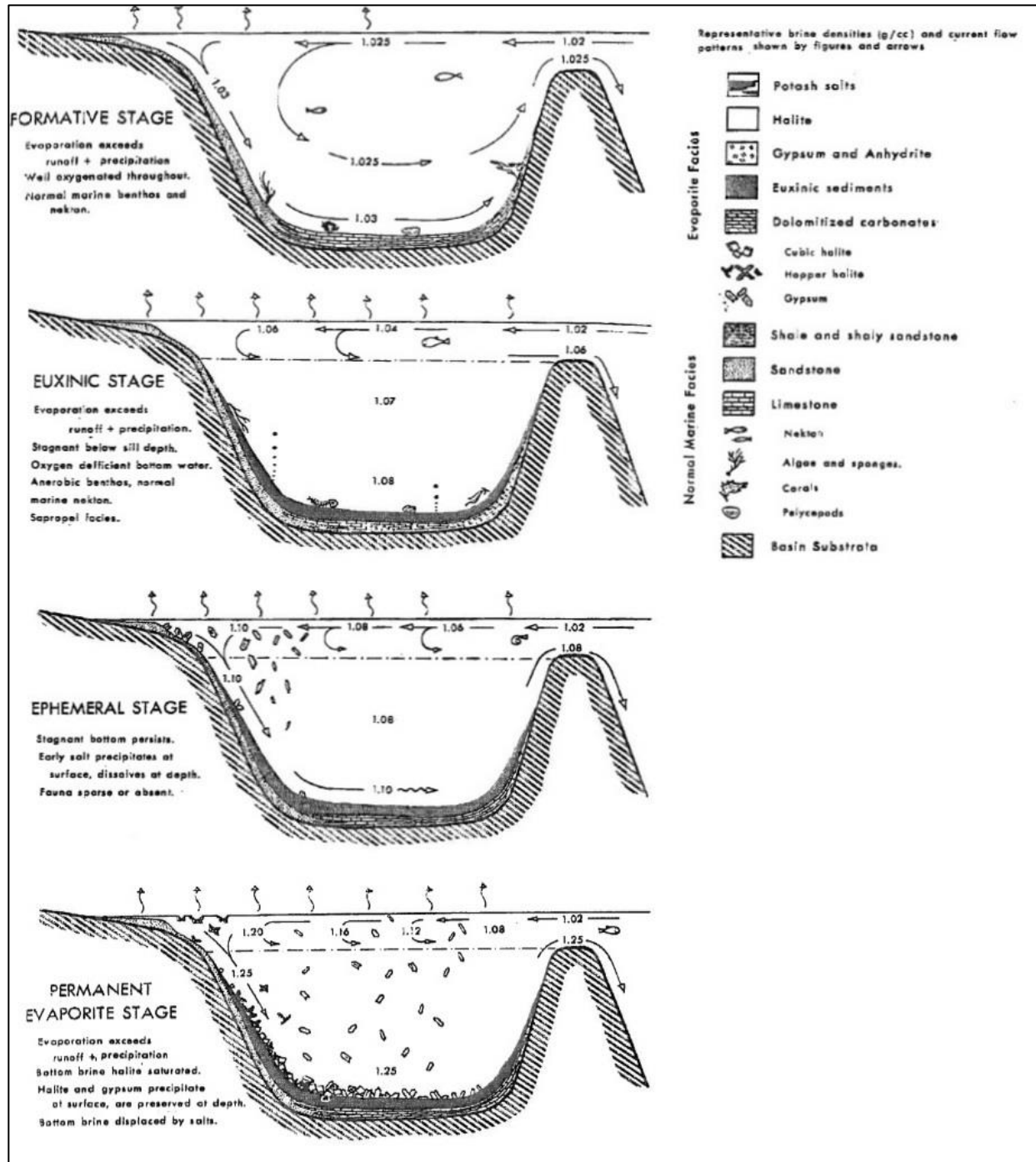


Figure 10. The four stages of the deep-water evaporite model (adapted from Schmalz, 1969)

Evaporite Formation has not been subject to repeated solution and redeposition as is made apparent by the layered structure of the formation. This layered structure includes the occurrence of thin (<1 cm) anhydrite beds in halite and the occurrence of solutinal diastems (Wardlaw and Schwerdtner, 1966).

Hypothetical models to describe the formation of this layered structure differ in detail, but are generally considered to be the result of variation in brine saturation over time (e.g. Grayston et al., (1964); Wardlaw & Schwerdtner (1966)). The Prairie Evaporite Formation has a sharp dissolution front in the East (Figure 12). East of this front, dissolution of halite occurred at various times and resulted in the partial or complete removal of halite and the collapse of the overlying formations (Grobe, 2000)

Well-oxygenated, shallow water conditions return with the carbonates of the Dawson Bay Formation and the redbeds of the Watt Mountain Formation. These formations form the youngest units of the Elk Point Group, although Grayston and colleagues (1964) state that the Watt Mountain Formation should be considered the oldest unit of the overlying Beaverhill Lake Formation because it belongs to a depositional cycle that continues in the Beaverhill Lake Formation.

2.1.2 CNRL 8B WD LIND 08-13-57-5W4 well

Field logs for CNRL 8B WD LIND 08-13-57-5W4 well are provided in Figure 11. They include gamma ray, compression wave velocity and density. Core recovery depths are also indicated in this Figure.

Waste disposal salt caverns are proposed in both the Prairie Evaporite and Lotsberg Salt formations at the location of the CNRL 8B WD LIND 08-13-57-5W4 well. Accordingly, properties of both these salt formations and the corresponding overlying cap rock formations (Watt Mountain and Ernestina Lake, respectively) are of primary interest. Given that the Ernestina Lake Formation is of limited thickness, and the potential zone of influence associated with the development of a cavern in the Lotsberg formation, additional testing was conducted on core samples from the overlying Cold Lake and Keg River formations.

The Prairie Evaporite Formation and the Lotsberg Formation are widespread in East-Central Alberta. The location of the proposed salt caverns in relation to the thickness distribution is shown in Figure 12 (Prairie Evaporite Formation) and Figure 13 and Figure 14 (Lotsberg Formation).

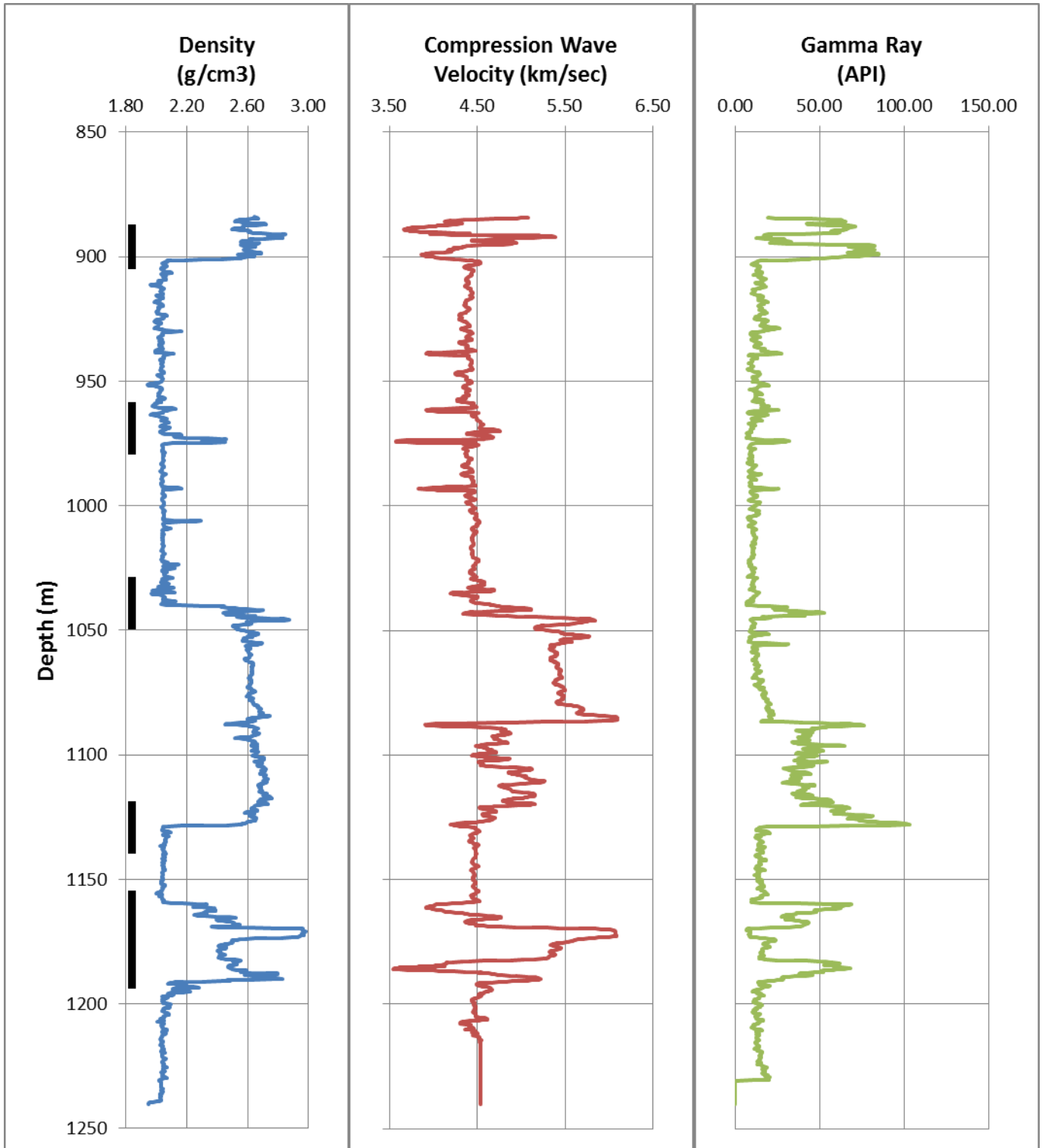


Figure 11. Field logs for CNRL 8B WD LIND 08-13-57-5W4 well. Core recovery depths are indicated by the black bars in the density log. (Logs obtained from GeoSCOUT database)

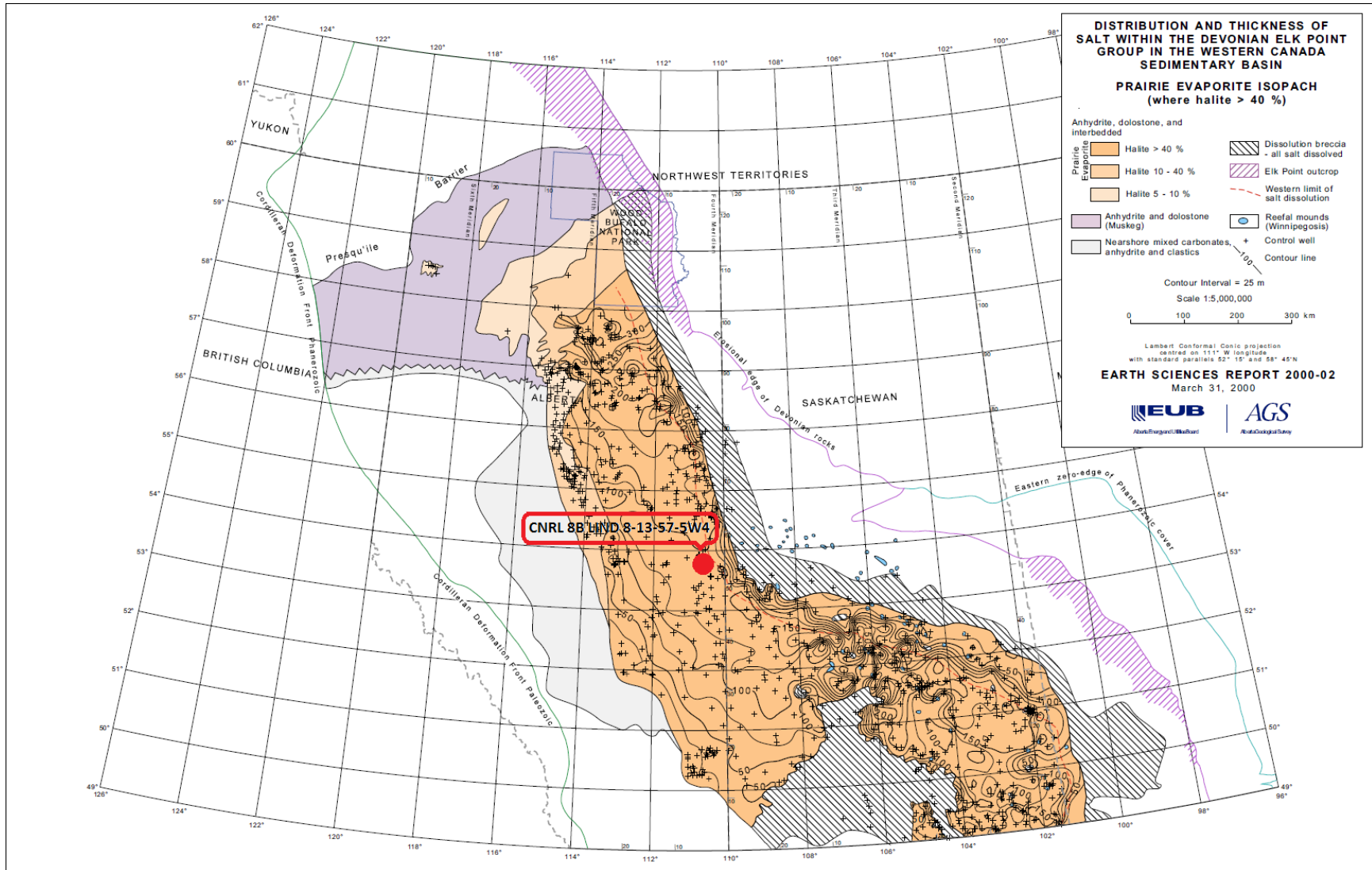


Figure 12. Thickness and distribution of the Prairie Evaporite Formation, the position of the study area is indicated by the red dot. (Adapted from Grobe (2000).

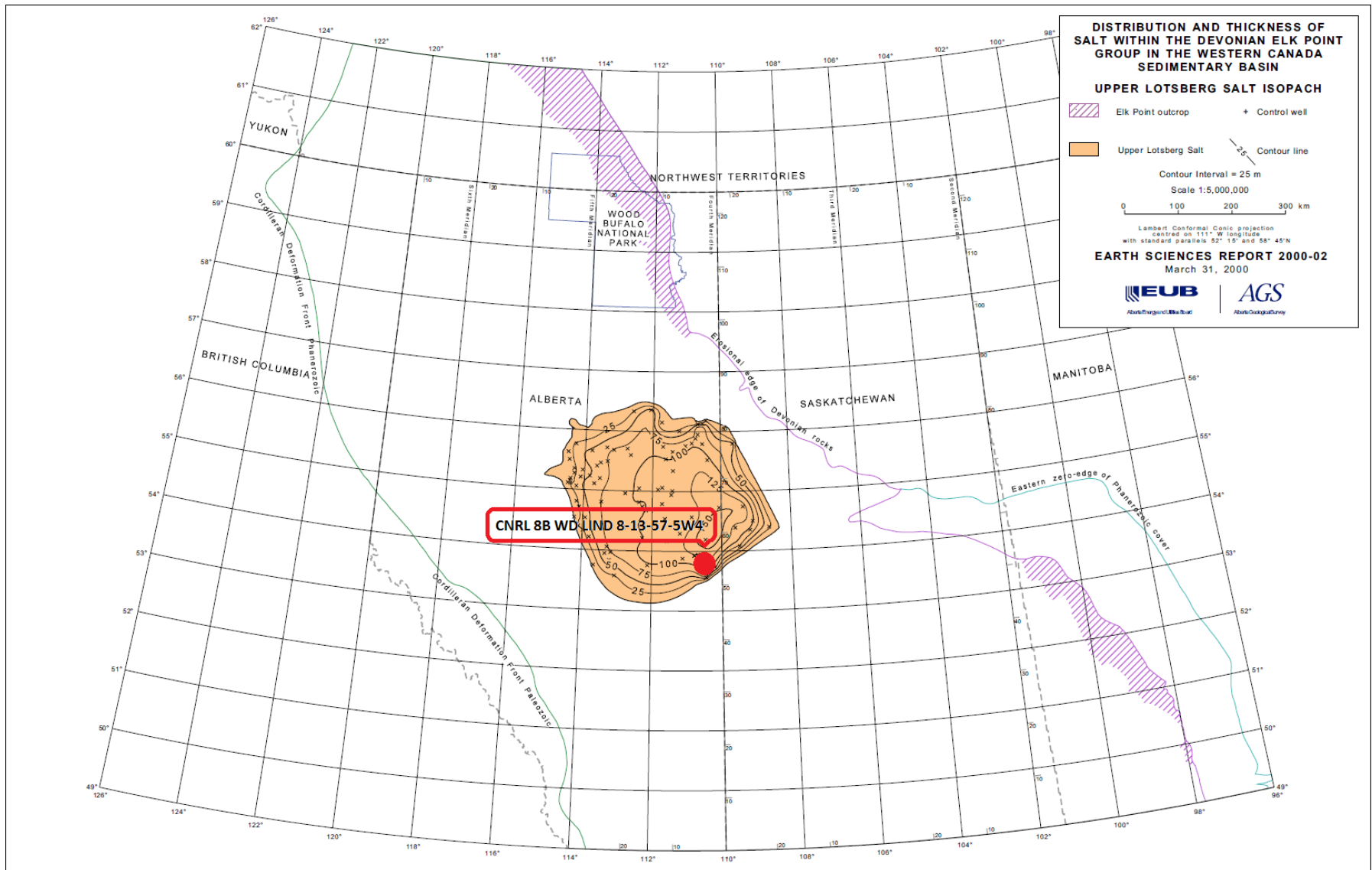


Figure 13. Thickness and distribution of the Upper Lotsberg Formation, the position of the study area is indicated by the red dot. (Adapted from Grobe (2000)).

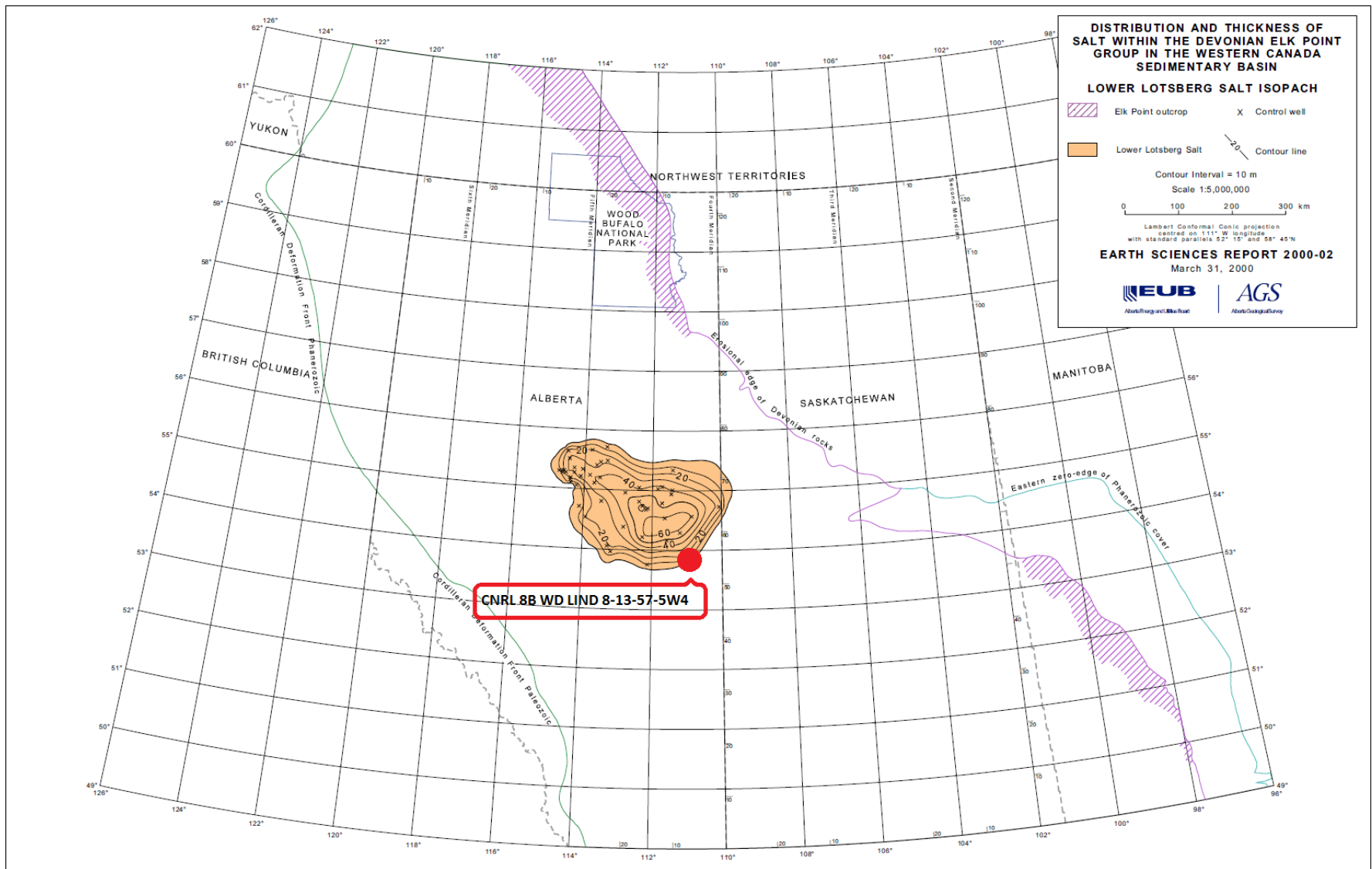


Figure 14. Thickness and distribution of the Lower Lotsberg Formation, the position of the study area is indicated by the red dot. (Adapted from Grobe (2000)).

3. GEOMECHANICAL TESTING PROGRAM

3.1 Core storage and specimen preparation

Core samples were obtained from the well designated CNRL 8B WD LIND 08-13-57-5W4. The 90 mm diameter (approximate) cores were delivered in lengths of 1.5 m. Upon receipt, they were photographed, encased in polyethylene, and transferred to 150 mm diameter Schedule 40 pipe. Free space within the pipe was filled with mineral oil, and samples were stored vertically in a core storage rack (Figure 15). A summary of the core is provided in Table 1. The modified average RQD (rock quality designation) was based on samples greater than 200 mm in length, to provide an indication of which samples were viable for testing:

$$RQD_{mod} = \frac{L_{sum\ of\ core\ pieces\ longer\ than\ 200\ mm}}{L_{total\ core\ run}} \quad (\text{Eqn. 1})$$

The complete core summary is provided in Appendix B.



Figure 15. Photograph of core storage at the University of Alberta (Edmonton, Alberta, Canada)

Table 1. Summary of CNRL 8B WD LIND 08-13-57-5W4

Core Run	Depth (m)	Cut/Received (m)	Formation	Average RQD _{mod} (%)
1	885.5-894.5	9.0/9.0	Watt Mountain	55
2	894.5-903.5	9.0/9.1	Watt Mountain Prairie Evaporite	43 65
3	960.0-969.0	9.0/9.0	Prairie Evaporite	40
4	969.0-978.0	9.0/9.0	Prairie Evaporite	63
5	1030.0-1039.0	9.0/9.0	Prairie Evaporite	98
6	1039.0-1048.0	9.0/8.8	Keg River	65
7	1120.0-1129.0	9.0/9.0	Contact Rapids	63
8	1129.0-1138.0	9.0/9.3	Cold Lake	91
9	1156.0-1165.0	9.0/9.0	Cold Lake	94
10	1165.0-1174.0	9.0/9.0	Cold Lake Ernestina Lake	91
11	1174.0-1183.5	9.5/9.4	Ernestina Lake	91
12	1183.5-1192.5	9.0/9.0	Ernestina Lake Lotsberg	80 69
13	1192.5-1201.5	9.0/9.0	Lotsberg	90
14	1201.5-1210.5	9.0/9.0	Lotsberg	90

3.2 Sample Preparation

Samples for geomechanical testing required specific dimensions related to the available testing equipment (constraints on diameter), length to diameter ratios and finishing tolerances.

In general, right cylindrical samples were prepared according to ASTM Standard D4353-08 - Specimen Preparation. It was noted that ASTM specifies that the diameter of the specimens for strength testing should be a minimum of ten times greater than the largest crystal size within the sample. This requirement could not be met for the majority of salt rock core, as the salt crystals ranged from 10 to 70 mm.

In the first step, parallel ends of the cylinder were created using a diamond saw (Figure 16). For samples of larger crystal size (i.e. most Prairie Evaporite Salt and all Lotsberg Salt), the original core was protected using chemical-resistant, flame-retardant PVC heat-shrink tubing to provide stability and minimize cracking.

Initially, the maximum diameter that could be accommodated in the triaxial cell was 76 mm, necessitating machining samples in a lathe with a diamond tipped bit. For all salt samples, as well as weathered core (portions of the Watt Mountain and Keg River formations), machining of the samples was difficult and samples tended to fracture and/or fail in the lathe (Figure 17). As a result, the decision was made to modify testing equipment to accommodate full size (89 mm) core.

Final preparation of the parallel ends of the samples (to meet tolerances as prescribed by ASTM Standard D4543 (2008)), was completed using the lathe or automated concrete sanding machine to remove any damaged material until an intact, smooth surface was acquired. Small chips on the parallel ends of the specimen were filled with epoxy to ensure a correct force-stress correlation. The ends were then finished with a hand-held automatic sander with fine grit sandpaper.



Figure 16. Cutting perpendicular ends.



Figure 17. Failure of core sample while lathing.

3.3 Laboratory assessment methodology

The laboratory component of the geomechanical assessment included both index testing and mechanical testing. Index testing describes the basic physical properties of the samples tested. Mechanical testing characterizes the strength and deformation properties of a sample under various stress and stress-path conditions. The following sub-sections provide a description of the testing carried out.

3.3.1 Water Content and Density

Water content of cores was determined by drying a sample in 105°C oven over successive 24 hour periods in general accordance with ASTM D2216. After each 24 hours period, the sample was placed in a desiccator and allowed to cool, and then weighed on an electronic scale with a resolution of 0.01 grams. When the difference in the calculated water content over successive periods was less than 0.1%, the sample was considered dry.

All specimens were measured with a Mitutoyo caliper accurate to 0.01 mm. Six diametric and six axial measurements were taken. Subsequently, all specimens were weighed using an electronic scale with an accuracy of 0.01 grams (a typical specimen weighted ~1500 grams). These values were used to calculate the bulk density of the rock core.

3.3.2 Particle Size Distribution

To determine the particle size distribution of the constitutive sediments in the clastic sedimentary rock samples, grinding of dried samples was required. To minimize grinding effort (so as not to impact size distribution), samples were ground to pass through the #40 sieve (0.42 mm). Sufficient material was then weighed out for completion of the test. Sodium metahexaphosphate was added to the sample together with distilled water and the sample was allowed to soak for a minimum of 72 hours. This allowed the dispersion of the clay/silt particles. The particle size distribution was carried out in accordance with ASTM D422-63 (2007), Standard Test Method for Particle Size Distribution of Soils.

Grain size of the salt formations was determined by measuring crystals on the sanded or lathed surfaces of specimen prior to geomechanical testing.

3.3.3 Insoluble Content of Salt Rocks

Core samples from the salt formations were dried in a similar process to rock core. The insoluble content was determined in general accordance with ASTM E534-08 Chemical Analyses of Sodium Chloride. Samples were ground by hand to less than 2.36 mm (# 8 sieve). A 25 gram (+/-) sample was placed in a high speed blender with approximately 200 ml of triple distilled water and blended for 5 minutes. Subsequently, the sample was transferred to a beaker with a magnetic stirrer and agitated for one hour. The resulting solution was filtered under vacuum through a 0.2 μm filter (pre-weighed). The filter retained the insoluble constituents in the solution.

3.3.4 Pore Water Chemistry

To provide some indication of migration of salt from the Lotsberg formation into Ernestina Lake, testing was carried out to determine the salt concentration of pore fluids within the Ernestina Lake Formation. Due to the low natural water content of the Ernestina Lake core, and the tightness of the formation, typical methods of extracting pore fluid (centrifuge and compression) could not be used. Based on work completed for the Geoscientific Site Characterization Plan (GSCP) for the Bruce Deep Geologic Repository (DGR) program, an alternative method in which pore water are extracted by

vacuum distillation of crushed core material, and hydro-geochemical analyses is conducted on leachate of the vacuum extracted (dried) crushed core material (Clark et al., 2010).

3.3.5 XRD and SEM analysis

X-ray diffraction analysis is the method by which multiple beams of x-ray create a three dimensional picture of the density of electrons of any crystalline structure. The aim is to identify—with a high degree of certainty—the composition of the molecules, on an atomic scale. X-Ray diffraction analyses were carried out by AGAT laboratories in Calgary on seven rock core samples (Table 2). A summary of the procedure provided by AGAT is given in Appendix C.

A scanning electron microscope (SEM) uses a focused beam of high-energy electrons to generate a variety of signals at the surface of solid specimens. The signals that derive from the interaction of sample and electron provide information on the external morphology (texture), chemical composition, and crystalline structure and orientation of materials making up the sample. In most applications, data are collected over a selected area of the surface of the sample, and a 2-dimensional image is generated that displays spatial variations in these properties. Areas ranging from approximately 1 cm to 5 microns in width can be imaged in a scanning mode using conventional SEM techniques. SEM imaging was carried out by AGAT laboratories in Calgary on seven rock core samples (Table 2). The images can be found in Appendix E.

Table 2. Samples analyzed by AGAT laboratories

Sample #	Depth	Formation	Analysis methods
1	896.9 m	Watt Mountain Formation	XRD and SEM
2	977.4 m	Prairie Evaporite Formation	XRD and SEM
3	1036.7 m	Prairie Evaporite Formation	XRD and SEM
4	1047.5 m	Keg River Formation	XRD and SEM
5	1177.6 m	Ernestina Lake Formation	XRD and SEM
6	1187.1 m	Ernestina Lake Formation	XRD and SEM
7	1207.8 m	Lotsberg Formation	XRD and SEM

3.3.6 Ultrasonic Wave Velocity

Aim

Measurement of ultrasonic wave velocity is a simple indirect means to evaluate geomechanical behaviour between samples of the same formation. The differences in measured values may be the

result of mineralogy, grain/crystal sizes or crack characteristics. These velocity measurements assess the homogeneity of the rock core, and provide a comparison between rock cores within a specific formation. Ultrasonic wave velocity measurements were performed on all BTS, UCS, CMC, CME, STC and creep samples prior to testing.

Apparatus

The apparatus consisted of two Sinco transducers, one that acts as the transmitter of the sonic pulse and converts electrical pulses into mechanical pulses. The second acts as a receiver that converts mechanical pulses into electrical pulses. These sensors were connected to a Terrametrics Sonic Pulse Generator that generated the signal and a Philips Oscilloscope on which the signal could be read.

Calibration

To determine the travel times through the sensor and provide a zero for subsequent readings on rock core, an aluminum specimen of known velocities was placed in the apparatus. Compressive and shear wave velocities were recorded. In addition, the two sensors were placed end to end and compressive and shear wave velocities were recorded.

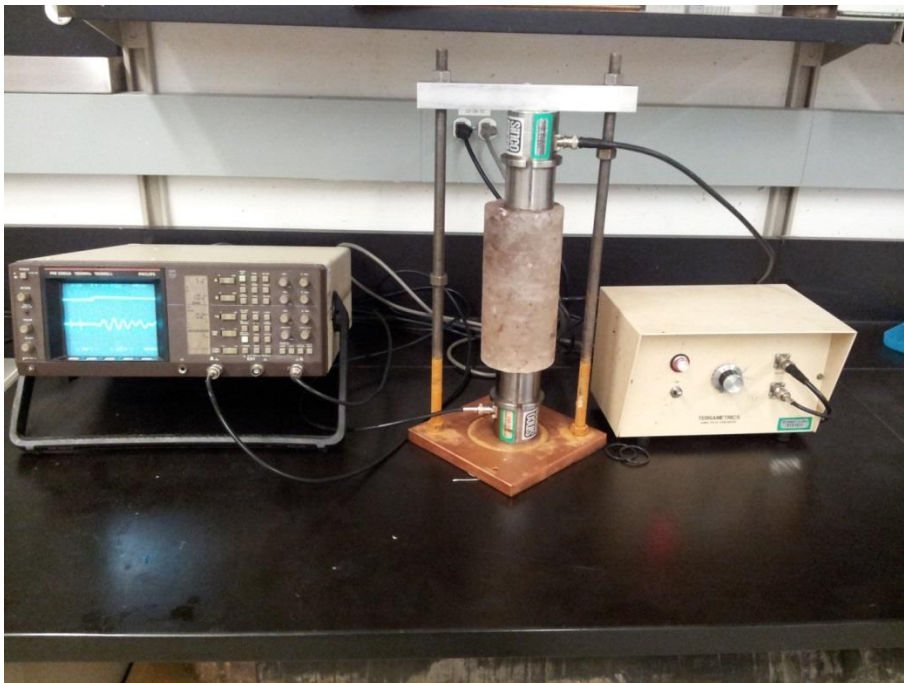


Figure 18. Left = Philips oscilloscope, Middle = Sample with pulse transmitter and receiver, Right = Pulse generator

Procedure

The testing was done in general accordance with ASTM D2845-08, Standard Test Method for Laboratory Determination of Pulse Velocities and Ultrasonic Elastic Constants of Rock. The ends of the samples were prepared with vacuum grease to facilitate the transmission of the signal from the sensors through the rock core. Measurements of compressive and shear wave velocities were completed for all samples along the longitudinal axis.

The compressive wave is the first to arrive, and its detection is relatively easy. The travel time is determined using the oscilloscope. The shear wave arrival may be obscured by reflections of the compressive wave and/or vibrations due to ringing of the transducers. The velocity of the wave is calculated as length of the sample divided by time.

Data Processing

P and S wave velocities and density can be used to calculate ultrasonic moduli, utilizing the following relationships.

$$\text{Young's Modulus} = E_{\text{dynamic}} = \frac{\rho(V_s^2)(3V_p^2 - 4V_s^2)}{(V_p^2 - V_s^2)} \quad (\text{Eqn. 2})$$

$$\text{Poisson's Ratio} = \nu_{\text{dynamic}} = \frac{V_p^2 - 2V_s^2}{2(V_p^2 - V_s^2)} \quad (\text{Eqn. 3})$$

Since accurate determination of the shear wave arrival was often not possible, the dynamic values are subject to significant uncertainty. They are mainly used to assess variation of properties within formations.

3.3.7 Brazilian Indirect Tension Tests (BTS)Aim

The tensile strength of a material is a measure of its ability to resist uniaxial tensile loads without yielding or fracture. A direct-pull uniaxial test is difficult to apply to rock and in many cases some type of indirect test is employed to determine tensile strength. The Brazilian test, where a disc of the test material is loaded across a diameter, is often employed.

Apparatus

The setup used for Brazilian indirect Tensile Strength (BTS) testing consisted of an MTS 815 load frame equipped with a protective chamber. The sample was placed in curved platens to overcome stress concentration problems (Mellor and Hawkes, 1971). Because of the relatively low force required (<50

kN) to reach failure and the high capacity of the load frame (approximately 2668 kN), an external load cell (accurate to 0.2 kN) was placed in the system to more accurately record the load on the sample. Load cell data was recorded using a DT80G Datalogger and displacement of the piston was recorded by the MTS system software. The setup can be seen in Figure 19.

A modified setup without curved platens was used for the Prairie Evaporite Formation and Lotsberg Formation specimens. This was done because initial testing with the use of curved platens resulted in the salt samples conforming to the curved shape of the platens before failure occurred, thereby distributing the load over a larger area which resulted in misrepresentative tensile strength values.

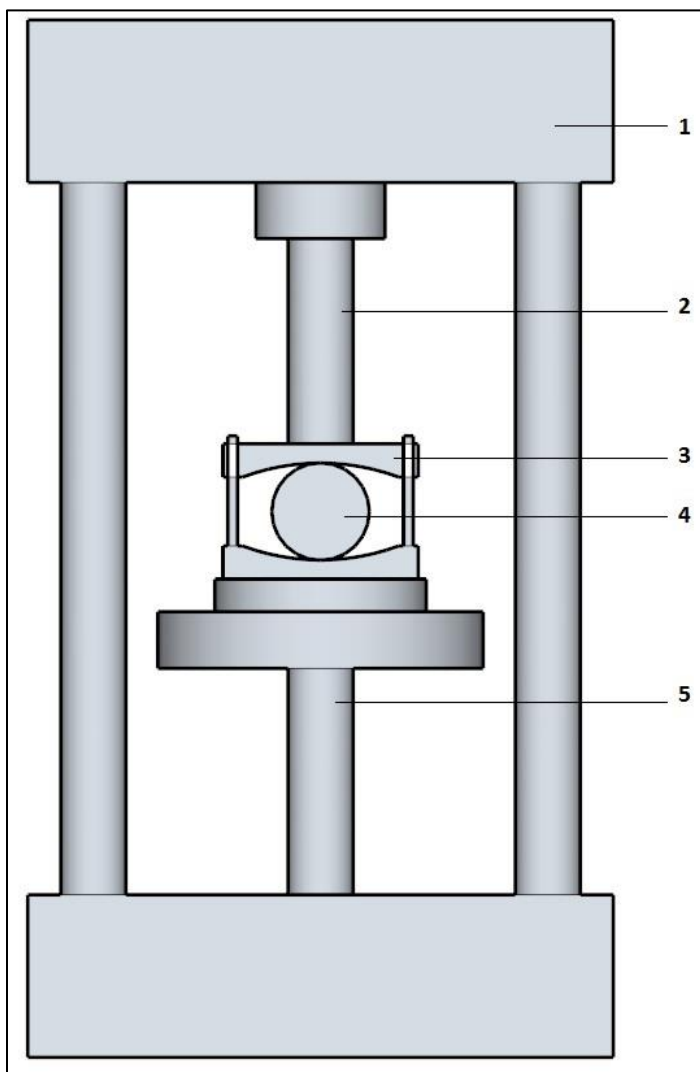


Figure 19. Setup of the BTS test. 1 = Load frame, 2 = Load cell, 3 = Curved platens, 4 = Sample, 5 = Hydraulic piston

Procedure

BTS testing was carried out in general accordance with ASTM Standard Test Method for Splitting Tensile Strength of Intact Rock Core Specimens (D3967-08), using displacement control mode on the MTS 815 frame. Depending on the material, a deformation rate of 0.15 – 0.30 mm per minute was chosen, corresponding to a diametric strain rate of $3.3 \times 10^{-5} \text{ s}^{-1}$ to $6.6 \times 10^{-5} \text{ s}^{-1}$. Once failure of the sample occurred, the load frame was stopped, the sample removed and photographed and the data files were written onto a backup disk. Load and displacement were recorded using the internal load cell and LVDT in the MTS frame, as well as through an external load frame and LVDT. This was done because of the high capacity of the MTS frame and the expected low loads needed to fail the samples.

Data Processing

Load and displacement were recorded through the MTS frame and through an external load cell and LVDT. When both datasets were available and in general agreement, the MTS data was used for final calculations. The indirect tensile strength was calculated as follows:

$$\sigma_T = \frac{2F}{\pi LD} \quad (\text{Eqn. 4})$$

where σ_T = strength in kPa, F is the force in kilo-Newton, L is the thickness of the sample in meters and D is the diameter of the sample in meters.

During a BTS test, compression of the sample induces tensile stresses normal to the diameter, parallel to the flat ends of the disc (Figure 20). Concerns have been raised that this test does not produce accurate results, because the assumption that the disc fails in tension might not be valid, especially if the ratio between the compressive and tensile strength of the material is low. Fairhurst (1964) shows an elaborate mathematical analysis of the method and concludes that for such materials, the tensile strength is underestimated. Fairhurst (1964) also shows that a larger contact surface increases the validity of the test by making the test more representative for the whole specimen rather than just a point in it. Mellor and Hawkes (1971) propose the use of curved platens to accomplish this larger contact area. It should be noted however, that this contact area should ideally be 9.46° ($\tan^{-1} \frac{1}{6}$) and should not increase during the testing procedure. In a review of the Brazilian method by Andreev (1991), based on experimental work, comparing Brazilian Tensile Strength values to uniaxial tensile strength values for the same materials, it is concluded that the Brazilian Tensile Strength test gives accurate and representative results for all materials that exhibit brittle failure, regardless of their compressive to tensile strength ratio.

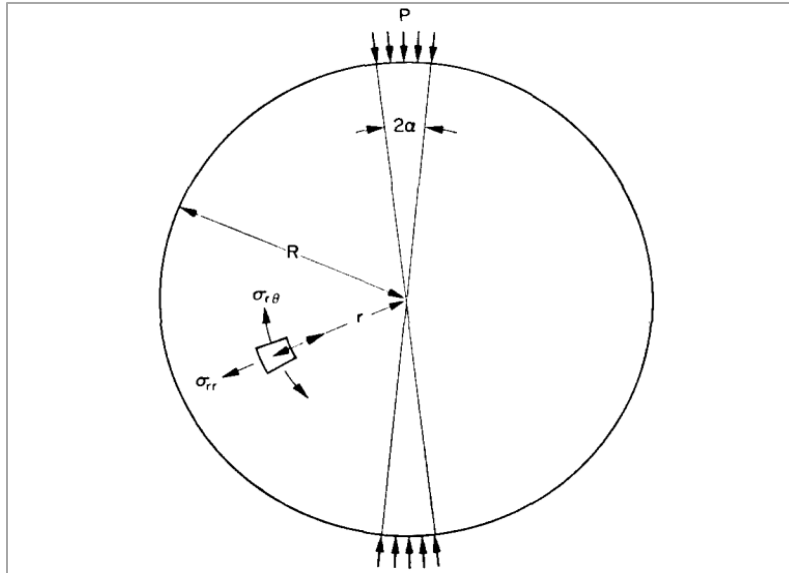


Figure 20. Compression (vertical in this image) results in tensile stress normal to the diameter of the sample. (Fairhurst, 1964)

3.3.8 Unconfined Compressive Strength (UCS)

Aim

The unconfined compressive strength (UCS) test is a triaxial test with zero confining pressure. The compressive strength of a material is a measure of its ability to resist uniaxial compressive loads without yielding or fracture. Young's modulus and Poisson's ratio can be determined from the elastic portion of the resulting stress-strain curve.

Most rocks are generally brittle, and failure normally takes place without much plastic flow and fracture occurs. However, this is not the case for rock salt, which may experience significant non-elastic deformation before failure.

Apparatus

The setup used for Unconfined Compressive Strength testing consisted of an MTS 815 load frame equipped with a protective chamber. Axial deformation was measured using Linear Voltage Displacement Transducer (LVDTs), along the longitudinal axis. To determine the diametric deformation of the sample during the elastic phase, three LVDTs were placed on the sample at mid-height and at 120 degrees from each other. LVDT data and load cell data was recorded using a DT80G Datataker and displacement of the piston was recorded by the MTS system software. A typical set-up is illustrated schematically in Figure 21.

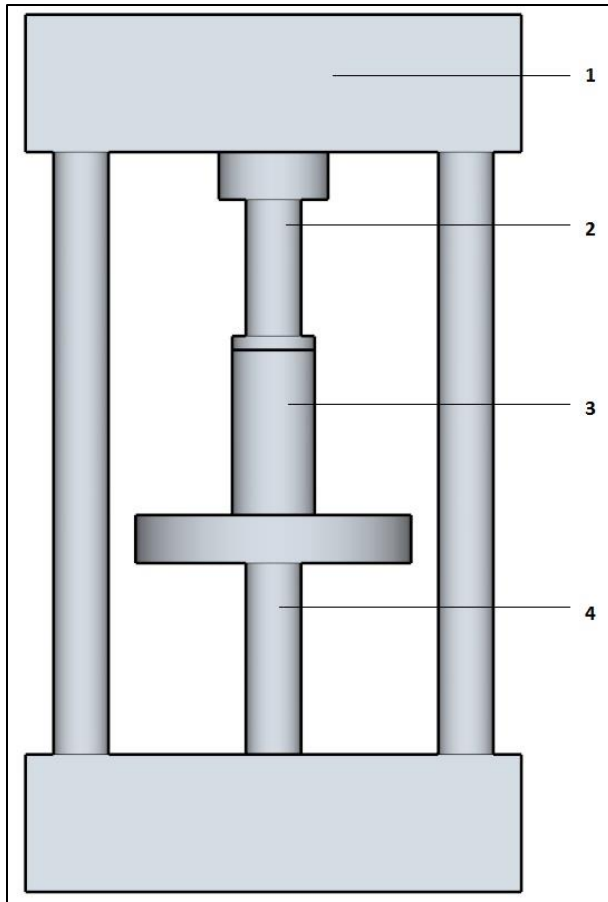


Figure 21. Setup of the UCS test. 1 = Load frame, 2 = Load cell, 3 = Sample, 4 = Hydraulic piston

Procedure

The testing was done in accordance with ASTM Standard Test Method for Compressive Strength and Elastic Moduli of Intact Rock Core Specimens (D7012-10). The testing was carried out using displacement control mode on the MTS frame. All tests were conducted on right circular cylindrical specimens. Depending on the material, typical deformation rates were in the range of 0.15 – 0.30 mm per minute, corresponding to a strain rate of $3.3 \times 10^{-5} \text{ s}^{-1}$ to $6.6 \times 10^{-4} \text{ s}^{-1}$. The intent was to induce failure within 4 to 15 minutes of the onset of loading. Once failure of the sample occurred, the load frame was stopped, the sample removed and photographed and the data files copied to a backup disk.

Load and displacement were recorded through the MTS frame and through an external load cell and LVDT. Furthermore, three LVDTs recorded diametric changes in the sample halfway between the parallel ends.

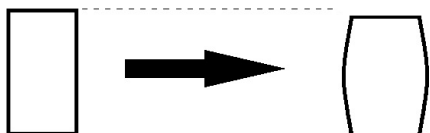
Data Processing

The axial stress on the sample was calculated as: $\sigma = \text{Force} / A_{\text{Corr}}$

Area corrections according to ASTM D5102 were utilized when the sample had undergone significant axial deformation as follows:

Brittle Failure: $A_{\text{Corr}} = A_0$  (Eqn. 5)

Cylindrical Failure: $A_{\text{Corr}} = \frac{A_0}{1 - \varepsilon}$  (Eqn. 6)

Barrel Failure: $A_{\text{Corr}} = \frac{A_0}{1 - 0.6\varepsilon}$  (Eqn. 7)

where A_0 is the original area and ε is the axial strain. Although commonly used for soils, these corrections are usually not required for rock specimen. However, because of the high axial and radial deformation commonly reached by salt rock samples, the use of area corrections was deemed necessary to ensure accurate results.

The unconfined compressive strength of a sample was taken as the highest stress recorded on the sample. The Young's modulus E was calculated from the slope of the stress – strain curve in the linear low strain regime, in which the sample is assumed to behave elastically. The Poisson's ratio ν is determined by from the ratio of the axial strain and diametric strain curve according to:

$$\nu = - \frac{\text{slope of the axial stress vs. strain curve}}{\text{slope of the diametric stress vs. strain curve}} \quad (\text{Eqn. 8})$$

3.3.9 Standard Triaxial Compression Test (STC)

Aim

A Standard Triaxial Test is schematically illustrated in Figure 22. The Aim of the triaxial test is to develop a failure criterion. From a series of triaxial tests, peak stresses (axial) are obtained for various confining stresses. By plotting in Mohr space, a 2D representation of the state of stress in the sample is

provided. A failure envelope can be defined, and the cohesion and internal friction angle can be determined. Alternatively, a p-q diagram may be constructed to determine the strength parameters.

Apparatus

The standard triaxial testing was carried out by CANMET Mining and Mineral Sciences Laboratories, Ground Control Program, a division of Natural Resources Canada. This laboratory was utilized for their capability of handling the full diameter 89 mm core of high strength rock. They utilized a test frame with 2600 kN capacity. Axial deformation was measured with three LVDTs and circumferential displacements with an MTS chain extensometer.

Procedure

Standard triaxial compression tests (STC) were carried out in accordance with ASTM Standard Test Method for Compressive Strength and Elastic Moduli of Intact Rock Core Specimens (D7012-10). Over the duration of the tests, measurements of axial load, and axial and circumferential deformations were recorded at periodic intervals.

A load/unload step was incorporated into the testing program to measure Young's modulus and Poisson's Ratio. Tests were conducted at various confining pressures, typically 5, 10, 15 and in-situ pressure (MPa) to allow the construction of a failure envelop.

Data Processing

All primary data processing was completed by CANMET Mining and Mineral Sciences Laboratories. Further processing was done by combining the STC data with UCS data in order to create p-q diagrams for the determination of angle of internal friction and cohesion. This was done by calculating the p and q value at failure according to

$$p = \frac{\sigma_1 + \sigma_3}{2} \quad (\text{Eqn. 9})$$

$$q = \frac{\sigma_1 - \sigma_3}{2} \quad (\text{Eqn. 10})$$

where σ_1 is the highest principle stress and σ_3 is the lowest principle stress (compression is defined as positive). Angle of internal friction and cohesion were determined by fitting a linear best-fit line through the data in p-q space: $q = \psi p + d$.

The angle of internal friction and cohesion were then calculated according to Lambe and Whitman (1991):

$$\phi = \arcsin(\tan \psi) \quad (\text{Eqn. 11})$$

$$c = \frac{d}{\cos \phi} \quad (\text{Eqn. 12})$$

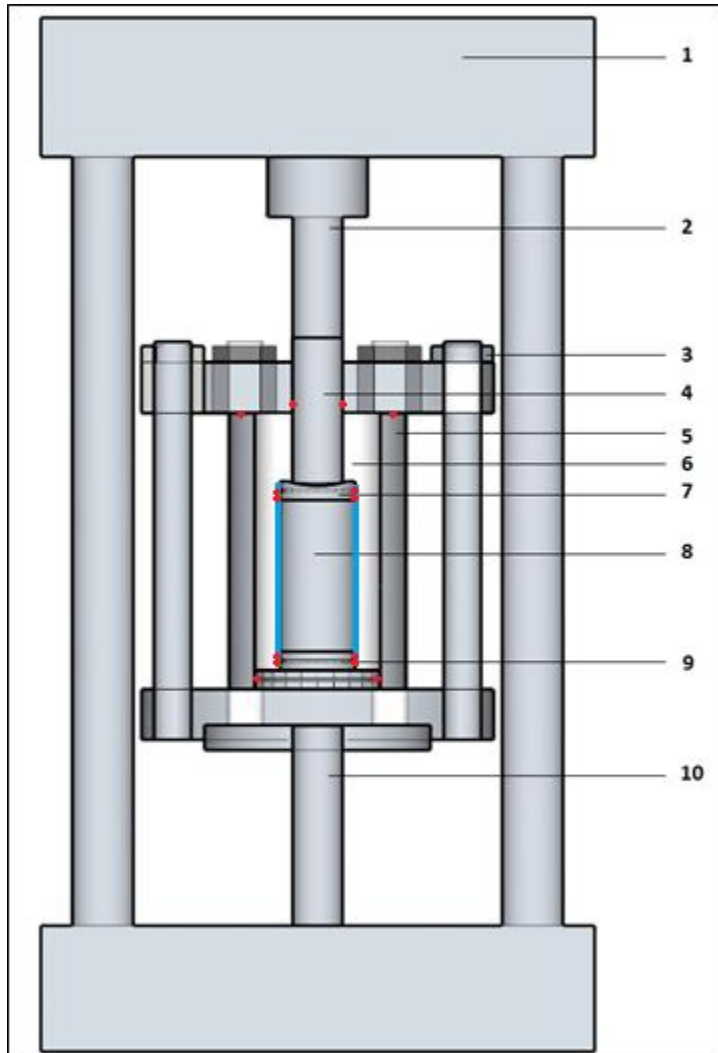


Figure 22. Schematic Set-Up Triaxial Testing. 1 = Load frame, 2 = Load cell, 3 = Triaxial cell bolt, 4 = Piston, 5 = Triaxial Cell, 6 = Confining fluid, 7 = Top platen, 8 = Specimen, 9 = Bottom Platen, 10 = Hydraulic Piston. O-rings are indicated in red, the sample membrane is indicated in blue.

3.3.10 Constant Mean Stress Tests

Aim

Mean stress is defined by Equation 13.

$$\sigma_m = \frac{\sigma_1 + \sigma_2 + \sigma_3}{3} \quad (\text{Eqn. 13})$$

In a triaxial test on cylindrical specimens, $\sigma_2 = \sigma_3 =$ confining pressure and therefore:

$$\sigma_m = \frac{\sigma_1 + 2\sigma_3}{3} \quad (\text{Eqn. 14})$$

The constant mean stress test is considered the most appropriate method for estimating the dilation limit of rock salt, as compared to standard triaxial testing (Mellegard and Pfeifle, 1998). This is of particular importance with respect to underground storage caverns.

Apparatus

Constant Mean Stress Triaxial Compression (CMC) and Constant Mean Stress Triaxial Extension (CME) testing was performed in a triaxial cell with either water or oil confining fluid to provide confining pressure. A Teledyne ISCO 260D syringe pump was used to apply the confining pressure. The triaxial cell was placed in either an INSTRON 600LX load frame or an MTS 370 load frame. The setup used was identical to the setup for STC testing shown in Figure 22. Both the INSTRON and MTS systems are equipped with internal load cells and LVDTs, which were used to measure the axial load and axial deformation respectively. Given the expected radial deformation in the samples, circumferential chain extensometers were not an appropriate option. In addition, the use of submersible LVDTs in a configuration similar to the one in UCS testing could not be accommodated in the triaxial cell.

For CMC tests, the piston and the top platen are two separate pieces and have a spherical contact surface to ensure that the axial load is applied along the longitudinal axis of the sample at all times. For CME tests, in which the confining pressure is greater than the axial pressure, the top platen must be integrated with the piston, as one piece. If not, confining fluid would penetrate the contact between the piston and top platen.

Penetration of the confining fluid into the sample and chemical interaction between the sample and the confining fluid was prevented by the use of a Viton membrane or two latex membranes, sealed at the top and bottom platens with four O-rings. Cell pressure data was recorded through Labview running in a Windows 7 environment while displacement and axial load data was recorded through either the INSTRON or MTS native software.

Calibration

Before performing tests on natural samples, calibrations were run using an aluminum sample of known properties. Two types of calibration tests were conducted.

- Compressibility calibration. In this test, the correlation between applied confining pressure and volume displacement was determined for both for water and oil. In addition, this calibration was carried out for samples of 76 mm and 89 mm in diameter. The exact volume of oil, and corresponding compressibility was not known to a satisfactory degree of precision to allow a purely theoretical correction factor to be applied. Given that internal LVDTs could not be accommodated within the triaxial cell, this calibration was used to correct the volume measurements, to allow calculation of volumetric strains in natural samples.
- Frame Stiffness. A second calibration procedure was used to assess the frame stiffness, by loading and unloading a sample of known strength and deformation properties. These tests indicated that the frame stiffness was not a factor relative to the formations tested.

Procedure

Before testing commenced, the cell pressure line was purged to remove all air, the pump reservoirs were filled and air was expelled from the system. For both CMC and CME tests, the sample was hydrostatically loaded to original in-situ pressure (assuming a pressure gradient of 23 kPa/m) in 5 minutes by programming an axial load gradient in the load frame software and a confining pressure gradient on the Teledyne ISCO pump controller. After the sample was hydrostatically loaded, the sample was kept under these conditions until all measured values had stabilized (load, axial deformation and pump volume). Next, the sample was either hydrostatically unloaded to a predetermined hydrostatic pressure of 5, 10, 15 MPa by programming gradients on the load frame and the ISCO pump, or kept at the original in-situ pressure. If the sample was partially unloaded, the sample was left at this new pressure again until all measured values had stabilized, before initiation of the next step.

During the next step, the sample was axially loaded to a differential load of 5 MPa in two minutes and subsequently unloaded to hydrostatic conditions (in two minutes) in order to determine the Young's modulus under in-situ conditions. Based on the UCS tests on the salt formations, a differential of 5 MPa was expected to still be within the elastic range. (In initial tests, a deformation control was used in the load/unload cycle, however, this provided spurious results.)

At the completion of the load/unload stage, the CMC and CME procedures diverge. In the CMC test, the axial stress is increased at a constant specified rate, and the confining stress is decreased

accordingly to maintain a constant mean stress. Conversely in the CME tests, the axial stress is decreased and the confining pressure is increased. During a CMC test, the axial load was increased at a set rate, while the confining pressure was lowered at a lower rate in order to keep the mean stress (σ_m) on the sample constant.

Both the CMC and CME tests were continued until failure of the sample occurred, or the capacity of the frame or zero confining pressure were reached. In the latter cases, the sample was allowed to creep until failure occurred under constant mean stress.

Data Processing

Data logging for the CMC and CME tests was done using Labview for the ISCO pump data and native software associated with the internal load cell and LVDT of either the INSTRON or MTS load frames. Axial stresses were calculated as load divided by sample area. Area corrections were not applied as all test parameters associated with the load frame were pre-programmed prior to the start of the test. Axial strain was calculated as axial deformation divided by original sample length. Diametric strains were calculated using the volume change recorded in the ISCO pump. Corrections were applied to account for volume changes due to compressibility of fluid in the system, piston movement and axial deformation. The remaining volumetric change was attributed to changes in the diameter of the specimen. The overall volumetric strain was calculated as:

$$\varepsilon_v = \varepsilon_a + 2 \varepsilon_d \quad (\text{Eqn. 15})$$

where ε_v is the volumetric strain, ε_a is the axial strain and ε_d is the diametric strain.

3.3.11 Creep Testing

Aim

The aim of creep testing is to investigate the permanent deformation behaviour of specimen at sub-failure differential stresses. This includes the dependence of strain rate on differential stress, as well as dilation behavior. By subjecting one specimen to a range of differential stresses, the stress-dependence of strain rate can accurately be described without the introduction of noise by inter-sample variability.

Apparatus

For the creep tests, a dual cell setup as depicted in Figure 23 was used. In the bottom cell, a piston with a diameter of 7 inch (177.8 mm) was used to provide axial loading to the sample in the top cell. Force is applied to the piston by application of pressure to the cell fluid (oil) in the bottom chamber.

The piston was fitted with a Teflon ring on its circumference to minimize friction during piston movement and to prevent leakage along the piston sidewall. The bottom cell was equipped with a Linear Variable Differential Transformer (LVDT) in order to measure displacement accurate to 0.01 mm. The LVDT was connected to a standalone Datataker to ensure continuous data logging. The top cell was equipped with a 3 inch (76.2 mm) piston. Confining pressure was applied to the cell fluid (oil). Pressures in the top (confining) and bottom (axial) cells were controlled by two separate Teledyne ISCO 260D syringe pumps connected to one Teledyne ISCO D-series controller. Data logging for the pumps was performed in Labview running in a Windows 7 environment. Chemical interaction between the sample and the confining fluid was prevented by the use of a Viton membrane, PVC heat-shrink tubing or two latex membranes, sealed at the top and bottom platens with four O-rings.

Calibration

Before performing tests on natural specimens, calibration tests were conducted using an aluminum sample, with known strength and deformation properties. Two types of calibration tests were performed:

- Load Calibration. In this test, the correlation between the applied pressure in the pump and applied load on the specimen was determined. Both loading and unloading relationships were determined. It also provided an indication of losses in load due to friction. The pressure-load curve that was obtained through this procedure was used to calculate the load on the samples in subsequent tests.
- Compressibility calibration. In this test, the correlation between applied confining pressure and volume displacement is determined. This calibration was performed as the exact compressibility of the oil used and the exact volume of oil in the system were not known to a satisfactory degree of precision. This second calibration run was used to correct the volume measurements on natural sample tests in order to obtain volumetric strain measurements.

Procedure

Multi-stage creep testing was carried out on both the Prairie Evaporite and Lotsberg formations. Before testing commenced, all lines were purged, pump reservoirs were filled and all air was expelled from the system. All samples were loaded to a hydrostatic stress state corresponding to their original depth, assuming a pressure gradient of 23 kPa/m. Loading to hydrostatic conditions was done by manually increasing the axial load and confining pressure in increments, such that the difference

between the axial and confining pressures was less than 10 percent. Once the sample had reached the desired hydrostatic pressure, the loads were maintained for approximately 24 hours. Subsequently, the confining pressure was decreased by a specified amount to apply differential stress to the sample. The change in confining pressure was achieved in less than 10 s and was therefore assumed to be instantaneous. This differential stress increment was maintained until steady state creep was apparent. When a sample had reached steady state creep, the differential stress was increased by lowering the confining pressure. This procedure was repeated for a minimum of 4 load stages or the sample failed.

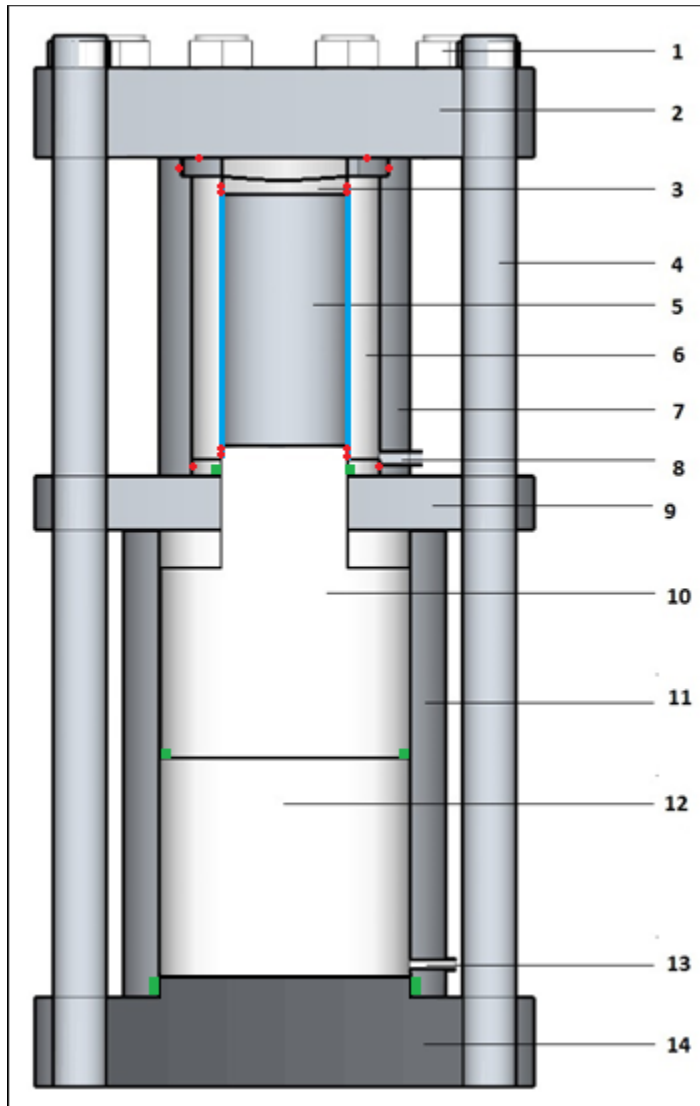


Figure 23. Creep Test Set Up. 1 = Top bolts, 2 = Top section creep cell, 3 = Top platen, 4 = Connecting rods, 5 = Creep specimen, 6 = Confining fluid, 7 = Top (creep) cell, 8 = Confining fluid inlet (from ISCO pump), 9 = Middle section, separates top and bottom cell, 10 = Piston, 11 = Bottom (piston) cell, 12 = Piston fluid (providing axial load on specimen), 13 = Piston fluid inlet (from ISCO pump), 14 = Bottom section. O-rings are indicated in red, u-cup seals in green, the sample membrane is indicated in blue.

Data processing

Data logging for creep tests was done using Labview for the Isco pump data and a Datataker for the LVDT data. For each stress state, the von Mises stress and the steady state strain rate were determined. A sample was assumed to have reached steady state flow when no significant change in strain rate occurred in three consecutive days. Depending on the von Mises stress, this generally took four to twelve days per load step. See Appendix D for the duration of each load step for every test. Subsequently, the data was fitted to a flow law.

$$\dot{\epsilon} = A \bar{\sigma}^n \quad (\text{Eqn. 16})$$

where $\dot{\epsilon}$ is the strain rate in s^{-1} , A is a material constant [$Pa^{-n} s^{-1}$], $\bar{\sigma}$ is the von Mises stress in Pa and n is a dimensionless material constant. The parameters A and n for Equation 15 were determined as follows.

Taking the natural logarithm on both sides of Equation 15 results in

$$\ln \dot{\epsilon} = n \ln \bar{\sigma} + \ln A \quad (\text{Eqn. 17})$$

This is a linear function in the form of $y = ax + b$. Plotting measured $\ln \dot{\epsilon}$ and $\ln \bar{\sigma}$ allows fitting of a linear function using simple linear regression which results in parameters a and b which represent n and $\ln A$ respectively. This method allows for simple fitting of an appropriate n and A value in Equation 15 to any dataset that shows roughly linear behavior in $\ln \dot{\epsilon} - \ln \bar{\sigma}$ space.

This procedure results in a purely empirical fit to describe flow behaviour. It should not be interpreted in terms of any specific mechanism of flow. This method assumes that only one mechanism of flow operates, whereas multiple mechanisms of flow may in general be active (e.g. Van Keken et al., (1993), Urai et al., (2008)).

3.4 Laboratory Results

3.4.1 Watt Mountain Formation

Characterization

The Watt Mountain Formation consists of a dolomitic shale and is the caprock overlying the Prairie Evaporite Formation. Approximately 16 m of continuous core was obtained from the Watt Mountain Formation (Core Run No. 1 and partial Core Run No. 2) over the interval 885.5 to approximately 901.5 m depth. The interface with the Prairie Evaporite is present near the bottom of Core Run 2. From approximately 896 m onwards, the rock core appeared weathered and oxidized as shown in Figure 24.

Index testing for the Watt Mountain samples consisted primarily of measurement of water content, the determination of bulk density and grain size distribution analyses. One sample was submitted for XRD and SEM analysis. Measured water contents ranged from less than 1 percent to near 7 percent by mass. The water contents were variable with depth as shown in Appendix D. Laboratory measured bulk densities ranged from 2.50 to 2.81 g/cm³ and in general, are in close agreement to the geophysical measurements as shown in Figure 25.

Grain size distribution was determined for a limited number of samples. The particles are predominantly sand sized in the samples tested, with approximately 20 percent finer than silt sizes. A plot of grain size distribution is provided in Appendix D.

One sample, from 896 m depth was sent to AGAT laboratories for XRD analyses. This sample consists mainly of anhydrite (47%) and dolomite (33%) with minor amounts of quartz (9%), illite (7%), kaolinite (3%) and potassium feldspar (1%). The fraction less than 3µm is approximately 27% of the rock volume. The analysis suggests that the sample consists of anhydrite (precipitated from evaporative seawater or formed through the dehydration of gypsum), carbonate (dolomite - precipitated from formation water or from the dolomitization of limestone) and sand/silt/clay (quartz, illite, kaolinite and potassium feldspar). SEM Photographs are provided in Appendix E.



Figure 24. Typical weathered core material from the Watt Mountain Formation

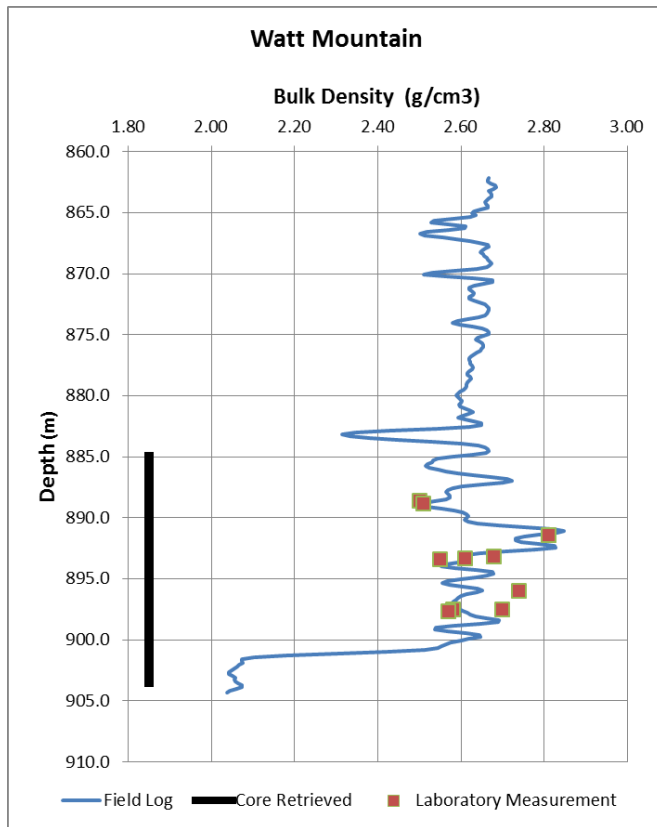


Figure 25. Comparison between laboratory and wireline log values for density in the Watt Mountain Formation

Geomechanical Test Results

Geophysical sonic logs indicated variability within the formation; therefore samples were selected from various depths to evaluate the strength properties.

Table 3 summarizes the samples prepared for geomechanical testing and the testing completed. In addition, the laboratory measured compressive and shear wave velocities, and the corresponding calculated values of Young's modulus and Poisson's ratio are also provided.

Table 3. Summary of Samples – Watt Mountain Formation

Core No.	Test	Depth (m)	Density (g/cm ³)	Laboratory Measurement			
				P Velocity (km/sec)	S Velocity (km/sec)	Ultrasonic Young's Modulus (GPa)	Ultrasonic Poisson's Ratio
Watt Mountain Formation							
3	STC	897.5	2.58	3.35	2.08	26.45	0.19
3	UCS	888.6	2.50	2.47	1.19	9.50	0.35
3	BTS	888.8	2.51	2.97	1.14	9.40	0.41
4	UCS	891.4	2.81	4.92	2.54	47.8	0.32
6	UCS	893.2	2.68	4.57	2.51	43.3	0.28
6	BTS	893.3	2.61	5.14	2.72	50.5	0.31
6	BTS	893.4	2.55	5.15	2.57	45.0	0.33
7	STC	896.0	2.74	4.55	2.86	52.5	0.19
10	STC	897.5	2.70	3.80	2.34	35.2	0.19
10	STC	897.7	2.57	3.54	2.20	29.5	0.19

Strength testing on the Watt Mountain Formation included indirect tension tests, unconfined compressive strength and triaxial testing. Test results are summarized in Table 4. Stress versus strain curves are provided in Appendix D.

BTS results varied from 0.99 to 8.77 MPa, however the sample with the lowest tensile strength may have had a pre-existing fracture. Significant variability was observed in the UCS tests with peak strengths differing by nearly one order of magnitude. Similarly, STC testing was inconclusive. Peak strengths decreased with increasing confining pressure, which is atypical behavior. In general, the results indicate significant variability in the strength properties for the Watt Mountain Formation, with

lower strengths evident near the interface with the Prairie Evaporite Formation, as well as in the upper reaches of the formation.

Table 4. Summary of Strength Testing – Watt Mountain Formation

Core No.	Depth	Confining Stress	Strength Values	Strain @ max.	Young's Modulus	Poisson's Ratio	Comments
	m	MPa	MPa		GPa		
Brazilian Indirect Tension			Indirect Tensile Strength	Diametric Strain			
3	888.7	n/a	0.99	0.0035	--	--	pre-fractured?
6	893.3	n/a	7.29	0.0075	--	--	
6	893.4	n/a	8.77	0.0053	--	--	
Unconfined Compression			Unconfined Compressive Strength	Axial Strain			
3	888.5	0	16.6	0.0043	6.09	n/a	Diametric Strains Suspect
4	891.2	0	102.0	0.0063	20.5	n/a	Diametric Strains Suspect Brittle explosive failure
6	893.2	0	142.0	0.0076	24.1	0.23	Brittle explosive failure
Standard Triaxial Compression			Differential Stress Failure @	Axial Strain			
3	888.5	5	34.7	0.0127	3.44	0.21	Mixed planar and conical shear, whole specimen.
7	896.0	10	93.3	0.0130	10.5	0.16	Planar shear, top part of specimen.
10	897.5	15	30.0	0.0223	1.53	0.16	Massive plastic deformation, barrel-shape, unlocalized failure.
10	897.7	20.6	21.2	0.0098	3.32	0.21	Massive plastic deformation, barrel-shape, unlocalized failure.

3.4.2 Prairie Evaporite Formation

Characterization

The Prairie Evaporite Formation is the uppermost of the salt formations, and is comprised primarily of halite. Examination of the core indicated the presence of intermittent thin anhydrite layers, generally less than 10 mm in thickness, and they were more pronounced in the upper portion of the formation, to approximately 975 m depth as shown in Figure 26. Shale interbeds are present with thicknesses ranging from 150 mm to over 300 mm. Crystal sizes in the cores examined ranged from 10 to 20 mm.

Approximately 29 m of core was obtained from the Prairie Evaporite Formation (end of Core 2, and Cores 3, 4 and 5), over the depth interval 901.5 m to 903.5 m, 960 to 978 m and 1030 m to 1039.0 m. The interface with the Keg River formation was identified at the start of Core Run 6 at approximately 1039.4 m.

Index testing on the Prairie Evaporite Formation consisted primarily of measurement of bulk density and determination of insoluble content. Measured bulk densities were very consistent and averaged 2.15 g/cm^3 , consistent with the density of halite. Figure 27 provides a comparison of geophysical log densities with those measured in the laboratory. Laboratory measured densities are consistently higher. The elevated density readings ($>2.20 \text{ g/cm}^3$) shown in Figure 27 are mostly likely associated with shale interbeds within the Prairie Evaporite Formation. Water content ranged from 800 ppm to 0.84%.

The insoluble content in the samples tested ranged from 0.06 to 5.4 percent by weight, with a more typical value of 0.7 percent. Two samples were submitted for XRD analysis (977.4 m and 1036.7 m). The results indicate that both samples are comprised predominantly of halite (greater than 60%), with lesser percentages of dolomite and illite, and minor amounts of quartz and gypsum. SEM photographs are provided in Appendix E.

Geomechanical Test Results

Table 5 summarizes the samples prepared for geomechanical testing and the testing completed. In addition, the laboratory measured compressive and shear wave velocities, and the corresponding calculated values of Young's modulus and Poisson's ratio are also provided. For a number of samples, it was difficult to ascertain a shear wave, likely due to interference associated with larger crystal sizes.

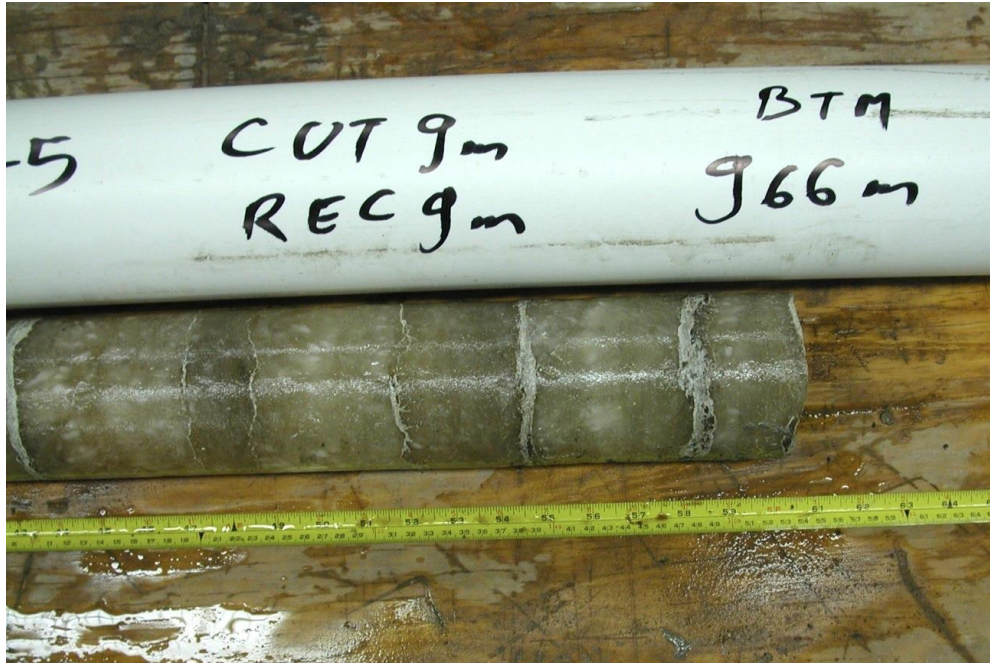


Figure 26. Anhydrite layers in the Prairie Evaporite Formation

Testing on the Prairie Evaporite Formation included indirect tension, unconfined compressive strength, constant mean stress compression tests as well as creep testing. The tension and unconfined compression test results are summarized in Table 6. The stress-strain curves for the unconfined compression tests are provided in Appendix D.

The unconfined compressive strengths of the Prairie Evaporite Formation were generally consistent and averaged approximately 27 MPa. Strains at failure were relatively large, ranging from 0.02 to nearly 0.04. Indirect tensile strength is slightly greater than 10 percent of the unconfined compressive strength.

Four core samples were prepared for testing under constant mean stress in compression. A summary of the results is presented in Table 7. Stress-strain curves are provided in Appendix D. The two tests conducted at a mean stress of 10 MPa did not fail during the CMC portion of the test. Confining pressure was decreased to approximately zero. In the second test, the sample was allowed to creep until failure occurred.

Four creep tests were conducted on samples from the Prairie Evaporite formation. Table 8 summarizes multi-stage test parameters. Axial strain-versus-time graphs are provided in Appendix D.

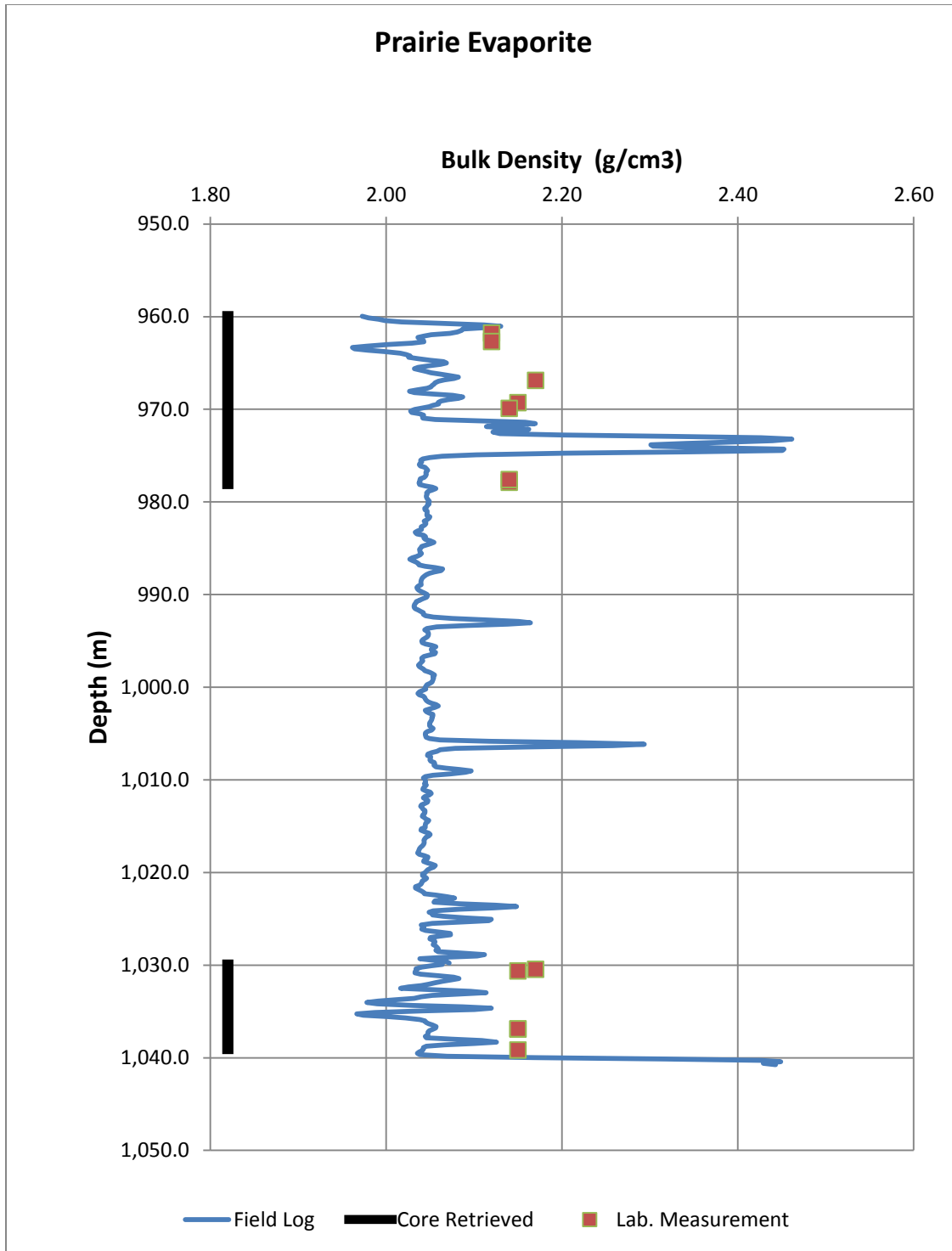


Figure 27. Comparison between laboratory and wireline log values for density in the Prairie Evaporite Formation

Table 5. Summary of Samples – Prairie Evaporite Formation

				Laboratory Measurement			
Core No.	Test	Depth (m)	Density (g/cm ³)	P Velocity (km/sec)	S Velocity (km/sec)	Ultrasonic Young's Modulus (GPa)	Ultrasonic Poisson's Ratio
Prairie Evaporite Formation							
15	BTS	961.8	2.12	2.31	n/a	--	--
15	BTS	961.85	2.12	2.44	n/a	--	--
15	Creep	962.7	2.12	3.77	2.16	24.9	0.26
18	CMC	966.9	2.17	4.66	n/a	--	--
20	CMC	969.3	2.15	3.94	2.39	29.7	0.21
20	UCS	969.9	2.14	4.33	2.56	34.5	0.23
25	UCS	977.9	2.14	3.30	1.43	12.2	0.38*
25	UCS	977.6	2.14	4.49	2.66	37.4	0.23
27	CMC	1030.65	2.15	3.07	n/a	--	--
31	Creep	1036.9	2.15	4.43	2.68	37.4	0.21
33	CMC	1039.19	2.15	4.48	2.36	31.4	0.31

Table 6. Summary of Strength Testing – Prairie Evaporite Formation

Core No.	Depth	Confining Stress	Strength Values	Strain @ max.	Young's Modulus	Poisson's Ratio	Comments
	m	MPa	MPa		GPa		
Brazilian Indirect Tension			Indirect Tensile Strength	Diametric Strain			
15	961.8	n/a	3.80	0.0237	--	--	No failure, test stopped manually
15	961.85	n/a	1.70	0.0228	--	--	
15	961.95	n/a	3.47	0.0232	--	--	No failure, test stopped manually
Unconfined Compression			Unconfined Compressive Strength	Axial Strain			
20	969.9	0	26.4	0.0390	1.23	0.23	Barrelling Failure
25	977.6	0	25.3	0.0228	2.02	n/a	Diametric Strains Suspect Barrelling Failure
25	977.9	0	30.4	0.0307	4.56	n/a	Diametric Strains Suspect Barrelling Failure

Table 7. Summary of Constant Mean Stress Testing – Prairie Evaporite Formation

Core No.	Depth	Mean Stress	Young's Modulus	σ_1 @ dilation	σ_3 @ dilation	Peak Deviator Stress	Axial Strain @ failure	Comments
	m	MPa	GPa	MPa	MPa	MPa		
Compression								
18	967.0	10.0	6.58	18.1	5.92	>27	n/a	Did not fail
20	969.3	15.0	7.01	18.3	13.4	30.6	0.0360	
27	1030.7	10.0	2.71	18.7	5.61	>30	0.0510	Failed by creep
31	1036.8	23.9	7.59	26.5	22.5	35.5	0.0226	

Table 8. Summary of Creep Testing - Prairie Evaporite Formation

Core No.	Depth	Consolidation Pressure	Temp.	σ_1 - σ_3	$\dot{\epsilon}$	Flow law	Comments
	M	MPa	°C	MPa	s ⁻¹		
15	962.65	22.14	20	5.2	1.33×10^{-10}	$\dot{\epsilon} = 4.06 \times 10^{-26} \sigma^{2.30}$	Sample failed on application of 20.2 MPa differential load
				10.2	3.06×10^{-10}		
				15.2	1.94×10^{-9}		
27	1031	23.71	20	10	0	$\dot{\epsilon} = 3.77 \times 10^{-53} \sigma^{5.95}$	
				12.5	6.83×10^{-11}		
				15	1.56×10^{-10}		
				17	4.38×10^{-10}		
				19	7.18×10^{-10}		
				21	1.44×10^{-9}		
31	1037	23.85	20	10.38	1.44×10^{-9}	$\dot{\epsilon} = 3.89 \times 10^{-32} \sigma^{3.21}$	
				12.78	2.14×10^{-9}		
				15.28	4.13×10^{-9}		
				17.79	7.27×10^{-9}		
				20.28	1.17×10^{-8}		
33	1039.01	23.90	20	5	2.01×10^{-10}	$\dot{\epsilon} = 7.71 \times 10^{-36} \sigma^{3.77}$	
				10	8.83×10^{-9}		
				15	8.72×10^{-9}		
				19	3.18×10^{-8}		

3.4.3 Keg River Formation

Characterization

The Keg River formation consists of dolomitized carbonates. Approximately 9 m of continuous core was obtained from this formation (Core Run 6) over the interval 1039.0 to 1048.0 m depth. The interface with the Prairie Evaporite is present near the top of Core Run 6 at 1039.4 m.

Index testing on Keg River core samples consisted primarily of determination of water content and measurement of bulk density. Water contents were generally low, less than 1 percent by mass in the samples tested. Figure 28 provides a comparison of measured bulk density with geophysical logs.

There is good agreement between these data sets. It is noted in the upper reaches of the formation, the density is quite variable.

One sample, from 1047.5 m depth was sent to AGAT laboratories for XRD analyses. This sample consists primarily of dolomite (90%) with minor calcite and traces of quartz. SEM photographs are provided in Appendix E.

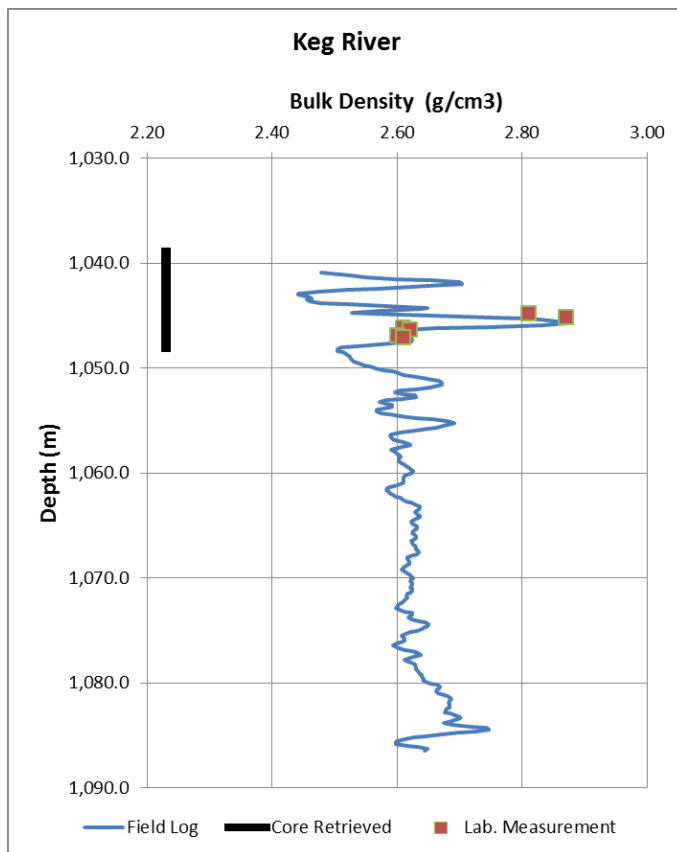


Figure 28. Comparison between laboratory and wireline log values for density in the Keg River Formation

Geomechanical Test Results

Table 9 summarizes the samples prepared for geomechanical testing and the testing completed. In addition, the laboratory measured compressive and shear wave velocities, and the corresponding calculated values of Young's modulus and Poisson's ratio are also provided.

Table 9. Summary of Samples – Keg River Formation

Core No.	Test	Depth (m)	Density (g/cm ³)	Laboratory Testing			
				P Velocity (km/sec)	S Velocity (km/sec)	Ultrasonic Young's Modulus (GPa)	Ultrasonic Poisson's Ratio
Keg River Formation							
36	UCS	1044.8	2.81	4.80	2.77	53.9	0.25
37	UCS	1045.1	2.87	3.08	1.54	18.2	0.33
37	STC	1046.1	2.61	5.50	3.41	72.1	0.19
37	STC	1046.3	2.62	3.51	n/a	n/a	n/a
38	UCS	1046.9	2.60	4.69	2.63	45.8	0.27
38	UCS	1047.1	2.61	5.01	2.71	49.5	0.29

Strength testing on the Keg River Formation included unconfined compressive strength and standard triaxial testing. Test results are summarized in Table 10. Stress versus strain curves are provided in Appendix D.

Table 10. Summary of Strength Testing – Keg River Formation

Core No.	Depth	Confining Stress	Strength Values	Strain @ max.	Young's Modulus	Poisson's Ratio	Comments
	m	MPa	MPa		GPa		
Unconfined Compression			Unconfined Compressive Strength	Axial Strain			
36	1044.8	n/a	74.5	0.0069	14.0	n/a	
37	1045.1	n/a	69.6	0.0064	15.8	n/a	
38	1046.8	n/a	107.0	0.0064	23.3	0.13	
38	1047.1	n/a	114.8	0.0043	23.3	0.34	
Standard Triaxial Compression			Differential Stress @ Failure	Axial Strain			
33	1040.3	5	41.5	0.0382	2.12	0.213	General shear, vertical

							splitting.
37	1045.3	10	189.5	0.0171	19.5	0.270	Planar shear, top part of specimen.
37	1046.1	15	154.0	0.0177	13.6	0.250	Planar shear mainly, top part of specimen,.
37	1043.3	24.1	176.9	0.0214	13.1	0.186	Multiple shear, top part of specimen mainly.

Unconfined compressive strengths ranged from approximately 74 to 115 MPa. All UCS samples failed at less than 0.01 strain, typically in an explosive manner. STC tests generally showed increasing differential stress at failure with increasing confining pressure as would be expected.

3.4.4 Cold Lake Formation

Characterization

The Cold Lake formation consists primarily of halite, and is considered relatively pure. However, based on observation of the core, color ranged from white translucent to rust colored, suggesting some impurities. In addition, significant clay content was noted near the interface with Ernestina Lake Formation, as illustrated in Figure 29. Approximately 19 m of core was obtained from the Cold Lake formation (Core Runs Nos. 8 and 9, and partial 10) over the interval 1129 to 1138 m, and 1156 to 1168.5 m depth.

Index testing was limited to measurement of bulk density, determining water content and insoluble content for the samples tested in unconfined compression. Water contents were low as expected, less than 0.4 percent. Insoluble content ranged from 0.05 to 2.44 percent; however these values do not reflect the higher clay content in the lower range of the formation (approximately 1160 to 1168.5 m depth).



Figure 29. Clay content of the Cold Lake Formation near the interface with the Ernestina Lake Formation

Geomechanical Test Results

Three samples from Cold Lake were tested in UCS. Table 11 summarizes the laboratory measured compressive and shear wave velocities, and the corresponding calculated values of Young's modulus and Poisson's ratio are also provided.

Table 11. Summary of Samples – Cold Lake Formation

Core No.	Test	Depth (m)	Density (g/cm ³)	P Velocity (km/sec)	S Velocity (km/sec)	Ultrasonic Young's Modulus (GPa)	Ultrasonic Poisson's Ratio
Cold Lake							
51	UCS	1137.8	2.08	4.27	2.43	31.2	0.26
52	UCS	1157.1	2.15	4.46	2.48	33.8	0.28
52	UCS	1157.3	2.15	4.16	2.36	30.2	0.26

Table 12 summarizes the unconfined compression test results. Stress versus strain curves are provided in Appendix D.

Table 12. Summary of Strength Testing – Cold Lake Formation

Core No.	Depth	Confining Stress	Strength Values	Strain @ max.	Young's Modulus	Poisson's Ratio	Comments
	m	MPa	MPa		GPa		
Unconfined Compression			Unconfined Compressive Strength	Axial Strain			
51	1137.8	n/a	18.0	0.0086	4.13	n/a	
52	1157.1	n/a	8.9	0.0085	1.51	0.38	
52	1157.3	n/a	17.9	0.0114	3.1	0.24	

Unconfined compressive strength ranged from approximately 9 to 18 MPa. Strains at peak strength were generally lower than those recorded in UCS tests in other salt formations.

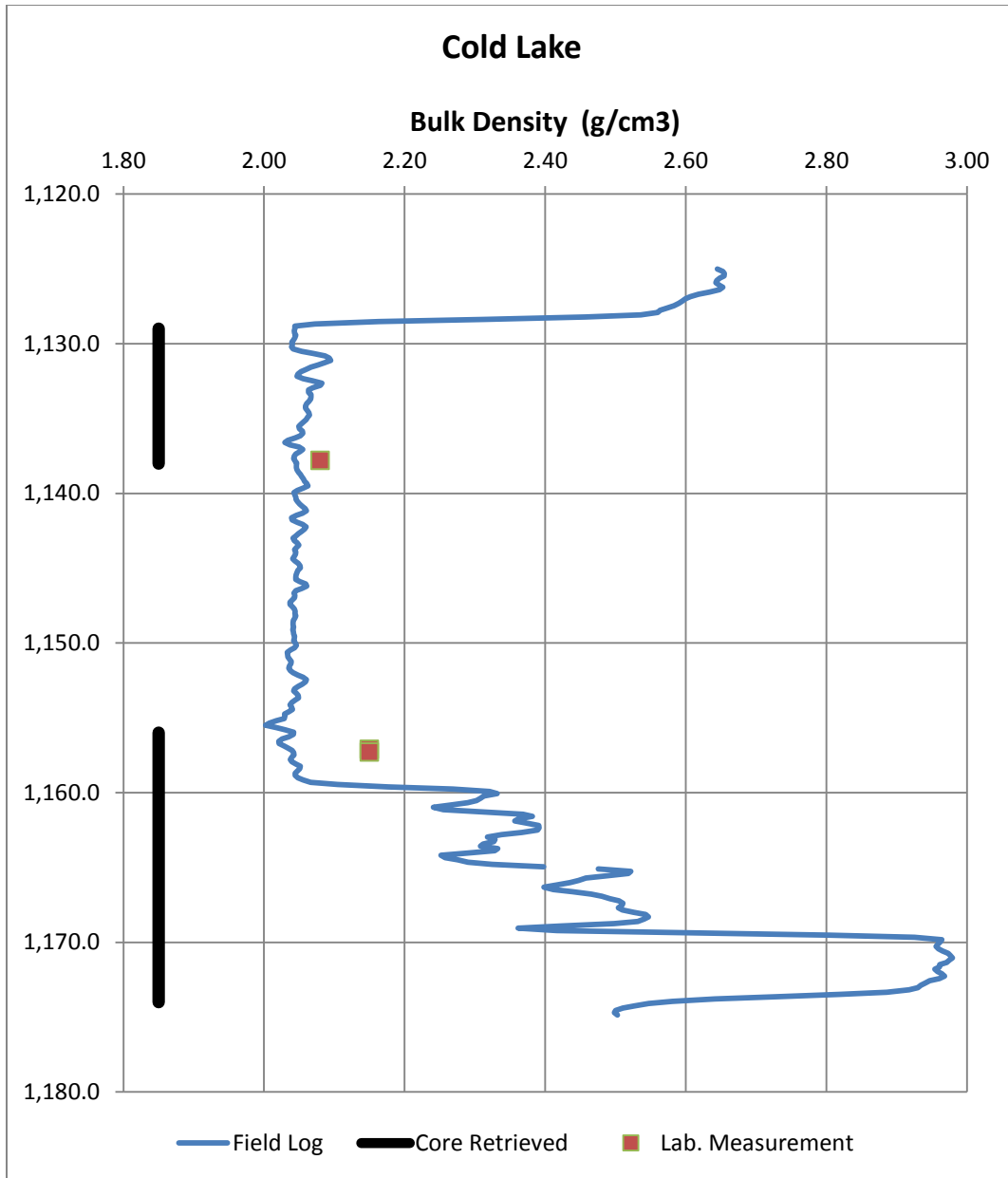


Figure 30. Comparison between laboratory and wireline log values for density in the Cold Lake Formation

3.4.5 Ernestina Lake Formation

Characterization

The Ernestina Lake Formation typically consists of a lower red shale, a middle carbonate and an upper anhydrite (Grayston et al., 1964). The presence of anhydrite is generally in agreement with the high bulk densities recorded from approximately 1169 to 1174 m. Significant salt inclusions are present from 1174 to 1182 m as shown in Figure 31. The red shale begins at approximately 1186 m as shown in Figure 32.

Approximately 21.5 m of continuous core was obtained from the Ernestina Lake Formation (Partial Core Run 10, and Core Runs Nos. 11 and 12) over the interval 1168.5 to 1190 m depth. The interface with the Lotsberg Formation is present in Core Run 12.

Index testing on the Ernestina Lake Formation included determination of water content, measurement of bulk density and grain size distribution. The water contents in the samples tested ranged from less than 0.5 percent to approximately 7.5 percent. There was a slight trend towards increasing water content with depth, as shown in Figure 16 in Appendix D.

The bulk density of the Ernestina Lake samples was generally consistent with depth over the interval sampled averaging approximately 2.50 g/cm^3 . The geophysical wireline logs indicate some variability with depth as shown in Figure 33. Grain size distribution was determined for a limited number of samples, as shown in Figure 17 in Appendix D. The core samples are a mixture of sand, silt and clay sizes. With increasing depth, the finer portion increases.

Two samples of core from the Ernestina Lake Formation were sent for XRD analyses at AGAT laboratories, Core 67 1177.6 m, and Core 73, 1187.1 m. Analysis of Core 67 indicates that it consists of calcite (62%), dolomite (30%) and halite (8%). The sample from core 73 consists mainly of anhydrite (86%) and dolomite (11%). Minor quartz (1%), halite (1%) and illite (1%) and traces of kaolinite potassium feldspar and gypsum are also found in this sample. SEM photographs are provided in Appendix E.

Analysis of the salinity of pore water was carried out on two samples, which showed that there was a considerable amount of NaCl dissolved in the pore water.

Geomechanical Test Results

Table 13 summarizes the samples prepared for geomechanical testing and the testing completed. In addition, the laboratory measured compression and shear wave velocities, and the corresponding calculated values of Young's modulus and Poisson's ratio are also provided.



Figure 31. Salt inclusions (dark) in the Ernestina Lake Formation



Figure 32. Red shale in the Ernestina Lake Formation

Table 13. Summary of Samples – Ernestina Lake Formation

Core No.	Test	Depth (m)	Density (g/cm ³)	P Velocity (km/sec)	S Velocity (km/sec)	Ultrasonic Young's Modulus (GPa)	Ultrasonic Poisson's Ratio
Ernestina Lake Formation							
66	STC	1177.2	2.45	5.15	n/a	--	--
67	UCS	1177.8	2.48	4.38	1.91	25.0	0.38
69	BTS	1180.7	2.53	2.37	n/a	--	--
69	BTS	1180.85	2.52	2.29	n/a	--	--
70	UCS	1183.26	2.47	4.48	2.15	30.0	0.35
70	UCS	1183.06	2.50	4.34	2.06	28.7	0.36
70	Creep	1183.44	2.54	5.34	2.95	54.6	0.28
70	BTS	1182.9				--	--
73	UCS	1186.86	2.54	4.38	2.39	37.5	0.29
73	BTS	1186.5	2.54	3.56	2.37	31.5	0.10
73	BTS	1186.55	2.55	4.37	2.6	42.3	0.23

Strength testing on the Ernestina Lake included indirect tensile strength, unconfined compressive strength and standard triaxial testing, and one creep test. Test results, with the exception of the creep test, are summarized in Table 14. Stress versus strain curves are provided in Appendix D.

Table 14. Summary of Strength Testing – Ernestina Lake Formation

Core No.	Depth	Confining Stress	Strength Values	Strain @ max.	Young's Modulus	Poisson's Ratio	Comments
	m	MPa	MPa		GPa		
Unconfined Compression			Unconfined Compressive Strength	Axial Strain			
67	1177.7	n/a	53.8	0.0155	7.05		
70	1183.1	n/a	52.1	0.0087	10.0	0.32	
73	1186.9	n/a	51.5	0.0068	10.0		
Standard Triaxial Compression			Differential Stress @ Failure	Axial Strain			
66	1177.2	7.0	74.79	0.0762	4.98	0.338	Massive, plastic deformation, whole specimen, no cracks.

69	1180.5	14.0	75.40	0.0307	4.02	0.325	Massive, plastic deformation, whole specimen, no cracks.
71	1183.7	21.0	65.21	0.0109	4.53	0.286	Planar shear across both ends of specimen
71	1184.8	27.3	65.24	0.0147	3.45	0.277	Planar shear, wedge-shape, bottom part.

Unconfined compressive strengths averaged approximately 52.5 MPa and were relatively consistent. However, the STC tests showed deviation from typical behavior. The differential stress at failure remained approximately constant, irrespective of confining pressure. Significant axial strains were also recorded, as much as 0.076.

One creep test was conducted on a sample from the Ernestina Lake Formation. Unlike the tests conducted on salt samples, the confining pressure was kept constant and the axial load was increased. The planned axial stress increments were based on the UCS test results, and corresponding estimated failure differential stress. However, the sample failed upon application of the second load increment. The corresponding strain versus time plot is provided in Appendix D.

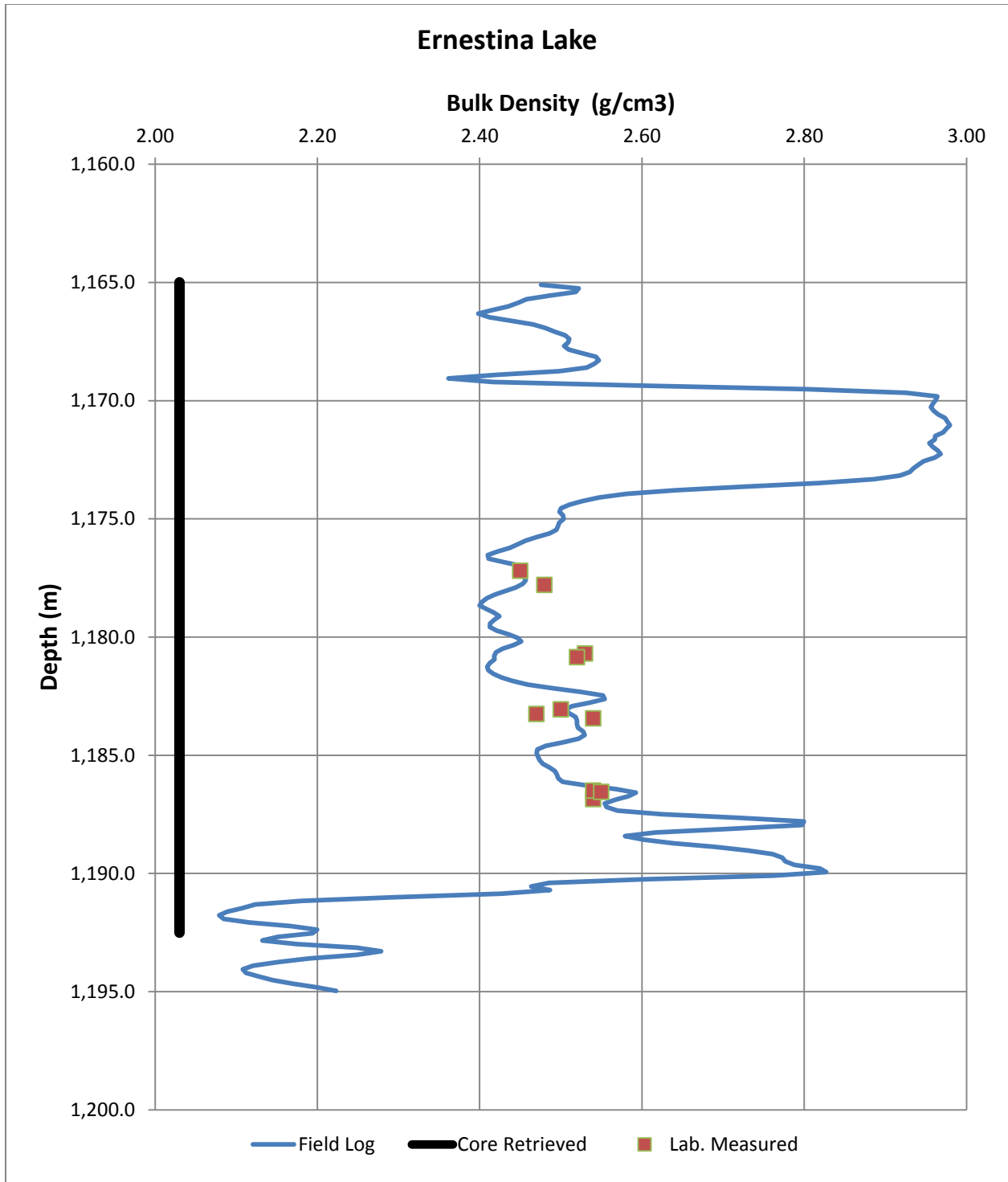


Figure 33. Comparison between laboratory and wireline log values for density in the Ernestina Lake Formation

3.4.6 Lotsberg Formation

Characterization

The Lotsberg Formation is said to consist primarily of halite (greater than 95 percent), and is considered relatively pure (e.g. Meijer Drees (1994), Grayston et al. (1964) and Grobe (2000)). However, based on observation of the core, color ranged from translucent to rust colored, suggesting some impurities (Figure 34). In addition, clay inclusions were noted extensively (Figure 35). Approximately 20.5 m of core was obtained from the Lotsberg Formation (Partial Core Run 12, and Core Runs No. 13 and 14) over the interval 1190 m to 1210.5 m depth.

The laboratory measured bulk density was on average 2.15 g/cm³, similar to the density of halite. Two samples had higher measured densities of 2.38 and 2.59 g/cm³, likely due to higher clay contents in the upper portion of the formation. Based on the density versus depth curve, it is expected that the Lotsberg formation becomes more homogeneously halite with depth. Crystal sizes in the samples examined were considerably larger than those observed in either the Cold Lake or Prairie Evaporite formation. Crystal sizes ranged from 20 mm up to 75 mm, which is nearly the full diameter of the core. Water content ranged from 500 ppm to 0.91%.

The insoluble content was measured in select samples of Lotsberg Salt, and ranged from 0.2 to nearly 40 percent, indicating a high degree of variability, particularly near the interface with the overlying Ernestina Lake formation. This higher clay content can also be observed in the density versus depth profile. One sample was submitted for XRD analysis (Core 87 – 1207.8 m), and results indicated nearly 99 percent halite.

Geomechanical Test Results

Table 15 summarizes the samples prepared for geomechanical testing and the testing completed. In addition, the laboratory measured compressive and shear wave velocities, and the corresponding calculated values of Young's modulus and Poisson's ratio are also provided. In many samples, a shear wave could not be ascertained. This is likely due to interference associated with the large crystal sizes.

Testing on the Lotsberg formation included indirect tension, unconfined compressive strength, constant mean stress compression and extension tests as well as creep testing. The tension and unconfined compression test results are summarized in Table 16. The stress-strain curves for the unconfined compression tests are provided in Appendix D.

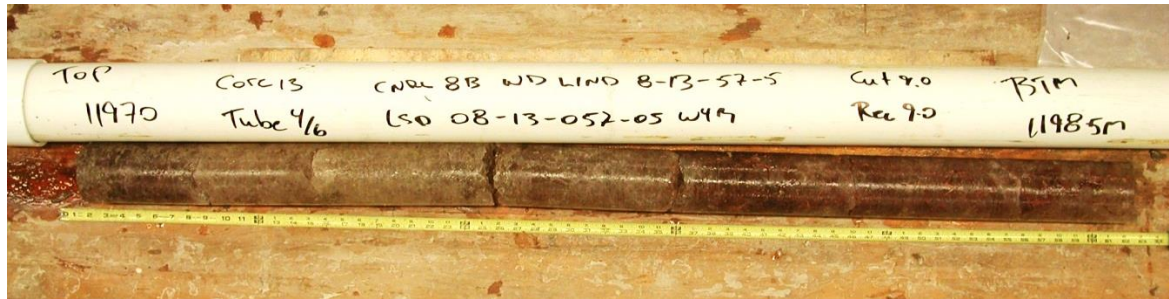


Figure 34. Lotsberg Formation with white translucent character on the left and red colouring on the right.



Figure 35. High clay content in the Lotsberg Formation, near the interface with the Ernestina Lake Formation

Table 15. Summary of Samples – Lotsberg Formation

Core No.	Test	Depth (m)	Density (g/cm ³)	P Velocity (km/sec)	S Velocity (km/sec)	Ultrasonic Young's Modulus (GPa)	Ultrasonic Poisson's Ratio
Lotsberg Formation							
76	UCS	1191.8	2.38	3.87	2.11	27.3	0.29
78		1195.3	2.16	2.59	n/a	--	--
79	CMC	1196.2	2.59	2.89	n/a	--	--
79	BTS	1195.9	2.18	4.00	1.87	20.8	0.36
79	CMC	1195.7	2.13	4.05	n/a	--	--
81	CMC	1198.9	2.15	3.30	n/a	--	--
81		1198.6	2.15	2.49	n/a	---	--
82	UCS	1200.6	2.14	4.48	2.48	34.0	0.29
82	Creep	1200.8	2.19	3.73	1.74	18.1	0.36

Core No.	Test	Depth (m)	Density (g/cm ³)	P Velocity (km/sec)	S Velocity (km/sec)	Ultrasonic Young's Modulus (GPa)	Ultrasonic Poisson's Ratio
86	UCS	1206.0	2.16	3.44	n/a	---	---
86	CMC	1207.1	2.15	3.39	n/a	---	---
87	UCS	1208.1	2.13	4.61	2.05	24.8	0.38

Table 16. Summary of Strength Testing – Lotsberg Formation

Core No.	Depth	Confining Stress	Strength Values	Strain @ max.	Young's Modulus	Poisson's Ratio	Comments
	m	MPa	MPa		GPa		
Brazilian Indirect Tension			Indirect Tensile Strength	Diametric Strain			
79	1195.8	---	1.64	0.0111			
81-1	1199.4	---	2.54	0.0127			
81-2	1199.5	---	2.13	0.0137			
Unconfined Compression			Unconfined Compressive Strength	Axial Strain			
76	1191.8	n/a	21.2	0.0060	4.24	0.24	
82	1200.6	n/a	19.5	0.0208	2.73	0.29	
86	1206.0	n/a	18.1	0.0149	2.95	n/a	
87	1208.1	n/a	18.8	0.0297	2.27	0.31	

The unconfined compressive strengths of the Lotsberg formation were generally consistent, and averaged 19.4 MPa. Strain at failure ranged from 0.006 to near 0.03. Indirect tensile strength is close to 10 percent of the unconfined compressive strength.

Table 17. Summary of Constant Mean Stress Testing – Lotsberg Formation

Core No.	Depth	Mean Stress	Young's Modulus	σ_1 @ dilation	σ_3 @ dilation	Peak Deviator Stress	Axial Strain @ failure	Comments
	m	MPa	GPa	MPa	MPa	MPa		
Compression								
79		15.0	6.40	24.3	10.5	37.6	0.0436	
81		10.0	6.27	24.2	2.94	>29.5		failed by creep

Core No.	Depth	Mean Stress	Young's Modulus	σ_1 @ dilation	σ_3 @ dilation	Peak Deviator Stress	Axial Strain @ failure	Comments
	m	MPa	GPa	MPa	MPa	MPa		
82		15.0	6.78	25.4	9.75	>35		failed by creep
86		10.0	7.01	26.5	9.23	>37		failed by creep
Extension								
78	1195.3	20.0	3.62	16.0	22.0	-10.25	0.6	
81	1198.8	15.0	3.89	11.3	16.8	-10.13	≈0.84	

Core samples were prepared for testing under mean stress conditions. Four tests were completed as compression tests and two as extension tests. A summary of the results is presented in Table 17.

One multi-stage creep test has been conducted on the Lotsberg Formation. A summary of the results is provided in Table 18.

Table 18. Summary of Creep Testing - Lotsberg Formation

Core No.	Depth	Consolidation Pressure	Temp.	σ_1 - σ_3	$\dot{\epsilon}$	Flow law	Comments
	m	MPa	°C	MPa	s ⁻¹		
82	1200.8	27.6	20	7.1	3.88×10^{-10}	$\dot{\epsilon} = 2.09 \times 10^{-50} \sigma^{5.75}$	Flow law based on 10.1 – 17.6 MPa stress range
				10.1	3.67×10^{-10}		
				15.1	4.02×10^{-9}		
				17.6	9.38×10^{-9}		

Axial strain versus time graphs are provided in Appendix D.

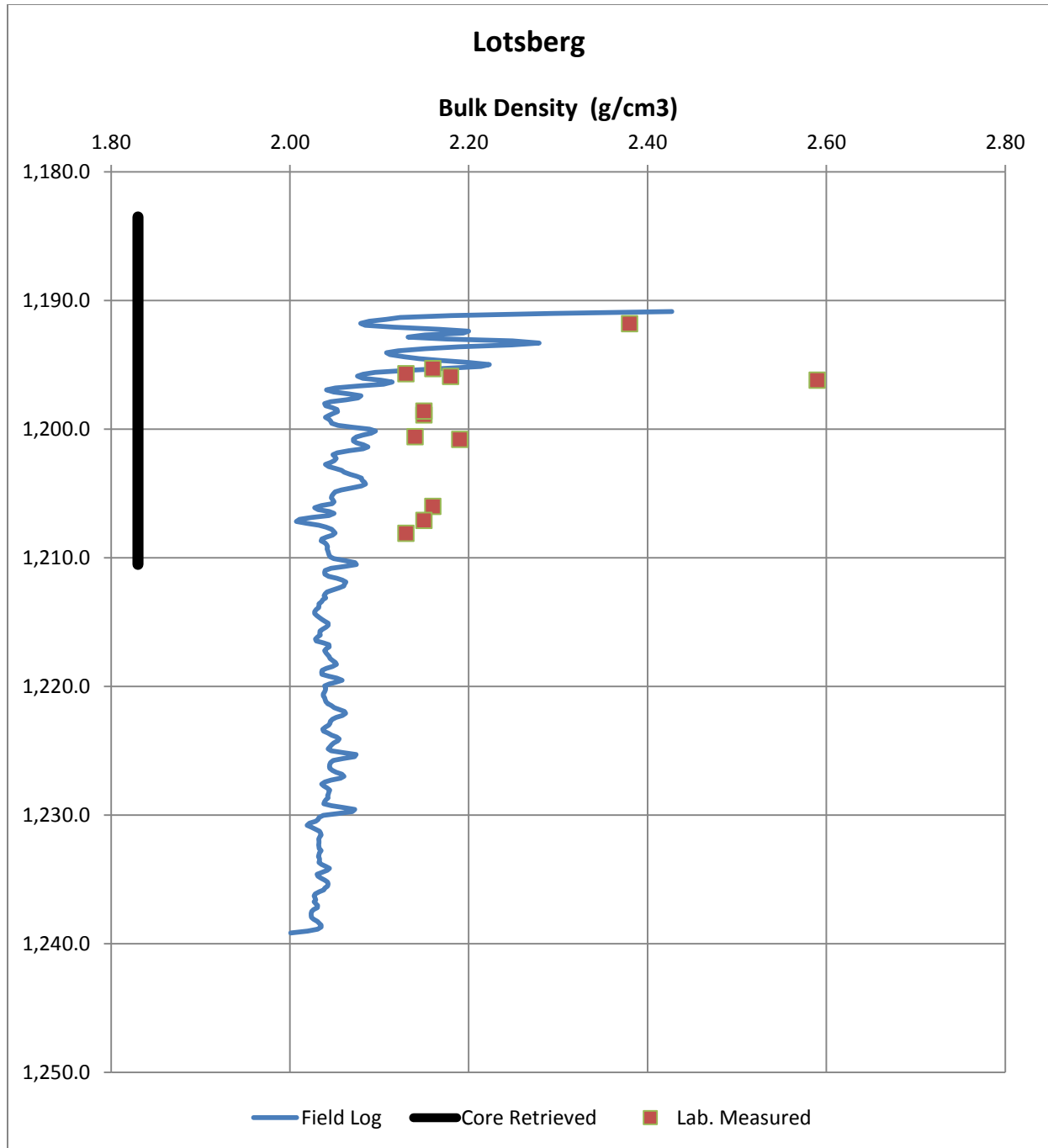


Figure 36. Comparison between laboratory and wireline log values for density in the Lotsberg Formation

4. NUMERICAL MODELLING

4.1 Aims and approach

To investigate and predict the long-term behaviour of the proposed salt caverns after abandonment, a numerical model was created using FLAC^{3D} (Fast Lagrangian Analysis of Continua) (Itasca Consulting Group Inc., 2013). FLAC^{3D} uses a finite difference methodology to predict mechanical behaviour in three-dimensional structures. Materials are represented by polyhedral elements within a three-dimensional grid. Each element is represented by the vector components of position, displacement, velocity and acceleration. These vectors respond to stresses and boundary restraints according to a prescribed stress-strain law. These stress-strain laws can be of a linear or non-linear nature, and materials can yield and flow, with the grid cells deforming and moving with the represented material.

For the purposes of cavern behaviour modelling, a model was created with the following characteristics:

- The local geology was represented by a simple 'layer-cake' stratigraphy with perfectly horizontal interfaces (i.e. no thickness variations or dipping of layers)
- The model was divided in 7 layers, representing from top to bottom: Overburden + Watt Mountain Formation, the Prairie Evaporite Formation, the Keg River Formation, the Cold Lake Formation, the Ernestina Lake Formation, the Lotsberg Formation and the basal redbeds or 'underburden'. Every layer has uniform properties throughout.
- The layers representing the Prairie Evaporite Formation and the Lotsberg Formation were modeled to behave according to the simple stress-strain relation $\dot{\epsilon} = A\bar{\sigma}^n$. All other layers behaved according to the Mohr-Coulomb failure envelope with a tension cut-off. Deformation was assumed to be isotropically elastic within the failure envelope. See Table 19 for the properties that were assigned to each formation.
- Salt cavern dimensions and geometry were based on sonar measurements of an already developed salt cavern in the Lotsberg Formation at the CNRL 8B WD LIND 08-13-57-5W4 well. The geometry was simplified to 12 layered discs (Figure 37). This resulted in a cavern of 100 m high and a maximum horizontal diameter of 75 m.
- The initial external stress (stress acting on the cavern wall from the outside) was calculated from the density of the overburden only; no external stress field was incorporated in the

model. The initial internal stress (stress acting on the cavern wall from the inside) was calculated for different scenarios;

- A brine filled cavern
- A cavern filled with graded sands
- A cavern filled with dense sands

For all models a wellhead pressure of ~4 MPa is present, which is in accordance with the wellhead pressure used by CNRL. The wall support pressure provided by the sands in the sand-filled models is calculated according to Rankine (1857). Figure 38 provides an overview of the different contributions to internal cavern pressure. It is assumed that the caverns are fully filled with one material and that the cavern is abandoned (the well is closed and the seal where the well enters the cavern is fully intact).

- The stress scenarios described above were applied to different cavern arrangements:
 - Scenario 1: One cavern in the Lotsberg Formation
 - Scenario 2: Two caverns in the Lotsberg Formation, separated by approximately 150 m horizontally. This scenario represents one cavern at the 01-13-57-5W4 location and one cavern at the 08-13-57-5W4 location
 - Scenario 3: One cavern in the Lotsberg Formation and one cavern in the Prairie Evaporite formation (vertical stacking).
 - Scenario 4: Two caverns in the Lotsberg Formation and two caverns in the Prairie Evaporite Formation, separated by approximately 150 m horizontally. This scenario represents vertical stacking at both the 01-13-57-5W4 location and the 08-13-57-5W4 location.

The different cavern arrangements are shown schematically in Figure 39.

- The vectors and the stress tensors for each grid point are calculated with time steps of 100000 seconds. Output in terms of stress state, displacement and surface subsidence is recorded after a modelled time of 1 year, 5 years, 20 years and 50 years.
- The model uses a total of approximately 500.000 polyhedral elements or “zones”. These zones are smaller close to the caverns and get progressively bigger away from the caverns. This was done to optimize model run time without compromising model resolution around the cavern. The model reaches to a depth of 1715 m (400 m below the Lotsberg Formation) and represents a surface area of 12.5 km² (circle with a radius of 2 km).
- The model ignores changes to the internal cavern pressure as a result of creep closure.

Table 19. Properties for the different formations in FLAC^{3D}

Formation	Simulation Model	Young's Modulus (GPa)	Poisson's Ratio	Cohesion (MPa)	Friction Angle (°)	Tensile Strength (MPa)	$\dot{\epsilon} = A \bar{\sigma}^n$	
							A	n
Caprock	M-C	4	0.4	6	35	8		
Watt Mountain								
Prairie Evaporite	Power law	7	0.25	1	39	3	1.35E-27	2.52
Keg River	M-C	15	0.28	6	51	3		
Cold Lake	M-C	3	0.25	2	40	2		
Ernestina Lake	M-C	8	0.3	2	40	2		
Lotsberg	Power law	7	0.26	1	39	2	2.00E-50	5.75
Underburden	M-C	8	0.3	2	40	2		

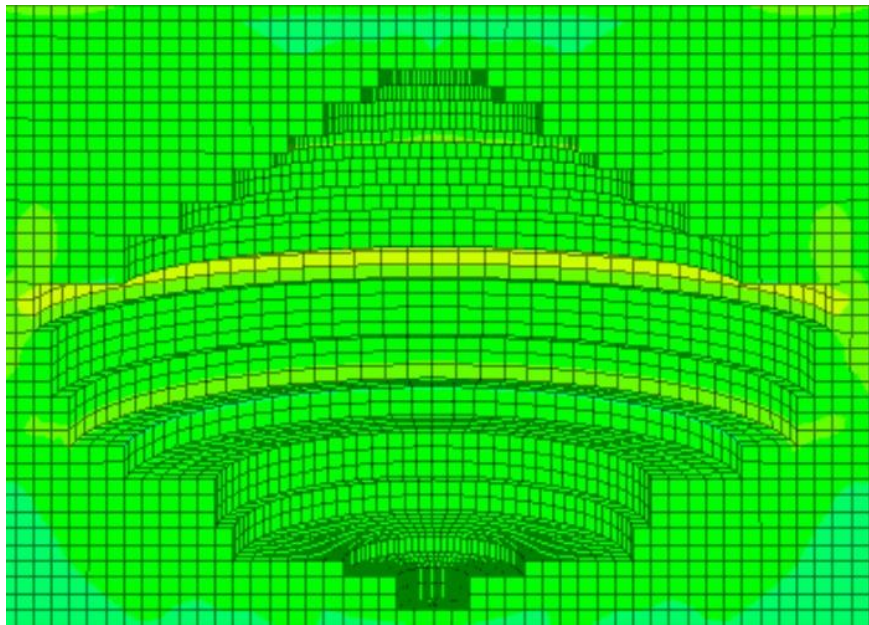


Figure 37. Geometry used for the salt caverns in the FLAC^{3D} model

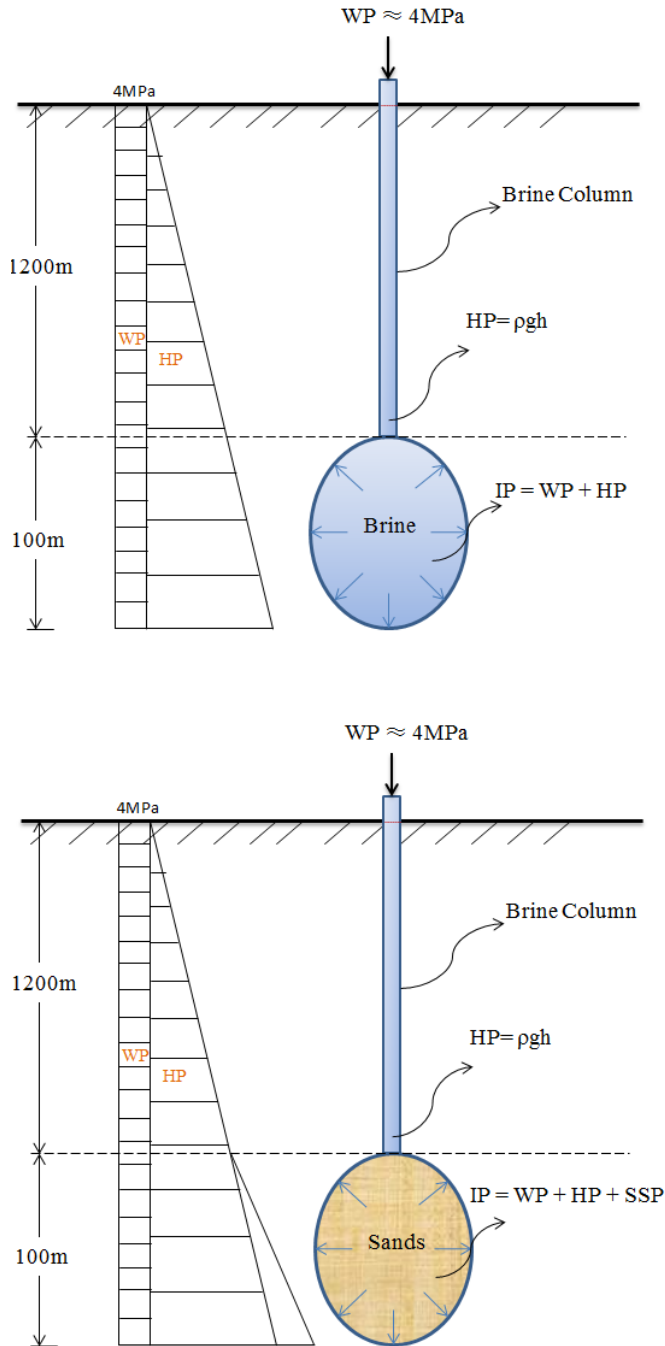


Figure 38. Visual representation of the different contributions to internal pressure (IP). WP = Wellhead pressure, HP = Hydrostatic pressure, SSP = Sand Support Pressure.

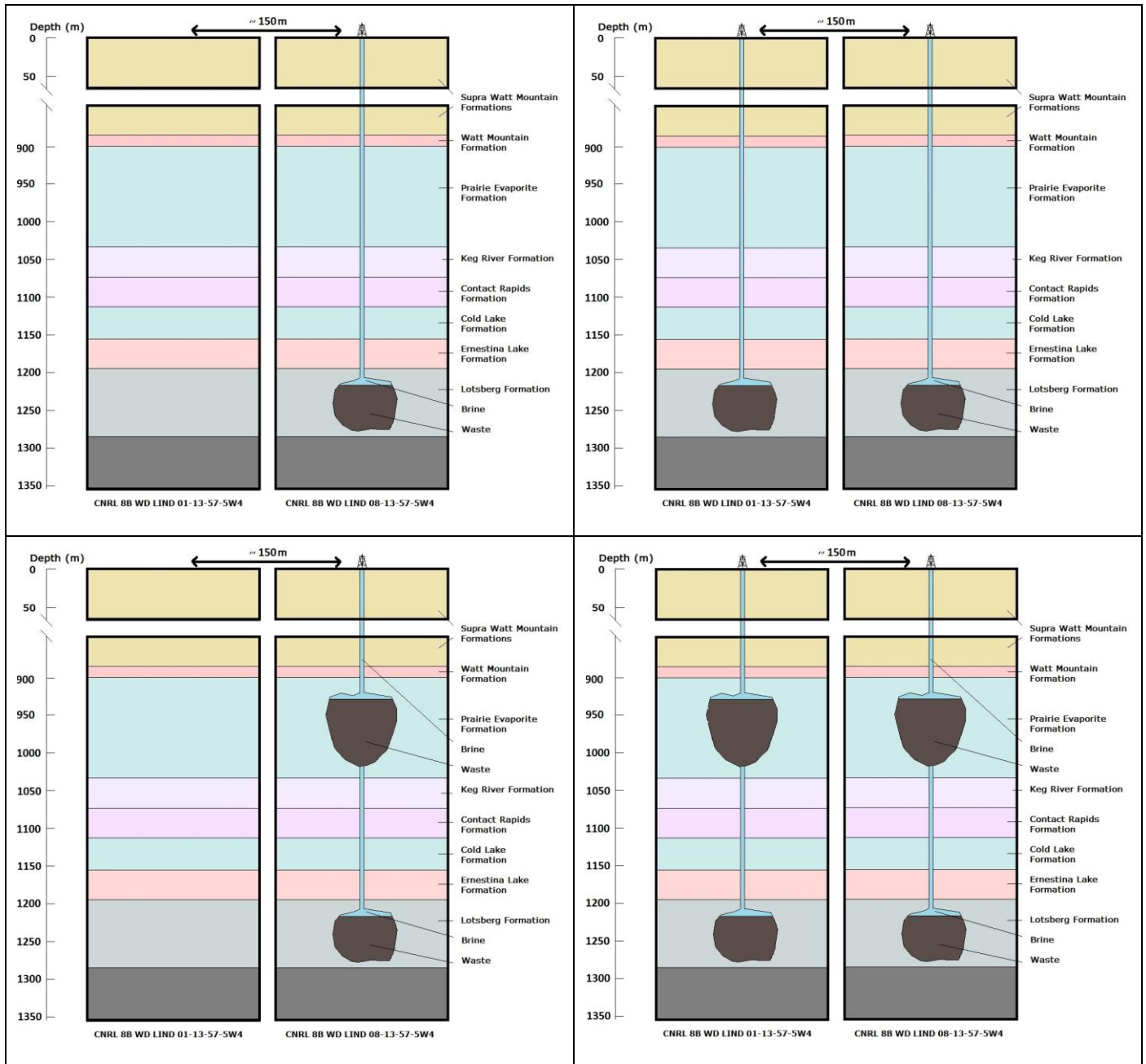


Figure 39. Salt cavern configurations. Top left = Scenario 1; top right = Scenario 2; bottom left = Scenario 3; bottom right = Scenario 4.

4.2 Results

The results of the numerical modelling are presented in Table 20 to Table 31. Figure 40 and Figure 41 show modelled shear stress and vertical displacement for two scenarios. Appendix F contains all vertical displacement and shear stress distributions for 50 year predictions.

Table 20. Scenario 1: One cavern in Lotsberg Formation - Brine case

	max vertical disp. (mm)	max shear stress (MPa)	Surface Subsidence (mm)		
			centre point	boundary point	max
1y	65.5	4.27	0	0	
5y	146.4	3.3	5.60E-06	0	0.11mm at 250m from the centre
10y	185.6	3	0.98	3.00E-06	1.18mm at 200m from the centre
20y	230.8	2.7	1.7	5.00E-05	1.95mm at 170m from the centre
50y	303.4	2.4	3.24	0.11	3.5mm at 150m from the centre

Table 21. Scenario 1: One cavern in Lotsberg Formation – Graded sands case

	max vertical disp. (mm)	max shear stress (MPa)	Surface Subsidence (mm)		
			centre point	boundary point	max
1y	57.2	3.9	0	0	
5y	120	3.1	4.00E-06	0	0.087mm at 250m from the centre
10y	144.8	2.7	0.74	1.40E-06	0.9mm at 200m from the centre
20y	171.7	2.6	1.4	2.70E-05	1.6mm at 170m from the centre
50y	218.5	2.2	2.36	6.00E-05	2.5mm at 150m from the centre

Table 22. Scenario 1: One cavern in Lotsberg Formation – Dense sands case

	max vertical disp. (mm)	max shear stress (MPa)	Surface Subsidence (mm)		
			centre point	boundary point	max
1y	55.4	3.66	0	0	
5y	114	2.9	3.30E-06	0	0.075mm at 250m from the centre
10y	137.1	2.5	0.63	1.44E-06	0.8mm at 200m from the centre
20y	159.5	2.3	1.47	1.80E-05	1.63mm at 170m from the centre
50y	181.4	2	2.2	3.60E-05	2.35mm at 150m from the centre

Table 23. Scenario 2: Two caverns in Lotsberg Formation - 8-13 with brine, 1-13 with dense sands

	max vertical disp. (mm)		max shear stress (MPa)		Surface Subsidence (mm)		
	8-13 Cavern	1-13 Cavern	8-13 Cavern	1-13 Cavern	centre point	boundary point	max
1y	74.5	47	4.3	3.4	0	0	
5y	147	107	3.4	2.8	1.60E-05	0	0.15mm at 200m from the centre
10y	186.8	127	3	2.5	2.21	7.00E-06	centre
20y	233.7	152	2.7	2.3	3.5	0.11	3.55mm at 50m from the centre
50y	310	190	2.4	2	6	0.28	centre

Table 24. Scenario 2: 8-13 with graded sands, 1-13 with dense sands

	max vertical disp. (mm)		max shear stress (MPa)		Surface Subsidence (mm)		
	8-13 Cavern	1-13 Cavern	8-13 Cavern	1-13 Cavern	centre point	boundary point	max
1y	57.1	50	3.88	3.7	0	0	
5y	120.4	105	3	2.8	1.20E-05	0	0.11mm at 200m from the centre
10y	146.4	133	2.8	2.6	1.85	5.60E-06	centre
20y	174.7	160	2.5	2.3	3.26	6.00E-05	3.28mm at 50m from the centre
50y	223.5	190	2.2	2.1	5	0.17	centre

Table 25. Scenario 2: 8-13 with dense sands, 1-13 with dense sands

	max vertical disp. (mm)		max shear stress (MPa)		Surface Subsidence (mm)		
	8-13 Cavern	1-13 Cavern	8-13 Cavern	1-13 Cavern	centre point	boundary point	max
1y	55.8	55.8	3.68	3.68	0	0	
5y	114.6	114.6	3.5	3.5	1.00E-05	0	0.11mm at 200m from the centre
10y	138.6	138.6	2.7	2.7	1.78	4.50E-06	centre
20y	162.3	162.3	2.5	2.5	3.3	5.50E-05	centre
50y	195.6	195.6	2	2	4.8	0.136	centre

Table 26. Scenario 3: One cavern in the PRVP, one in the LTBG – Brine in PRVP, dense sands in LTBG

	max vertical disp. (mm)		max shear stress (MPa)		Surface Subsidence (mm)		
	LTBG Cavern	PRVP Cavern	LTBG Cavern	PRVP Cavern	centre point	boundary point	max
1y	40	60	3.65	2	0	0	
5y	100	130.5	2.8	1.5	0.418	1.00E-07	1.87mm at 200m from the centre
10y	111	262	2.5	1.2	5.8	2.25E-05	6.5mm at 150m from the centre
20y	120	394	2	1.1	10.6	0.12	12mm at 150m from the centre
50y	130	692.5	1.9	1	22.4	0.47	24.4mm at 150m from the centre

Table 27. Scenario 3: Graded sands in PRVP, dense sands in LTBG

	max vertical disp. (mm)		max shear stress (MPa)		Surface Subsidence (mm)		
	LTBG Cavern	PRVP Cavern	LTBG Cavern	PRVP Cavern	centre point	boundary point	max
1y	55.3	20	3.67	1	0	0	
5y	111	40	2.8	0.8	6.80E-05	e-8	0.4mm at 200m from the centre
10y	132.7	65	2.5	0.7	1.44	1.40E-05	1.6mm at 150m from the centre
20y	153	90	2.3	0.55	2.53	5.80E-05	2.9mm at 150m from the centre
50y	180	130	2	0.5	5.43	0.18	6mm at 150m from the centre

Table 28. Scenario 3: Dense sands PRVP, dense sands in LTBG

	max vertical disp. (mm)		max shear stress (MPa)		Surface Subsidence (mm)		
	LTBG Cavern	PRVP Cavern	LTBG Cavern	PRVP Cavern	centre point	boundary point	max
1y	55.5	1.7	3.67	0.3	0	0	
5y	114	4	2.8	0.27	7.60E-06	2.00E-09	0.064mm at 400m from the centre
10y	136.7	6	2.5	0.25	0.48	4.00E-06	0.68mm at 200m from the centre
20y	159	9	2.3	0.15	1.23	4.00E-05	1.4mm at 170m from the centre
50y	190	12	2	0.12	2	0.112	2.13mm at 150m from the centre

Table 29. Scenario 4: Two caverns in the PRVP, two in the LTBG – Brine in PRVP, dense sands in LTBG

	max vertical disp. (mm)		max shear stress (MPa)		Surface Subsidence (mm)		
	LTBG Cavern	PRVP Cavern	LTBG Cavern	PRVP Cavern	centre point	boundary point	max
1y	50	64.4	3.67	2	0	0	
5y	90	130.2	3	1.5	1.14	1E-7	2.88mm at 150m from the centre
10y	100	270	2.5	1.3	14	1E-5	centre
20y	110	410	2	1.1	24.3	1E-4	centre
50y	120	718	1.9	1	48	0.57	centre

Table 30. Scenario 4: Graded sands in PRVP, dense sands in LTBG

	max vertical disp. (mm)		max shear stress (MPa)		Surface Subsidence (mm)		
	LTBG Cavern	PRVP Cavern	LTBG Cavern	PRVP Cavern	centre point	boundary point	max
1y	55.4	20	3.67	1	0	0	
5y	106	40	2.8	0.8	0.188	1E-8	0.57mm at 150m from the centre
10y	133.5	64	2.5	0.7	3.7	1E-5	centre
20y	154.3	92	2.3	0.55	5.88	1E-5	centre
50y	180	150	2	0.5	12.1	0.23	centre

Table 31. Scenario 4: Dense sands in PRVP, dense sands in LTBG

	max vertical disp. (mm)		max shear stress (MPa)		Surface Subsidence (mm)		
	LTBG Cavern	PRVP Cavern	LTBG Cavern	PRVP Cavern	centre point	boundary point	max
1y	55	2	3.67	0.3	0	0	
5y	114	4.2	2.8	0.27	2.00E-05	e--9	0.11mm at 150m from the centre
10y	138.1	8	2.5	0.25	1.47	5.00E-06	centre
20y	161.6	11.8	2.3	0.15	2.9	5.00E-05	centre
50y	190	17	2	0.12	4.38	0.14	centre

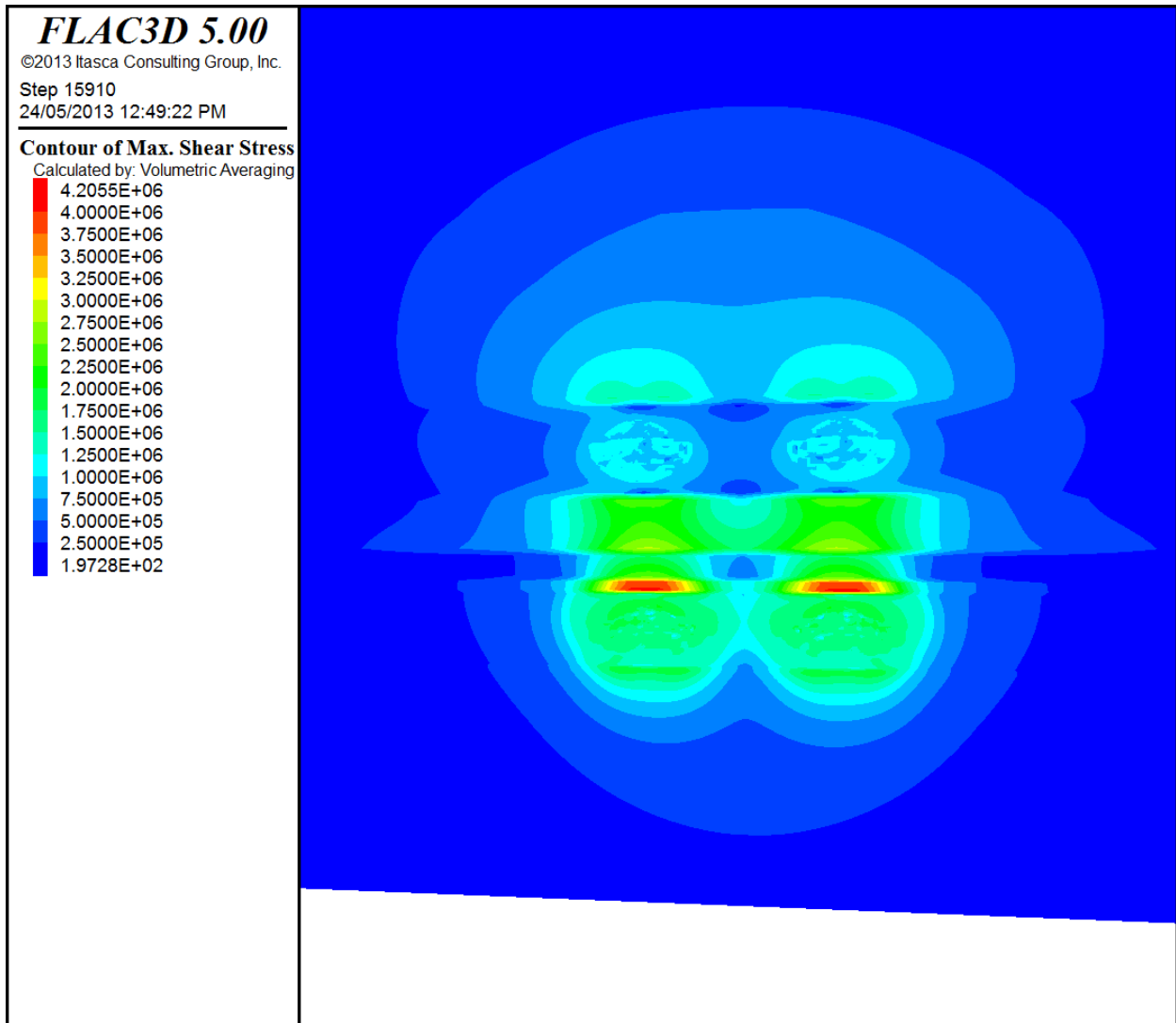


Figure 40. Graphical representation of the maximum shear stress (in Pa) experienced over a 50 year period for a four cavern configuration. The caverns in the Prairie Evaporite Formation are filled with brine and the caverns in the Lotsberg are filled with dense sands.

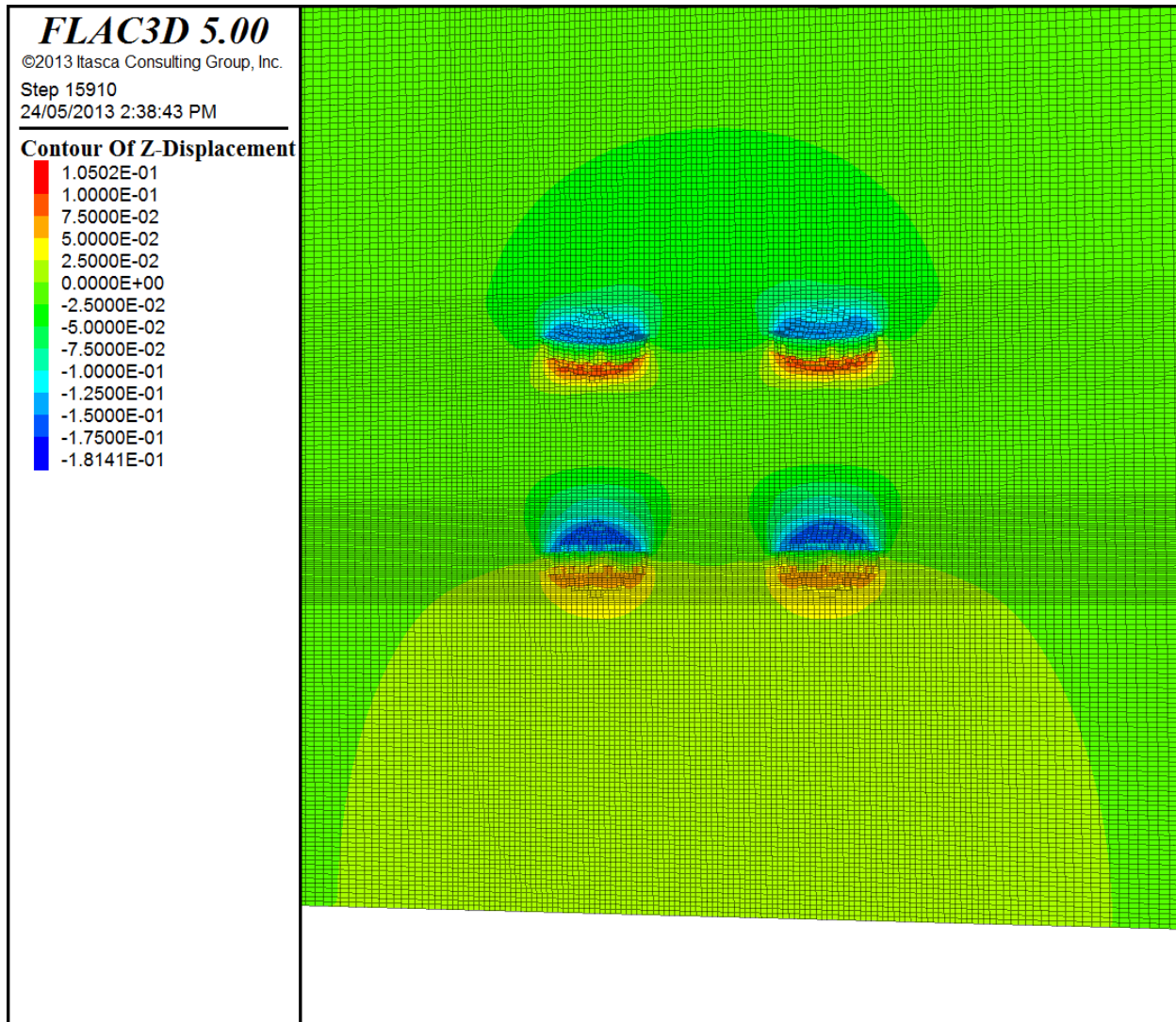


Figure 41. Graphical representation of the total vertical displacement (in m) experienced over a 50 year period for a four cavern configuration. The caverns in the Prairie Evaporite Formation are filled with graded sands and the caverns in the Lotsberg are filled with dense sands. Positive values represent upward movement.

The results of the FLAC^{3D} models show that the highest shear stresses occur in the immediate vicinity of the salt caverns. The magnitude of the maximum shear stress depends on the material filling the cavern. Shear stresses are highest when the internal cavern pressure is lowest. The highest shear stresses are reached right after abandonment and reach values of less than 4.3 MPa after one year. The highest surface subsidence is reached for a four cavern configuration in which both caverns in the Prairie Evaporite Formation are abandoned for 50 years while filled with brine.

5. DISCUSSION

5.1 Geological setting

The study of the geological setting for this project served three main goals: (1) To gain a general understanding of the geological history of the area, thereby ensuring tectonic stability both in the past and in the future (on an engineering timescale in the order of 10.000 years), (2) to assess the lateral continuity of formations around the CNRL 8B WD LIND 08-13-57-5W4 well and (3) to assess the continuity of the geophysical wireline properties within formations both vertically and laterally.

5.1.1 Geological history and tectonic stability

The geological history of the Western Canada Sedimentary Basin is a long and complex one, involving a platformal stage during which sediments were deposited transgressively onto the Precambrian crystalline basement, a transitional stage during which arches and basins developed and a final stage in which the basin served as a foreland basin for the Rocky Mountains in the west (Porter et al., 1982). In general though, the stratigraphy of the basin as a whole is relatively simple and has been described as a 'layer-cake type stratigraphy' (Dusseault et al., 2001). The absence of tectonic activity in the basin (Wardlaw and Schwerdtner (1966), Porter et al. (1982), Dusseault et al. (2001), Bachu and Stewart (2002)) minimized the occurrence of large fault systems that could act as potential leak pathways.

The stratigraphy of the Devonian Elk Point Group in the East-Central Alberta basin, which is of particular interest for this project, follows this trend and has a simple 'layer-cake' structure (Hamilton, (1971), Grobe (2000)) with no evidence for major faults.

5.1.2 Lateral continuity of formations

The Devonian Elk Point Group in the East-Central Alberta basin has been the subject of several studies regarding formation thicknesses and the lateral extent of formations (Hamilton, (1971), Meijer Drees (1994), Grobe (2000)). Because of the economic value of rock salt, these studies have focussed mainly on the Prairie Evaporite Formation and the Lotsberg Formation. Figure 12 to Figure 14 in Section 2 show the thickness distribution of the Prairie Evaporite Formation and the Lotsberg Formation. The Prairie Evaporite Formation varies slightly throughout the East-Central Alberta basin and has a sharp dissolution front approximately 30 km east of CNRL 8B WD LIND 08-13-57-5W4 well. Near the dissolution front, the thickness quickly diminishes (Grobe, 2000). The Lotsberg Formation is thickest in the centre of the basin and progressively gets thinner towards the edges of the basin.

To get a more local picture around the CNRL 8B WD LIND 08-13-57-5W4 well and to assess the lateral continuity of the other formations of the Elk Point Group, geophysical wireline logs available through GeoSCOUT (Geologic, 2013) were obtained and processed in RokDoc (Ikon Science, 2013). Only wells with a True Vertical Depth of more than 1.000 m were used, as to get a complete picture of the Elk Point Group. The bore hole deviation logs show that all wells are essentially vertical, so that no corrections need to be applied to obtain formation thicknesses. Formation thicknesses vary slightly throughout the study area, but are reasonably consistent for all formations. The variations in depth below the surface are mainly due to topography of the surface although a very slight dip towards the southwest can be observed for the Elk Point Group in general. This matches the observations of Hamilton (1971). The wireline logs with the interpreted formation boundaries are shown in Appendix A.

5.1.3 Vertical and lateral continuity of formation properties

Although the formations of the Elk Point Group are laterally consistent in thickness and are virtually horizontal (except for the slight dip towards the southwest mentioned before), there is considerable vertical variation in geophysical properties (see Appendix A). Throughout a formation, vertical patterns for a certain properties (such as Gamma Ray (GR) or density) are generally consistent from well to well, although the amplitude of local maxima and minima varies. Well 10-13-60-04W4, for which only GR values are available, forms an exception with much lower values for GR than any other well. This is potentially due to an incorrect calibration factor used in post-processing of the GR tool data.

All salt formations (including the Cold Lake Formation) show very consistent GR, density and Vp (P-wave velocity) logs with only very local spikes. The caprock formations (Watt Mountain Formation and Ernestina Lake Formation) show considerable variation in properties with depth however. The Keg River Formation shows a steady increase in GR, Vp and density with depth.

Visual inspection of the Ernestina Lake Formation core confirmed the variation of properties with depth. Figure 42 shows core photographs of core material that is considered to be the same formation, illustrating this variation.

The high clay content observed in the Lotsberg Formation near the interface gives incentive to doubt the vertical and lateral continuity of properties in the Lotsberg Formation since numerous authors (e.g. Meijer Drees (1994), Grayston et al. (1964) and Grobe (2000)) mention the extremely high halite content of over 95% of the formation. Because of the history of repeated dissolution and re-precipitation, it is likely that the Lotsberg Formation will vary in composition and properties both



Figure 42. Three photographs of core material from the Ernestina Lake Formation

vertically and laterally. If the Lotsberg Formation is indeed composed of almost exclusively halite in other locations, this will almost certainly affect the geophysical properties of the formation. Visual

inspection of the core material suggests that the Lotsberg Formation has higher halite content and lower clay content at greater depth, although it is uncertain how this trend continues beyond 1210 m, which is the maximum depth for which core material is available.

Considering the similarities in wireline logs from well to well over tens of kilometers, it is thought that on this scale, lateral variation within the formations are minor (except for the Lotsberg Formation, for which no reliable assessment can be made). Vertical variations within formations however, seem to be of much larger magnitude. This concept of lateral continuity and vertical variation fits the geological history of the basin, where depositional conditions were probably similar over a large area and where temporal variation was of much greater importance.

5.2 Laboratory testing program

This section discusses the results obtained during the laboratory program. In the first part of the section, the discussion is organized by formation. In the latter portion, discussion focuses on testing issues common to all formations.

5.2.1 Watt Mountain Formation

The Watt Mountain Formation is the caprock formation for the Prairie Evaporite Formation (top cavern). Geomechanical testing on specimens from the Watt Mountain Formation showed considerable variation in strength properties. Tensile strength calculated from BTS tests show a tensile strength varying from 0.99 MPa to 8.77 MPa and unconfined compressive strength ranges from 16.6 MPa to 142 MPa. The triaxial tests also show a wide range of strengths (Figure 43) and a confident calculation of the angle of internal friction and cohesion cannot be made based on Mohr-Coulomb.

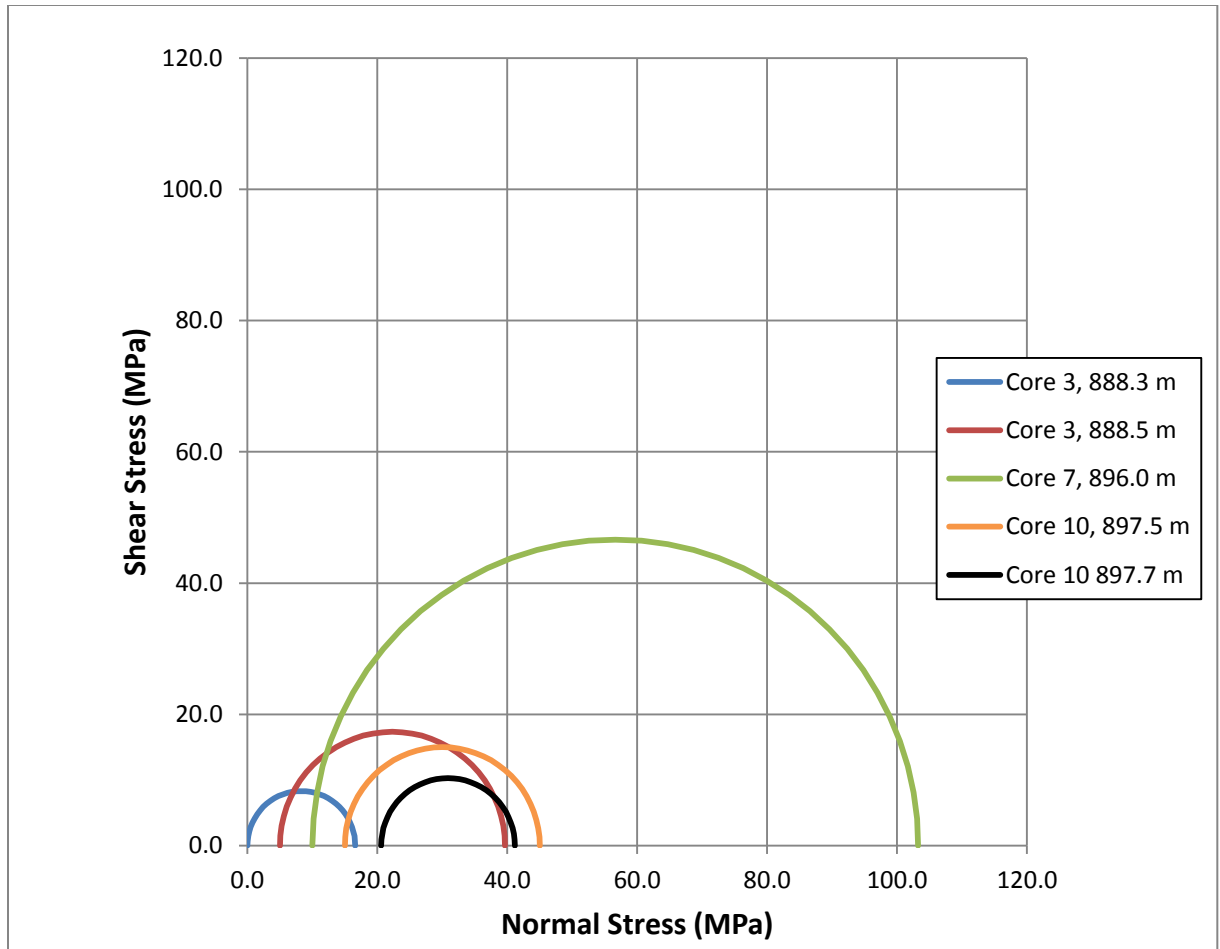


Figure 43. Mohr Coulomb Failure Circles – Watt Mountain Formation

All test data was plotted in p-q space, as shown in Figure 44. These data suggest an internal friction angle of approximately 60° with no apparent cohesion. However, these values are suspect due to the high sample-to-sample variability in the Watt Mountain Formation.

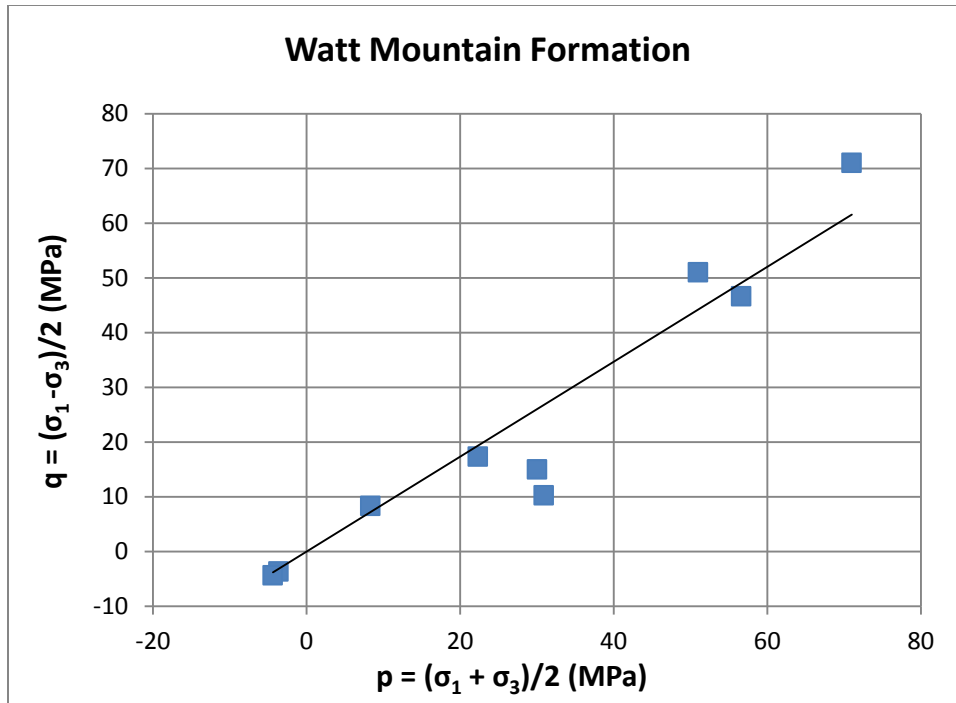


Figure 44. A p-q diagram for the Watt Mountain Formation.

The variation in measured strengths is thought to be primarily due to variable composition with depth within the Formation. Figure 45 shows plots of V_p and E against depth, as well as properties extracted from geophysical wireline logs for comparison. Differential stress at failure measured in the UCS and STC tests, versus depth is plotted in Figure 46. It shows an increase in strength towards the middle of the formation, and a decrease towards both the upper and lower interface. The same trend can be seen in the static (laboratory) values for the Young's Modulus, as well as the laboratory values for the sonic velocity. Although not as pronounced, similar trends are visible in the geophysical wireline values in Figure 45.

This trend of variable strength throughout the formation is the most probably cause for the unrealistically high angle of internal friction and lack of cohesion that was determined from the p-q diagram (Figure 44). It is likely that the angle of internal friction is much lower than 60° (probably closer to a more typical value of 40°) and that the cohesion varies throughout the formation. However, with the amount of data available for this study, it is not possible to confirm this.

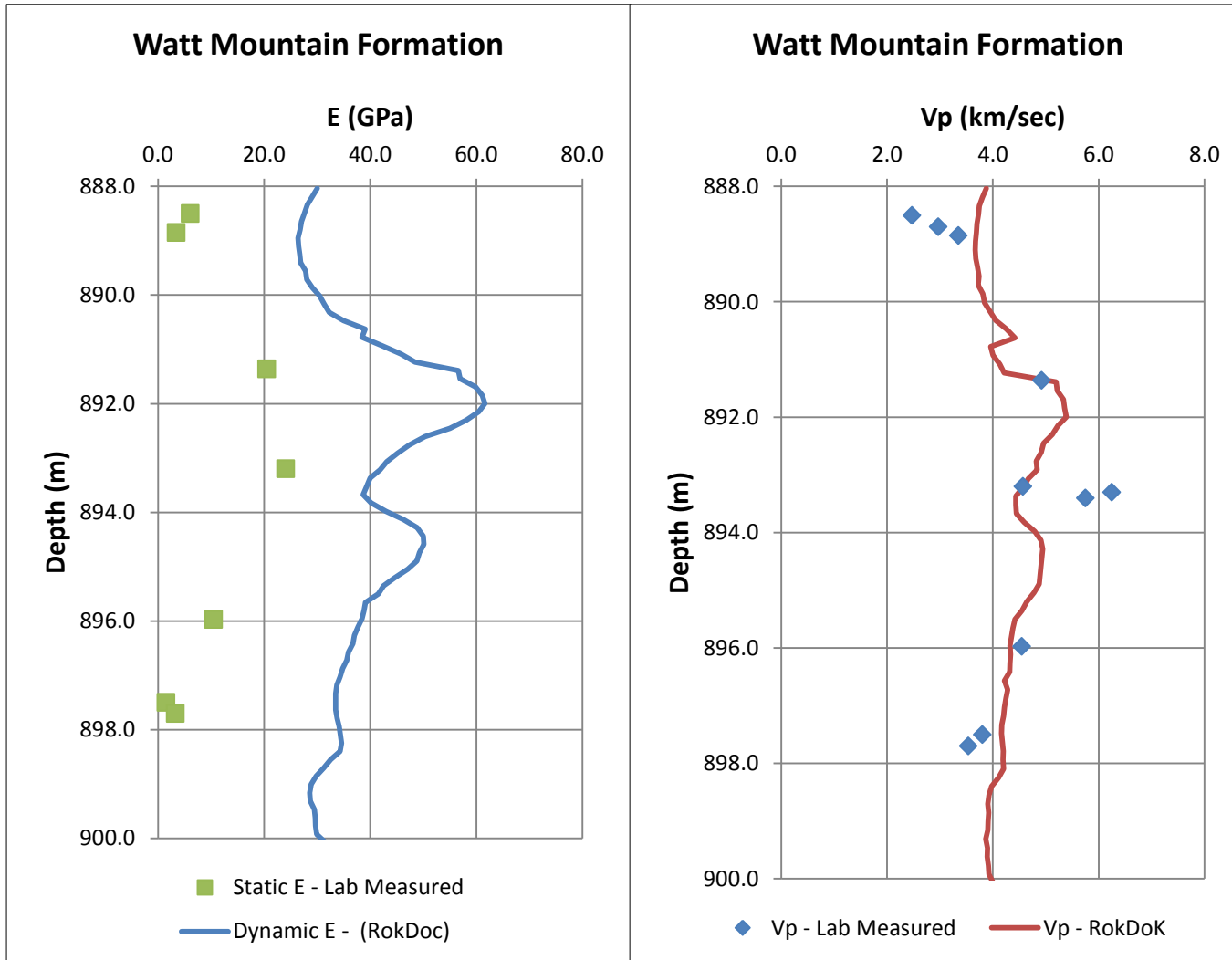


Figure 45. Comparison of Lab Measured Values with Field Logs - Watt Mountain

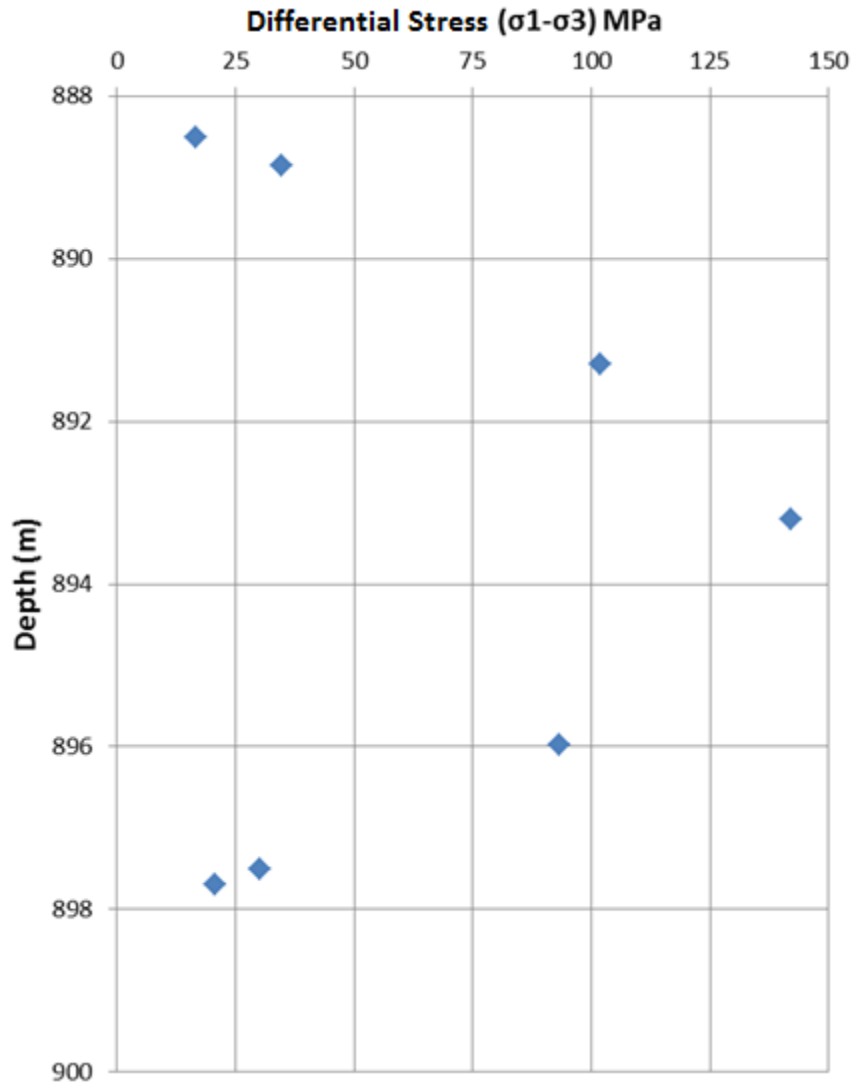


Figure 46. Differential Stress (UCS and STC) at failure versus Depth – Watt Mountain Formation

Although the trends in static (laboratory) and dynamic (geophysical) values for the Young's Modulus are similar, the absolute values differ by approximately 30-40 GPa. This difference can be attributed to the fact that rock samples are neither elastically isotropic, nor ideally elastic. The presence of micro-cracks, which may have (partially) been induced by the original coring, unloading and sample preparation, have a large effect on the elastic moduli, may be the cause for this discrepancy (Kings, 1969).

In general, an increase in sonic velocity corresponds to an increase in both tensile and compressive strength of the formation. The wide range of properties within the same formation raises the question as to what extent the Watt Mountain Formation can be characterized by a single set of

strength properties. For modelling purposes, it might be desirable to use sonic logs as input parameters, as these demonstrate the variability of strength parameters with depth.

5.2.2 Prairie Evaporite Formation

Geomechanical testing on specimens from the Prairie Evaporite Formation shows fairly consistent properties at the depths tested. The measured unconfined compressive strength was in range of 25.3 to 30.4 MPa. Axial strains at failure ranged from 2.3% to 3.9%, which is due to the tendency of the rock salt to flow. None of the samples failed catastrophically, but strength decreased slowly. During testing, small inter-crystalline tensile cracks could be seen forming parallel to the direction of the applied stress. These cracks allowed the sample to deform to high strains without a sudden loss in strength.

BTS testing on the first two samples was carried out using curved platens as described in Section 3, and as recommended by Mellor & Hawkes (1971) to overcome stress concentration problems. For these samples, using the curved platens proved to be an obstacle, as the samples would mold to the shape of the platens before failure could occur. This allowed the applied force to be distributed over a much larger area and thereby invalidated the test results. For one test, the sample was placed between two flat surfaces and two thin pieces of compressible material, to overcome the stress concentration problem without allowing the sample to mold to any surface as recommended by Fuenkajorn (1988). The resultant tensile strength of 1.7 MPa is slightly less than the 10% of the unconfined compressive strength.

Creep testing on Prairie Evaporite samples shows that flow laws in the form of $\dot{\epsilon} = A \sigma^n$ provide an adequate fit to observed creep behavior on a sample to sample basis, but a general flow law for the entire formation is less exact and is characterized by significant uncertainties (Figure 47 and Figure 48). The best-fit flow law that results from the fitting procedure described in Section 3 fits the laboratory data reasonably well (power law fit and observed laboratory data stay within one order of magnitude). However, it generally underestimates strain rates at relatively high differential stresses (greater than 15 MPa). This effect is expected to be more pronounced at higher differential stresses, as the slope of flow law as seen in Figure 47 is less steep than the envelope of the generated laboratory data (solid lines in Figure 47). It is therefore recommended that the flow law is only used for differential stresses up to 21 MPa, since this is the maximum differential stress that has been used in the laboratory and a reasonable fit has been confirmed for this stress range.

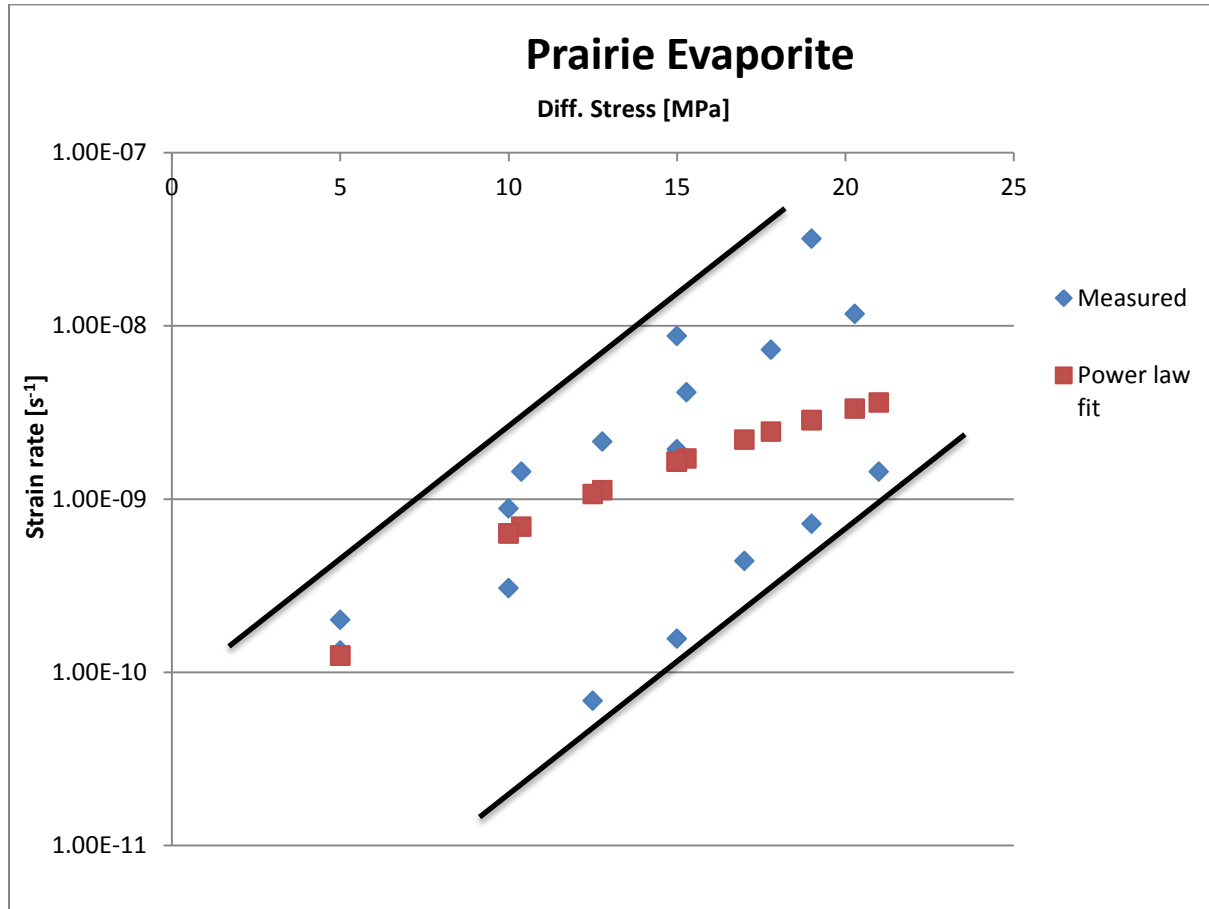


Figure 47. Power law fit – Entire Prairie Evaporite Formation. Black lines indicate the steady-state strain rate envelope observed in this study.

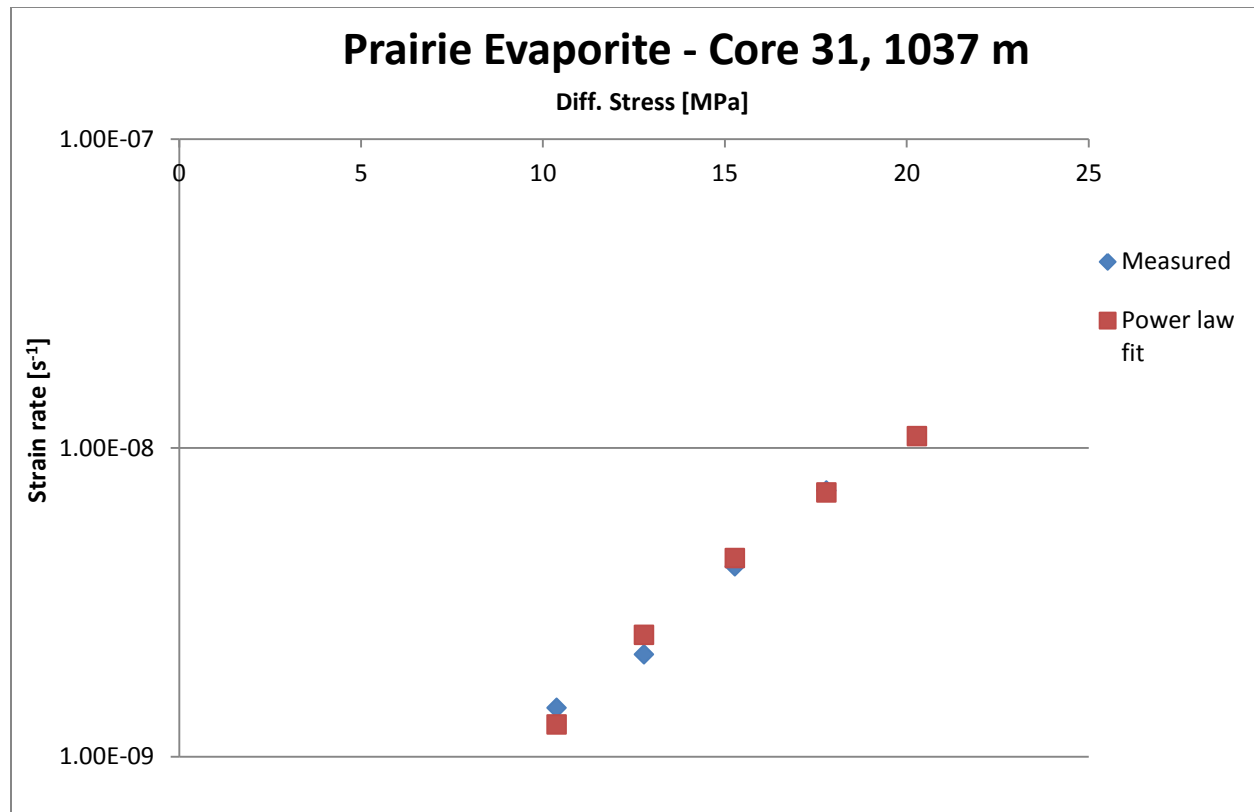


Figure 48. Power law fit – Core 31, 1037 m, Prairie Evaporite

The highest steady-state strain rate that is expected at a differential stress of 20 MPa is approximately $1 \times 10^{-7} \text{ s}^{-1}$ which is equivalent to 0.8% strain per day. Such a strain rate will inevitably cause damage to the formation and will most likely lead to failure within a month. Therefore, it is highly recommended that differential stresses are kept to an absolute minimum at all times by maintaining a cavern pressure that is close or equal to the geostatic pressure at the depth of the cavern.

Figure 49 presents a comparison of laboratory-measured values of E and V_p , compared with those generated in RokDoc. The discrepancy between static and dynamic values for the Young's Modulus is fairly constant at approximately 25-30 GPa. It is important to note that there is a distinct difference between the laboratory E values obtained during UCS testing and those obtained during CMC testing. UCS values for the Young's Modulus range from 1.2 to 4.6 GPa, whereas the CMC values are fairly constant at 6.2 to 7.2 GPa. This is thought to be due to micro-crack closure under confining pressure during the CMC tests. The presence or absence of micro-cracks has a large effect on the static value of the Young's Modulus. For the purposes of salt cavern excavation at depth, the CMC values for the static Young's Modulus are expected to be most representative.

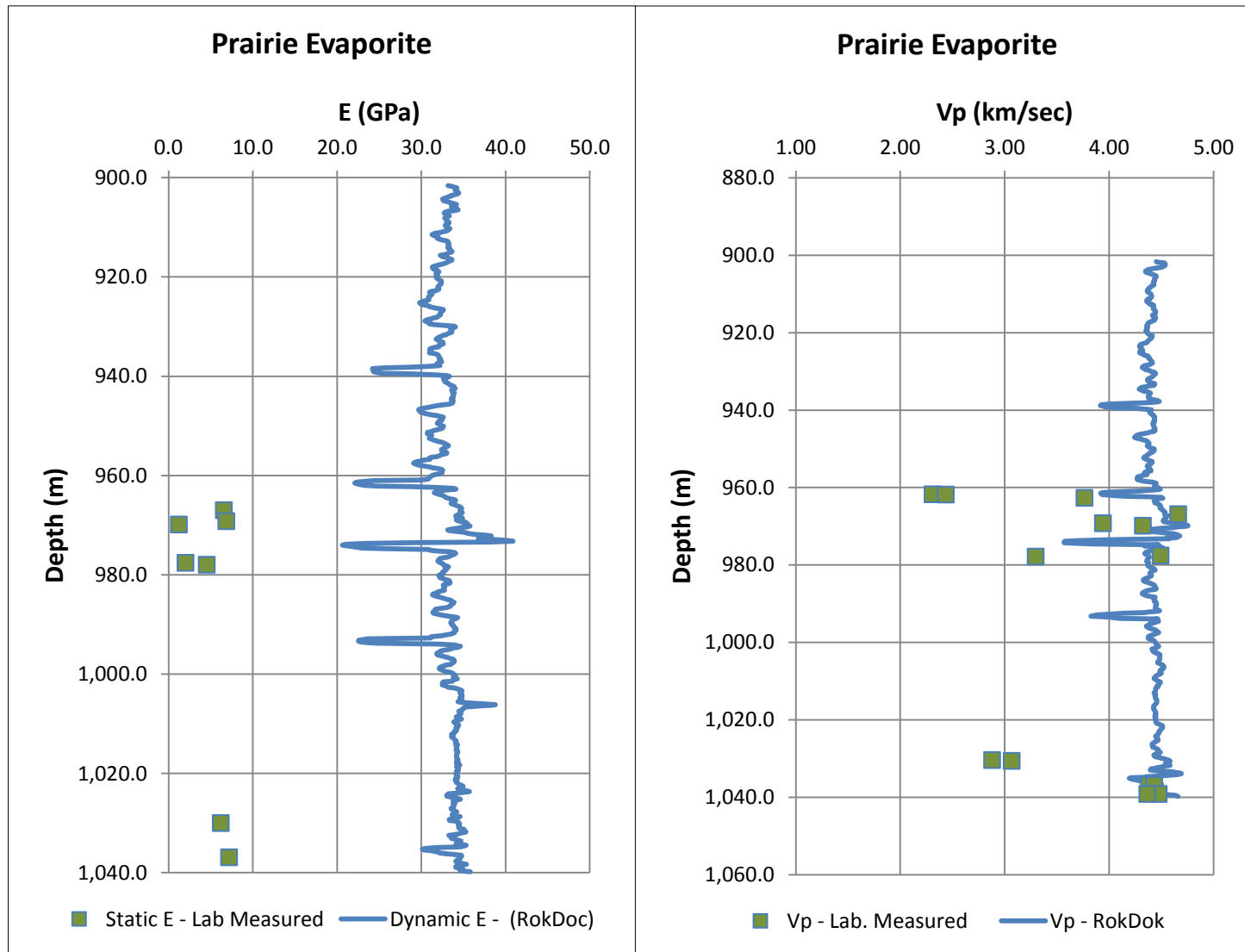


Figure 49. Comparison of Laboratory Measured Values with Geophysical Logs – Prairie Evaporite Formation

5.2.3 Keg River Formation

Samples of the Keg River Formation were tested in standard triaxial and unconfined compression testing. The formation has a wide range of strengths, but overall the formation shows relatively high stresses at failure. The p-q diagram for the Keg River formation is provided in Figure 50.

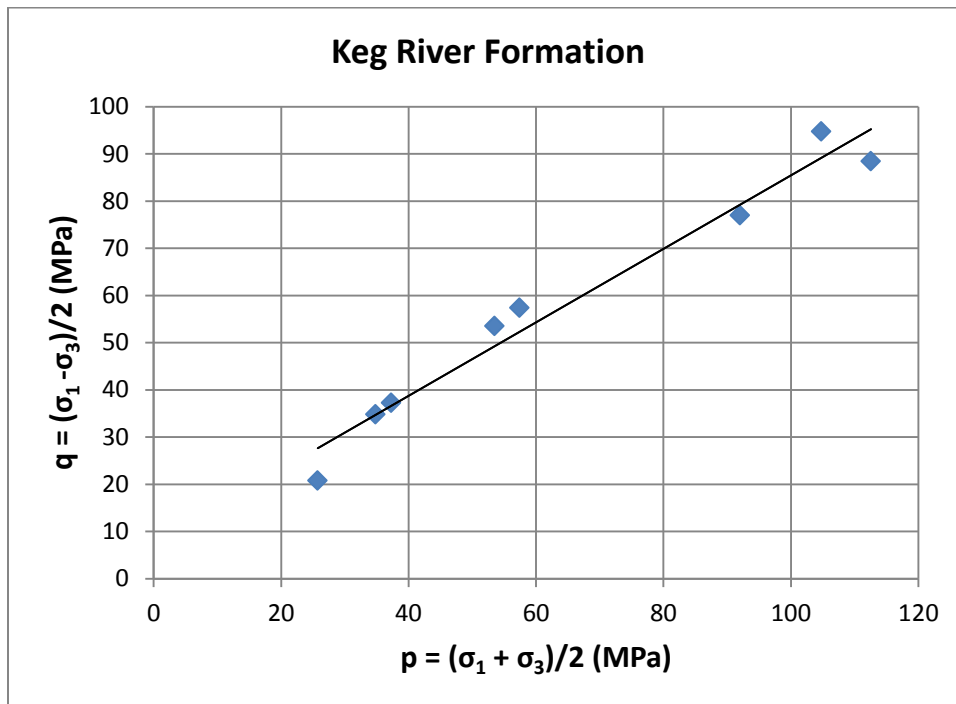


Figure 50. A p-q diagram – Keg River Formation

The unconfined compressive strengths range from 74.5 MPa to 144.8 MPa and the differential stresses at failure in STC testing ranges from 46.5 MPa to 201.0 MPa. Based on the p-q diagram, a friction angle of 51° and cohesion of 6 MPa have been calculated based on a best fit through the data points. These parameters are somewhat suspect, because of the high sample-to-sample variability within the Keg River Formation.

Just as in the Watt Mountain Formation, static values for the Young's Modulus are approximately 30-40 GPa lower than the dynamic values. Laboratory values for sonic velocity are slightly less than the values obtained from wireline logs, with the exception of one point at 1045.1 m which is anomalously low for unknown reasons. The static values for the Poisson's ratio are much more variable than the approximately constant value of 0.28 obtained from geophysical wireline logs. This is most probably due to the use of a limited number of radial LVDTs that could be installed for diametric strain measurements. The dynamic values are thought to be more representative for the actual Poisson's ratio.

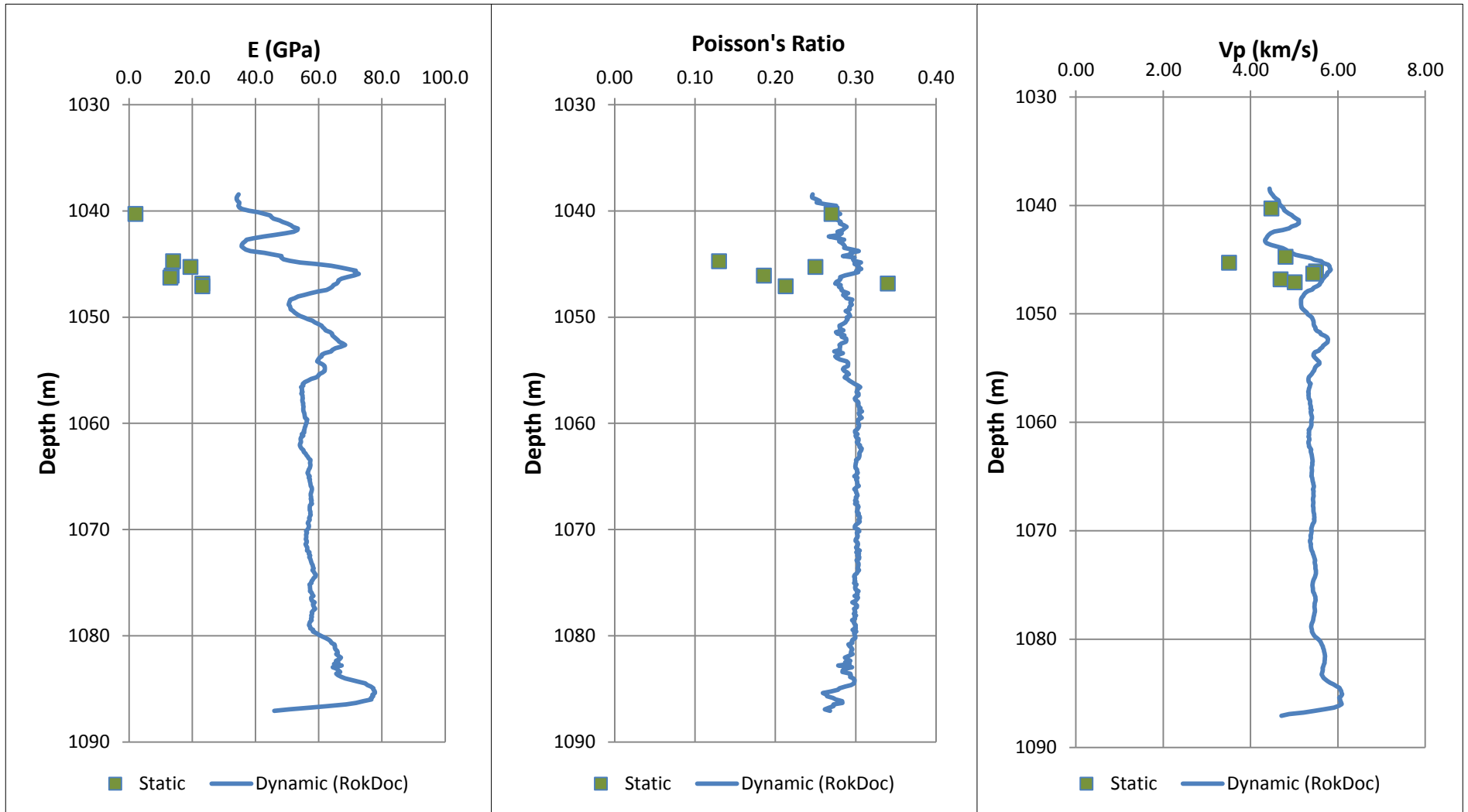


Figure 51. Comparison of Laboratory Measured and Geophysical Data – Keg River Formation

5.2.4 Cold Lake Formation

Samples of the Cold Lake Formation have only been used for UCS testing as the formation is neither a caprock formation nor a formation in which caverns are planned. Unconfined compressive strengths range from 8.9 MPa to 18.0 MPa with axial strains at failure ranging from 0.85% to 1.14%, which is lower than both the other rock salt formations tested in this project. This is probably due to the very large crystal sizes (up to ~60 mm) in the formation as well as the purity of the formation. Inter-crystalline tensile cracking such as in the Prairie Evaporite was largely prohibited by the large crystal size, and no strain could be accommodated through deformation in clay. This caused the samples to fail at lower stresses and smaller strains.

5.2.5 Ernestina Lake Formation

The Ernestina Lake Formation is the caprock formation to the Lotsberg Salt in which the lower caverns are planned. Tensile strength calculated from BTS test show a narrow range of values from 3.8 MPa to 5.7 MPa and unconfined compressive strength ranges from 51.5 MPa to 53.8 MPa in the samples. Triaxial testing shows less consistent results however, with differential stress at failure decreasing with increasing confining stress. The p-q diagram shown in Figure 24 clearly indicates this inconsistency. No failure criterion that encompasses the complete formation could be generated.

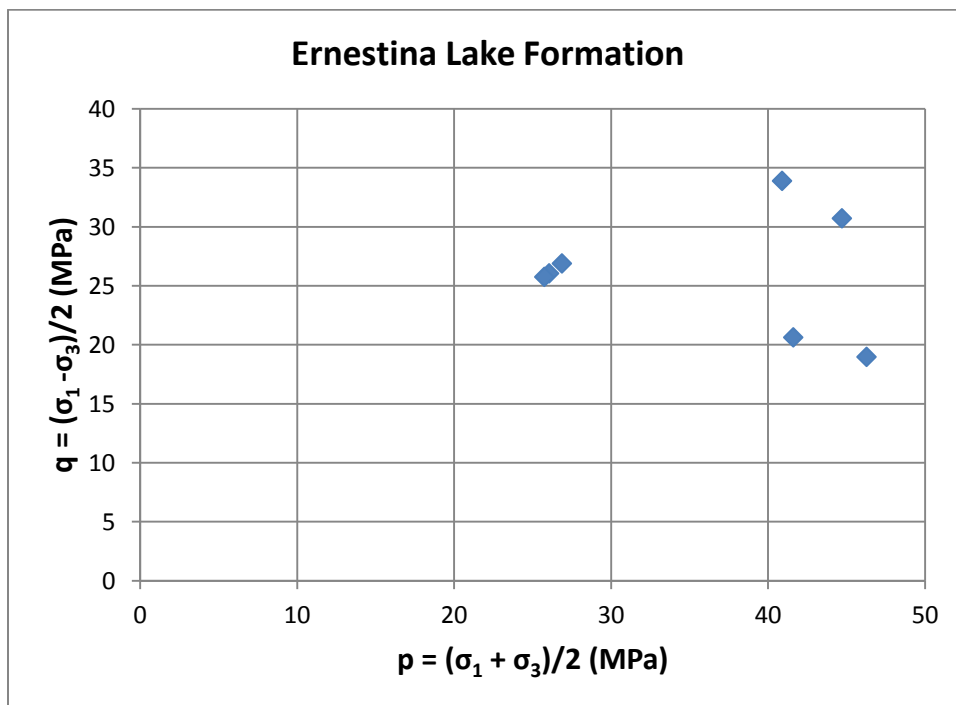


Figure 52. A p-q diagram – Ernestina Lake Formation

Figure 53 shows the differential stress at failure versus depth. It is also compared to the dynamic E values generated from the geophysical wireline logs, and the laboratory measured E values.

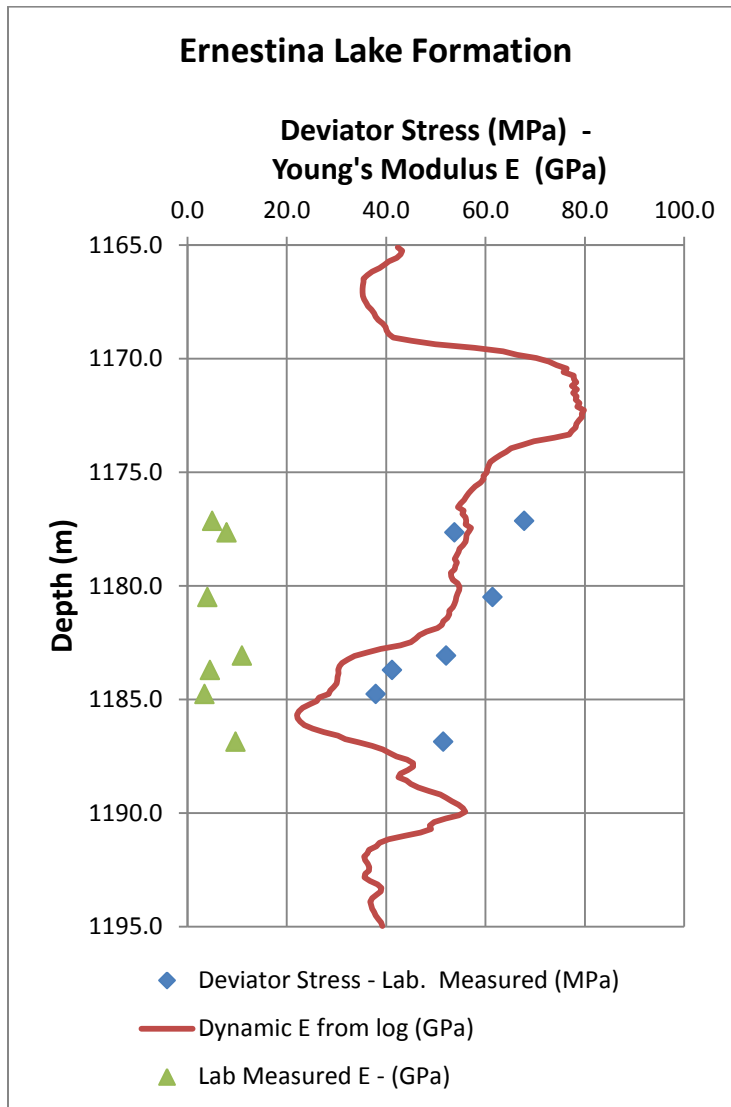


Figure 53. Correlation between differential stress at failure and Young's Modulus for Ernestina Lake Formation

This variation in strength with depth may be explained by different sample composition. The increasingly weaker samples came from increasingly greater depth, closer to the interface with the Lotsberg formation. Closer to the Lotsberg Formation, the salt content of the Ernestina becomes much higher and salt crystals can easily be found upon visual inspection. This increase in salt content is the

result of the geological history of the Lotsberg Formation, which has undergone repeated dissolution and re-precipitation when the Ernestina Lake Formation was already deposited on top of it. The increase in salt content is also confirmed by pore water analysis and is easily visible in geophysical wireline logs of the sonic velocity, with a sudden drop in the sonic velocity at 1182 m, as shown in Figure 54. The Poisson's ratio stays more or less constant over the entire formation.

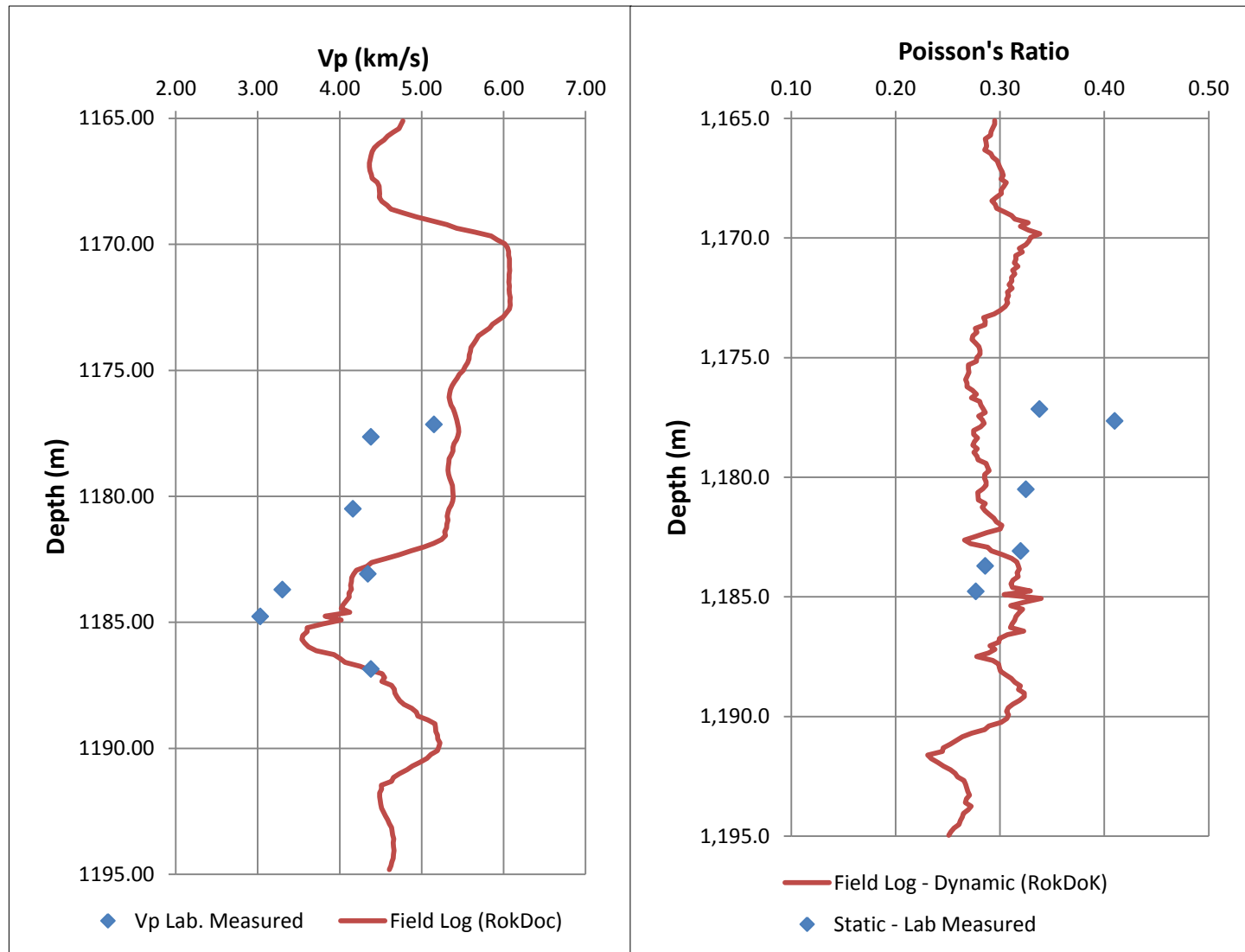


Figure 54. Vp and Poisson's Ratio, Comparison of Laboratory Measured with Field Log (RokDoc) – Ernestina Lake

It is worth noting that while the laboratory values for the sonic velocity show the same trend as the wireline logs, the static Young's Modulus stays more or less constant around the 1182 m mark. The Young's Modulus determined from UCS testing ranges from 7.9 GPa to 11.0 GPa while the values determined from triaxial testing are lower at 3.5 GPa to 5.0 GPa. This trend is the opposite of what other formations show and also directly opposes what would be expected according to King (1969), since micro-cracks close at higher confining stresses and this should result in higher values for the Young's Modulus. The reason for this inconsistency remains unclear.

5.2.6 Lotsberg Formation

The Lotsberg Formation is the formation in which the lower cavern has been planned and at the time of writing, development is ongoing. UCS tests show that the unconfined compressive strength of the formation is fairly consistent at 18.1 MPa to 21.2 MPa. Tensile strength ranges from 1.6 MPa to 2.5 MPa, which is approximately 10% of the unconfined compressive strength. The slightly lower strengths compared to the Prairie Evaporite Formation are most likely due to the higher clay content (up to 38%) and the much larger crystal sizes (up to approximately 70mm) in the Lotsberg Formation. Figure 35 shows a typical Lotsberg Formation specimen, demonstrating the high clay content. The clay inclusions weaken the formation by providing limited cohesion while the large crystals weaken the formation by allowing only very limited inter-crystalline cracking to accommodate strain. This causes samples to fail at lower axial strains and lower differential stresses than the Prairie Evaporite Formation.

As mentioned before, the Lotsberg Formation has a high variability in clay content. This also influences the extent to which geomechanical properties can be extrapolated to formation scale.

If the Lotsberg Formation is indeed composed of almost exclusively halite in other locations, this will almost certainly affect the geomechanical properties of the formation. Depending on the crystal size, the Lotsberg Formation might behave more like the Cold Lake Formation (in the case of large crystals) or the Prairie Evaporite Formation (in the case of smaller crystals). With the data available, it is not possible to make any predictions about the behaviour of the Lotsberg Formation at any other location than the CNRL 8B WD LIND 08-13-57-5W4 well, which is the well for which geomechanical testing has been performed. Even for this well, the determined geomechanical properties are limited to the depth interval for which tests have been performed (approximately the top 20 m of the formation). The formation might have different properties at greater depth. As mentioned before, visual inspection of the core material suggests that the Lotsberg Formation has higher halite content and lower clay content at greater depth, although it is uncertain how this trend continues beyond 1210 m, which is the maximum depth for which core material is available.

5.2.7 Sample preparation

Samples were prepared in such a way as to minimize the influence of sample preparation on the test results. Since a band saw was unavailable, a diamond saw with water as a coolant was used to cut the samples from the original core. To prevent sample dissolution and cracking, the sample was protected with chemical-resistant flame-retardant PVC heat-shrink tubing. This generally provided a smooth, clean cut with no apparent fracturing and produced much better results than dry cutting or cutting without Heat-Shrink Tubing. When required by the testing equipment, samples were machined to 76 mm diameter using a lathe. Lathing was done by repeatedly taking 0.07 mm off the diameter until the desired diameter was reached. To evaluate the potential effects of machining, two comparable samples from the Lotsberg Formation were tested in uniaxial compression, one sample at core diameter, one sample machined to 76 mm. The unconfined compressive strength of the full diameter sample was 18.1 MPa while the strength of the lathed sample was 18.8 MPa. It is therefore assumed that lathing does not noticeably affect the outcome of the geomechanical experiments.

When the ends of the sample were cut, small chips usually appeared along the circumference. To make sure that the contact area with the platens matched the cross sectional area of the sample, such chips were filled with epoxy. Because of the small amount of epoxy used, it is assumed that this treatment did not influence the outcome of the geomechanical experiments.

5.2.8 Late failure in CMC compared to UCS

The failure of most samples that were used in CMC testing occurred at very low or no confining stress. In most cases, when the confining pressure reached zero, the sample did not fail. In those cases, the axial stress could not be increased to a higher value, due to the nature of the CMC test, which required the mean stress to stay constant. When the sample was left at a constant axial stress and no confining stress, failure would usually occur within 15 minutes, after the sample had deformed axially by several percent. The stress-displacement curve was then extrapolated to the failure strain to give an estimate of the differential stress at failure (Figure 55). These values were always much higher than the values from UCS testing, while the stress state was essentially the same (no confining stress, pure axial loading). This discrepancy is most probably due to the different stress paths and loading rates that were applied in the different tests. UCS testing was done by imposing a rate of deformation (0.2 mm/min for salt samples) and leaving stress as a variable. For a typical sample of approximately 150 mm high this implies that a constant axial strain rate of $2.2 \times 10^{-5} \text{ s}^{-1}$ was imposed on the sample. CMC testing was done by controlling the load and leaving the strain rate as a variable. When the sample did not fail at the highest possible differential load, the stress state on the sample was kept constant until failure

occurred. Sinha (1982) compared the uniaxial compressive strength values for columnar-grained ice at constant strain rate and constant stress rate boundary conditions and concluded that constant stress rate conditions resulted in higher uniaxial compressive strength values. It is proposed here that a similar process is responsible for the discrepancy found between UCS and CMC testing in this project.

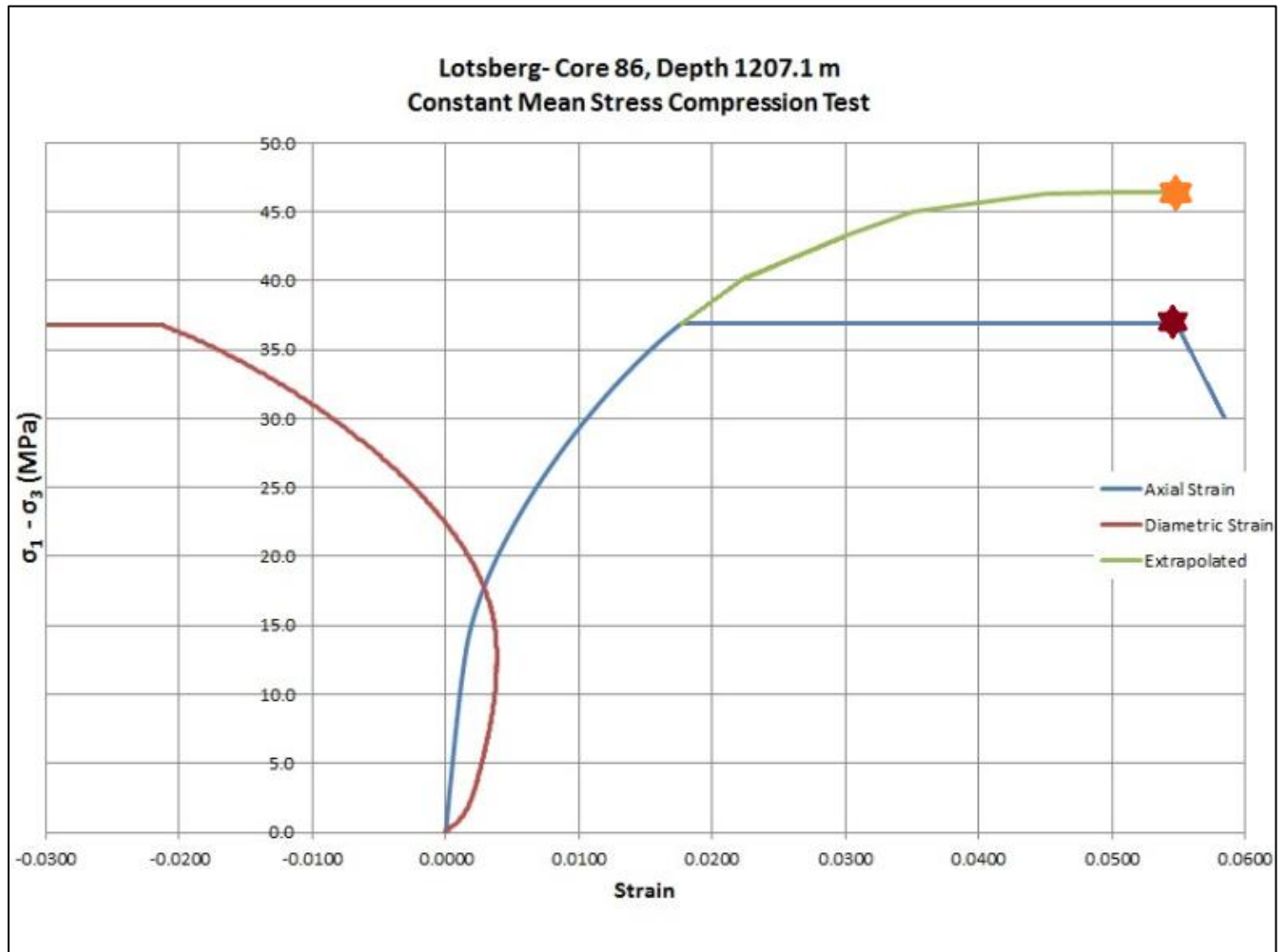


Figure 55. The red star represents the strain at which failure occurred. When the first part of the axial strain curve (the part during which stresses were not constant) is extrapolated to this stress, an estimate of the differential stress at failure (orange star) can be made.

5.2.9 Dilatancy

Constant Mean Stress Compression (CMC) and Constant Mean Stress Extension (CME) tests were performed to investigate the dilatancy behavior of the Lotsberg Formation and the Prairie Evaporite Formation. In Figure 56, the point at which each specimen reached the dilatancy boundary (i.e. when dilation commenced) is shown in stress invariant space, where I_1 is the first invariant of the stress tensor and J_2 is the second invariant of the deviatoric stress tensor.

$$I_1 = \sigma_{11} + \sigma_{22} + \sigma_{33} \quad (\text{Eqn. 18})$$

$$J_2 = \frac{1}{6} [(\sigma_1 - \sigma_2)^2 + (\sigma_2 - \sigma_3)^2 + (\sigma_3 - \sigma_1)^2] \quad (\text{Eqn. 19})$$

The dilatancy boundary is defined as the point where the derivative of the volumetric strain curve reaches zero and a further increase in deviatoric stress will cause the sample volume to increase. This point is also known as the crack damage threshold, the damage critical point or the compression/dilatancy (C/D) boundary (Alkan et al., 2007). Figure 56 also shows two empirical rock salt dilatancy boundary laws by Spiers et al. (1988) and Ratigan et al. (1991).

The onset of dilatancy is a very important parameter for rock salt, since this is the point where damage starts occurring. Dilatancy in rock salt is generally ascribed to the development of micro-cracks (e.g. Peach and Spiers, (1996); Schulze et al., (2001); Stormont and Fuenkajorn, 1993); (Popp and Kern, 2000) and is associated with increasing permeability, increasing damage and the potential for creep failure. Even at volumetric strains of less than 0.2 %, deformation-induced dilatancy can increase the permeability of rock salt by several orders of magnitude (from $\leq 10^{-21} \text{ m}^2$ to $\sim 2 \times 10^{-16} \text{ m}^2$) (Peach and Spiers, 1996). Peach and Spiers (1996) suggest that percolation theory (see Grimmitt (1999) for an elaborate discussion of percolation theory in general) can explain this sudden and extreme increase in permeability in a satisfactory manner. The use of a semi-empirical equation (Eqn. 20), relating the permeability to the stress dependent aperture of cracks by using the cubic law for fracture flow has been used to develop a percolation model that predicts the development of permeability with dilation (Alkan, 2009):

$$[k(\sigma_3)]^{1/3} = m - n \ln(\sigma_3), \quad (\text{Eqn. 20})$$

where k is permeability in m^2 , m is a constant related to aperture width and n is the standard deviation of the surface roughness. This model shows that percolation theory can be used to successfully predict the development of permeability in rock salt.

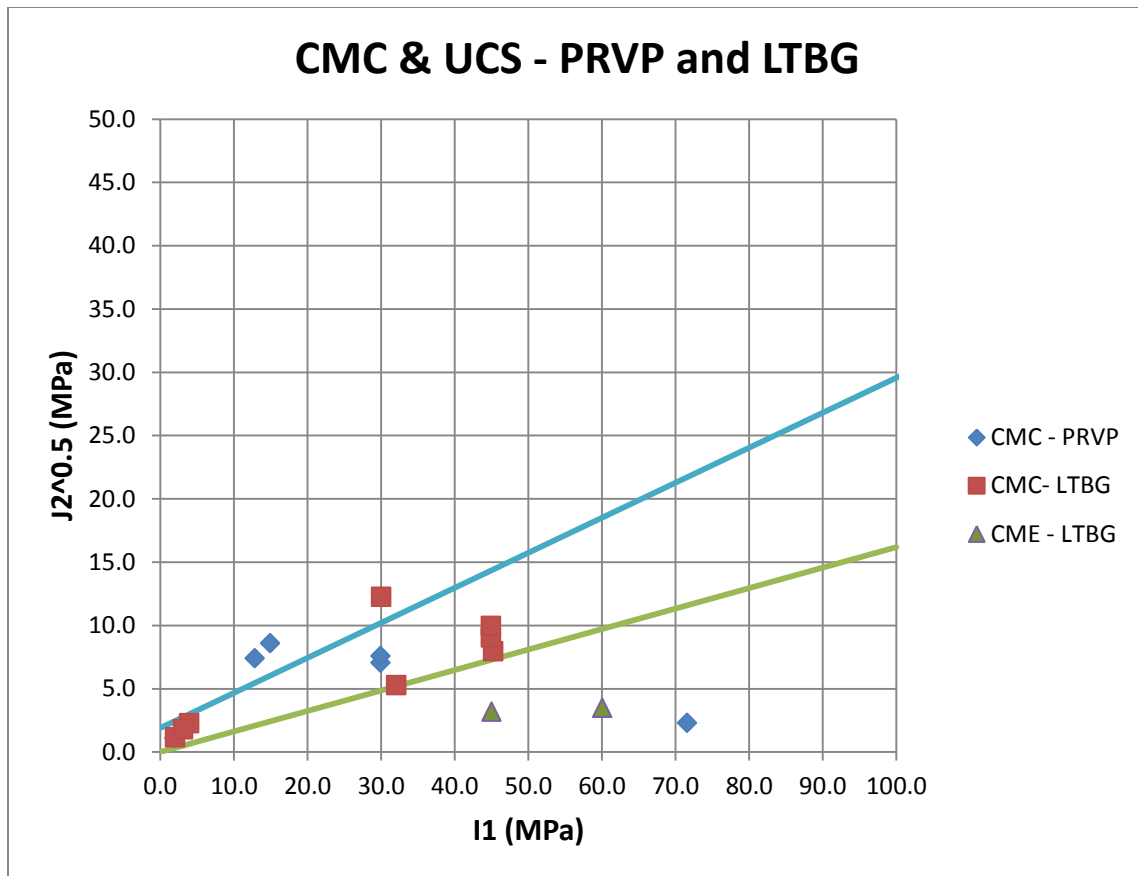


Figure 56. I1 vs J2^{0.5} Plot. Blue line = Spiers et al. (1988), Green line = Ratigan et al. (1991)

The CMC tests on the Lotsberg Formation show general agreement with both Spiers et al. (1988) and Ratigan et al., (1991). An increase in mean stress corresponds with a dilatancy boundary at a higher differential stress. The CME tests on the Lotsberg Formation however, do not correspond to either Spiers et al. (1988) or Ratigan et al. (1991). This might be attributed to inter-sample variability, although no confident causal attribution is currently possible due to the limited number of completed tests. Other possible causes for the observed discrepancy involve the nature of the samples used. The samples used in this study are natural rock core samples of variable purity and with possible coring-induced damage. The samples used by Spiers et al. (1988) were extremely pure in composition and synthetic, ensuring no pre-existing damage to the samples.

Both CME tests show dilatancy at relatively low differential stress values (and therefore low J_2 values). This is possibly due to preferential orientation of pre-existing microcracks. If the preferred orientation of pre-existing micro-cracks in a plane parallel to the samples' ends, these cracks would open during CME testing, while they would be forced to close during CMC testing. In CMC tests, new

micro-fractures would have to be formed in different orientations, which would explain the discrepancy between the CMC and CME test results in the Lotsberg Formation.

The CMC test results on the Prairie Evaporite Formation do not show any correlation with either Spiers et al. (1988) or Ratigan et al. (1991). In fact, there seems to be a trend of a lower J_2 value for higher I_1 values. This is thought to be the result of inter-sample variability.

The fact that several samples start dilating earlier than predicted by either dilatancy boundary law is important to note. It illustrates the potential for permeability to increase at low differential stress states. This is especially important because of the extremely fast (critical) development of permeability as shown in experimental work (Peach and Spiers, 1996) and as predicted by percolation models (Alkan, 2009). This extreme increase in permeability might compromise the sealing capacity of salt cavern walls and could potentially lead to leaking.

5.2.10 Stress path influence on creep

The failure and creep behaviour of rock salt is primarily a function of stress state, and therefore a function of the absolute values of the three principal stresses and the stress geometry (Hunsche and Albrecht, 1990a). Additionally, it is known that the stress path influences the flow behavior of rock salt (e.g. Wawersik and Hannum (1980), Desai and Varadarajan (1987), Hunsche and Albrecht (1990), Jandakaew, (2003, unpublished M.Sc. thesis, available online)).

Conventional multi-stage creep testing on rock materials is done by incrementally increasing the axial stress while keeping the confining stress constant (ASTM D4406-93: Standard Test Method for Creep of Cylindrical Rock Core Specimens in Triaxial Compression). For this project, in order to mimic the stress conditions of salt cavern excavation as closely as possible, it was decided to alter this procedure so that the axial stress (representing the overburden) was constant and the confining stress was incrementally decreased to impose a differential stress on the sample. During radially unloading creep testing, the mean stress of the sample decreases as the differential stress increases. This mimics the expected change in stress state around salt caverns, where the magnitude of the horizontal stresses decrease due to the removal of salt. This decreasing mean stress increases the potential for micro-cracks to form and makes the accommodation of creep by grain boundary sliding easier. During conventional creep testing, both micro-crack development and grain boundary sliding get increasingly difficult because of the increasing mean stress. It is therefore expected that micro-crack development and grain boundary sliding occur at lower differential stresses during radially unloading creep testing when compared to conventional creep testing.

Wawersik and Hannum (1980) compared conventional, radially unloading and constant mean stress creep testing on rock salt and concluded that conventional creep tests resulted in the highest creep rates.

Yang et al. (1999) investigated the influence of confining pressure on the steady-state strain rate of rock salt and concluded that for the same differential stress, higher creep rates were achieved at lower confining stresses.

Jandakaew (2003, unpublished M.Sc. thesis, available online) compared creep behaviour of rock salt as predicted by conventional creep testing and radially unloading creep testing. It was concluded that radially unloading creep testing resulted in higher creep rates than conventional creep testing. Comparison to monitored creep around salt caverns led to the conclusion that radially unloading creep testing gave more accurate predictions of creep behaviour for this specific purpose.

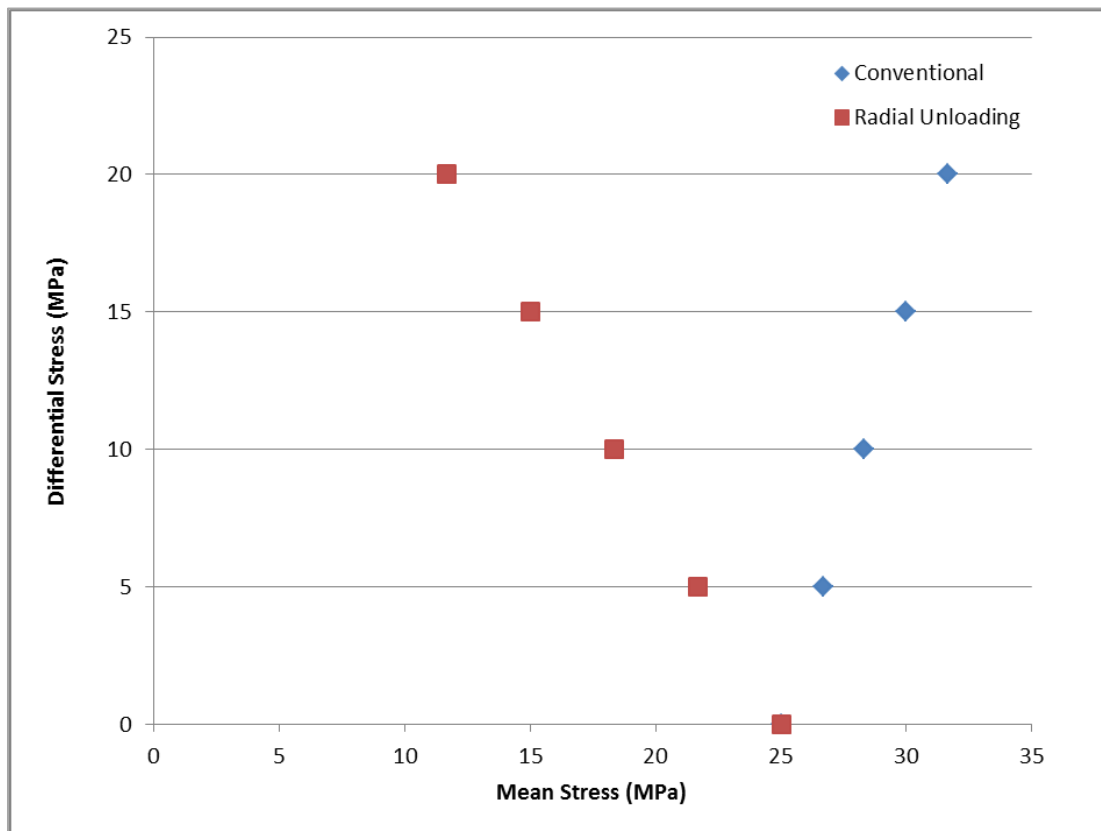


Figure 57. Comparison of stress paths for conventional and radially unloading creep testing. Both tests start at 25 MPa hydrostatic pressure and increase the differential stress by increments of 5 MPa.

5.3 Numerical modelling

5.3.1 Justification of Scenarios and density choices

The numerical models made in FLAC^{3D} represent different potential geometries and filling strategies. The particular configurations that were modelled were chosen to represent realistic scenarios and to study cavern interaction. Cavern development is currently ongoing in the Lotsberg Formation at the 01-13-57-5W4 location. This configuration is represented by Scenario 1. It is likely the next cavern will be developed in the Lotsberg Formation at the 08-13-57-5W4 location but less certain as to whether caverns will be developed in the Prairie Evaporite Formation at the same location. To account for both possibilities, as well as to study horizontal and vertical cavern interaction in isolation, Scenario 2 and 3 were created respectively. Scenario 4 represents a possible final configuration with two caverns at each location.

Because the caverns are created for waste storage, it can be safely assumed that they will be filled with predominantly sandy material. Because both gravity-driven compaction and creep-driven compaction are expected to occur over time, dense sands were modelled in every scenario with more than one cavern. The caverns with dense sands represent the older caverns.

5.3.2 Assumptions

The modelling of the different scenarios required a number of assumptions.

- Most importantly, it is assumed that all formations can be represented by one set of strength and/or creep parameters. This is not realistic, but more complex modelling was not possible with the information available.
- It is assumed that all formations are perfectly flat and of uniform thickness.
- There are no boundary stresses applied to the external boundaries of the model. This assumption is defensible because of the long-term tectonic stability of the modelled area.
- The wellhead pressure of approximately 4 MPa, which is present during cavern development, is assumed to remain on the cavern after abandonment. This might lead to an overestimation of internal cavern pressure.
- The internal pressure is assumed to be independent of cavern volume. Because the caverns' volume will decrease over time, this leads to an underestimation of internal cavern pressure.

5.3.3 Implications

The modelling results for all scenarios and density choices show that failure is not expected to occur anywhere in the model and that shear stresses dissipate quickly to values below 4.3 MPa. The greatest modelled surface subsidence of 48mm in Scenario 4, at the centre of the subsidence bowl, is largely the result of the brine-filled caverns in the Prairie Evaporite Formation caverns. It is highly unlikely that caverns will remain brine-filled for 50 years. When graded sands or dense sands are modelled for Scenario 4, maximum surface subsidence is modelled to be 12.1 mm and 4.38 mm respectively. Similarly, large vertical displacements around the salt caverns are predicted for brine-filled caverns. Again, these values quickly diminish when a more realistic choice is made for the material filling the cavern.

Generally, the predictions made by the FLAC^{3D} models can be divided into predictions about stress state and predictions about response to the stress state (e.g. failure, creep and displacement). Because of limited amount of assumptions necessary for the stress predictions, it is thought that the stress state predictions are fairly reliable. However, predictions related to the response to the stress state (i.e. strains) are thought to be less reliable as they rely on more assumptions and simplifications. As noted before, the formations of interest are highly variable in strength properties, which is not captured by the model presented here. Moreover, the model does not account for dilatancy, which starts well before failure occurs. This has implications for permeability and fluid infiltration as well as related issues such as tensile failure and long-term fluid isolation.

Improvements to the current model could be made by allowing strength and creep properties to vary throughout formations (both vertically and laterally) and by accounting for dilatancy. Additionally, sensitivity of the results to changes in strength parameters, creep parameters, model size, grid size and time step duration should be assessed.

5.4 General discussion

5.4.1 Comparison to other work

The strength, creep and elastic parameters of rock salt presented in this study were compared to published data. Liang et al. (2007) report peak stresses in UCS tests, as well as values for Young's Modulus and Poisson's ratio. Yang et al. (1999) performed creep testing at room temperature at a range of different confining stresses and deviatoric stresses. Hunsche and Hampel (1999) reported uniaxial creep rates at 22 °C. All these results are presented in Table 32. Wawersik and Zeuch (1986) summarized creep rates for rock salt from 5 locations at a 23 °C to 160 °C and differential stresses from 8.3 MPa to 24 MPa. They concluded that 5×10^{-8} to $1 \times 10^{-9} \text{ s}^{-1}$ was the typical range for rock salt creep rates.

Table 32. Creep, strength and elastic properties from other authors.

Authors and year							
Test methods							
Liang et al., 2007 UCS testing	Lithology	Peak stress UCS (MPa)	Axial strain at failure (%)	Young's Modulus (GPa)	Poisson's ratio (-)		
	Rock salt	20.27	0.54	4.4	0.31		
	Rock salt	17.06	0.52	5.9	0.31		
	Salt+Anhydrite	23.29	0.47	7.6	0.16		
	Salt+Anhydrite	17.29	0.52	5.3	0.30		
Yang et al., 1999 Creep testing (creep rates in s^{-1})	Differential stress (MPa)	Confining stress (MPa)					
		0	1.8	3.6	5.4	7.18	10.8
	14.3	0.6×10^{-8}	0.2×10^{-8}	0.7×10^{-9}	0.3×10^{-9}		
	21.5	2.0×10^{-7}	6×10^{-8}	2×10^{-8}	1.2×10^{-8}	0.8×10^{-8}	0.2×10^{-8}
	28.7	7×10^{-7}	9×10^{-8}	7×10^{-8}	4×10^{-8}	1.8×10^{-8}	1×10^{-8}
	35.9					1.3×10^{-7}	
Hunsche and Hampel, 1999 Uniaxial creep	Differential stress (MPa)	No confining stress					
	12	2.0×10^{-10} to $1.0 \times 10^{-9} \text{ s}^{-1}$					
	14	2.5×10^{-10} to $1.27 \times 10^{-9} \text{ s}^{-1}$					

The values for steady-state creep rates, UCS peak strength, Young's Modulus and Poisson's ratio presented for rock salt in this study are very close to values presented in previous work. The main discrepancy is the axial strain at failure in UCS testing presented by Liang et al. (2007) of approximately 0.5%. This is significantly smaller than the axial strains reached in this study, which were 2.3 to 3.9% for the Prairie Evaporite Formation and 0.6 to 3.0% for the Lotsberg Formation. This discrepancy could be due to differences in stress history, loading rate, composition or grain size.

5.4.2 Dynamic and static elastic moduli

Throughout all formations studied in this project a large discrepancy between the static and dynamic values for the Young's Modulus and Poisson's ratio was apparent. For the Young's Modulus, the static values were consistently much lower than the dynamic values. For the Poisson's ratio, the static values were much more variable than the dynamic values

For the Young's Modulus, the difference between static and dynamic values is thought to be due to two processes operating side by side. The first cause is the presence of micro-cracks in the samples. These micro-cracks hardly affect the dynamic value for the Young's Modulus, but significantly lower the static value (Kings, 1969). The second cause is the difference in the frequency of the applied strain. Dynamic measurements rely on small strain amplitudes at a high frequency, whereas static measurements rely on relatively large strain amplitudes at a low frequency (during CMC testing, one load-unload cycle took 4 minutes). Rocks become stiffer as the frequency of the applied strain increases, which increases the Young's Modulus (Mashinsky, 2003). For numerical modelling and strength evaluation purposes, the static values of the Young's Modulus are assumed to be most representative since they were obtained in a setting similar to a natural setting (i.e. larger strains at low frequency).

The high variability of the static values for the Poisson's ratio is thought to be due to the limited amount of radial deformation measurements that could be taken during testing. During UCS testing, three radial LVDTs at mid-height were used, whereas during STC testing, a chain extensometer at mid-height was used. Neither of these methods reflects the average radial deformation over the whole sample. For this reason, it is assumed that the dynamic value for the Poisson's ratio is more representative.

5.4.3 Salt creep: mechanism of flow

In the temperature and stress range that creep testing was performed in this study, four microstructural processes can operate to accommodate flow. These processes are dislocation creep, crystal plasticity combined with micro-cracking, fluid-assisted grain-boundary migration and fluid-assisted grain-boundary diffusional creep or “pressure solution”. Microstructural analysis of naturally deformed salt has shown that all of these processes are important in nature and that the relative importance of each of these processes depends strongly on grain size, impurity content, stress path and fluid chemistry (Urai et al., 2008).

The rock salt samples in this study had water contents of 500 ppm up to 0.91%, which is more than sufficient to allow pressure solution creep (Urai et al., 2008). However, due to the average grain size of the samples (>1 cm), pressure solution creep can only accommodate creep rates slower than 10^{-12} s^{-1} (Spiers et al., 1990). Therefore, pressure solution creep does not account for the creep rates observed in this study.

Because of the high apparent n -values (up to 5.95) that are observed in this study, as well as the relatively short duration of the performed tests, creep is most likely primarily accommodated by dislocation creep (Urai et al., 2008), although all four aforementioned processes probably operated simultaneously with varying degrees of significance.

5.4.4 Scaling problems

When applying geomechanical properties obtained in laboratory experiments to geological or engineering reality, it is important to realize the differences in spatial and temporal scale. The laboratory experiments in this project were performed on samples ranging from $1.7 \times 10^{-4} \text{ m}^3$ (BTS) to $1.2 \times 10^{-3} \text{ m}^3$ (CMC, UCS, creep) with test duration ranging anywhere from 5 minutes (UCS, BTS) to 7 weeks (creep). The salt caverns on which this project is focused will have a volume in the order of 10^5 - 10^6 m^3 and will affect rock masses of volumes several orders of magnitude higher. Moreover, the caverns will have to be stable for thousands to tens of thousands of years. Extrapolating laboratory data over this many orders of magnitude cannot be done without careful consideration for potential errors.

The ASTM requirement concerning particle size to diameter ratio (the diameter of any sample should be at least 10 times larger than the largest particle in the sample) is designed to ensure that a geomechanical test on a sample is representative for the material as a whole, rather than being dependant on the composition and orientation of the particles in a particular sample. In this project, this requirement could not be met for all Lotsberg Formation and Cold Lake Formation samples and some of the Prairie Evaporite Formation samples due to the original core size and the large crystal sizes in these

formations. This means that implementation of properties such as unconfined compressive strength or tensile strength should be done with the utmost care and the realization that the actual strength of the formation may be stronger or weaker.

Implementation of other properties such as Young's Modulus and Poisson's ratio is expected to be easier due to the time and scale independent nature of these properties. Implementation of creep data is expected to be fairly straightforward within the range for which the flow laws are designed (differential stresses up to 21 MPa). The n -value of the flow laws, as well as the transition from primary to secondary creep upon every increase of differential stress implies that dislocation creep is the dominant deformation mechanism by which the salt formations deform. For the time scale of this project (order of tens of thousands of years), pressure solution creep is thought to be unimportant and can safely be neglected (Spiers et al., 1990). Diffusion creep mechanisms such as Nabarro-Herring creep and Cobble creep are also unimportant at the temperatures of interest and dislocation glide is thought to operate at higher differential stresses. This implies that the flow laws obtained in the lab should apply at full scale as well.

5.4.5 Estimating properties away from the well

Even though major lateral variation in properties is not evident from geophysical wireline logs, no confident estimations can be made about strength and creep properties away from the CNRL 8B WD LIND 08-13-57-5W4 well. Methods developed to calculate geomechanical properties away from wells generally rely on seismic survey data and are almost exclusively aimed at reservoir geomechanics (e.g. Gray et al. (2012), Al-ruwaili et al. (2003), Sengupta et al. (2011)). Although the quality of seismic data in salt has improved since the development of 3D seismic acquisition, it is still notoriously difficult to get adequate seismic data in salt (Perez et al., 2008). Moreover, the extreme capital investment needed for 3D seismic acquisition on land makes this option unavailable for a waste disposal project in which there is no opportunity to earn back the investment.

Geological (depositional) models based on interpolation of well data could potentially be used for most formations, but considering the well spacing of several kilometers between wells that penetrate the Elk Point Group, uncertainties would be high and resolution would be low.

A potential way to increase the accuracy of property calculation away from wells is to acquire shear wave velocity logs (V_s logs) for wells in addition to the conventional compressional wave velocity logs (V_p logs). V_p and V_s logs can be used to calculate dynamic bulk elastic properties such as Young's Modulus and Poisson's ratio through Equations 2 and 3 respectively. In combination with GR and bulk density logs, more accurate estimations of lithology and strength properties can be made per well,

leading to an increased amount of data that can be used for interpolation of well data. Although it is possible to estimate V_s logs from V_p logs (Greenberg and Castagna, 1992), this method relies on the availability of lithology, porosity and water saturation data. Even if all this data is available, the model uses typical V_p/V_s ratios (and therefore typical elastic properties) for the assigned lithology to estimate the V_s logs. Although this usually results in reasonable estimates, it is by no means as precise as the use of an actual V_s log.

With the data that is currently available for this study, confident estimations about geomechanical properties away from CNRL 8B WD LIND 08-13-57-5W4 well cannot be made.

6. CONCLUSIONS

6.1 Geological setting

On a large scale, the geological setting was investigated using scientific and industrial research papers. On a regional scale, the resolution was enhanced by the use of geophysical wireline logs for ten wells in the study area. Based on this work, the following conclusions can be presented:

- Due to absence of tectonic activity, the stratigraphy of the Devonian Elk Point Group in the East-Central Alberta Basin is of a `layer-cake` type structure, with no evidence for major faults. It is predicted that on the timescales relevant for engineering purposes (in the order of 10.000 years), the area can be considered as tectonically stable.
- The distribution and thickness of the formations of the Elk Point Group are known to a high degree of accuracy. Formations show little variation in thickness and are sub-horizontal with a slight dip to the southwest.
- Variation in composition and properties within formations is thought to be significant. Based on the geophysical wireline logs, lateral variation are minor and most variation within formations occurs in the vertical dimension (variation with depth). This concept of lateral continuity and vertical variation fits the geological history of the basin, where depositional conditions were probably similar over a large area and where temporal variation was of much larger importance. An exception to this is the Lotsberg Formation which, due its history of repeated dissolution and reprecipitation, will likely vary in composition and properties both vertically and horizontally.

6.2 Laboratory testing program

This report documents the results of the laboratory testing program carried out on core recovered from CNRL 8B WD LIND 08-13-57-5W4. The testing program included both index testing to describe the physical properties of the rock core, and geomechanical testing to evaluate strength and deformation properties of rock core samples under a variety of stress and stress path conditions. These properties are required to estimate the mechanical response of caverns.

The formations of primary interest included the Lotsberg (lower) and Prairie Evaporite (upper) salt Formations, and the associated overlying caprock formations; Ernestina Lake and Watt Mountain, respectively. Additional limited geomechanical testing was carried out on samples obtained from intermediate formations (Cold Lake – Salt, and Keg River) located below the Prairie Evaporite Formation and above the Lotsberg Formation.

The testing completed included: 12 Brazilian Indirect Tension Tests, 20 Unconfined Compression Tests, 12 Standard Triaxial Compression Tests, 9 Constant Mean Stress tests, and 6 Multi-Stage Creep Tests.

The results of the laboratory tests were analysed and compared to geophysical wireline log data from the CNRL 8B WD LIND 08-13-57-5W4 well. Based on this, the following conclusions can be presented:

- The Watt Mountain Formation shows considerable variation in strength properties with depth, with low strength materials present near the interface with Prairie Evaporite. There is a reasonable correlation between the laboratory measured strength and wireline Young's Modulus. Although laboratory and wireline values of Young's Modulus show the same trend with depth, there is an offset in absolute values of approximately 30 to 40 GPa. This offset is thought to be due to the presence micro-cracks in the sample, as well as the different strain amplitudes and frequencies applied by static and dynamic testing.
- Strength properties were relatively consistent in the Prairie Evaporite samples tested. High axial strains are reached before failure in all geomechanical tests as rock salt tends to flow relatively easily. Creep testing on the Prairie Evaporite Formation shows that flow laws in the form of $\dot{\epsilon} = A \bar{\sigma}^n$ are adequate to describe creep behavior on a sample to sample basis, but a general flow law for the entire formation is less exact and leaves more room for error. The best-fit flow law for the entire formation describes the strain rates observed in this study accurate within one order of magnitude, but generally underestimate strain rates at differential stresses greater than 15 MPa. This effect is expected to get progressively more pronounced at even greater differential stresses.

- The Keg River Formation consistently shows high strength values, with an estimated angle of internal friction of 51° and cohesion of 6 MPa. Similar to Watt Mountain results, static values for Young's Modulus are approximately 30-40 GPa lower than the dynamic values. The static values for the Poisson's ratio are variable. The dynamic value of 0.28 are thought to be more representative for the actual Poisson's ratio.
- Unconfined compressive strengths in the Cold Lake formation ranged from 8.9 MPa to 18.0 MPa with corresponding axial strains ranging from 0.85% to 1.14%. These strains are lower than both other rock salt formations tested.
- Consistent results were obtained for BTS and UCS tests for samples from the Ernestina Lake Formation, with an average UCS of approximately 52 MPa. Significant variability was evident in STC tests, and no failure criterion could be generated that encompasses the complete formation. This variation is thought to be mainly due to differences in composition of the formation with depth, particularly with respect to increasing salt content near the interface with the Lotsberg Formation. One creep test on the Ernestina Lake Formation suggests it may mimic the behavior of the underlying salts, due to the elevated salt content.
- Strength tests completed on the Lotsberg Formation shows little variation, for both the UCS and BTS tests. Insoluble content, typically consisting of clay, are significantly elevated in the upper portions of the formation, with maximum measured values of 38 percent. This lends some concern to establishing lateral continuity of the formation, as it is typically described as very pure (>95%) halite. The presence or absence of clay inclusions will certainly affect the geomechanical properties. With available data, it is not possible to make any estimation about the behaviour of the Lotsberg Formation at any other location than the 8-13 well.
- The application and implementation of the properties in the laboratory experiments performed in this study should done with the utmost care and the realization that both the spatial and temporal scales in geological and engineering reality are very different from those in the laboratory.

- Dilatancy behavior of the Lotsberg Formation and the Prairie Evaporite Formation has been assessed by means of CMC and CME testing. The Lotsberg Formation specimens show general agreement with the dilatancy boundary laws of Spiers (1988) and Ratigan et al. (1991). The lower outcome of the CME test on Lotsberg Formation specimen can adequately be explained. The trend shown by Prairie Evaporite Formation specimens does not correlate to either Spiers (1988) or Ratigan et al. (1991) and is thought to be the results of inter-sample variability, since no known geomechanical mechanism would produce such results. It emphasizes that it is difficult to treat the formations in this project as clearly defined “boxes” with homogeneous properties.
- Reported creep results are based on multi-stage tests in which the axial load remained constant while the radial stress was decreased (unloaded), mimicing the stress conditions of salt cavern excavation as closely as possible. It was concluded by Jandakaew (2003), that radially unloading creep testing resulted in higher creep rates than conventional creep testing. Comparison to monitored creep around salt caverns led to the conclusion that radially unloading creep testing gave a more accurate representation of creep behaviour for this specific purpose.
- In general, geophysical measurements of density and dynamic velocities can be used to infer strength parameters for a formation, when considered in conjunction with laboratory testing. However, there is no appropriate correlation from geophysical measurements to deformation parameters, more specifically deformation behavior under creep conditions.

6.3 Modelling

Different cavern configurations and choices for cavern-filling materials were evaluated in FLAC^{3D}. Based on the different FLAC^{3D} models, the follow conclusions are presented:

- For realistic choices of cavern configuration and the material filling the cavern, surface subsidence over a 50 year period is expected to be less than 12.1 mm. Shear stresses in the rock volume influenced by cavern development are expected to stay well below 5 MPa and failure is not expected to occur anywhere in the system.

- These predictions are based on a number of assumptions and simplifications. It is thought that predictions about the stress state are more reliable than predictions about response to the stress state, namely strain or deformation.
- The models in FLAC^{3D} did not account for dilatancy, which has implications for long-term fluid isolation and possible tensile failure related to fluid infiltration.
- Improvements to the model could be made by allowing intra-formation variability, accounting for dilatancy and by assessing the sensitivity of the model to changes in strength parameters, creep parameters, model size, grid size and time step duration.

REFERENCES

- ASTM Standard D422-63, 2007. Standard Test Method for Particle-Size Analysis of Soils. ASTM International, West Conshohocken, PA, 2007
- ASTM Standard D2845, 2008. Standard Test Method for Laboratory Determination of Pulse Velocities and Ultrasonic Elastic Constants of Rock. ASTM International, West Conshohocken, PA, 2008
- ASTM Standard D2216, 2010. Standard Test Method for Laboratory Determination of Water (Moisture) Content of Soil and Rock by Mass. ASTM International, West Conshohocken, PA, 2010
- ASTM Standard D3967, 2008. Standard Test Method for Splitting Tensile Strength of Intact Rock Core Specimens. ASTM International, West Conshohocken, PA, 2008
- ASTM Standard D4543, 2008. Standard Practices for Preparing Rock Core as Cylindrical Test Specimens and Verifying Conformance to Dimensional and Shape Tolerances. ASTM International, West Conshohocken, PA, 2009
- ASTM Standard D5102, 2009. Standard Test Method for Unconfined Compressive Strength of Compacted Soil-Lime Mixtures. ASTM International, West Conshohocken, PA, 2009
- ASTM Standard D7012, 2010. Standard Test Method for Compressive Strength and Elastic Moduli of Intact Rock Core Specimens under Varying States of Stress and Temperatures. ASTM International, West Conshohocken, PA, 2010
- ASTM Standard E534, 2008. Standard Test Methods for Chemical Analysis of Sodium Chloride. ASTM International, West Conshohocken, PA, 2008
- Alkan, H., 2009. Percolation model for dilatancy-induced permeability of the excavation damaged zone in rock salt. *International Journal of Rock Mechanics and Mining Sciences* 46, 716–724.
- Alkan, H., Cinar, Y., Pusch, G., 2007. Rock salt dilatancy boundary from combined acoustic emission and triaxial compression tests. *International Journal of Rock Mechanics and Mining Sciences* 44, 108–119.
- Al-ruwaili, S.B., Saudi Aramco, Chardac, O., Schlumberger, 2003. 3D model for rock strength and in-situ stresses in the Khuff formation of Ghawar field, methodologies and applications, in: Middle East Oil Show, 9-12 June 2003, Bahrain. Society of Petroleum Engineers, p. 9.
- Andreev, G.E., 1991. A review of the Brazilian test for rock tensile strength determination. *Mining Science and Technology* 13, 445 – 465.
- Bachu, S., Stewart, S., 2002. Geological Sequestration of Anthropogenic Carbon Dioxide in the Western Canada Sedimentary Basin: Suitability Analysis. *Journal of Canadian Petroleum Technology* 41, 1–23.

- Bérest, P., Brouard, B., 2003. Safety of Salt Caverns Used for Underground Storage Blow Out; Mechanical Instability; Seepage; Cavern Abandonment. *Oil & Gas Science and Technology* 58, 361–384.
- British Petroleum, 2012. BP Statistical Review of World Energy June 2012.
- Chalaturnyk, R.J., Don Scott, J., Özüm, B., 2002. Management of Oil Sands Tailings. *Petroleum Science and Technology* 20, 1025–1046.
- Chan, K.S., Munsonz, D.E., Bodner, S.R., Fossum, A.F., 1996. Cleavage and Creep Fracture of Rock Salt. *Acta mater* 44, 3553–3565.
- Clark, I., Jackson, R., Liu, I., Heagle, D., 2010. Technical Report: Vacuum Distillation Experiments on DGR Core.
- CNRL Press Release, 2013. CNRL First Quarterly Results 2013.
- Crickmay, C.H., 1954. Paleontological correlation of Elk Point and equivalents, in: Ralph Leslie Rutherford Memorial Volume, Symposium, Western Canada Sedimentary Basin, AAPG. Tulsa, OK, pp. 143–158.
- Desai, C.S., Varadarajan, A., 1987. A constitutive model for quasi-static behavior of rock salt. *Journal of Geophysical Research* 92, 445–456.
- Dusseault, M.B., Bachu, S., Davidson, B.C., 2001. Carbon Dioxide Sequestration Potential in Salt Solution Caverns in Alberta, Canada. Solution Mining Research Institute, pp. 1–15.
- Fairhurst, C., 1964. On the validity of the “Brazilian” test for brittle materials. *International Journal of Rock Mechanics and Mining Sciences* 1, 535–546.
- Fokker, P.A., 1995. The behaviour of salt and salt caverns. PhD. Thesis, Delft University of Technology.
- Fuenkajorn, K., 1988. Borehole closure in salt.
- Geologic, 2013. GeoSCOUT.
- Gray, D., Anderson, P., Logel, J., Delbecq, F., Schmidt, D., Schmid, R., 2012. Estimation of stress and geomechanical properties using 3D seismic data. *First Break* 30, 59–68.
- Grayston, L.D., Sherwin, D.F., Allan, J.F., 1964. Middle Devonian, in: McCrossan, R.G., Glaister, R.P. (Eds.), *Geological*. Alberta Society of Petroleum Geologists, Calgary, pp. 48–62.
- Greenberg, M.L., Castagna, J.P., 1992. Shear-wave velocity estimation in porous rocks: Theoretical formulation, preliminary verification and applications. *Geophysical Prospecting* 40, 195–209.
- Grimmett, G., 1999. Percolation, 2nd ed. Springer-Verlag, Berlin.
- Grobe, M., 2000. Distribution and Thickness of Salt within the Devonian Elk Point Group, Western Canada Sedimentary Basin. Calgary.

- Hamilton, W., 1971. Salt in East-Central Alberta. Research Council of Alberta Bulletin 29, 1–68.
- Hunsche, U., Albrecht, H., 1990. Results of True Triaxial Strength Tests on Rock Salt. Engineering Fracture Mechanics 35, 867–877.
- Hunsche, U., Hampel, A., 1999. Rock salt — the mechanical properties of the host rock material for a radioactive waste repository 52, 271–291.
- Ikon Science, 2013. RokDoc.
- Itasca Consulting Group Inc., 2013. FLAC3D.
- Jandakaew, M., 2003. Experimental Assessment of stress path effects on rock salt deformation. http://sutir.sut.ac.th:8080/sutir/bitstream/123456789/1142/2/mongkhol_fulltext.pdf.
- Kings, M.S., 1969. Static and Dynamic Elastic Moduli Of Rocks Under Pressure. The 11th U.S. Symposium on Rock Mechanics (USRMS) June 16-19 1969 Berkely, CA. 1–24.
- Lambe, T.W., Whitman, R.V., 1991. Soil Mechanics.
- Liang, W., Yang, C., Zhao, Y., Dusseault, M.B., Liu, J., 2007. Experimental investigation of mechanical properties of bedded salt rock. International Journal of Rock Mechanics and Mining Sciences 44, 400–411.
- Mashinsky, E.I., 2003. Differences Between Static and Dynamic Elastic Moduli of Rocks: Physical Causes. Russian Geology and Geophysics 44, 953–959.
- McGehee, J.R., 1949. Pre-Waterways Paleozoic Stratigraphy of Alberta Plains. AAPG Bulletin 33, 603–609.
- Meijer Drees, N.C., 1994. Devonian Elk Point Group of Western Canada Sedimentary Basin., in: Geological Atlas of the Western Canada Sedimentary Basin. Canadian Society of Petroleum Geologists and Alberta Research Council, Calgary, pp. 129–147.
- Mellegard, K.D., Pfeifle, T.W., 1998. Laboratory Evaluation of Mechanical Properties of Rock Using an Automated Triaxial Compression Test With a Constant Mean Stress Criterion. American Society for Testing and Materials.
- Mellor, M., Hawkes, I., 1971. Measurement of Tensile Strength by Diametral Compression of Discs and Annuli. Engineering Geology 5, 173–225.
- Pattinson, R.L., 1944. Patent Application.
- Pattinson, R.L., 1957. Method of storing gases or liquids.
- Peach, C.J., Spiers, C.J., 1996. Influence of crystal plastic deformation on dilatancy and permeability development in synthetic salt rock. Tectonophysics 256, 101–128.

- Perez, M.A., Clyde, R., Ambrosio, P.D., Leavitt, T., Nutt, L., Johnson, C., Williamson, D., 2008. Meeting the Subsalt Challenge. *Oilfield Review* 20, 32–45.
- Popp, T., Kern, H., 2000. Monitoring the state of microfracturing in rock salt during deformation by combined measurements of permeability and P- and S- wave velocities. *Physics and Chemistry of the Earth, Part A: Solid Earth and Geodesy* 25, 149–154.
- Porter, J.W., Price, R.A., McCrossan, R.G., 1982. The Western Canada Sedimentary Basin. *Philosophical Transactions of the Royal Society of London, Series A, Mathematical and Physical Sciences* 305, 169–192.
- Rankine, W.J.R., 1857. On the stability of loose earth. *Philosophical Transactions of the Royal Society of London* 147, 9–27.
- Ratigan, J.L., Van Sambeek, L.L., DeVries, K.L., Nieland, J.D., 1991. The influence of seal design on the development of disturbed rock zone in the WIPP alcove seal tests. Rep. RSI-0400, RE/SPEC Inc., Rapid City, SD.
- Schmalz, R.F., 1969. Deep-Water Evaporite Deposition: A Genetic Model. *AAPG Bulletin* 53, 798–823.
- Schulze, O., Popp, T., Kern, H., 2001. Development of damage and permeability in deforming rock salt. *Engineering Geology* 61, 163–180.
- Schutjens, P.M.T.M., Spiers, C.J., 1999. Intergranular Pressure Solution in NaCl: Grain-To-Grain Contact Experiments under the Optical Microscope. *Oil & Gas Science and Technology* 54, 729–750.
- Sengupta, M., Dai, J., Volterrani, S., Dutta, N., Rao, N.S., Al-Qadeeri, B., Kidambi, V.K., 2011. Building a seismic-driven 3D geomechanical model in a deep carbonate reservoir, in: *SEG Technical Program Expanded Abstracts 2011*. Society of Exploration Geophysicists, pp. 2069–2073.
- Spiers, C.J., Peach, C.J., Brzesowsky, R.H., Schutjens, P.M.T.M., Liezenberg, J.L., Zwart, H.J., 1988. Long-term rheological and transport properties of dry and wet salt rocks, 2nd Conference of the Mechanical behaviour of Salt.
- Spiers, C.J., Schutjens, P.M.T.M., Brzesowsky, R.H., Peach, C.J., Liezenberg, J.L., Zwart, H.J., 1990. Experimental determination of constitutive parameters governing creep of rocksalt by pressure solution. *Geological Society, London, Special Publications* 54, 215–227.
- Stormont, J.C., Fuenkajorn, K., 1993. Dilation-induced permeability changes in rock salt. U.S. Department of Commerce, pp. 1–10.
- Thoms, R.L., Gehle, R.M., 2000. A brief history of salt cavern use, in: *8th World Salt Symposium*. The Hague.
- U.S. Energy Information Administration, 2012. Canada. <http://www.eia.gov/countries/cab.cfm?fips=CA>.

- Urai, J.L., Schléder, Z., Spiers, C.J., Kukla, P.A., 2008. Flow and Transport Properties of Salt Rocks, in: Dynamics of Complex Intracontinental Basins: The Central European Basin System. pp. 277–290.
- Van Keken, P.E., Spiers, C.J., Van den Berg, A.P., Muyzert, E.J., 1993. The effective viscosity of rocksalt: implementation of steady-state creep laws in numerical models of salt diapirism. *Tectonophysics* 225, 457–476.
- Wardlaw, N.C., Schwerdtner, W.M., 1966. Halite-Anhydrite Seasonal Layers in the Middle Devonian Prairie Evaporite Formation, Saskatchewan, Canada. *Geological Society of America Bulletin* 77, 331–342.
- Wawersik, W.R., Hannum, D.W., 1980. Mechanical Behavior of New Mexico Rock Salt in Triaxial Compression Up to 200C. *Journal of Geophysical Research* 85, 891–900.
- Wawersik, W.R., Zeuch, D.H., 1986. Modeling and Mechanistic Interpretation of Creep of Rock Salt Below 200C. *Tectonophysics* 121, 125–152.
- Yang, C., Daemen, J.J.K., Yin, J.-H., 1999. Experimental investigation of creep behavior of salt rock. *International Journal of Rock Mechanics and Mining Sciences* 36, 233–242.

ACKNOWLEDGEMENTS

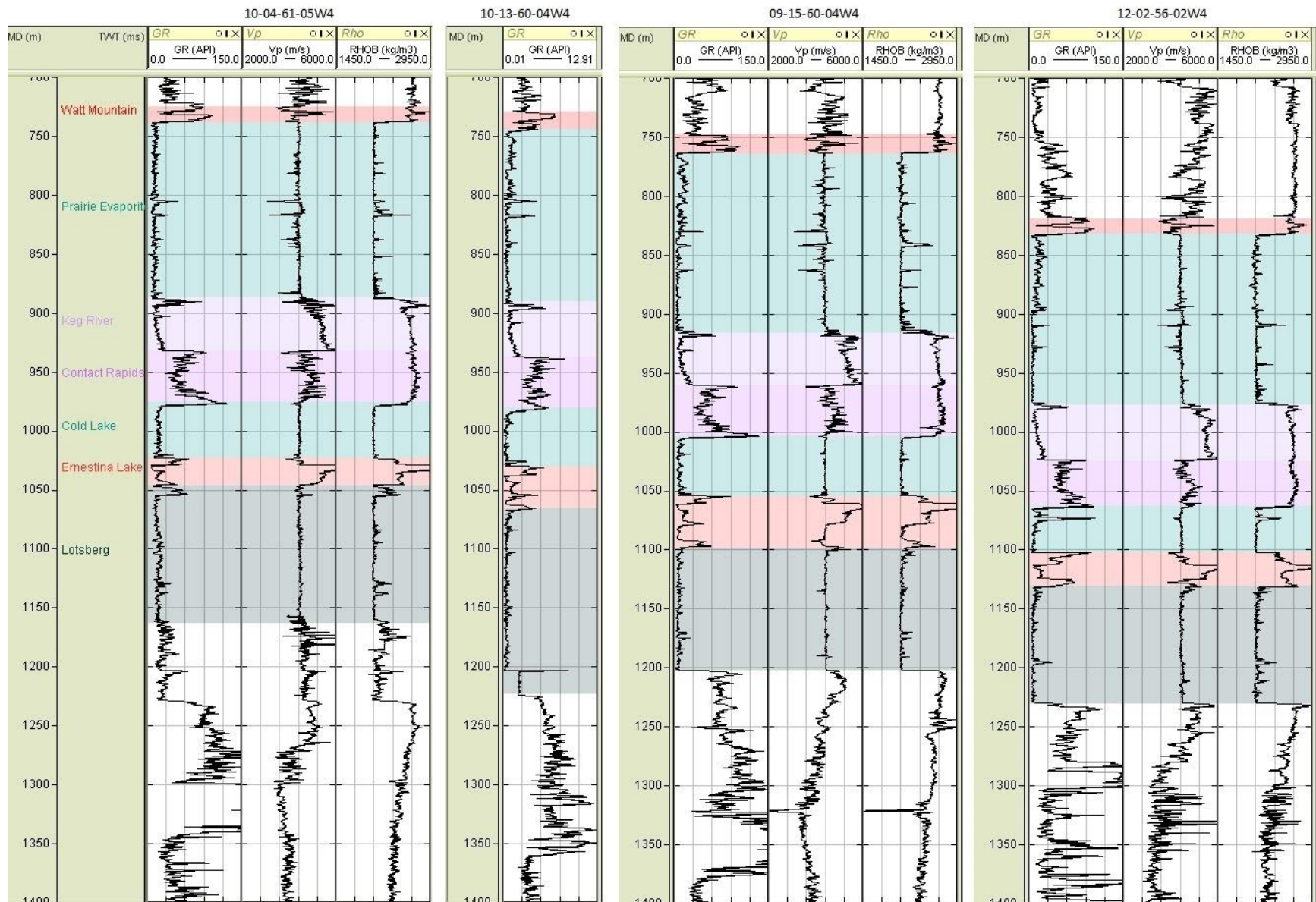
First and foremost, I would like to thank Tanya Schulz, who spent a year in the lab with me, setting up test after test and who reviewed this manuscript. I would also like to thank Steve Gamble, who provided technical assistance and advice every step along the way. Li (Meryl) Meng is thanked for contributing to the numerical modelling results. Both my supervisors, Professor Rick Chalaturnyk and Professor Chris Spiers are sincerely thanked for offering me the opportunity to work at the University of Alberta once again. It has been a wonderful experience, both professionally and personally.

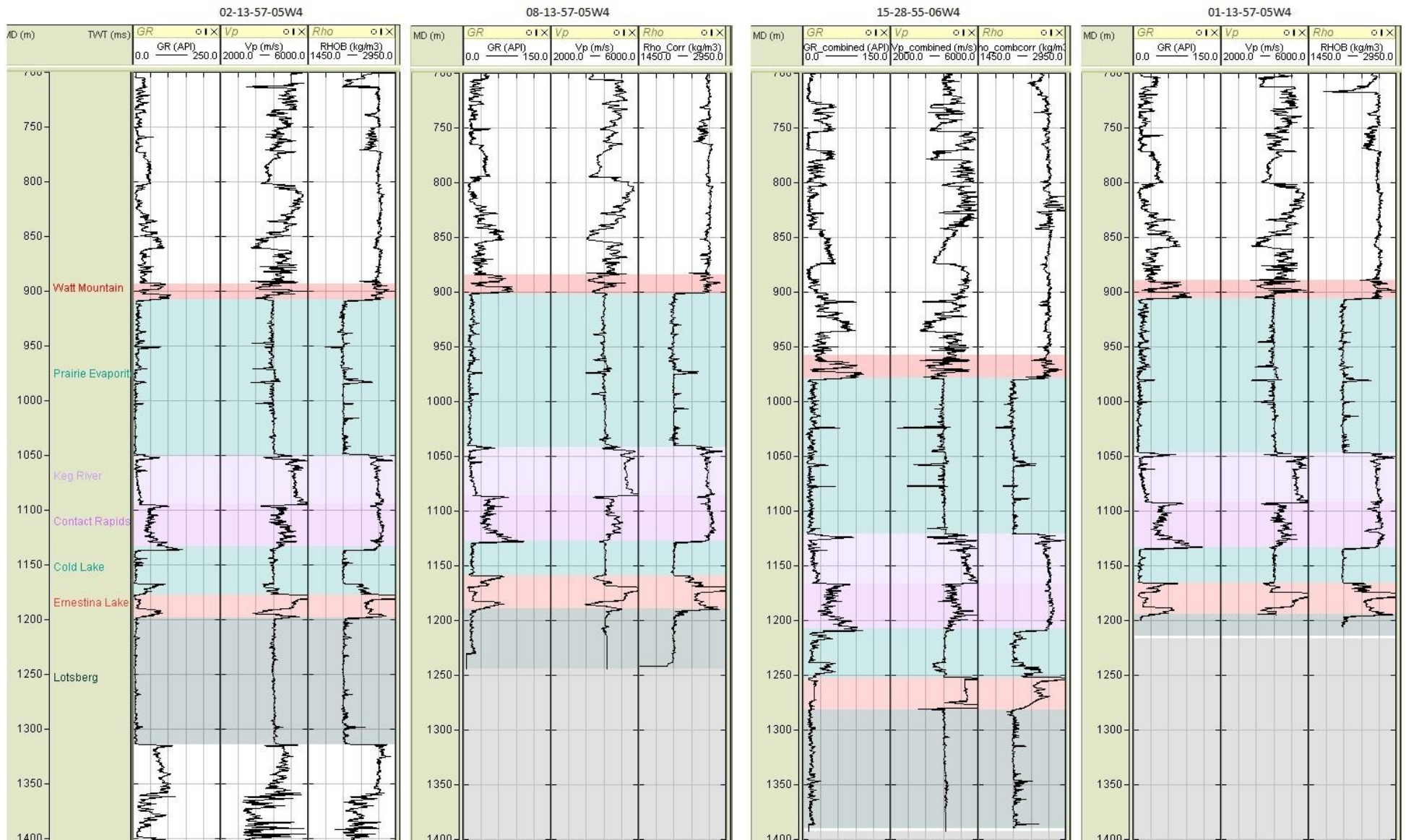
Appendix A

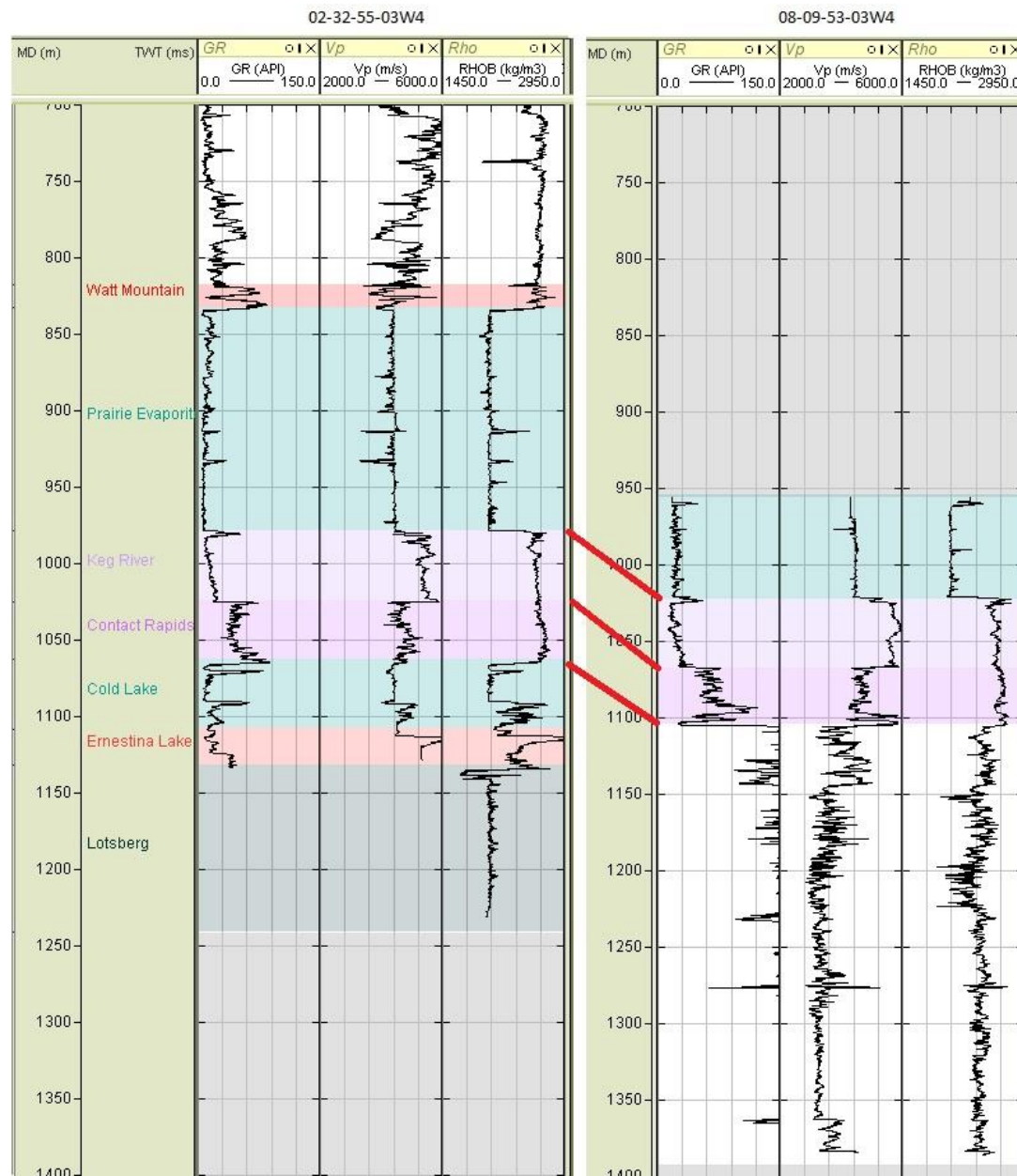
Well logs for geological setting

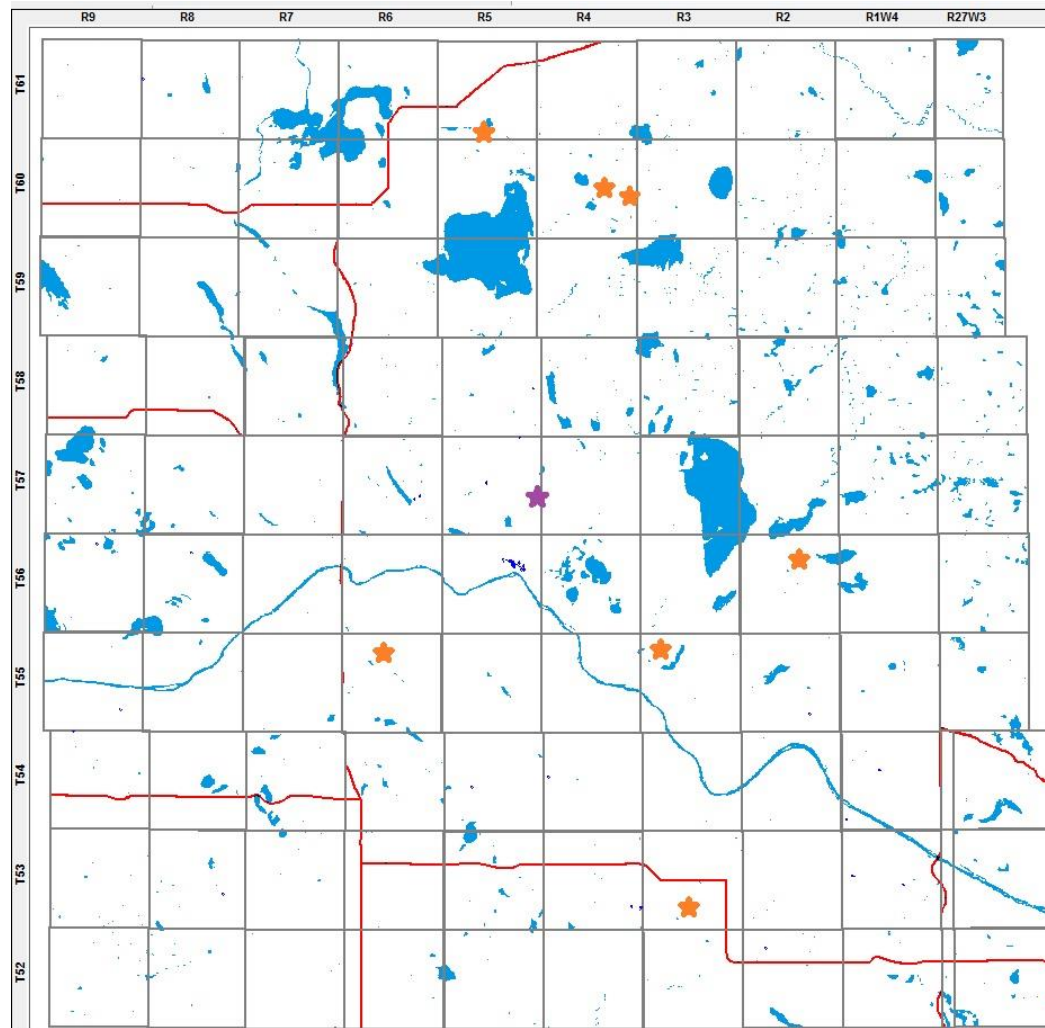
Contains:

- Geophysical wireline logs for 10 wells
- A map showing the location of the wells









Location of the 10 wells used in the characterization of the local geological and depositional setting. Each orange star represents one well, the purple star represents three closely spaced wells (among which, the CNRL 8B WD LIND 08-13-57-5W4 well). The side of each grey square is 6 miles or ~9.65 km. Townships and ranges are presented at the top and left. The centre of this image approximately corresponds to 53.8877 N, 110.6025 W. (Map produced in geoSCOUT)

Appendix B

Core Log Summary

Contains:

- A summary of the core that was available for testing

CNRL 8B WD LIND 08-13-57-5W4								
U of A Core No.	Tube#	Cut# [m]	REC# [m]	Top# [m]	Btm# [m]	Storage Rack Position	Formation	RQD
Core 1								
1	1/6	9.0	9.0	885.5	887.0	I-J	Watt Mountain	18%
2	2/6	9.0	9.0	887.0	888.5	M-N	Watt Mountain	70%
3	3/6	9.0	9.0	888.5	890.0	K-L	Watt Mountain	74%
4	4/6	9.0	9.0	890.0	891.5	M-N	Watt Mountain	49%
5	5/6	9.0	9.0	891.5	893.0	C-D	Watt Mountain	54%
6	6/6	9.0	9.0	893.0	894.5	B-C	Watt Mountain	63%
Core 2								
7	2/7	9.0	9.1	894.5	896.0	I-J	Watt Mountain	49%
9	3/7	9.0	9.1	896.0	897.5	F-G	Watt Mountain	48%
10	4/7	9.0	9.1	897.5	899.0	A-B	Watt Mountain	32%

CNRL 8B WD LIND 08-13-57-5W4								
U of A Core No.	Tube#	Cut# [m]	REC# [m]	Top# [m]	Btm# [m]	Storage Rack Position	Formation	RQD
11	5/7	9.0	9.1	899.0	900.5	F-G	Watt Mountain/Prairie Evaporite	31%
12	6/7	9.0	9.1	900.5	902.0	A-B	Prairie Evaporite	75%
13	7/7	9.0	9.1	902.0	903.5	H-I	Prairie Evaporite	90%
Core 3								
14	1/6	9.0	9.0	960.0	961.5	B - C	Prairie Evaporite	
15	2/6	9.0	9.0	961.5	963.0	G-H	Prairie Evaporite	100%
16	3/6	9.0	9.0	963.0	964.5	B-C	Prairie Evaporite	38%
17	4/6	9.0	9.0	964.5	966.0	B-C	Prairie Evaporite	0%
18	5/6	9.0	9.0	966.0	967.5	M-N	Prairie Evaporite	16%
19	6/6	9.0	9.0	967.5	969.0	G-H	Prairie Evaporite	42%

CNRL 8B WD LIND 08-13-57-5W4								
U of A Core No.	Tube#	Cut# [m]	REC# [m]	Top# [m]	Btm# [m]	Storage Rack Position	Formation	RQD
Core 4								
20	1/6	9.0	9.0	969.0	970.5	A-B	Prairie Evaporite	59%
21	2/6	9.0	9.0	970.5	972.0	B-C	Interbed	64%
22	3/6	9.0	9.0	972.0	973.5	L-M	Interbed	21%
23	4/6	9.0	9.0	973.5	975.0	C-D	Interbed/Prairie Evaporite	69%
24	5/6	9.0	9.0	975.0	976.5	L-M	Prairie Evaporite	100%
25	6/6	9.0	9.0	976.5	978.0	O-P	Prairie Evaporite	n/a
Core 5								
27	1/6	9.0	9.0	1030.0	1031.5	D-E	Prairie Evaporite	100%
28	2/6	9.0	9.0	1031.5	1033.0	K-L	Prairie Evaporite	100%
29	3/6	9.0	9.0	1033.0	1034.5	A-B	Prairie Evaporite	90%

CNRL 8B WD LIND 08-13-57-5W4								
U of A Core No.	Tube#	Cut# [m]	REC# [m]	Top# [m]	Btm# [m]	Storage Rack Position	Formation	RQD
30	4/6	9.0	9.0	1034.5	1036.0	A-B	Prairie Evaporite	100%
31	5/6	9.0	9.0	1036.0	1037.5	D-E	Prairie Evaporite	100%
32	6/6	9.0	9.0	1037.5	1039.0	K-L	Prairie Evaporite	95%
Core 6								
33	1/6	9.0	8.8	1039.0	1040.5	G-H	Keg River	84%
34	2/6	9.0	8.8	1040.5	1042.0	F-G	Keg River	32%
35	3/6	9.0	8.8	1042.0	1043.5	C-D	Keg River	67%
36	4/6	9.0	8.8	1043.5	1045.0	B-C	Keg River	85%
37	5/6	9.0	8.8	1045.0	1046.5	H-I	Keg River	60%
38	6/6	9.0	8.8	1046.5	1048.0	H-I	Keg River	45%
Core 7								

CNRL 8B WD LIND 08-13-57-5W4								
U of A Core No.	Tube#	Cut# [m]	REC# [m]	Top# [m]	Btm# [m]	Storage Rack Position	Formation	RQD
39	1/6	9.0	9.0	1120.0	1121.5	K-L	Contact Rapids	
40	2/6	9.0	8.8	1121.5	1123.0	F-G	Contact Rapids	56%
41	3/6	9.0	8.8	1123.0	1124.5	G-H	Contact Rapids	68%
42	4/6	9.0	8.8	1124.5	1126.0	A-B	Contact Rapids	
43	5/6	9.0	8.8	1126.0	1127.5	C-D	Contact Rapids	65%
44	6/6	9.0	8.8	1127.5	1129.0	H-I	Contact Rapids	64%
Core 8								
45	2/7	9.0	9.3	1129.0	1130.5	I-J	Cold Lake	84%
47	3/7	9.0	9.3	1130.5	1132.0	C-D	Cold Lake	98%
48	4/7	9.0	9.3	1132.0	1133.5	C-D	Cold Lake	
49	5/7	9.0	9.3	1133.5	1135.0	F-G	Cold Lake	

CNRL 8B WD LIND 08-13-57-5W4								
U of A Core No.	Tube#	Cut# [m]	REC# [m]	Top# [m]	Btm# [m]	Storage Rack Position	Formation	RQD
50	6/7	9.0	9.3	1135.0	1136.5	G-H	Cold Lake	
51	7/7	9.0	9.3	1136.5	1138.0	D-E	Cold Lake	100%
Core 9								
52	1/6	9.0	9.0	1156.0	1157.5	D-E	Cold Lake	90%
53	2/6	9.0	9.0	1157.5	1159.0	F-G	Cold Lake	94%
54	3/6	9.0	9.0	1159.0	1160.5	D-E	Cold Lake	
55	4/6	9.0	9.0	1160.5	1162.0	H-I	Cold Lake	100%
56	5/6	9.0	9.0	1162.0	1163.5	H-I	Cold Lake	90%
57	6/6	9.0	9.0	1163.5	1165.0	I-J	Cold Lake	89%

CNRL 8B WD LIND 08-13-57-5W4								
U of A Core No.	Tube#	Cut# [m]	REC# [m]	Top# [m]	Btm# [m]	Storage Rack Position	Formation	RQD
Core 10								
58	1/6	9.0	9.0	1165.0	1166.5	F-G	Cold Lake	
59	2/6	9.0	9.0	1166.5	1168.0	D-E	Cold Lake/Ernestina Lake	92%
60	3/6	9.0	9.0	1168.0	1169.5	D-E	Ernestina Lake	83%
61	4/6	9.0	9.0	1169.5	1171.0	F-G	Ernestina Lake	90%
62	5/6	9.0	9.0	1171.0	1172.5	I-J	Ernestina Lake	100%
63	6/6	9.0	9.0	1172.5	1174.0	B-C	Ernestina Lake	94%
Core 11								
64	1/7	9.0	9.0	1174.0	1174.5	K-L	Ernestina Lake	
65	2/7	9.5	9.4	1174.5	1176.0	I-J	Ernestina Lake	100%

CNRL 8B WD LIND 08-13-57-5W4								
U of A Core No.	Tube#	Cut# [m]	REC# [m]	Top# [m]	Btm# [m]	Storage Rack Position	Formation	RQD
66	3/7	9.5	9.4	1176.0	1177.5	B-C	Ernestina Lake	
67	4/7	9.5	9.4	1177.5	1179.0	I-J	Ernestina Lake	92%
68	5/7	9.5	9.4	1179.0	1180.5	D-E	Ernestina Lake	
69	6/7	9.5	9.4	1180.5	1182.0	G-H	Ernestina Lake	80%
70	7/7	9.5	9.4	1182.0	1183.5	I-J	Ernestina Lake	91%
Core 12								
71	1/6	9.0	9.0	1183.5	1185.0	C-D	Ernestina Lake	87%
72	2/6	9.0	9.0	1185.0	1186.5	C-D	Ernestina Lake	
73	3/6	9.0	9.0	1186.5	1188.0	A-B	Ernestina Lake	73%
74	4/6	9.0	9.0	1188.0	1189.5	G-H	Ernestina Lake	
75	5/6	9.0	9.0	1189.5	1191.0	G-H	Contact w Upper Lotsberg	69%

CNRL 8B WD LIND 08-13-57-5W4								
U of A Core No.	Tube#	Cut# [m]	REC# [m]	Top# [m]	Btm# [m]	Storage Rack Position	Formation	RQD
76	6/6	9.0	9.0	1191.0	1192.5	H-I	Upper Lotsberg	68%
Core 13								
77	1/6	9.0	9.0	1192.5	1194.0	L-M	Upper Lotsberg	100%
78	2/6	9.0	9.0	1194.0	1195.5	H-I	Upper Lotsberg	92%
79	3/6	9.0	9.0	1195.5	1197.0	N-O	Upper Lotsberg	92%
80	4/6	9.0	9.0	1197.0	1198.5	N-O	Upper Lotsberg	63%
81	5/6	9.0	9.0	1198.5	1200.0	O-P	Upper Lotsberg	100%
82	6/6	9.0	9.0	1200.0	1201.5	L-M	Upper Lotsberg	95%
Core 14								
83	1/6	9.0	9.0	1201.5	1203.0	N-O	Upper Lotsberg	100%

CNRL 8B WD LIND 08-13-57-5W4								
U of A Core No.	Tube#	Cut# [m]	REC# [m]	Top# [m]	Btm# [m]	Storage Rack Position	Formation	RQD
84	2/6	9.0	9.0	1203.0	1204.5	N-O	Upper Lotsberg	83%
85	3/6	9.0	9.0	1204.5	1206.0	M-N	Upper Lotsberg	72%
86	4/6	9.0	9.0	1206.0	1207.5	K-L	Upper Lotsberg	100%
87	5/6	9.0	9.0	1207.5	1209.0	O-P	Upper Lotsberg	88%
88	6/6	9.0	9.0	1209.0	1210.5	A-B	Upper Lotsberg	97%

Appendix C

Methodology

Contains:

- A description of the methodology for X-ray diffraction as performed by AGAT Laboratories, Calgary

BULK & CLAY PROCEDURES

1. Crush dry rock sample until grains disintegrate completely.
2. Weigh empty beaker and put sample in it. Weigh again “total weight”. ($\approx 3\text{g}$ of sample).
3. Add 50 mL of distilled water, plus a few drops of Sodium Metaphosphate.
4. Put in ultrasonic bath for 2 (two) hours.
5. Stir sample and pour out top portion into test tube.
6. Centrifuge for 5 minutes at 600 rpm.
7. Pour out top portion into another test tube for the clay fraction ($<3\mu\text{m}$) sample.
8. Recombine the coarser residue in the first test tube with the residue in the beaker and weigh this “bulk sample” (after drying completely). Subtract this weight from the “total weight” to get the clay fraction weight.
9. Centrifuge the “clay fines” in the second test tube for 20 minutes at maximum rpms.
10. Pour out most of the water then shake test tube using Vortex Mixer.
11. Pipette onto a glass slide.
12. Put the slide on the hot plate (low) until dry then run sample in XRD.
13. Then put slide in a glycol vapour bath overnight (glycolated clay); Smectite will swell and be recognized.
14. If chlorite suspected, then treat the remaining sample in the test tube with diluted HCl and leave overnight (acidized clay). If chlorite was present in the sample this test causes it to disappear.
15. Run the “clay fraction” slide from 2-38 degrees.
 16. Grind the “bulk sample” and spread the powder on an aluminum holder then run from 4-58 degrees.



Appendix D

Laboratory Test Results

Contains:

- Stress-strain curves and other graphs for performed testing
- Photographs of failed samples

1.1 Watt Mountain Formation

1.1.1 Unconfined Compression Tests

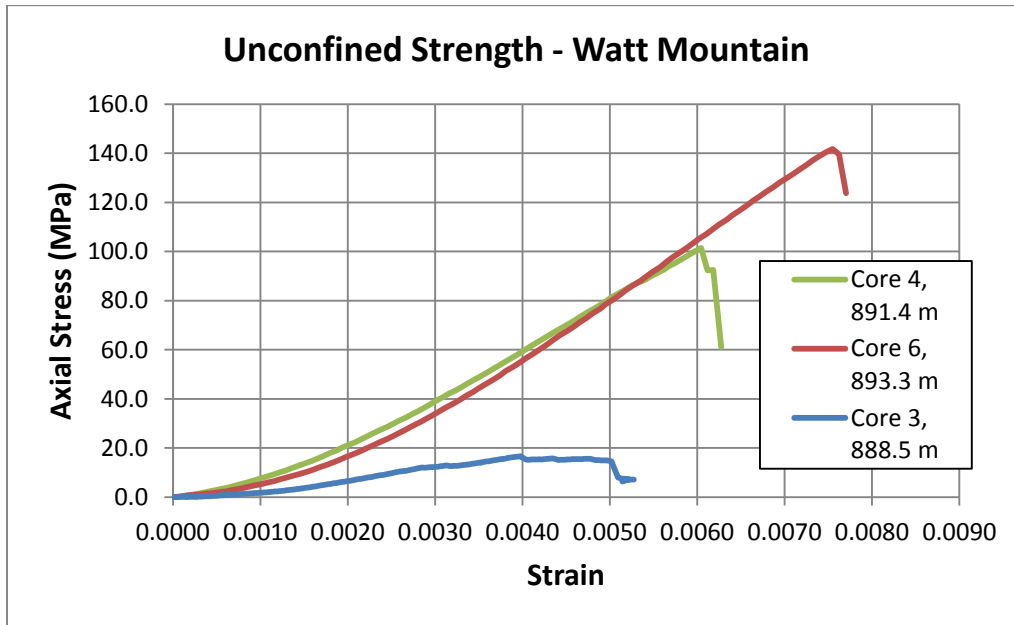


Figure 1. Unconfined Compression Test Stress-Strain Curves – Watt Mountain



Photograph 1. Failure in Unconfined Compression – Watt Mountain

1.1.2 Standard Triaxial Compression Tests

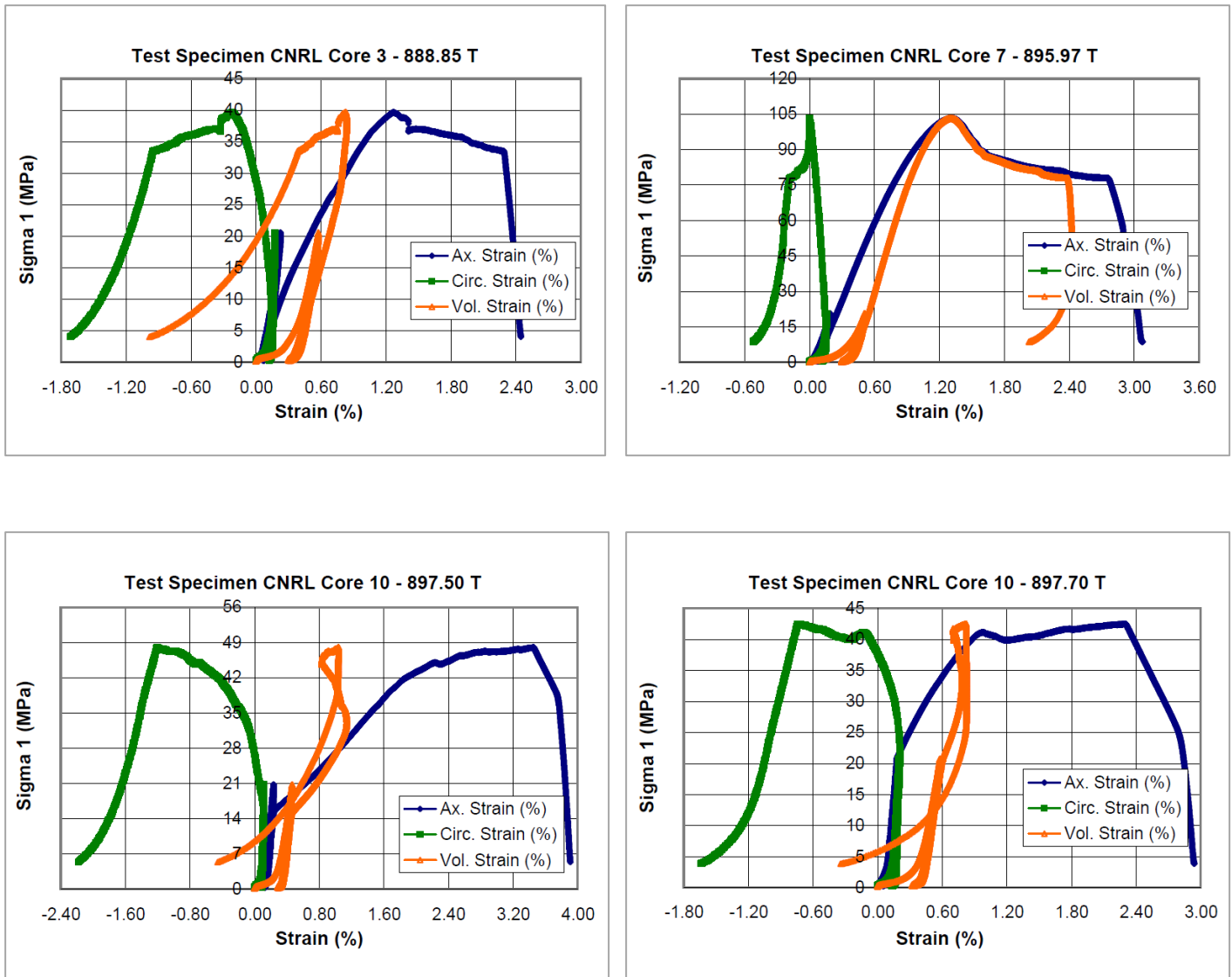
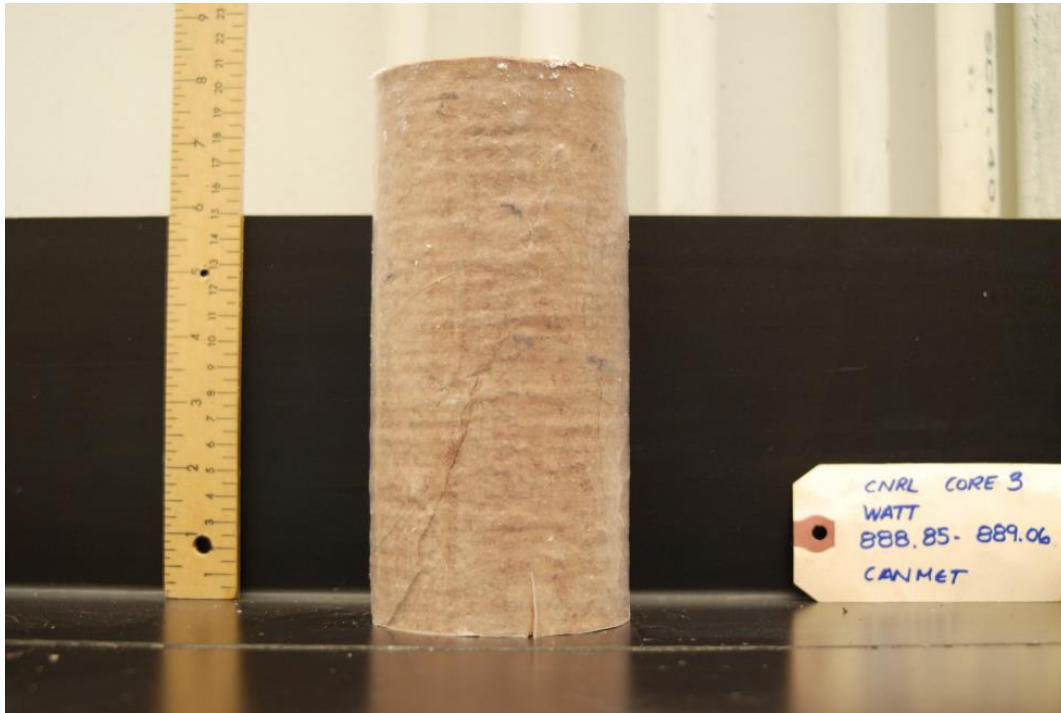


Figure 2. Standard Triaxial Tests Stress Strain Curves – Watt Mountain



Photograph 2. Failure in Standard Triaxial Compression Test – Watt Mountain

1.1.3 Index testing

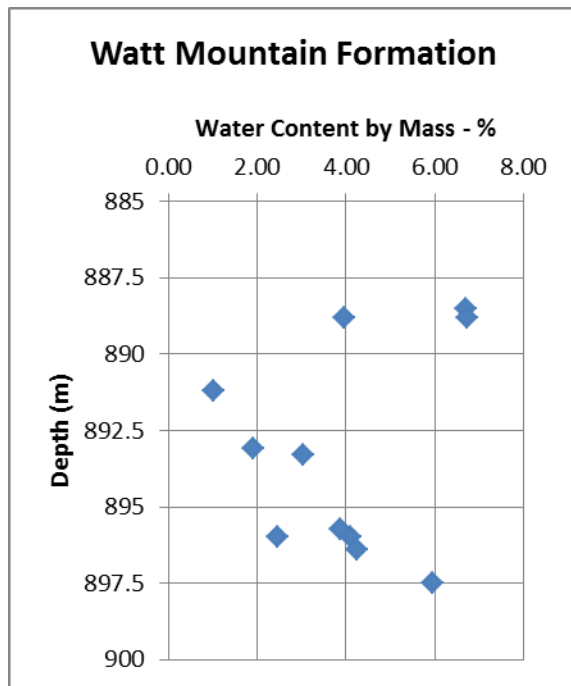


Figure 3. Water Content versus Depth – Watt Mountain

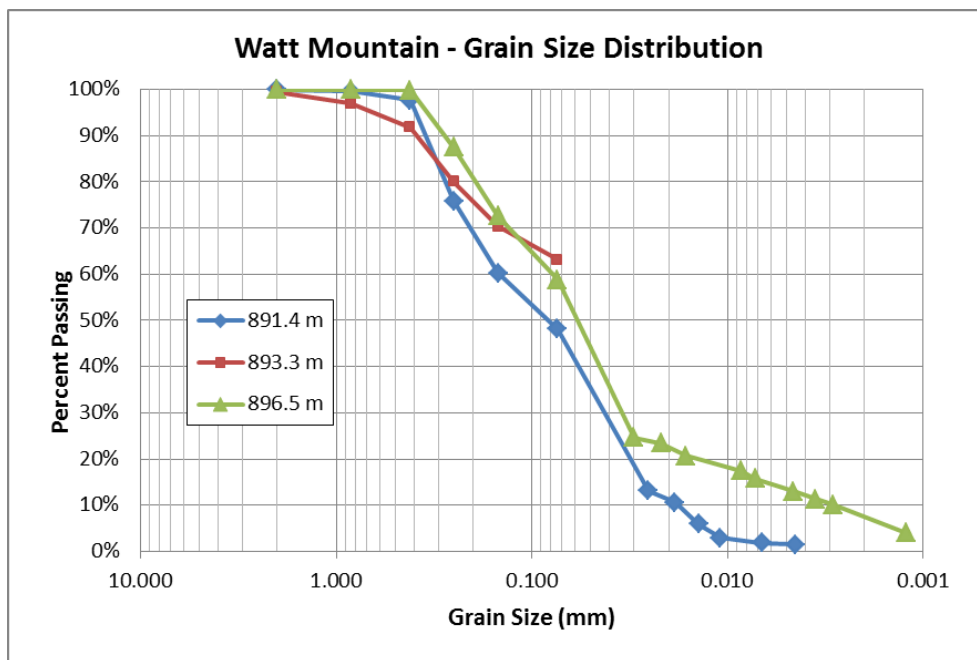


Figure 4. Grain Size Distribution – Watt Mountain

1.2 Prairie Evaporite Formation

1.2.1 Unconfined Compression Tests

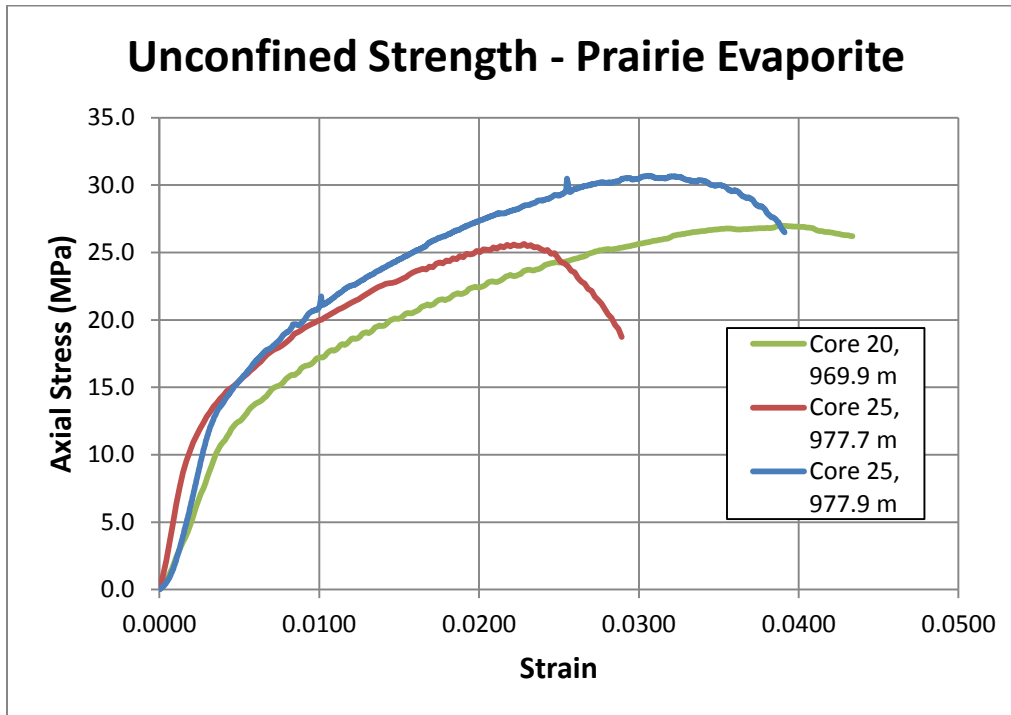


Figure 5. Unconfined Compression Tests –Stress-Strain Curves Prairie Evaporite



Photograph 3. Failure in Unconfined Compression – Prairie Evaporite

1.2.2 Constant Mean Compression Tests

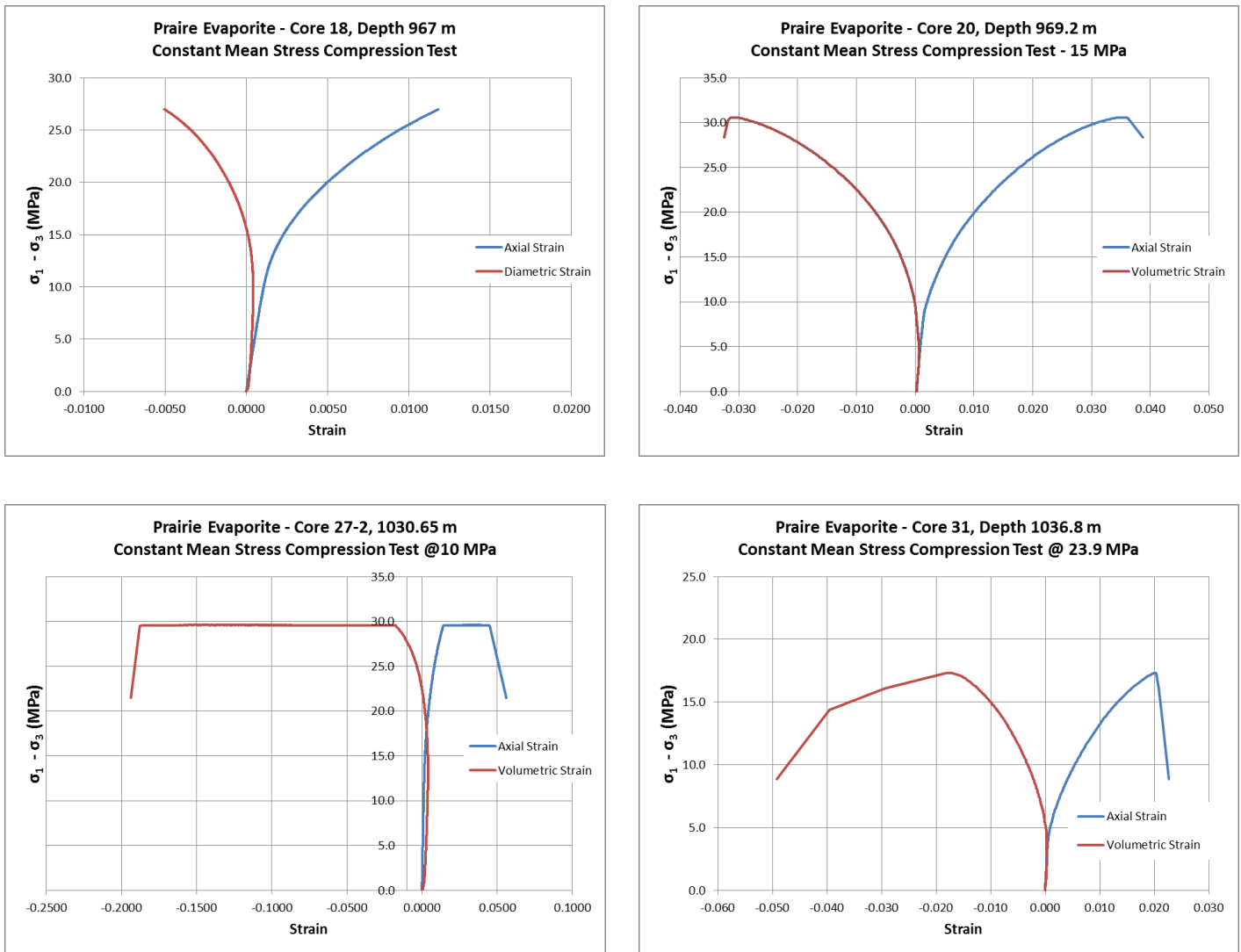


Figure 6. Constant Mean Compression Test – Stress Strain Curves – Prairie Evaporite



Photograph4. Failure in Constant Mean Compression Test – Prairie Evaporite

1.2.3 Creep

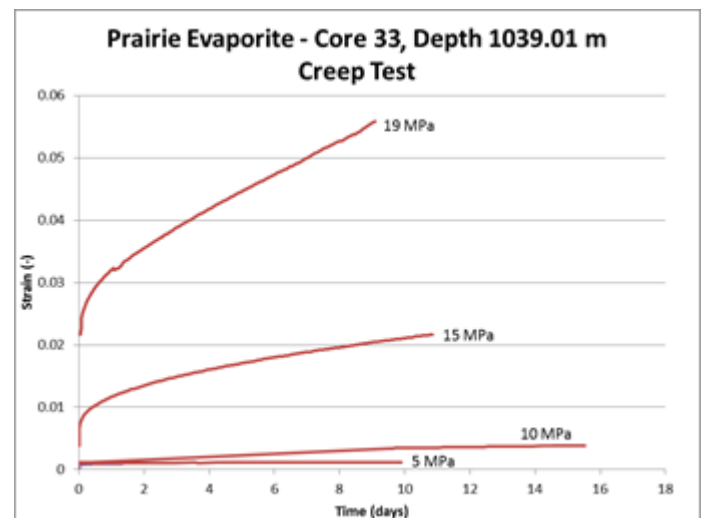
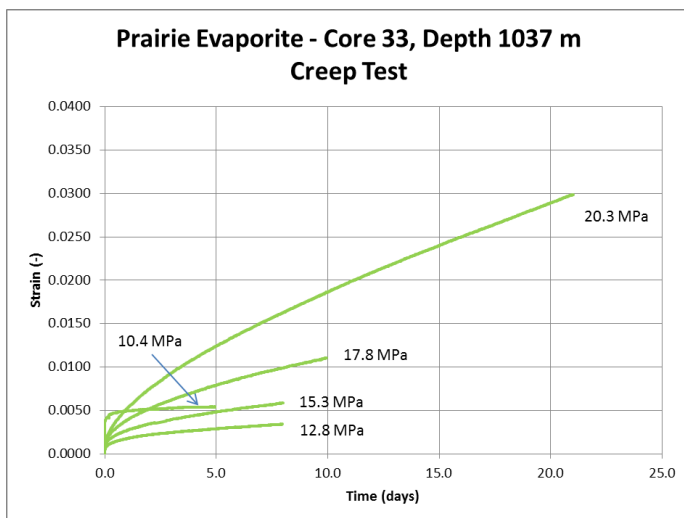
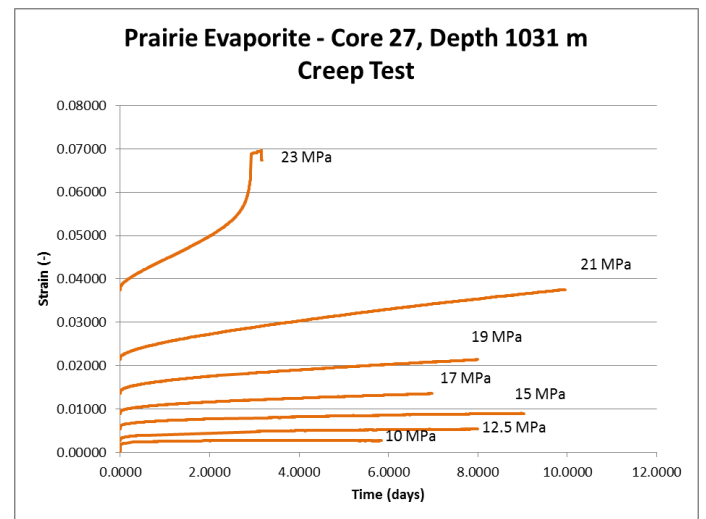
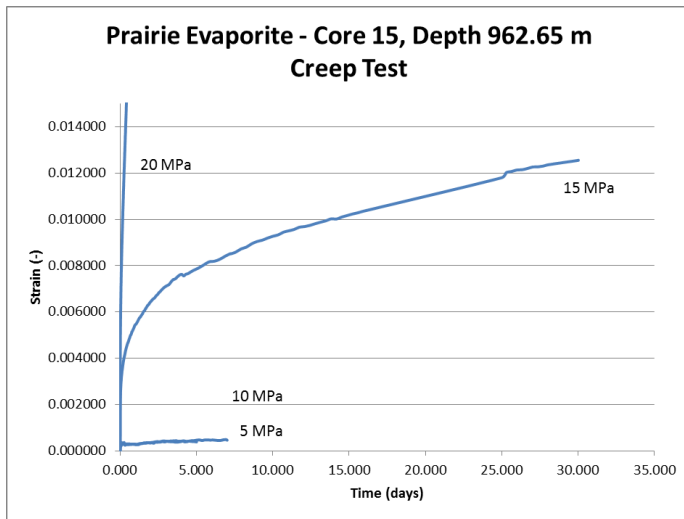
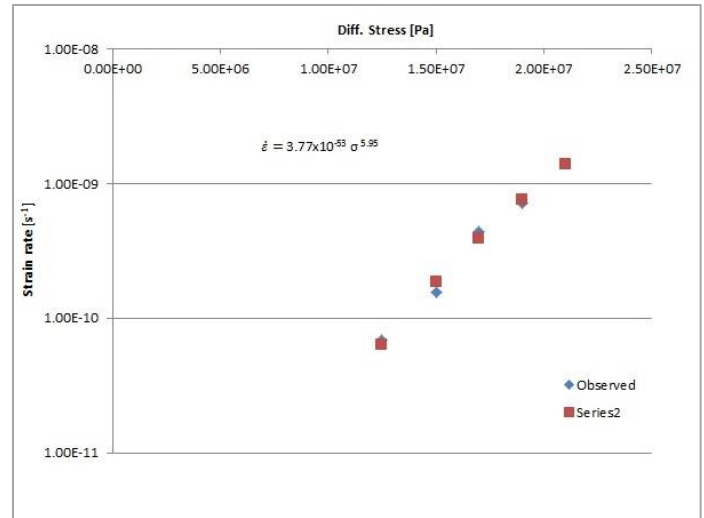
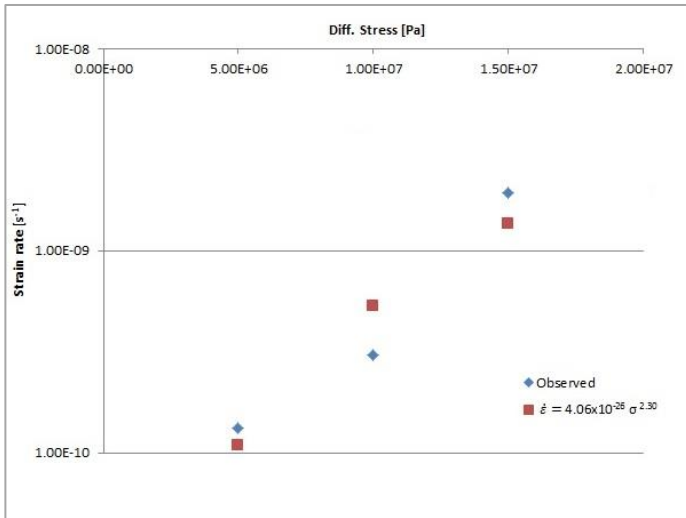


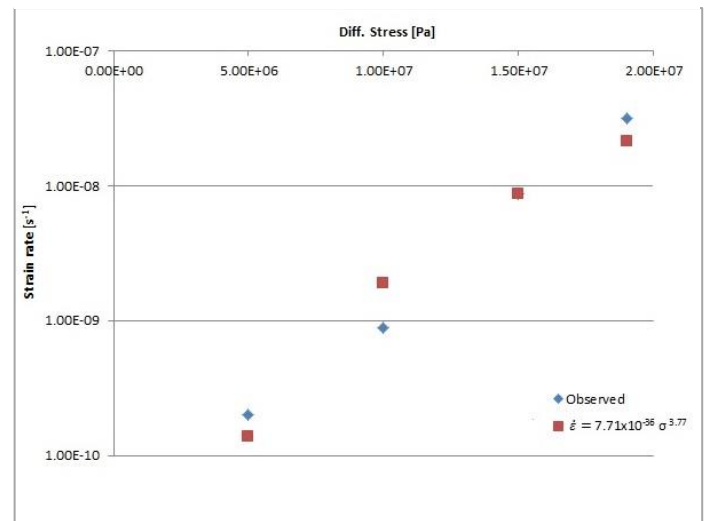
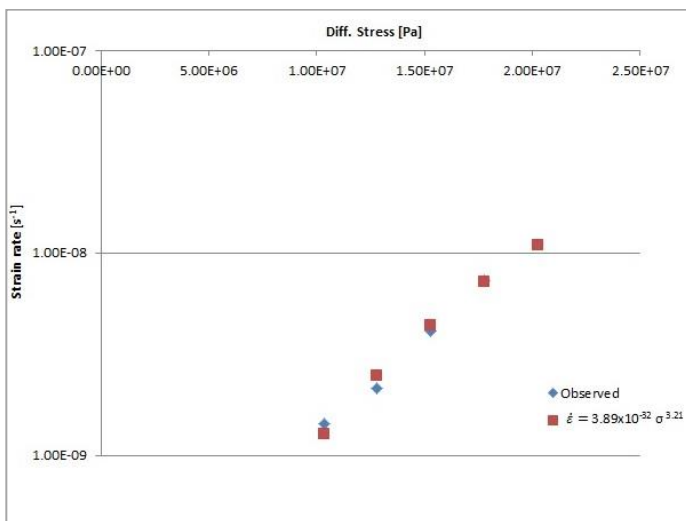
Figure 7. Creep Testing Prairie Evaporite Formation

1.2.4 Creep – flow law fitting



Prairie Evaporite Core 15 962.65 m – Flow law fitting

Prairie Evaporite Core 127 1031 m – Flow law fitting



Prairie Evaporite Core 33 1037 m – Flow law fitting

Prairie Evaporite Core 33 1039.01 m – Flow law fitting

Figure 8. Flow law fitting – Prairie Evaporite Creep Test Samples

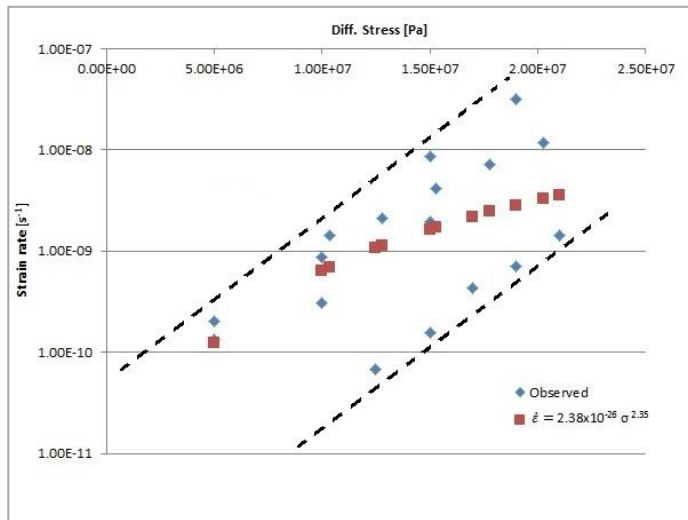


Figure 9. Flow law fitting – Prairie Evaporite Formation



Photograph 5. Failure in Creep – Prairie Evaporite

1.3 Keg River Formation

1.3.1 Unconfined Compression Test

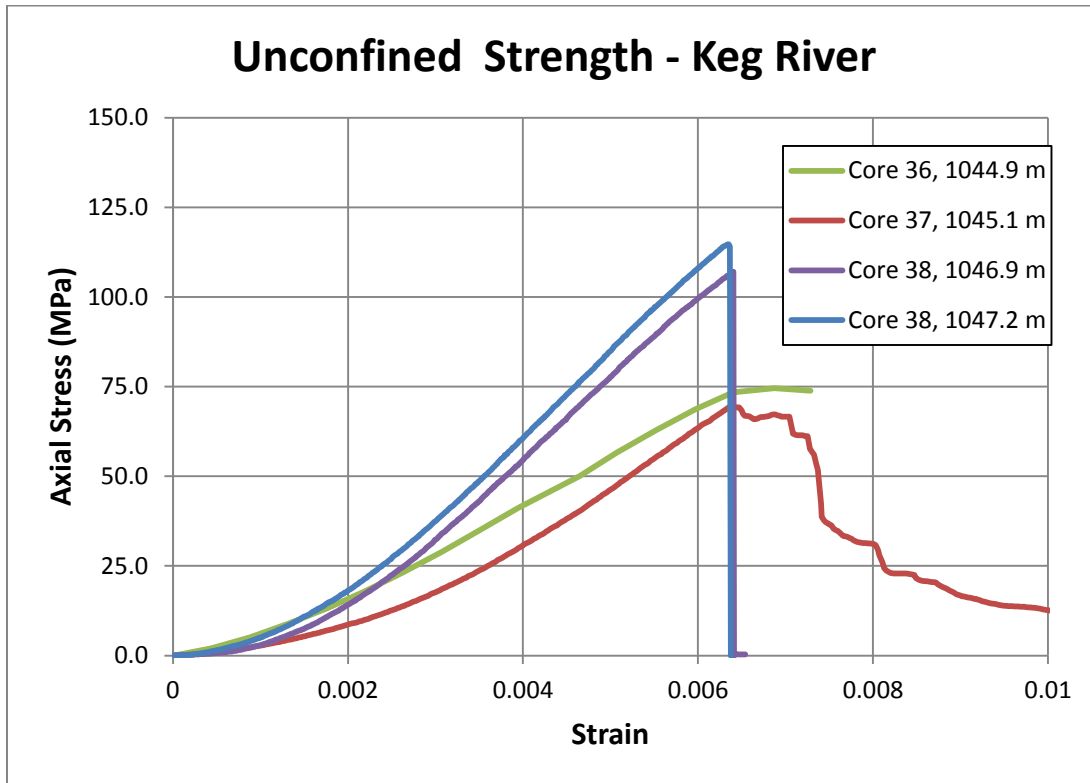
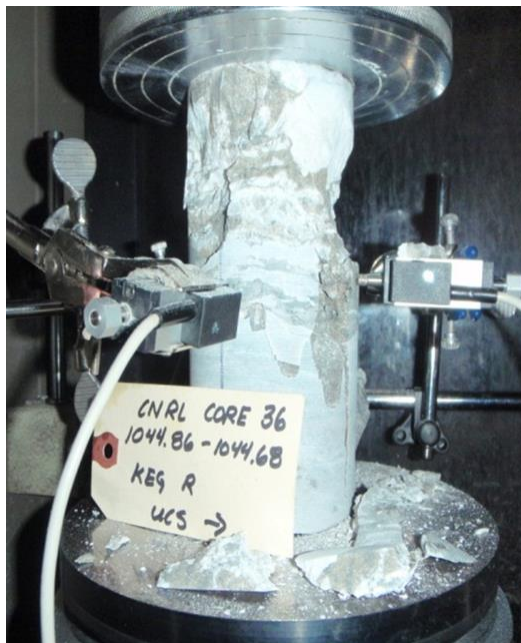


Figure 10. Unconfined Compression Test – Stress Strain Curves – Keg River



Photograph 6. Failure in Unconfined Compression Keg River

1.3.2 Standard Triaxial Compression

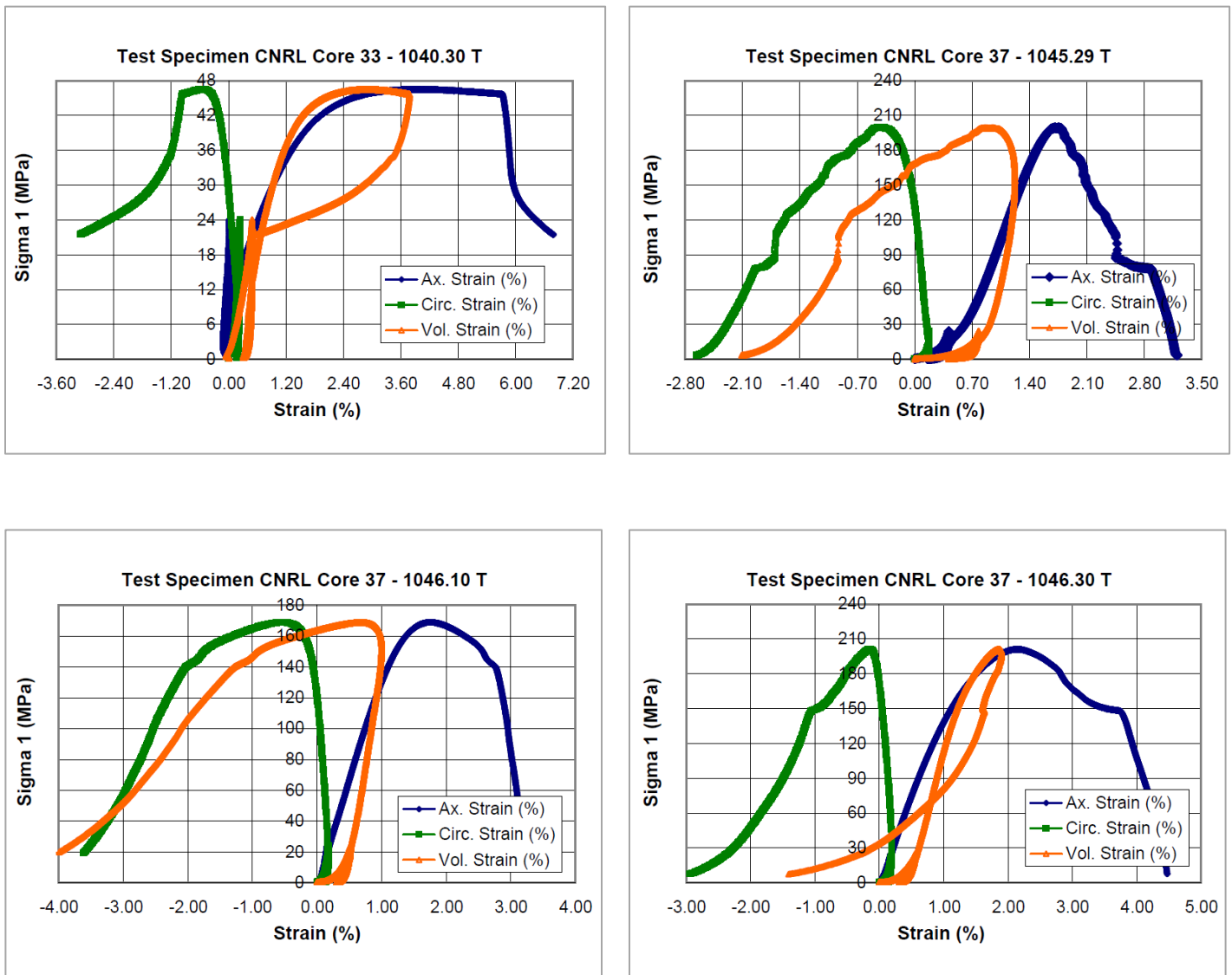


Figure 11. Standard Triaxial Compression Tests – Stress – Strain Curves – Keg River



Photograph 7. Failure in Standard Triaxial Compression – Keg River

1.4 Cold Lake Formation

1.4.1 Unconfined Compression Strength Test

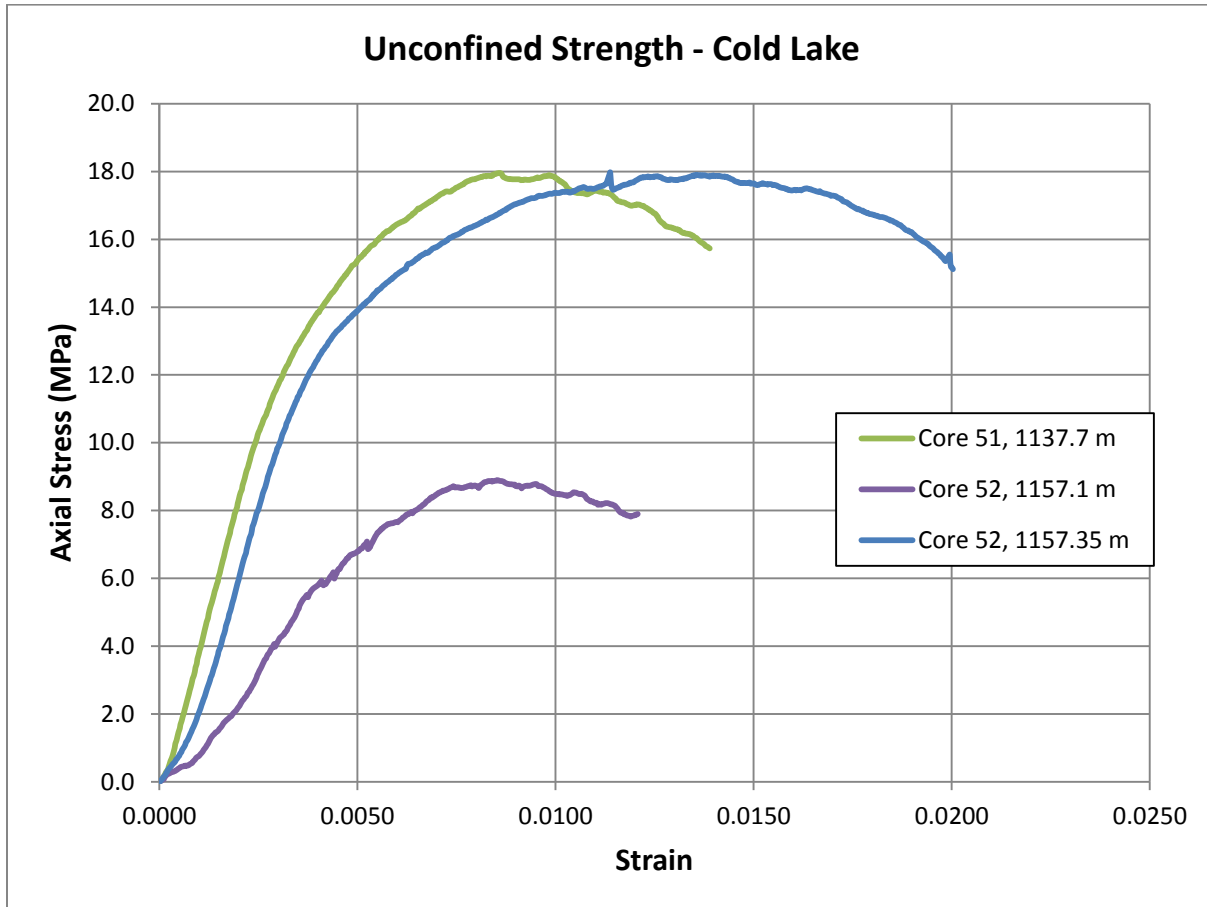


Figure 12. Unconfined Compression Test – Stress – Strain Curves – Cold Lake Formation



Photograph 8. Failure in Unconfined Compression Test – Cold Lake

1.5 Ernestina Lake Formation

1.5.1 Unconfined Compression Test

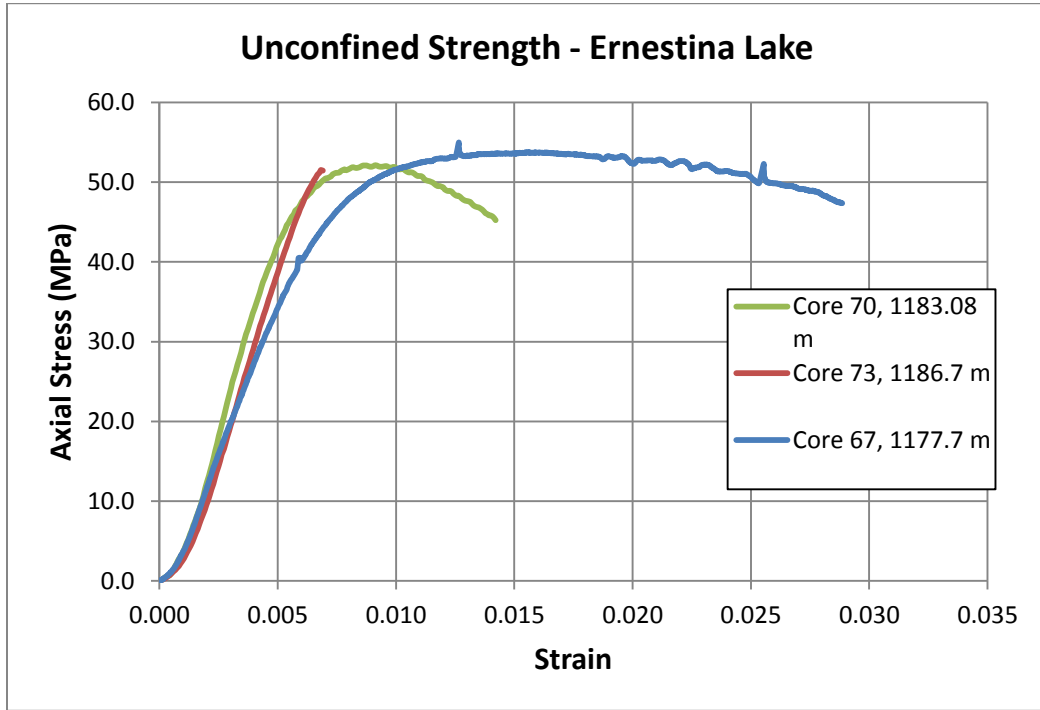


Figure 13. Unconfined Compression Test Stress Strain Curves – Ernestina Lake



Photograph 9. Failure in Unconfined Compression Ernestina Lake

1.5.2 Standard Triaxial Compression

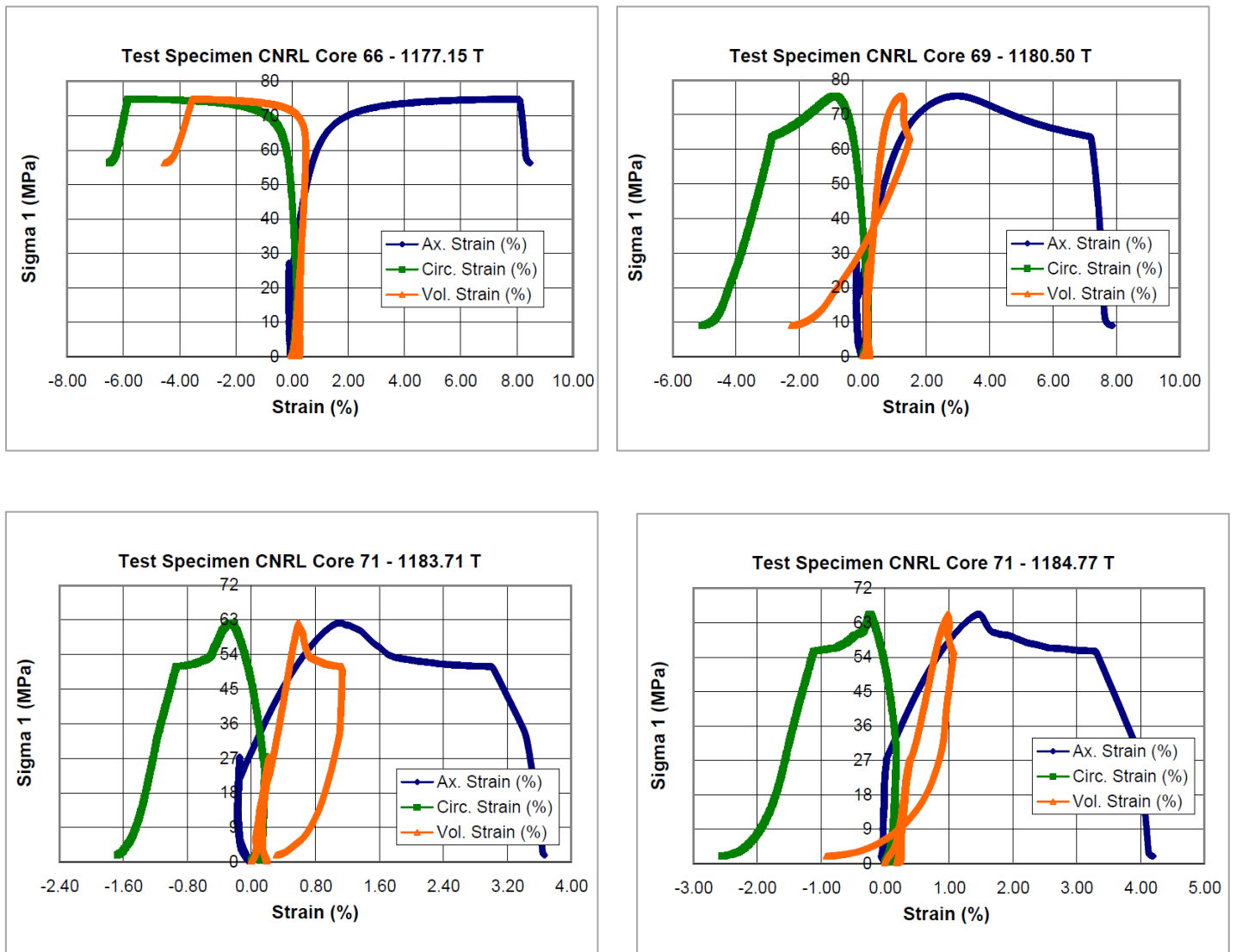
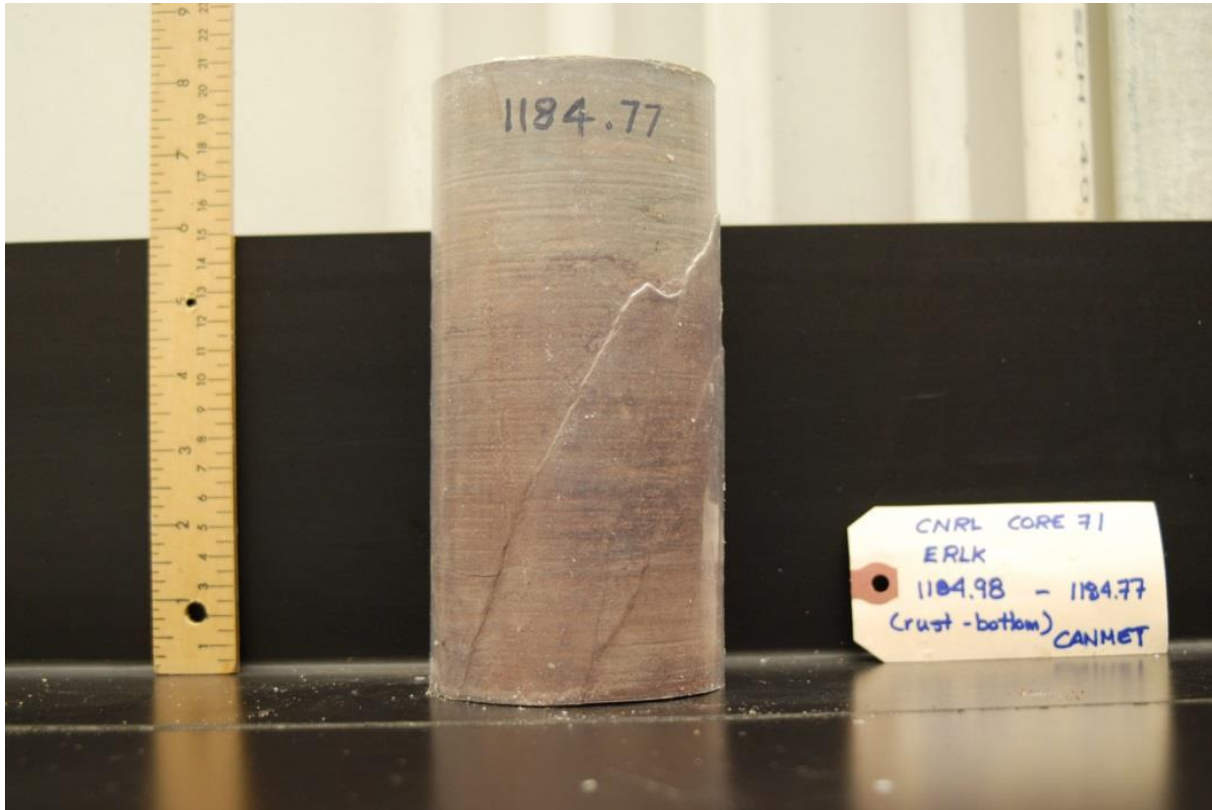


Figure 14. Standard Triaxial Compression Stress Strain Curves – Ernestina Lake



Photograph 10. Failure in Standard Triaxial Compression – Ernestina Lake

1.5.3 Creep

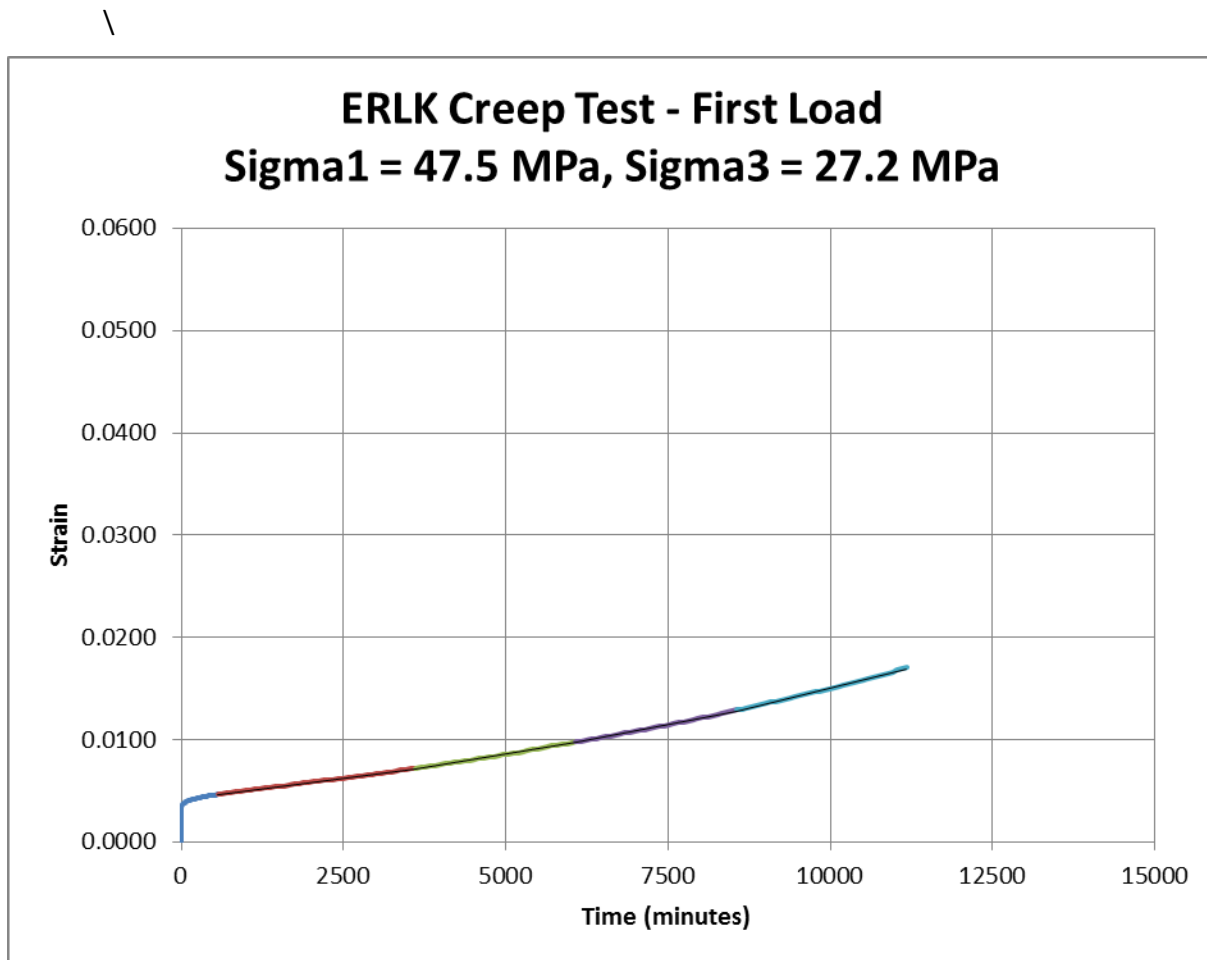


Figure 15. Creep Test – Ernestina Lake

1.5.4 Index testing

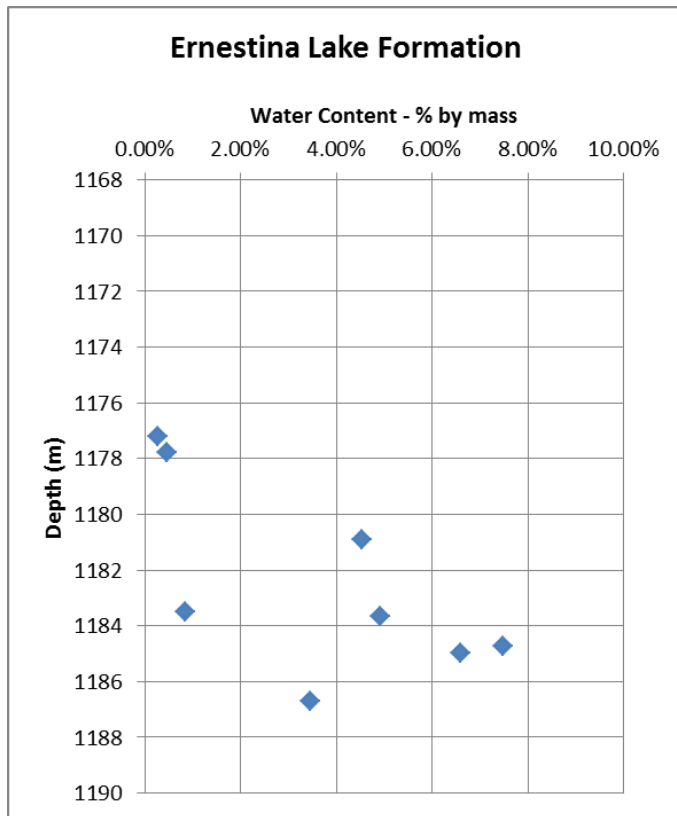


Figure 16. Water Content versus Depth - Ernestina Lake

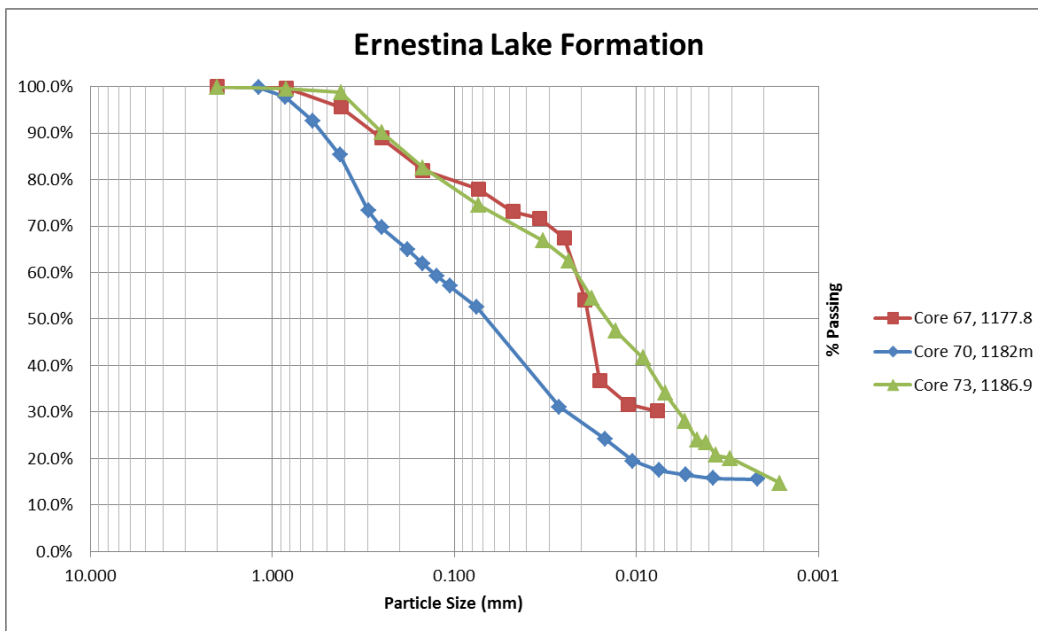


Figure 17. Grain Size Distribution – Ernestina Lake

1.6 Lotsberg Formation

1.6.1 Unconfined Compression Strength

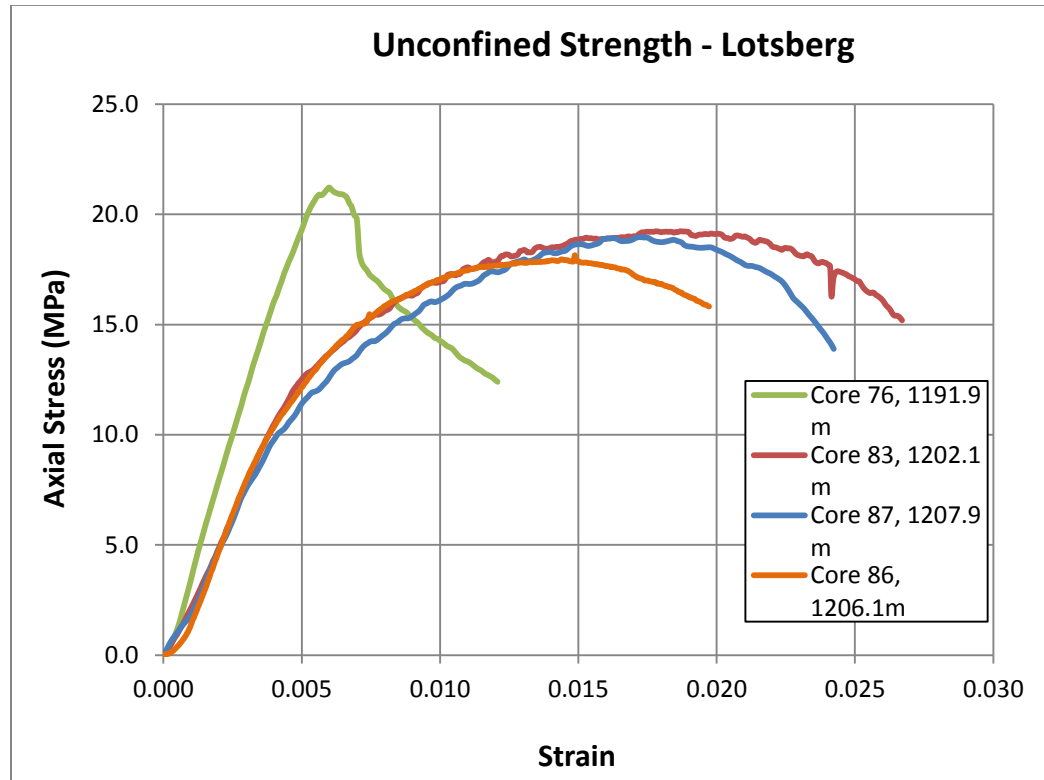


Figure 18. Unconfined Compressive Strength – Stress-Strain Curves - Lotsberg



Photograph 11. Failure in Unconfined Compression - - Lotsberg

1.6.2 Constant Mean Compression Tests

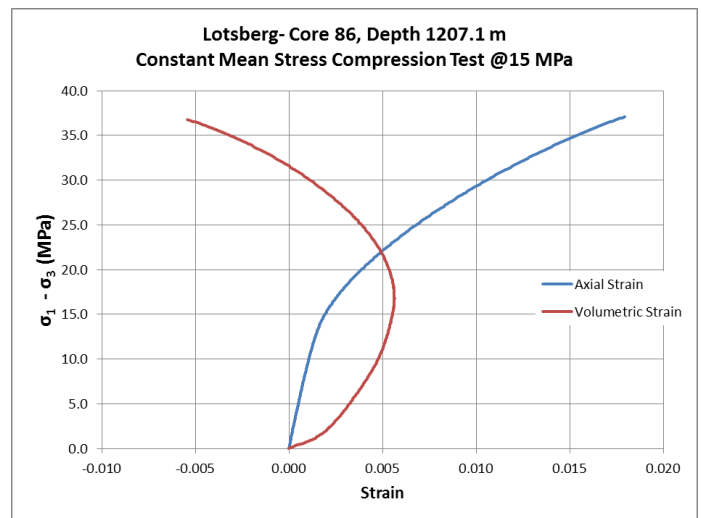
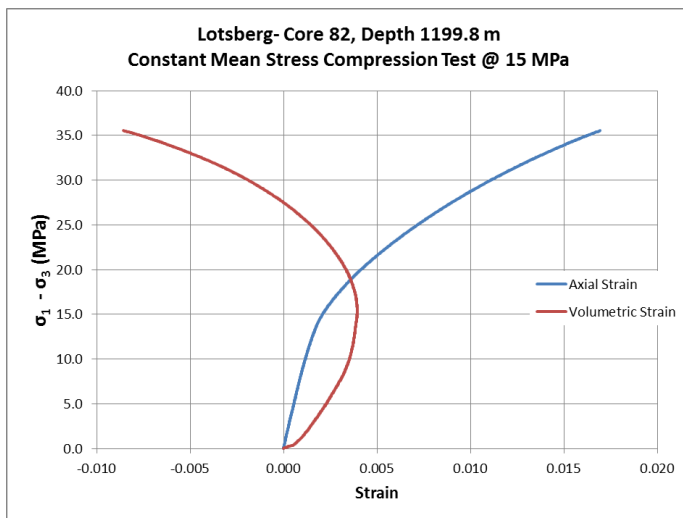
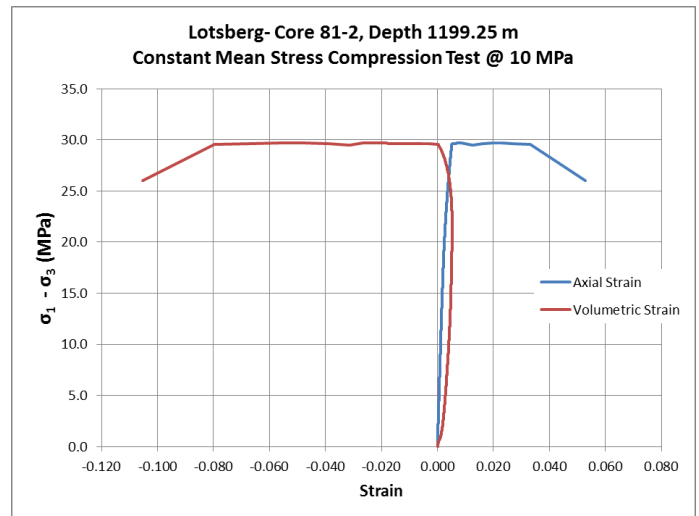
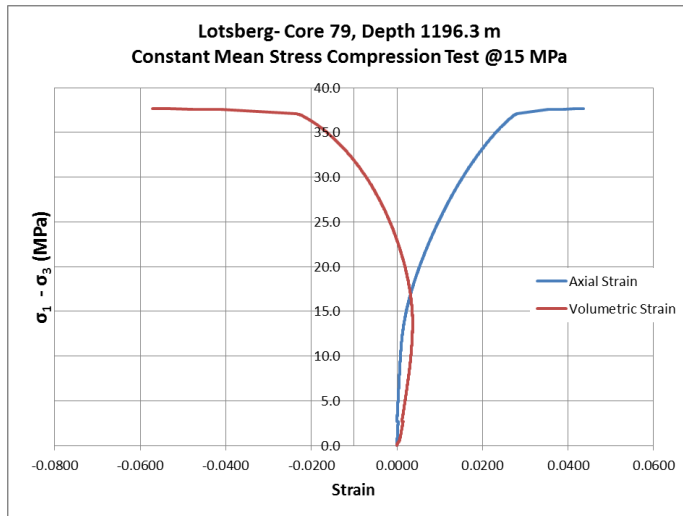


Figure 19. Constant Mean Compression Tests - Lotsberg



Photograph 12. Failure in Constant Mean Compression Test - Lotsberg

1.6.3 Constant Mean Extension Tests

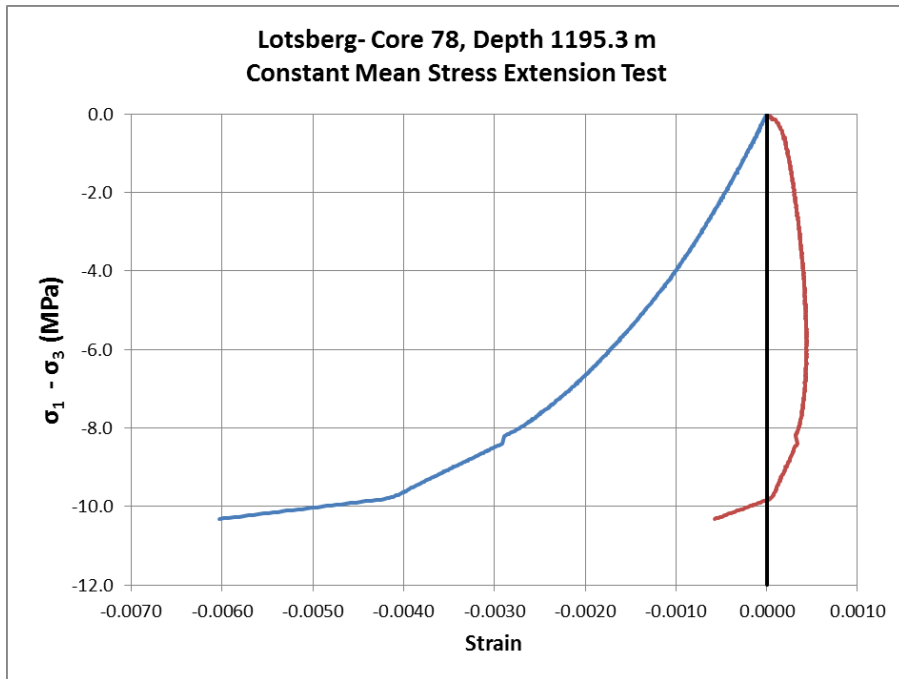
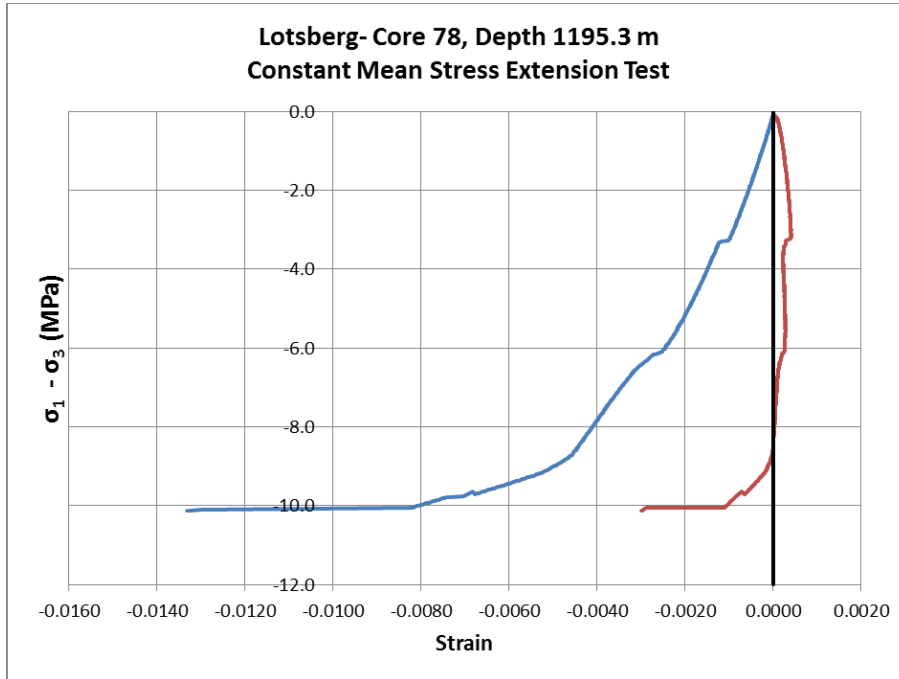


Figure 20. Constant Mean Extension Tests - Lotsberg

1.6.4 Creep

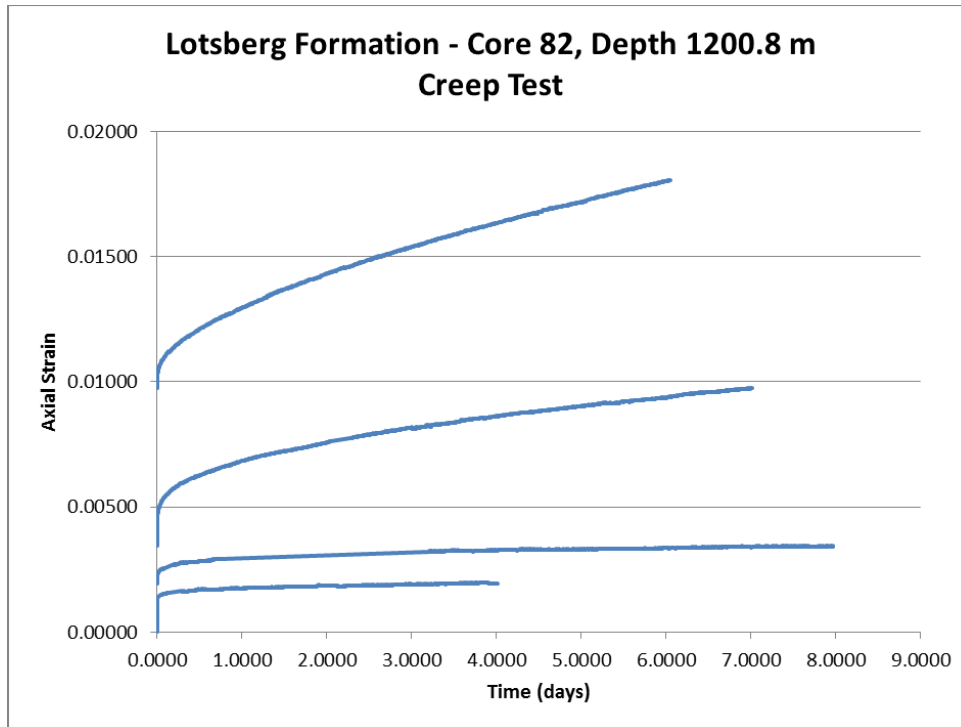


Figure 21. Strain versus Time – Creep Test Lotsberg

1.6.5 Creep – flow law fitting

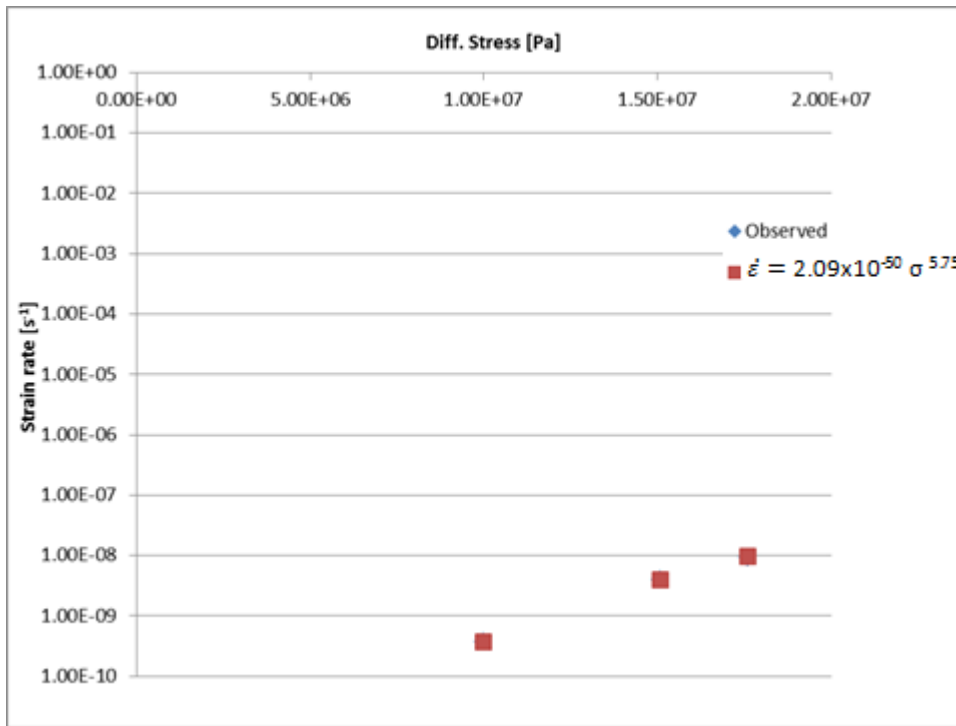


Figure 22. Strain versus Differential Stress - Lotsberg

Appendix E

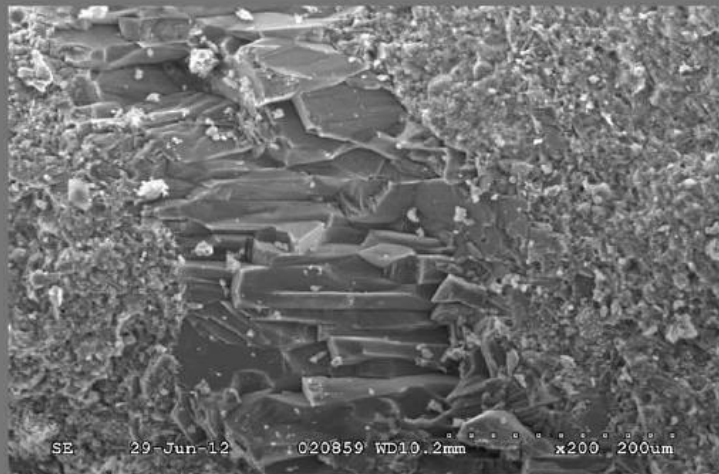
SEM Photographs

Contains:

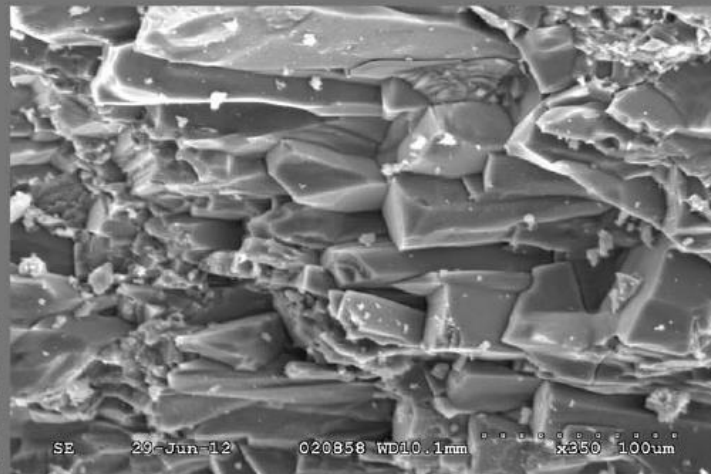
- Six sets of four SEM photographs from samples of various depths

UNIVERSITY OF ALBERTA
DEPT. OF CIVIL & ENVIRONMENTAL ENGINEERING

JULY, 2012
A15801



1
2
3
4
5
6
7
8
9
10
11
12
13
14

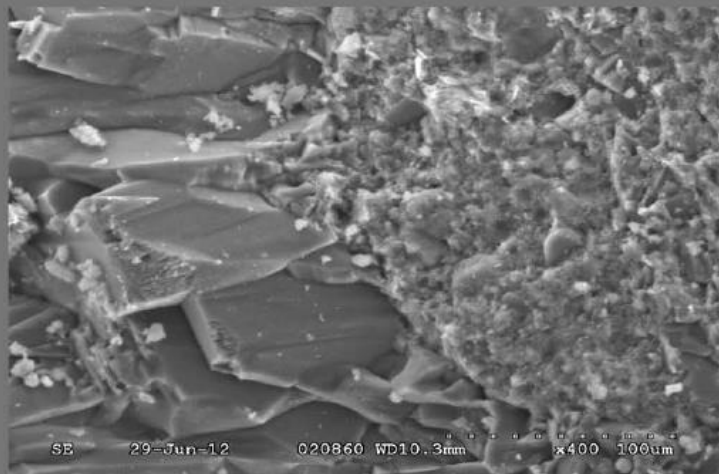


1
2
3
4
5
6
7
8
9
10
11
12
13
14

A B C D E F G H I J K L M N O P Q

1/2
3/4

A B C D E F G H I J K L M N O P Q



1
2
3
4
5
6
7
8
9
10
11
12
13
14

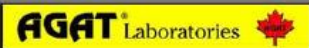
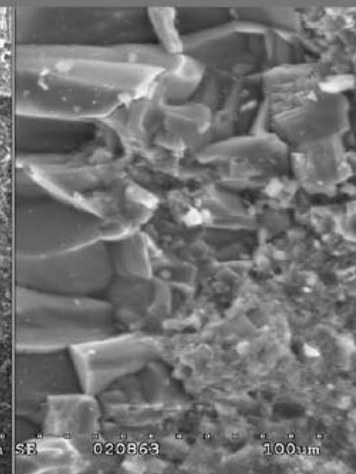
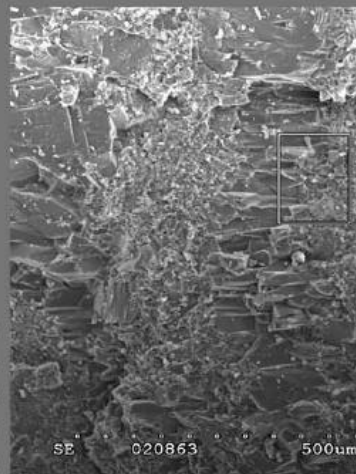
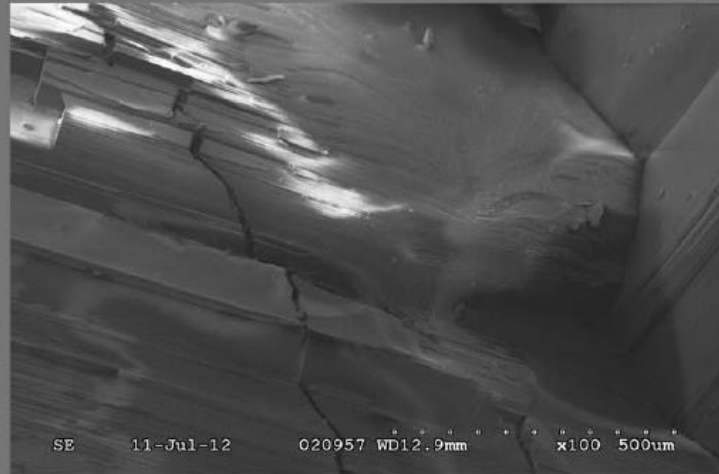
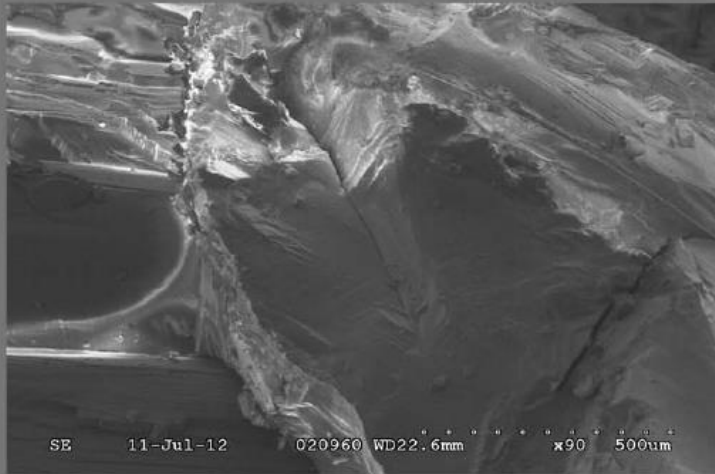
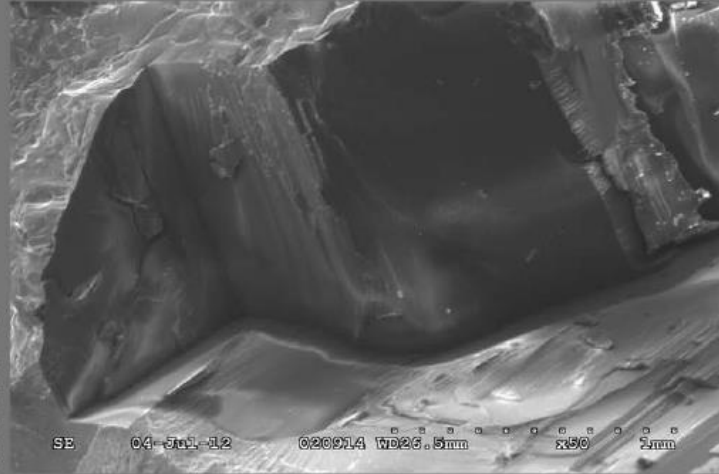
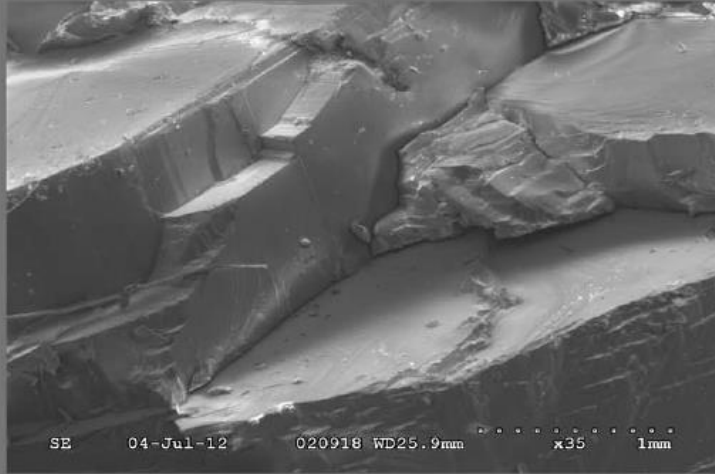


PLATE #1

Sample 01: Core 09, 896.9m

UNIVERSITY OF ALBERTA
DEPT. OF CIVIL & ENVIRONMENTAL ENGINEERING

JULY, 2012
A15801



1
2
3
4
5
6
7
8
9
10
11
12
13
14
1/2
3/4
A B C D E F G H I J K L M N O P Q

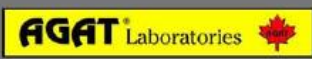
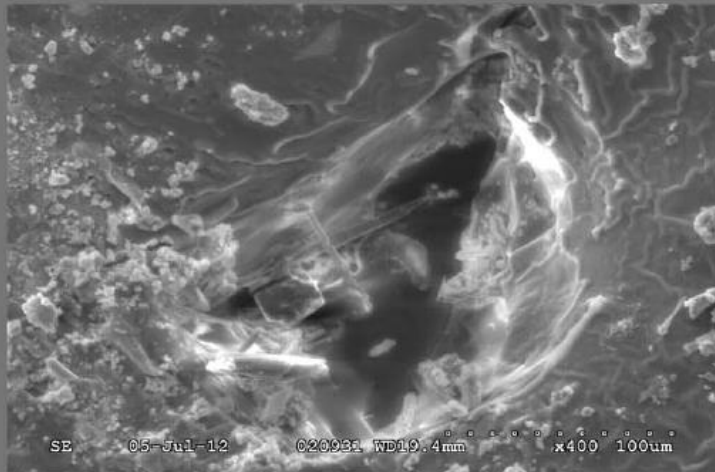


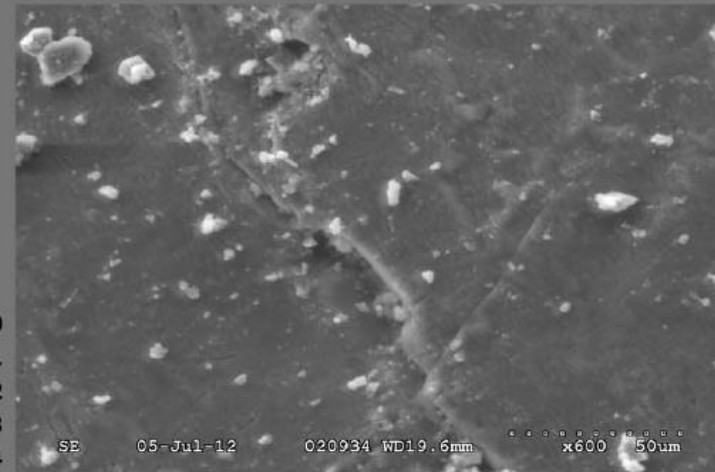
PLATE #2
Sample 02: Core 25, 977.4

UNIVERSITY OF ALBERTA
DEPT. OF CIVIL & ENVIRONMENTAL ENGINEERING

JULY, 2012
A15801



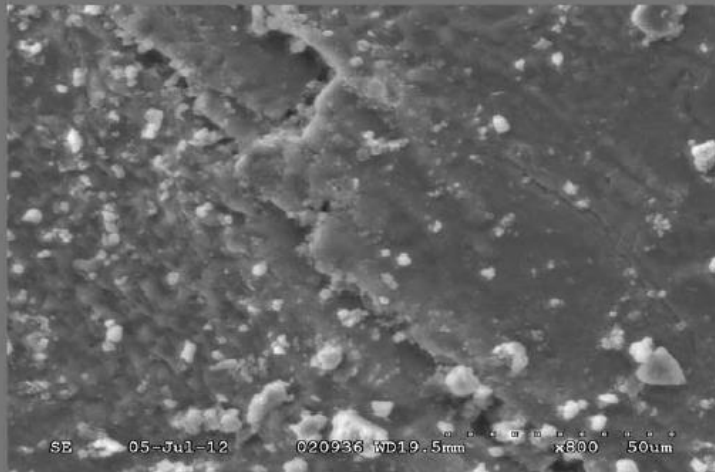
1
2
3
4
5
6
7
8
9
10
11
12
13
14



A B C D E F G H I J K L M N O P Q

1/2
3/4

A B C D E F G H I J K L M N O P Q

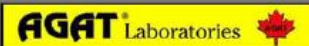


1
2
3
4
5
6
7
8
9
10
11
12
13
14



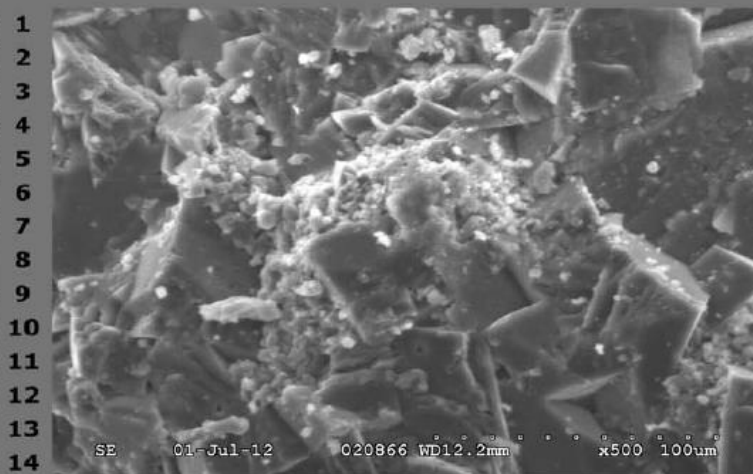
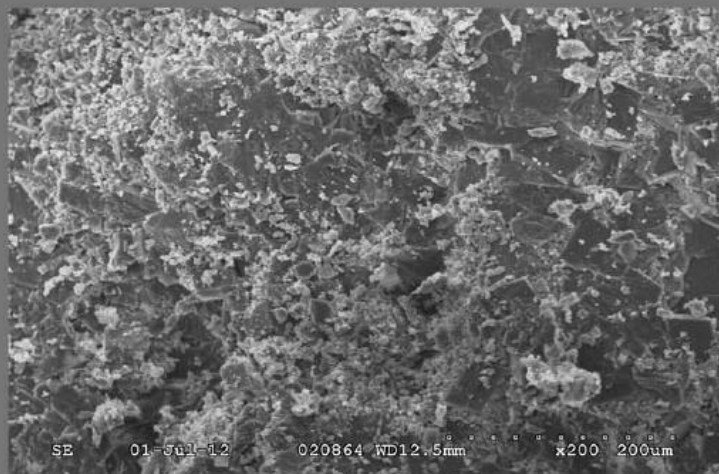
PLATE #3

Sample 03: Core 31, 1036.7m



UNIVERSITY OF ALBERTA
DEPT. OF CIVIL & ENVIRONMENTAL ENGINEERING

JULY, 2012
A15801



A B C D E F G H I J K L M N O P Q

A B C D E F G H I J K L M N O P Q

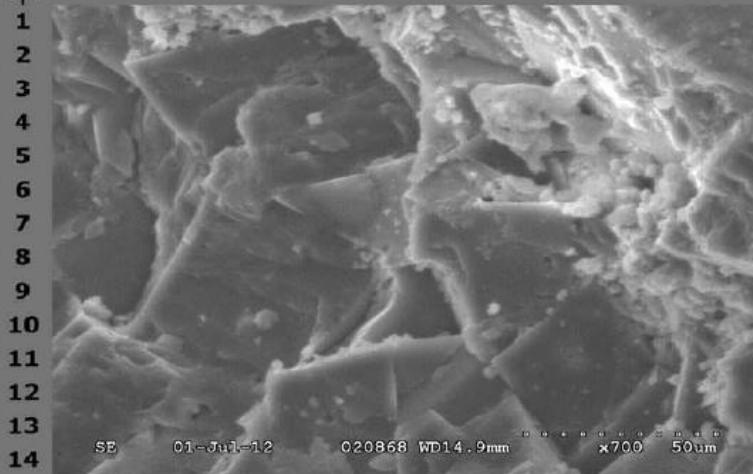
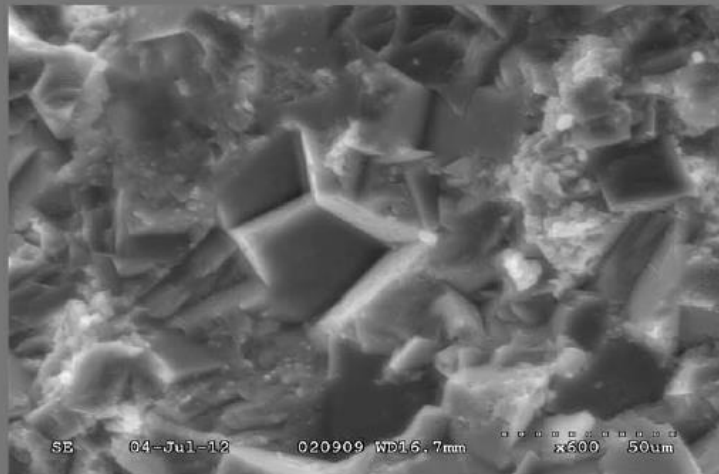
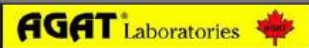


PLATE #4

Sample 04: Core 38, 1047.5m

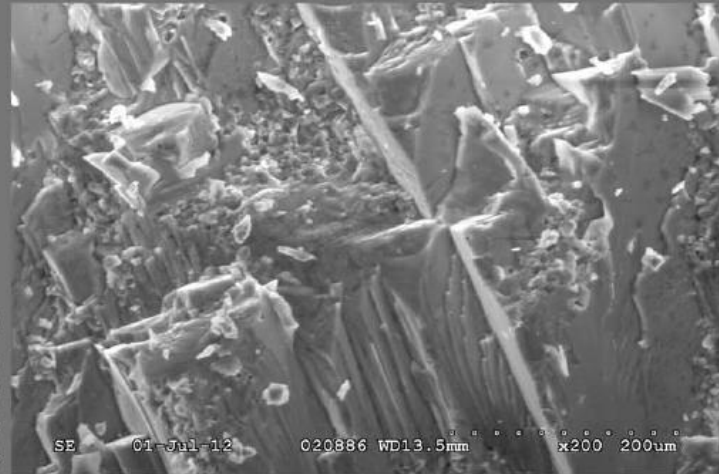


UNIVERSITY OF ALBERTA
DEPT. OF CIVIL & ENVIRONMENTAL ENGINEERING

JULY, 2012
A15801



1
2
3
4
5
6
7
8
9
10
11
12
13
14

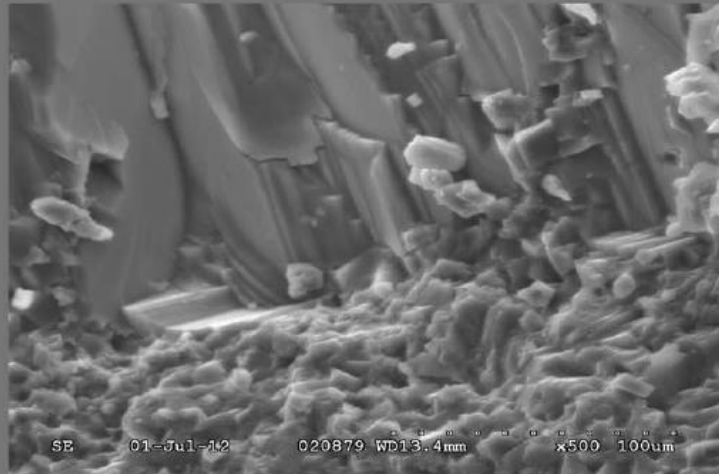


1
2
3
4
5
6
7
8
9
10
11
12
13
14

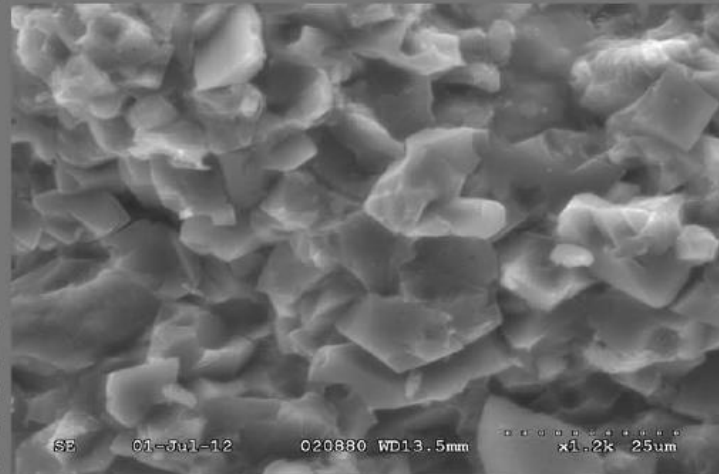
A B C D E F G H I J K L M N O P Q

1/2
3/4

A B C D E F G H I J K L M N O P Q



1
2
3
4
5
6
7
8
9
10
11
12
13
14



1
2
3
4
5
6
7
8
9
10
11
12
13
14

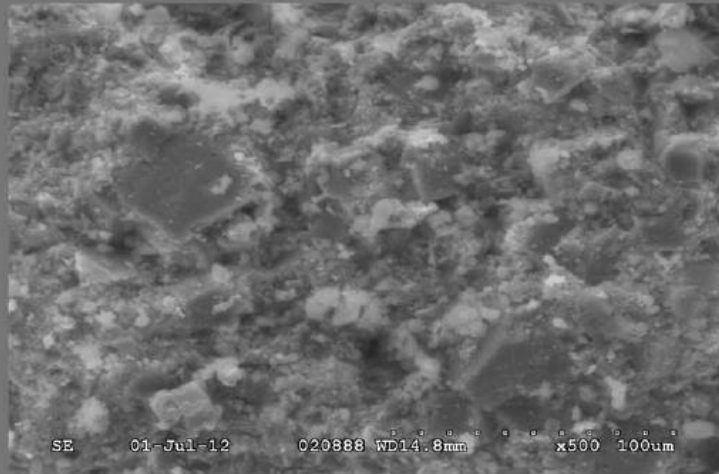
PLATE #5

Sample 05: Core 68, 1177.6m

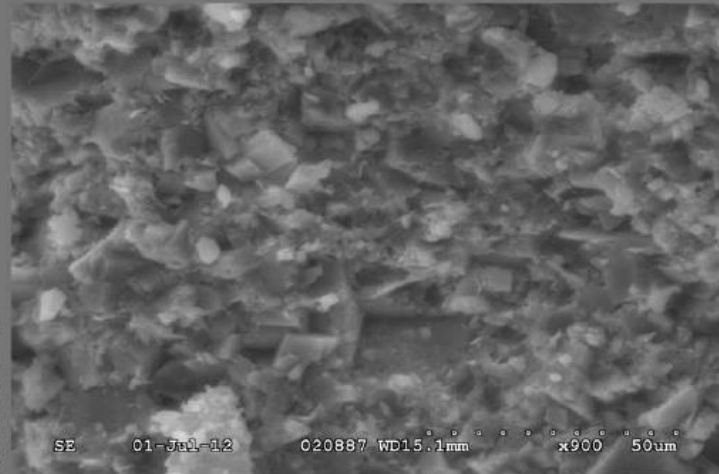


UNIVERSITY OF ALBERTA
DEPT. OF CIVIL & ENVIRONMENTAL ENGINEERING

JULY, 2012
A15801



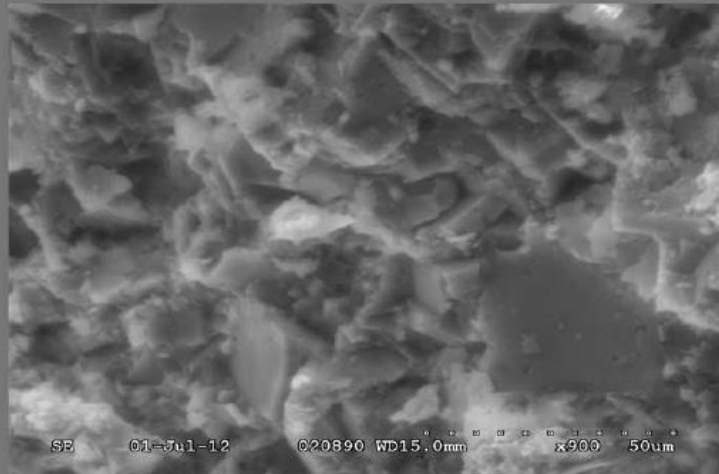
1
2
3
4
5
6
7
8
9
10
11
12
13
14



A B C D E F G H I J K L M N O P Q

1/2
3/4

A B C D E F G H I J K L M N O P Q



1
2
3
4
5
6
7
8
9
10
11
12
13
14

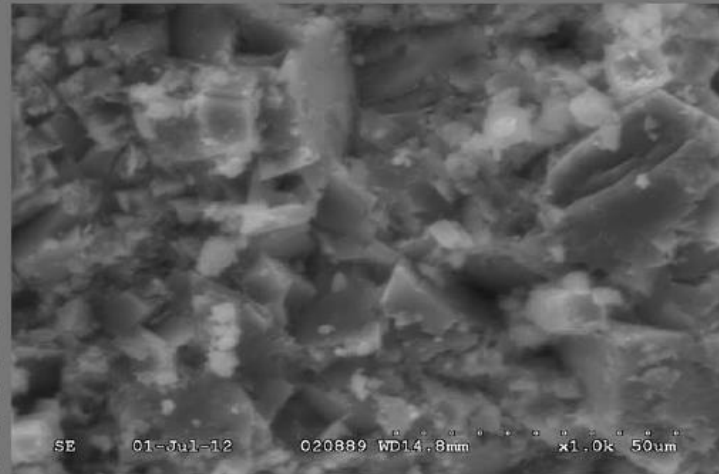


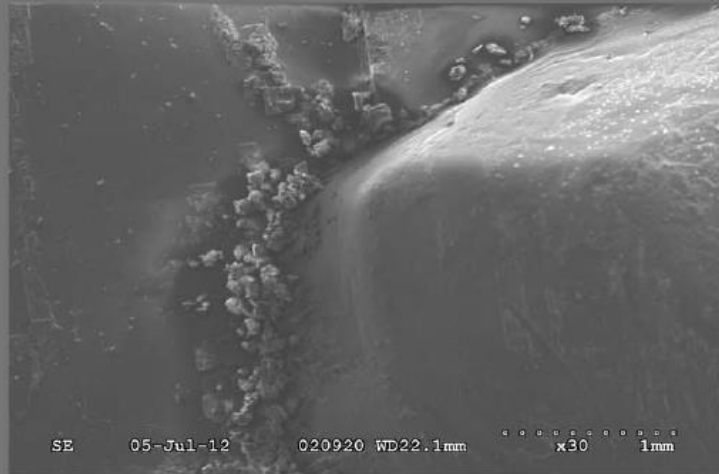
PLATE #6

Sample 06: Core 73, 1187.1m

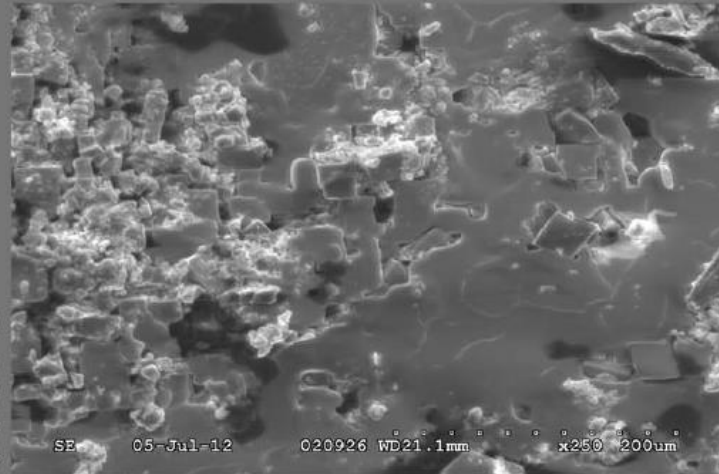


UNIVERSITY OF ALBERTA
DEPT. OF CIVIL & ENVIRONMENTAL ENGINEERING

JULY, 2012
A15801



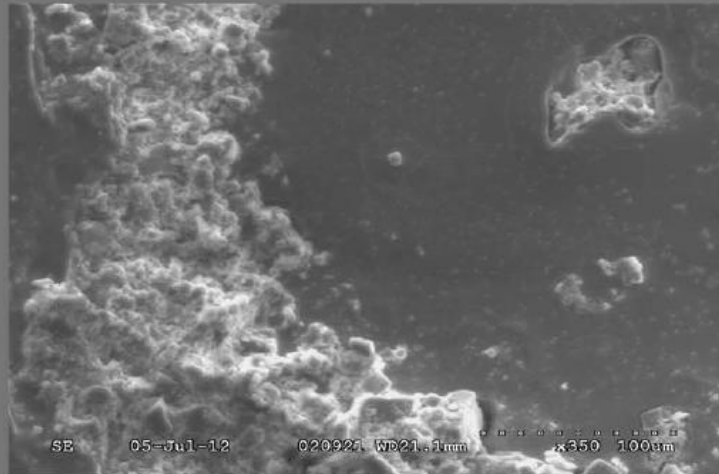
1
2
3
4
5
6
7
8
9
10
11
12
13
14



1/2
3/4

A B C D E F G H I J K L M N O P Q

A B C D E F G H I J K L M N O P Q



1
2
3
4
5
6
7
8
9
10
11
12
13
14

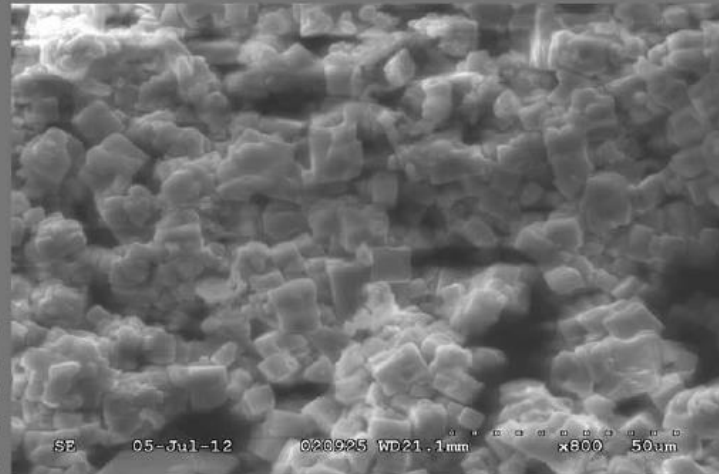


PLATE #7

Sample 07: Core 87, 1207.8m



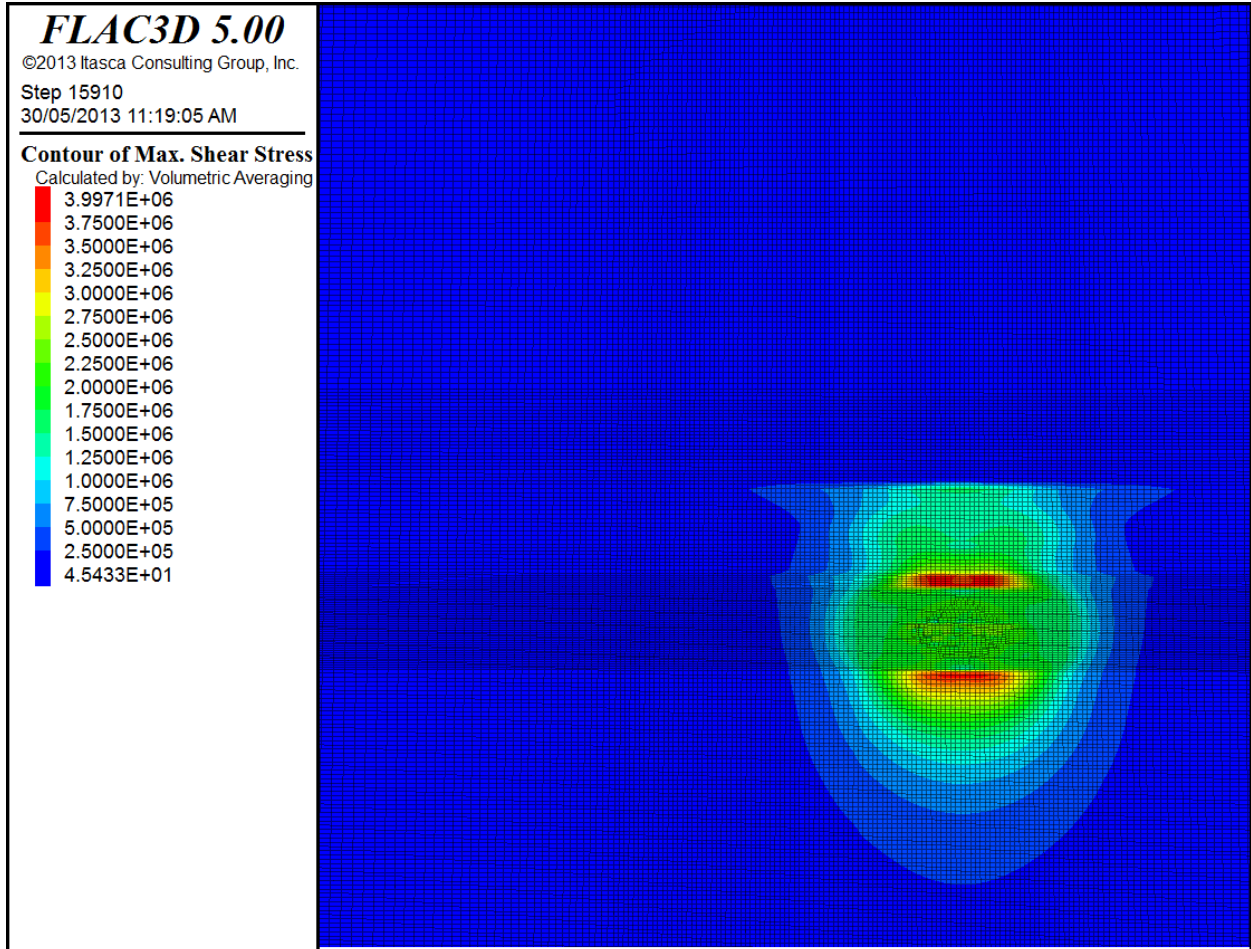
Appendix F

Numerical Modelling Results

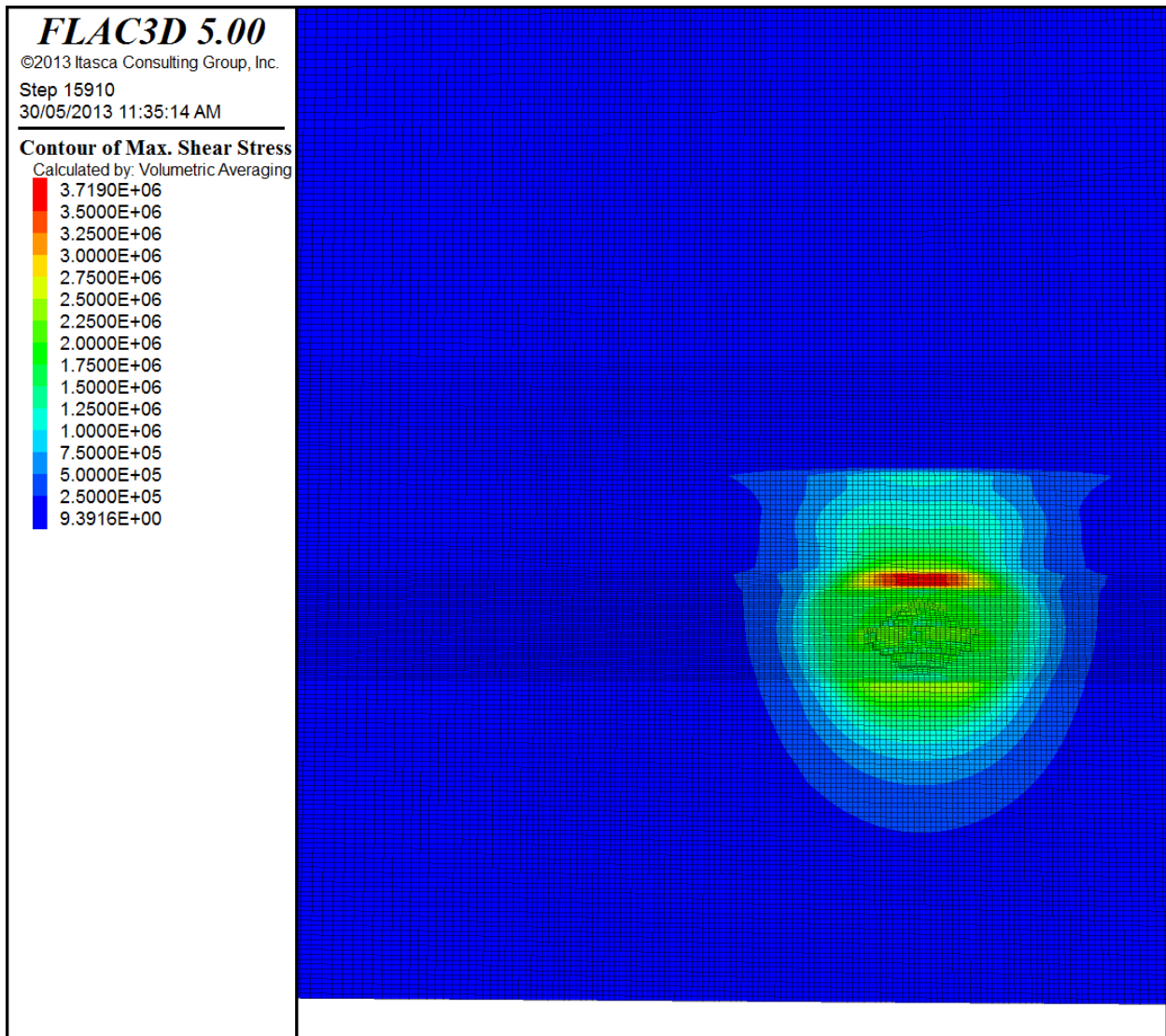
Contains:

- Graphical representations of maximum shear stress experienced over a 50 year period for all configurations
- Graphical representations of total vertical displacement over a 50 year period for all configurations

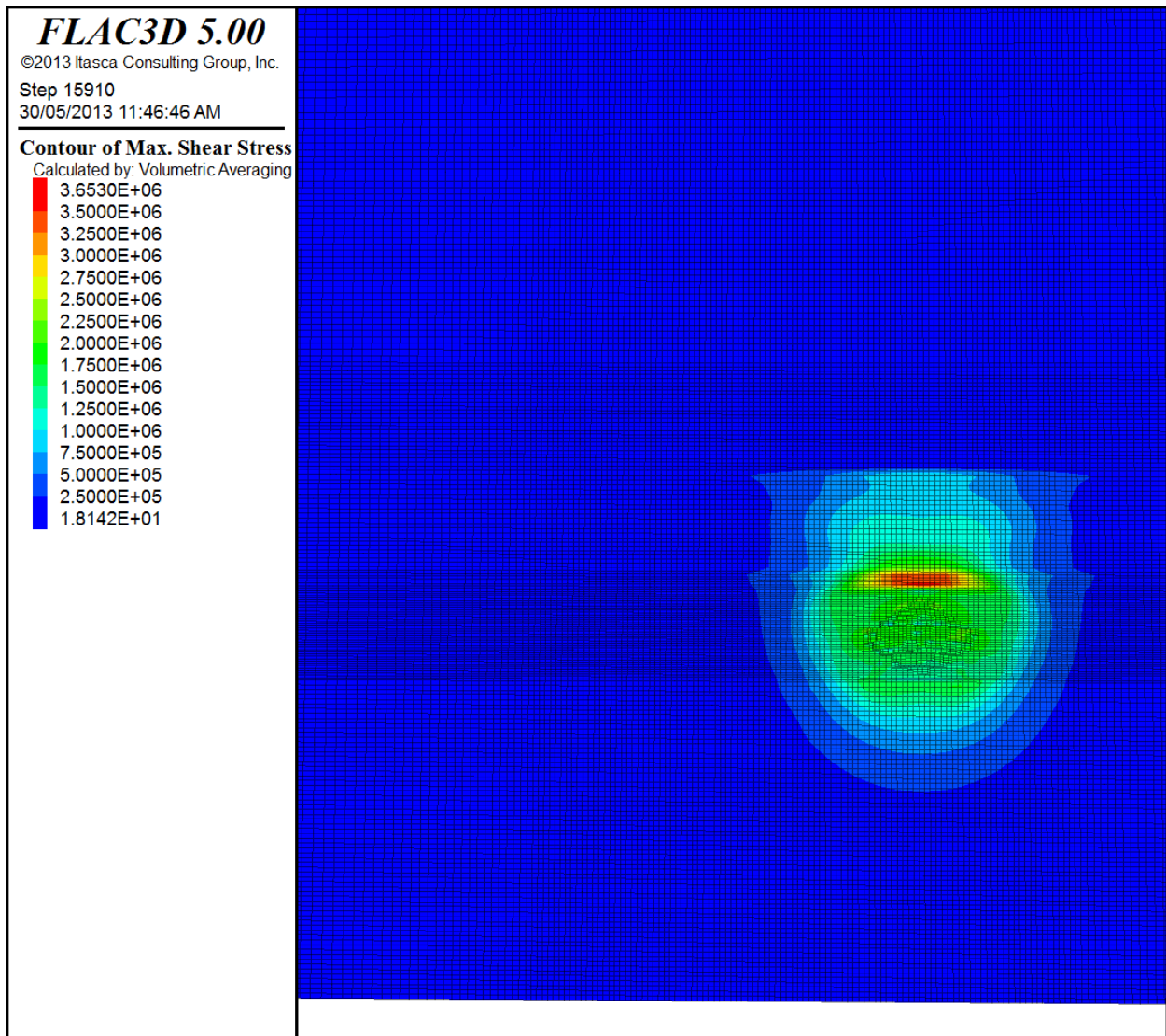
ONE CAVERN IN THE LOTSBERG FORMATION



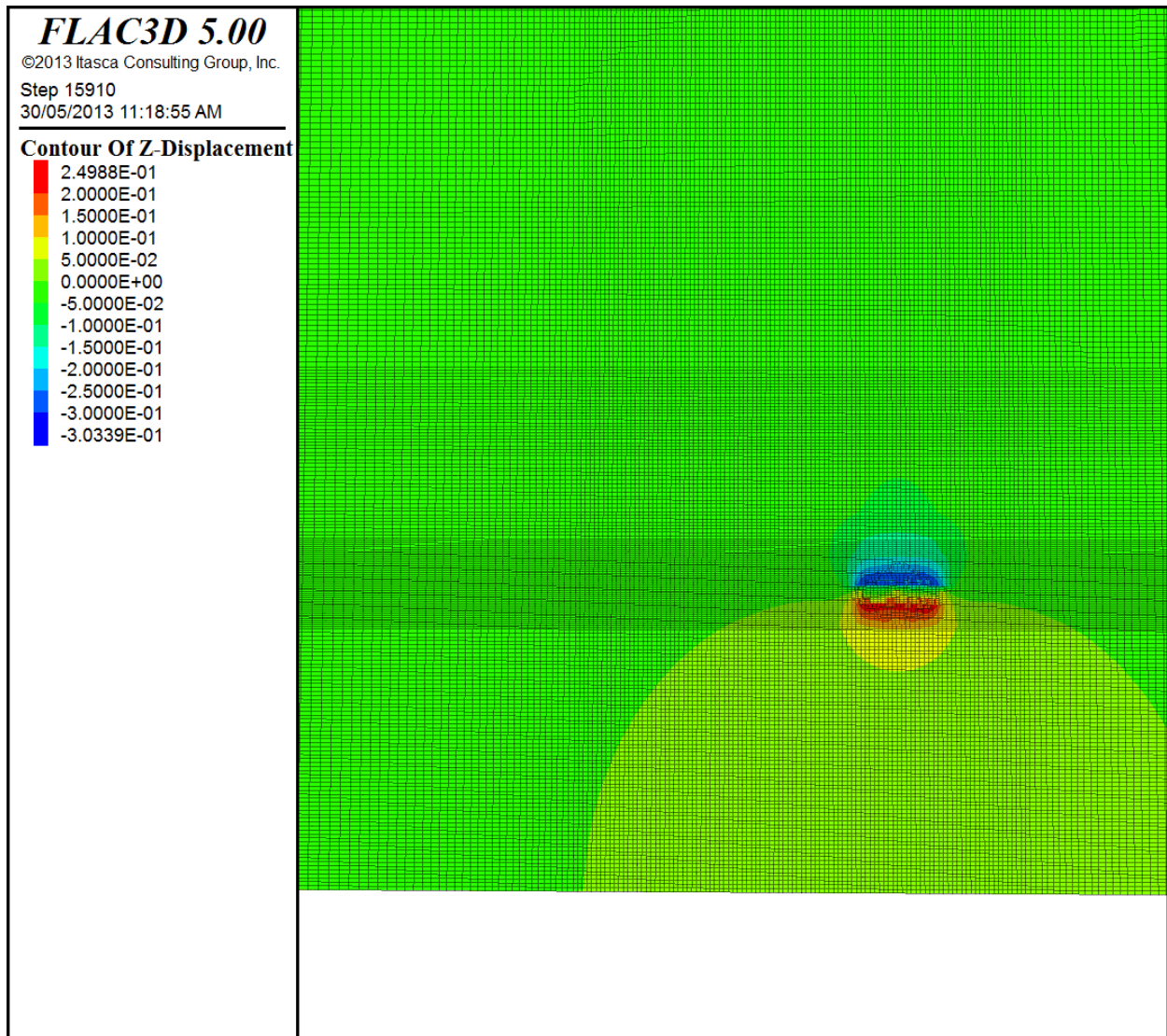
Maximum shear stress (in Pa) over a 50 year period. Cavern is filled with brine.



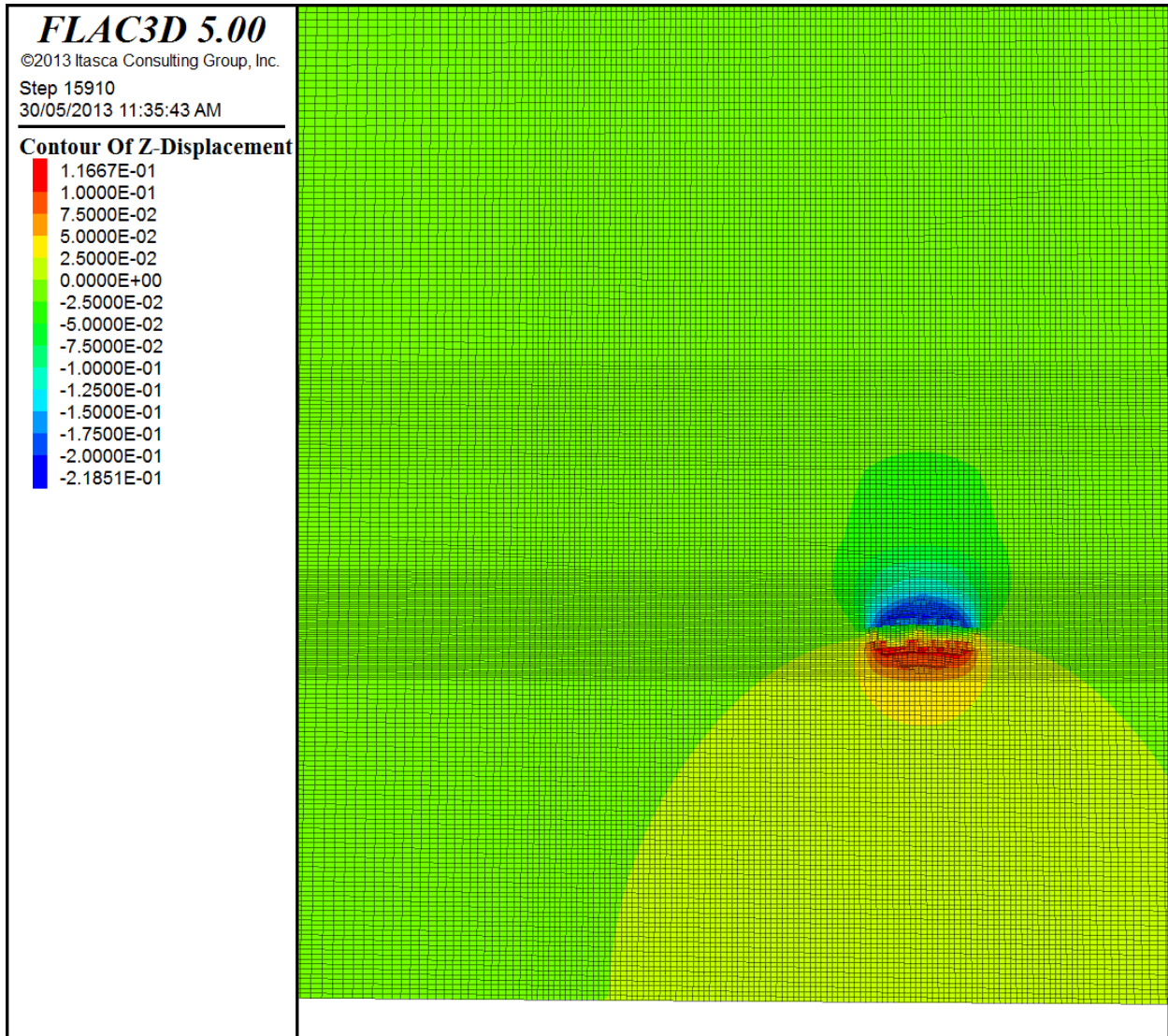
Maximum shear stress (in Pa) over a 50 year period. Cavern is filled with graded sands.



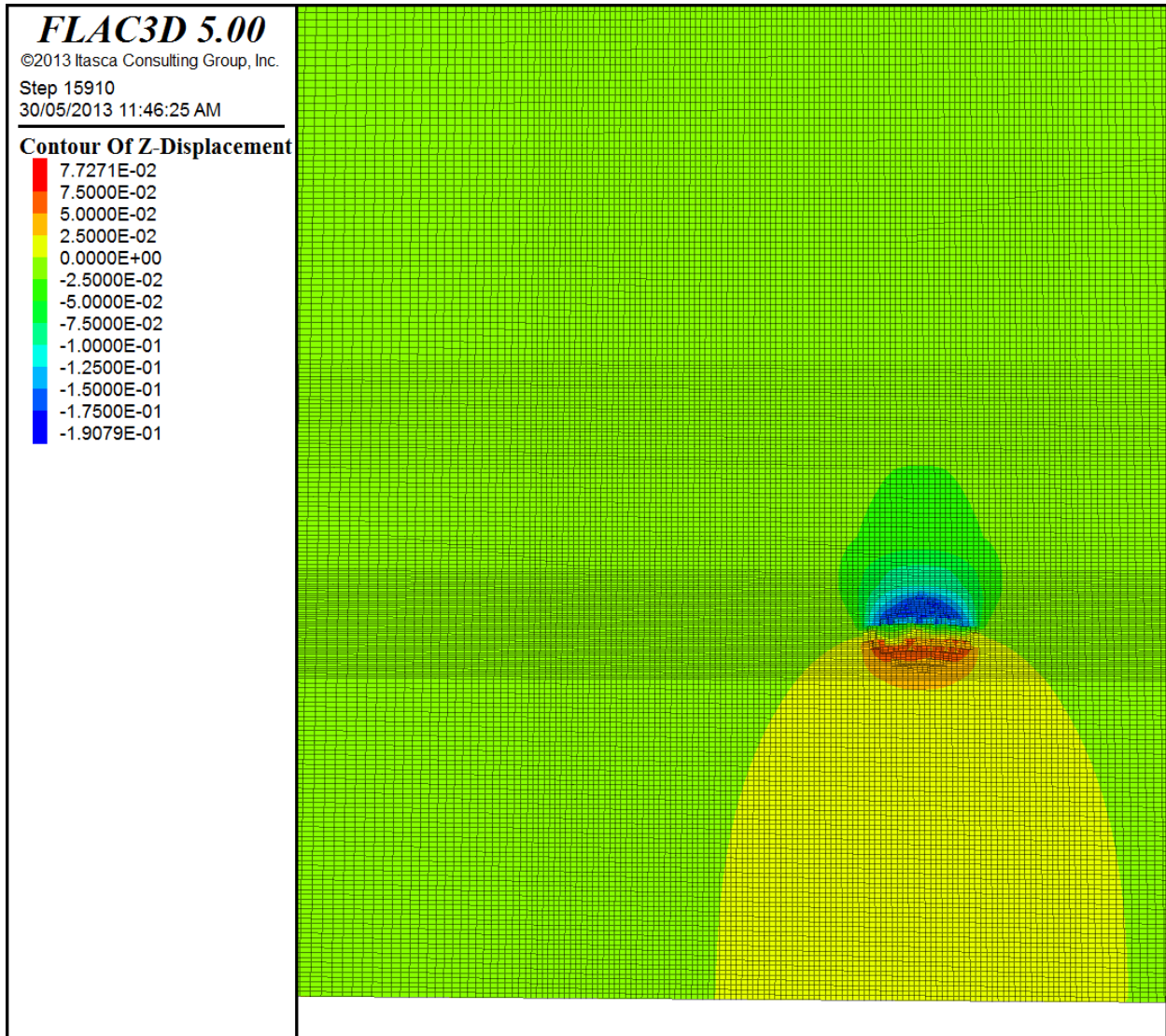
Maximum shear stress (in Pa) over a 50 year period. Cavern is filled with dense sands.



Total vertical displacement (in m) over a 50 year period. Cavern is filled with brine. Positive values represent upward movement.

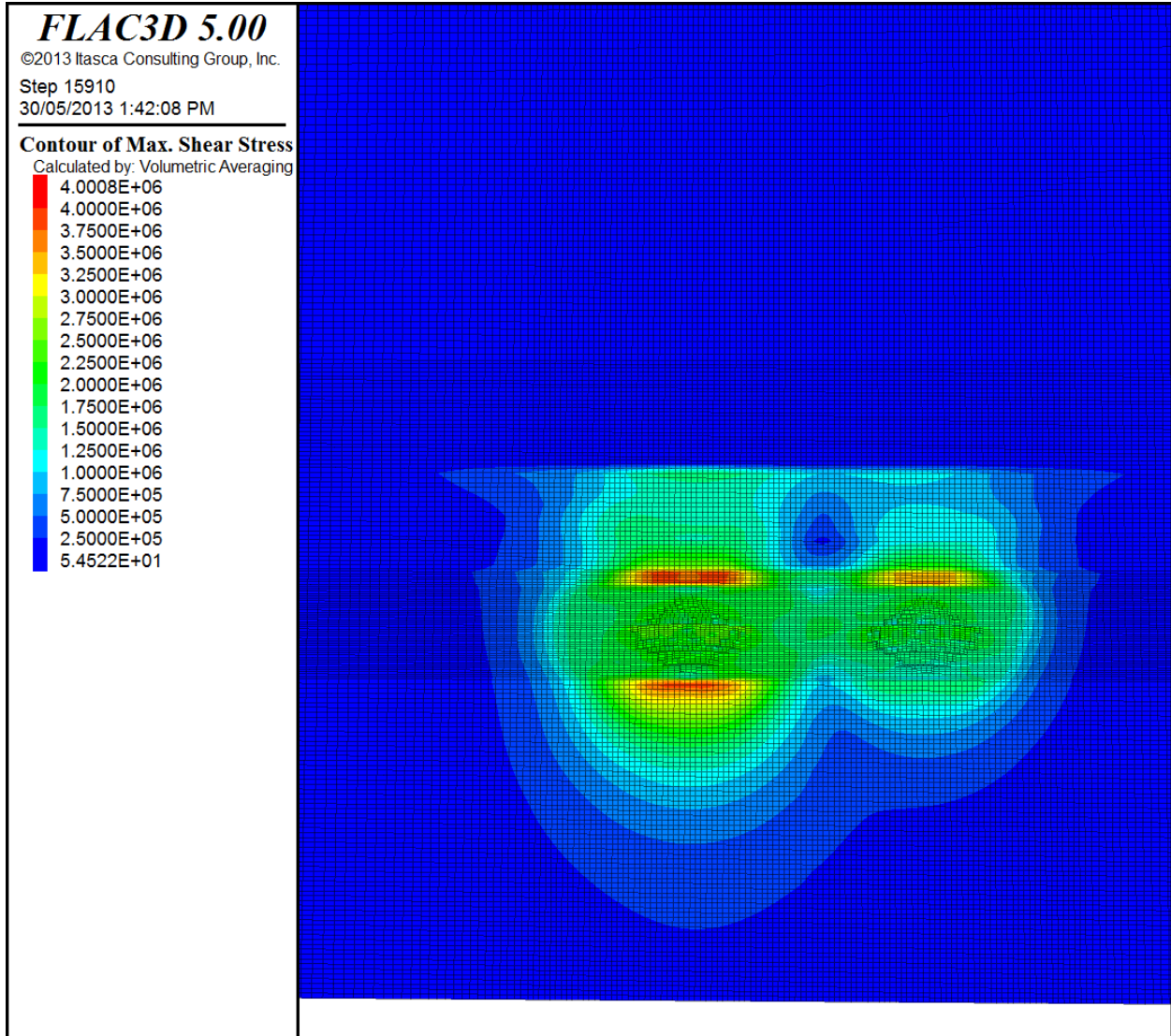


Total vertical displacement (in m) over a 50 year period. Cavern is filled with graded sands. Positive values represent upward movement.

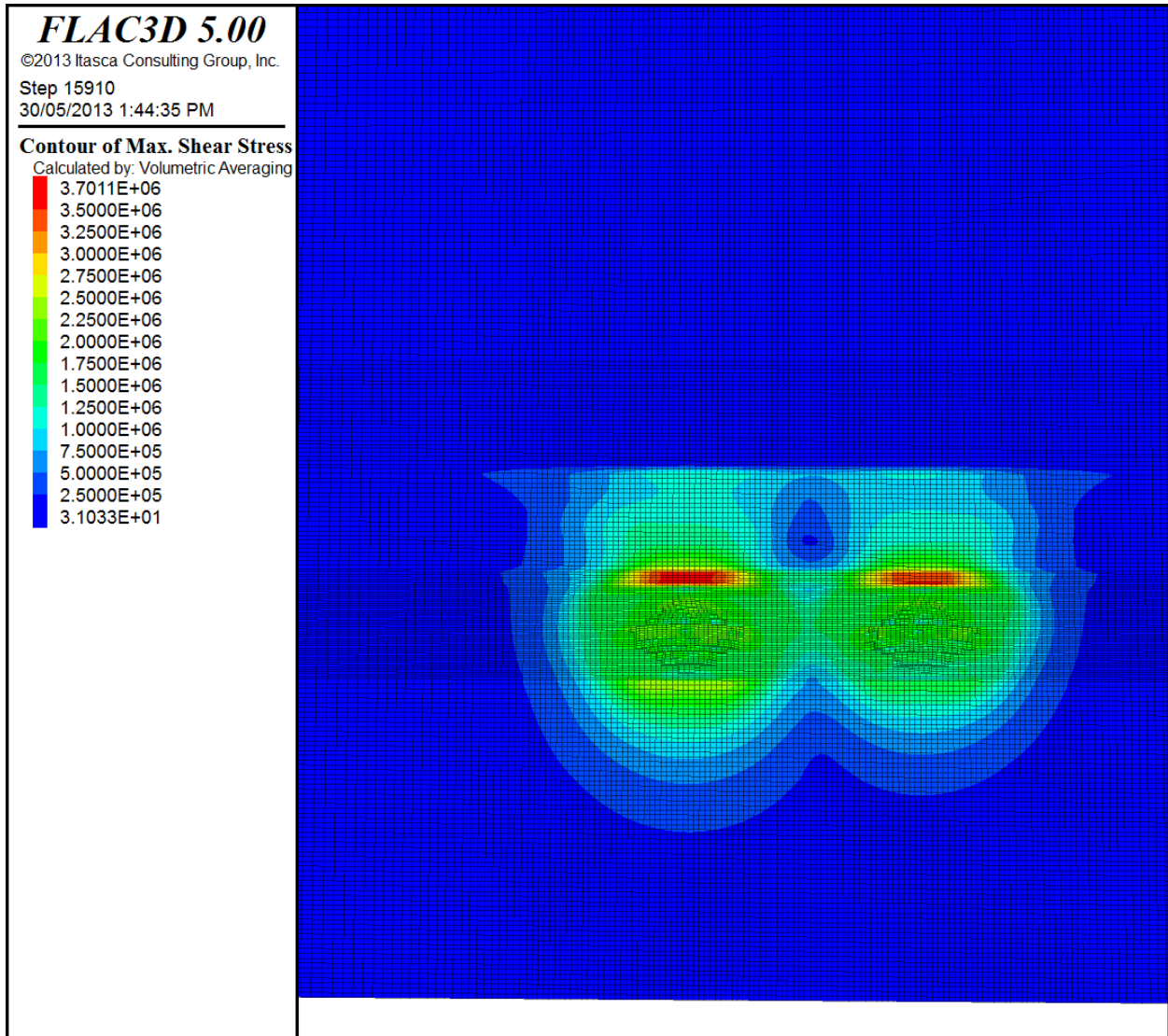


Total vertical displacement (in m) over a 50 year period. Cavern is filled with dense sands. Positive values represent upward movement.

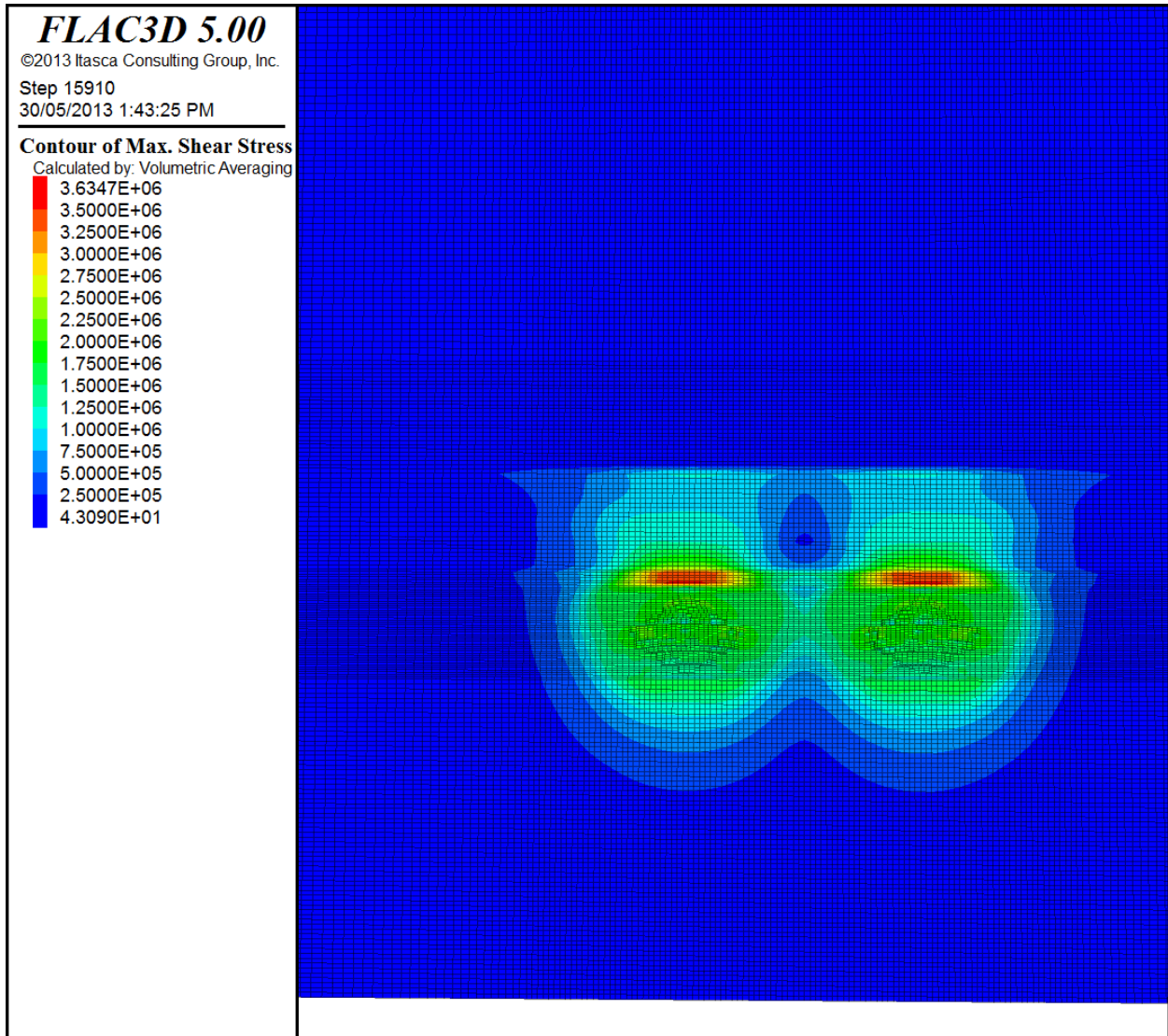
TWO CAVERNS IN THE LOTSBERG FORMATION



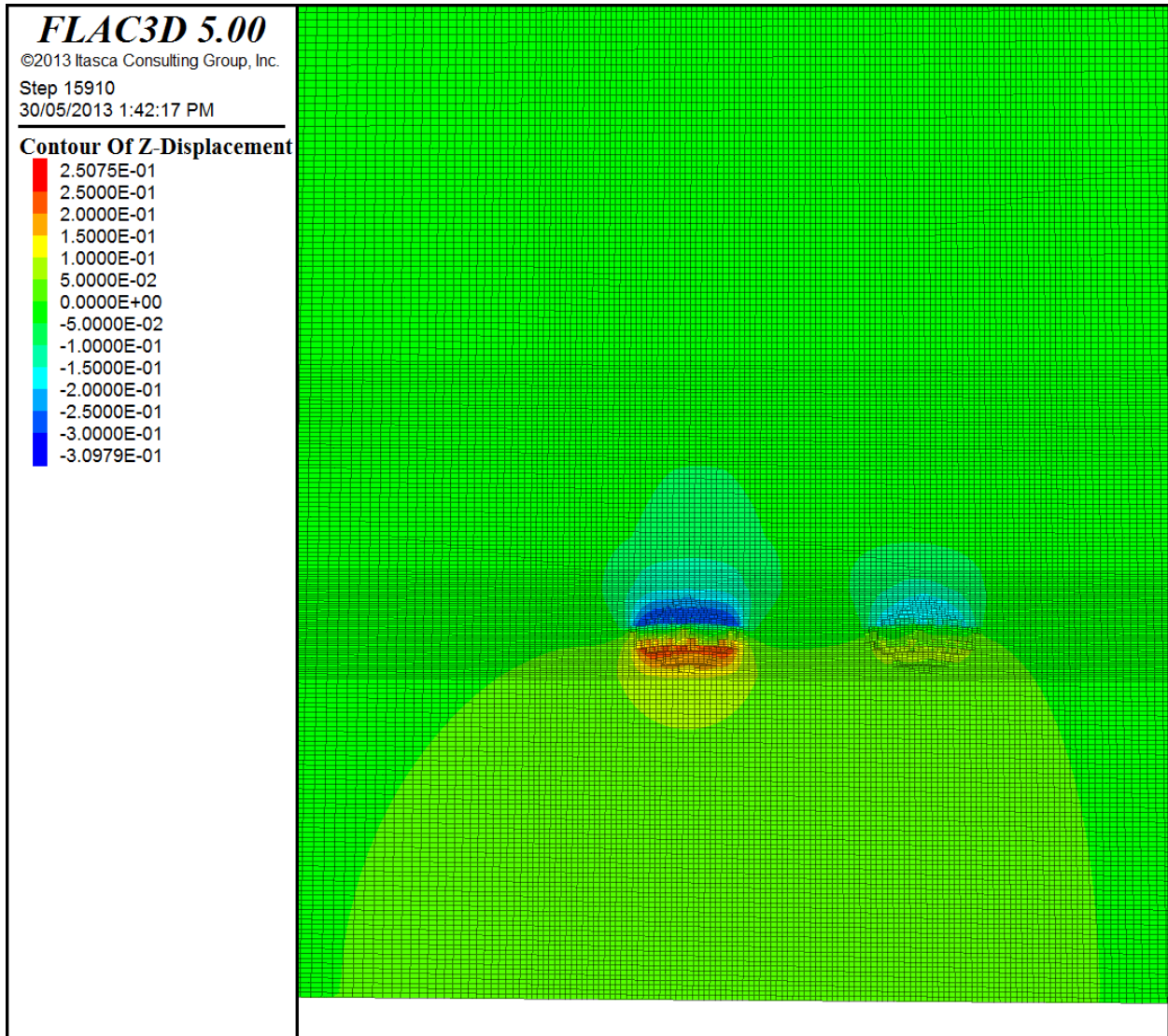
Maximum shear stress (in Pa) over a 50 year period. Cavern is on the left is filled with brine, cavern on the right is filled with dense sands.



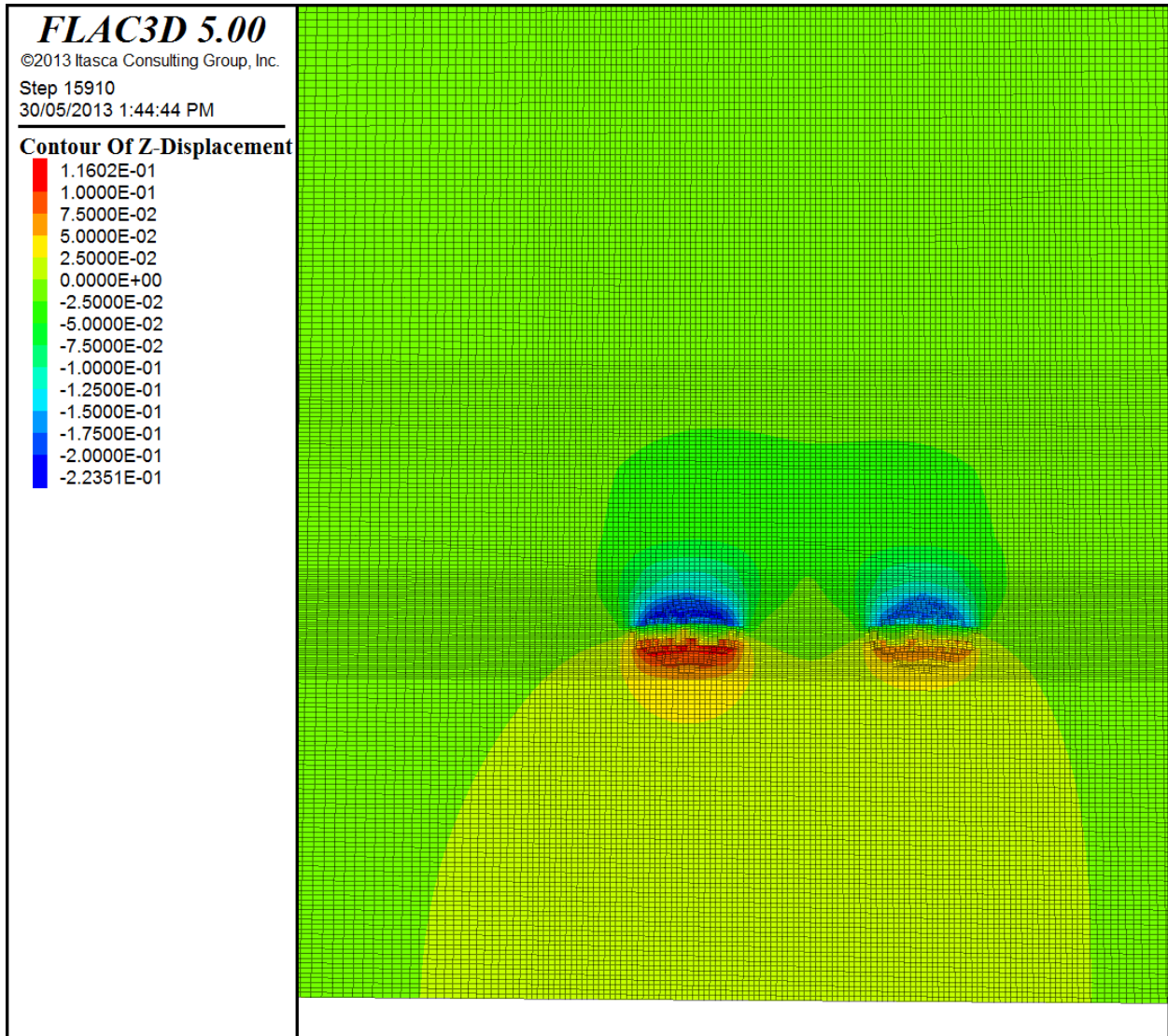
Maximum shear stress (in Pa) over a 50 year period. Cavern is on the left is filled with graded sands, cavern on the right is filled with dense sands.



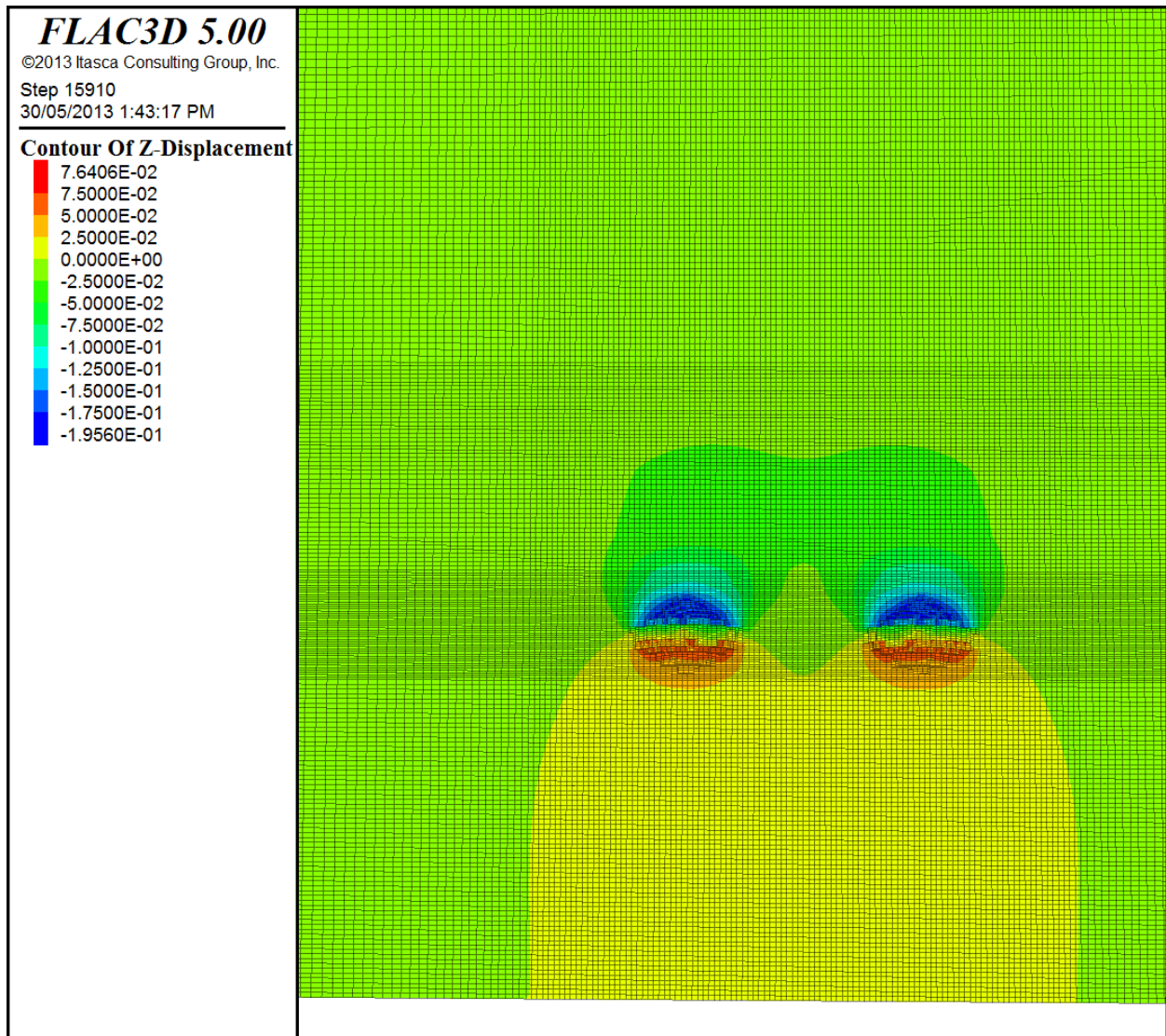
Maximum shear stress (in Pa) over a 50 year period. Both caverns are filled with dense sands.



Total vertical displacement (in m) over a 50 year period. Cavern is on the left is filled with brine, cavern on the right is filled with dense sands. Positive values represent upward movement.

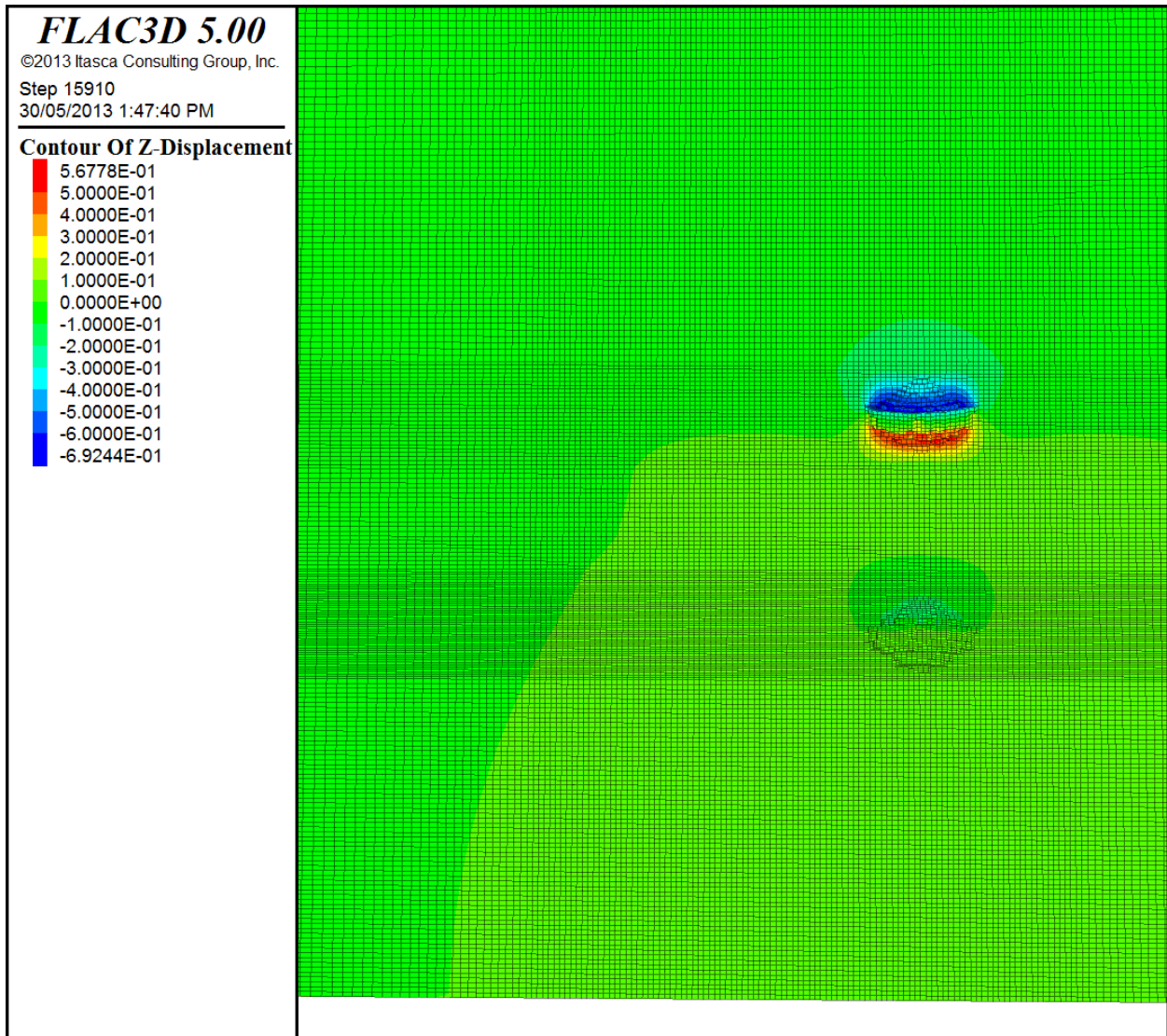


Total vertical displacement (in m) over a 50 year period. Cavern is on the left is filled with graded sands, cavern on the right is filled with dense sands. Positive values represent upward movement.

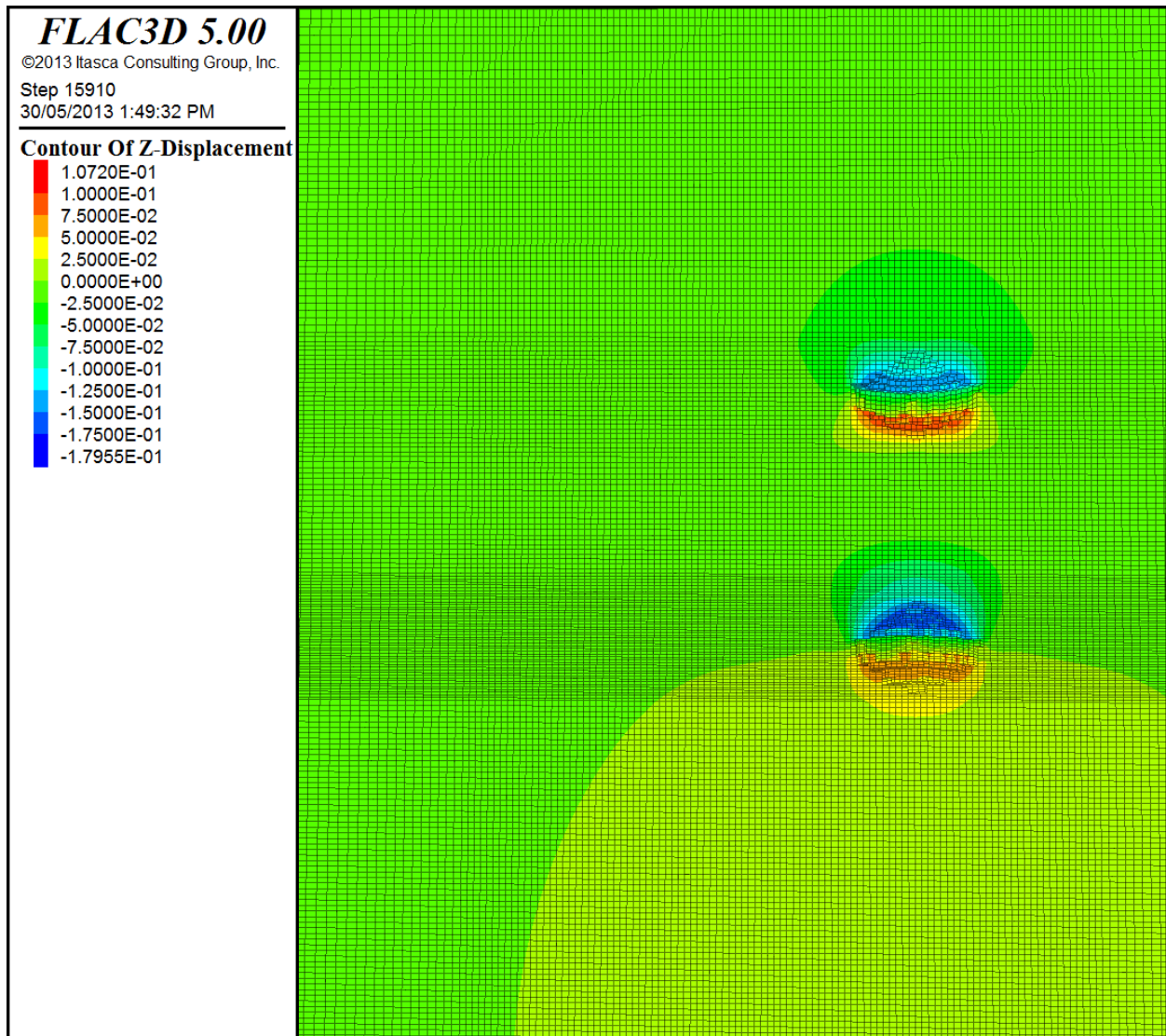


Total vertical displacement (in m) over a 50 year period. Both caverns are filled with dense sands. Positive values represent upward movement.

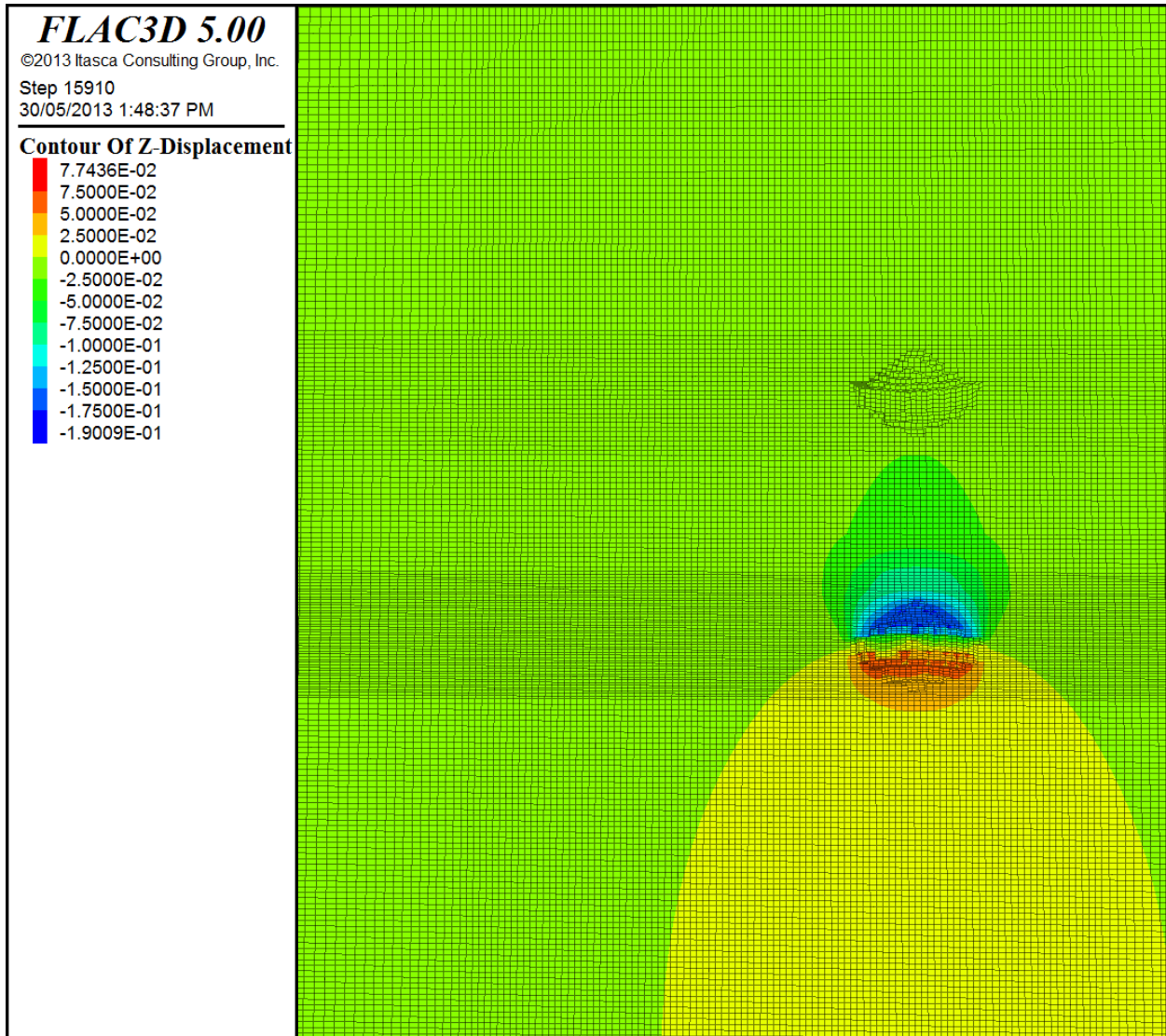
ONE CAVERN IN THE LOTSBERG FORMATION, ONE CAVERN IN THE PRAIRIE EVAPORITE FORMATION



Total vertical displacement (in m) over a 50 year period. Cavern in the Prairie Evaporite Formation is filled with brine, cavern in the Lotsberg Formation is filled with dense sands. Positive values represent upward movement.

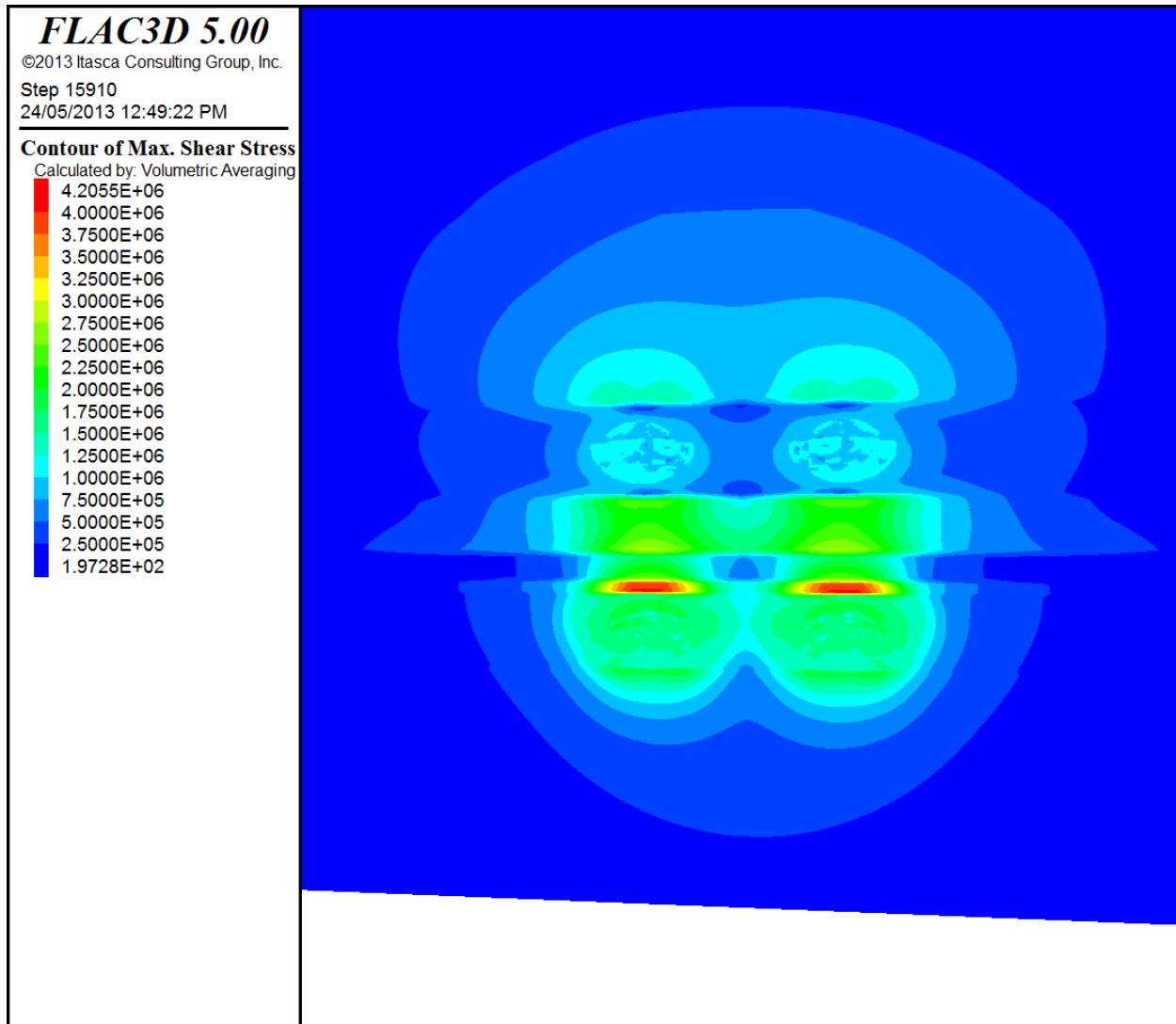


Total vertical displacement (in m) over a 50 year period. Cavern in the Prairie Evaporite Formation is filled with graded sands, cavern in the Lotsberg Formation is filled with dense sands. Positive values represent upward movement.

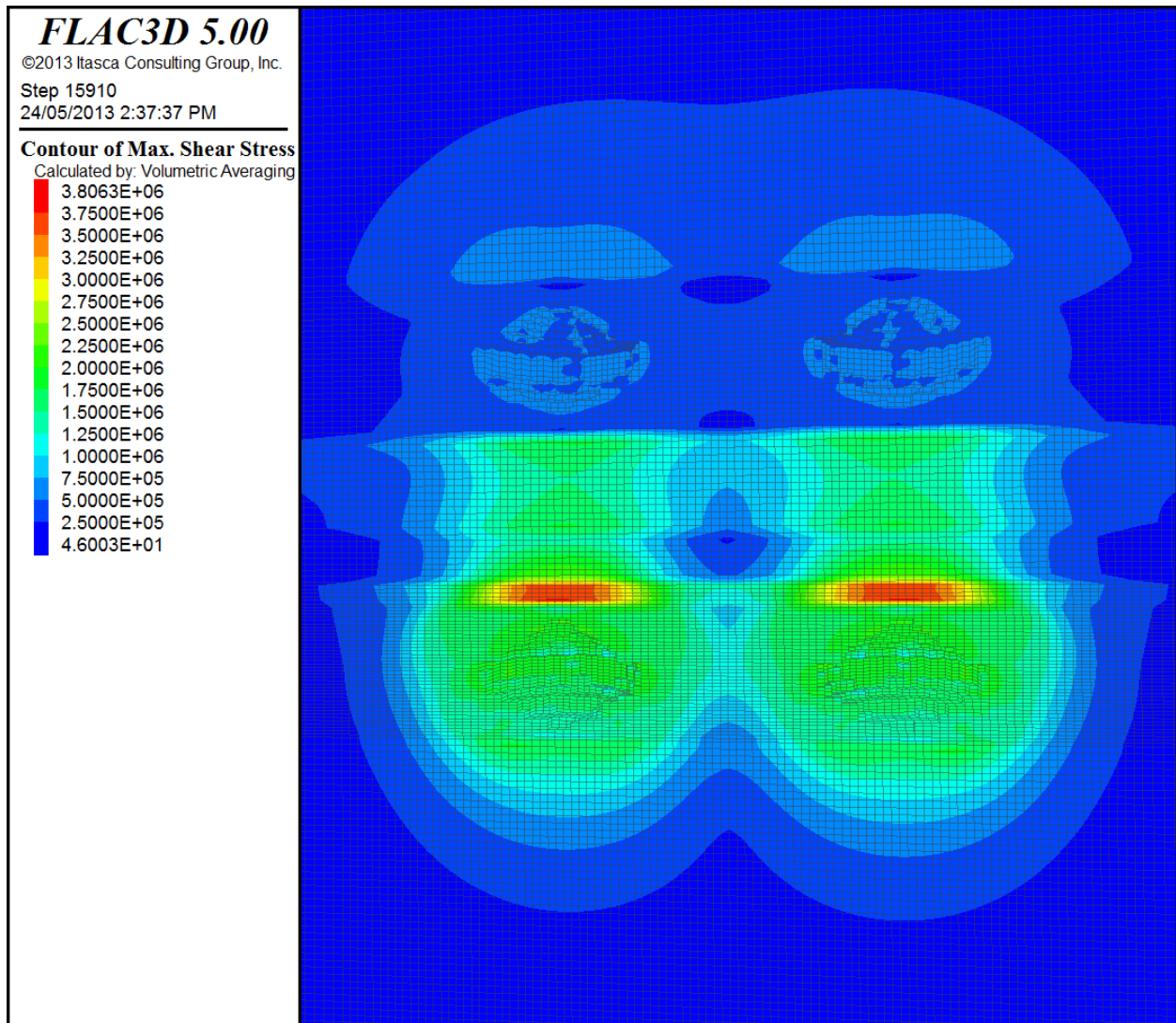


Total vertical displacement (in m) over a 50 year period. Both caverns are filled with dense sands. Positive values represent upward movement.

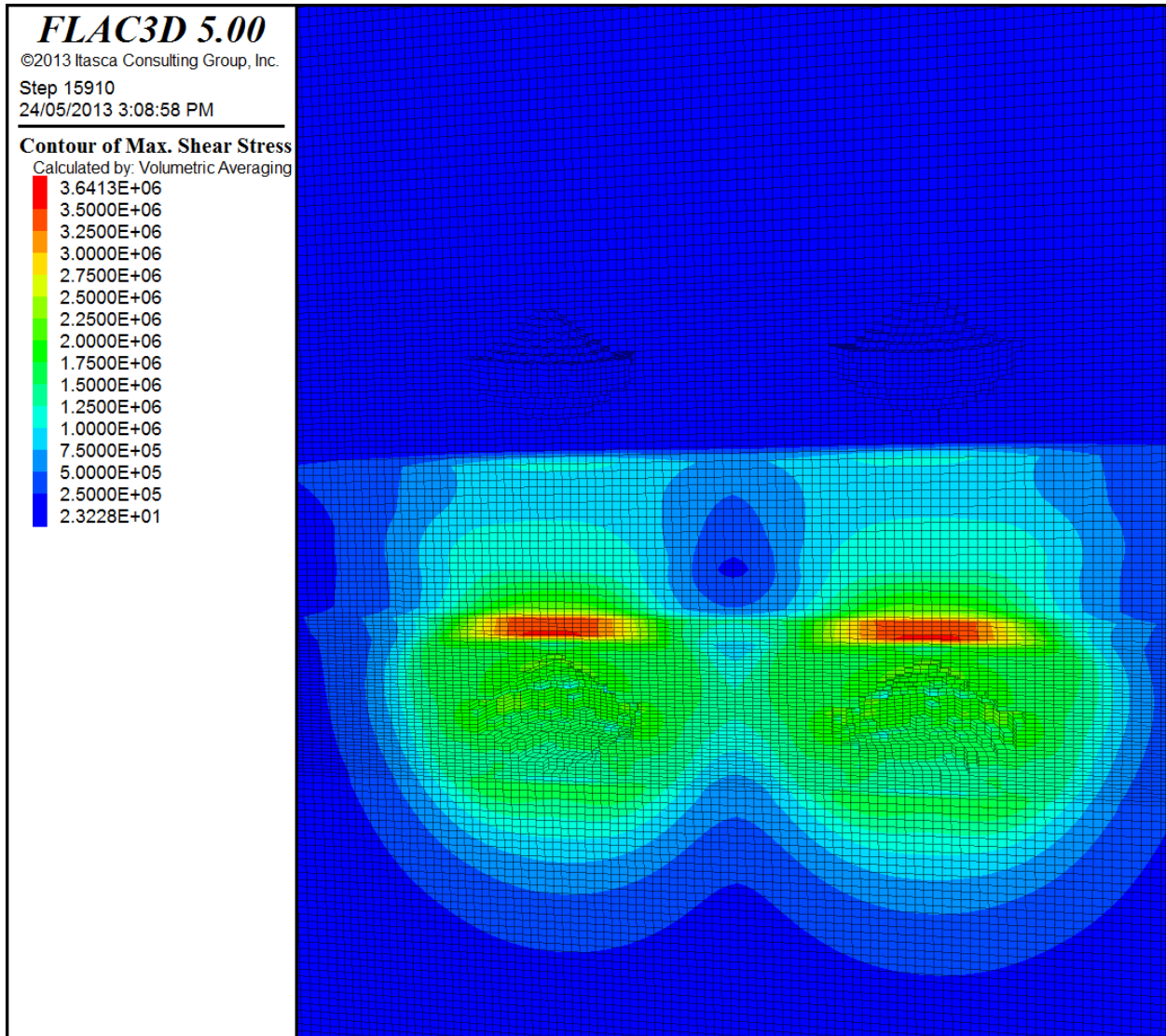
TWO CAVERNS IN THE LOTSBERG FORMATION, TWO CAVERNS IN THE PRAIRIE EVAPORITE FORMATION



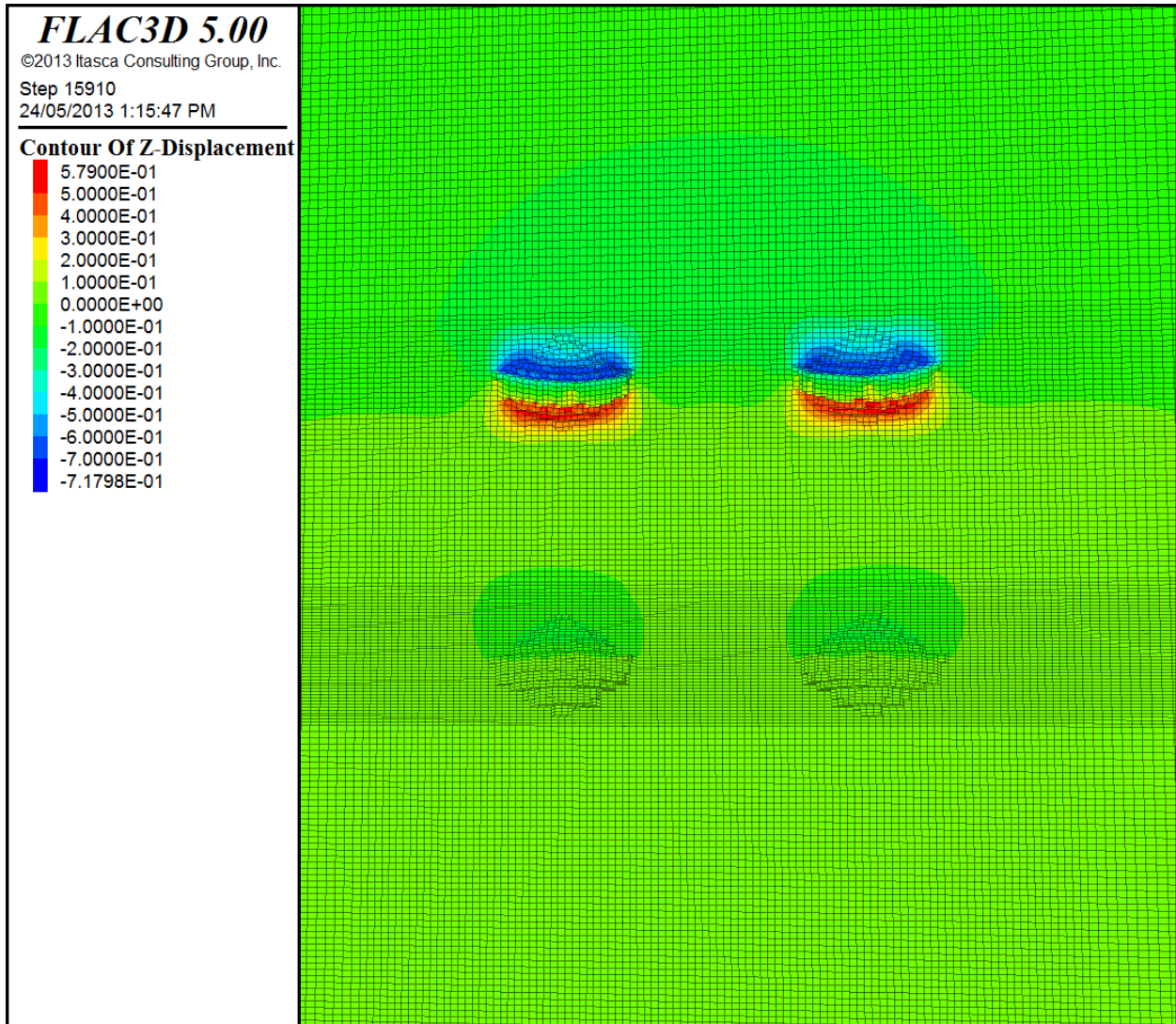
Maximum shear stress (in Pa) over a 50 year period. The caverns in the Prairie Evaporite Formation are filled with brine, the caverns in the Lotsberg Formation are filled with dense sands.



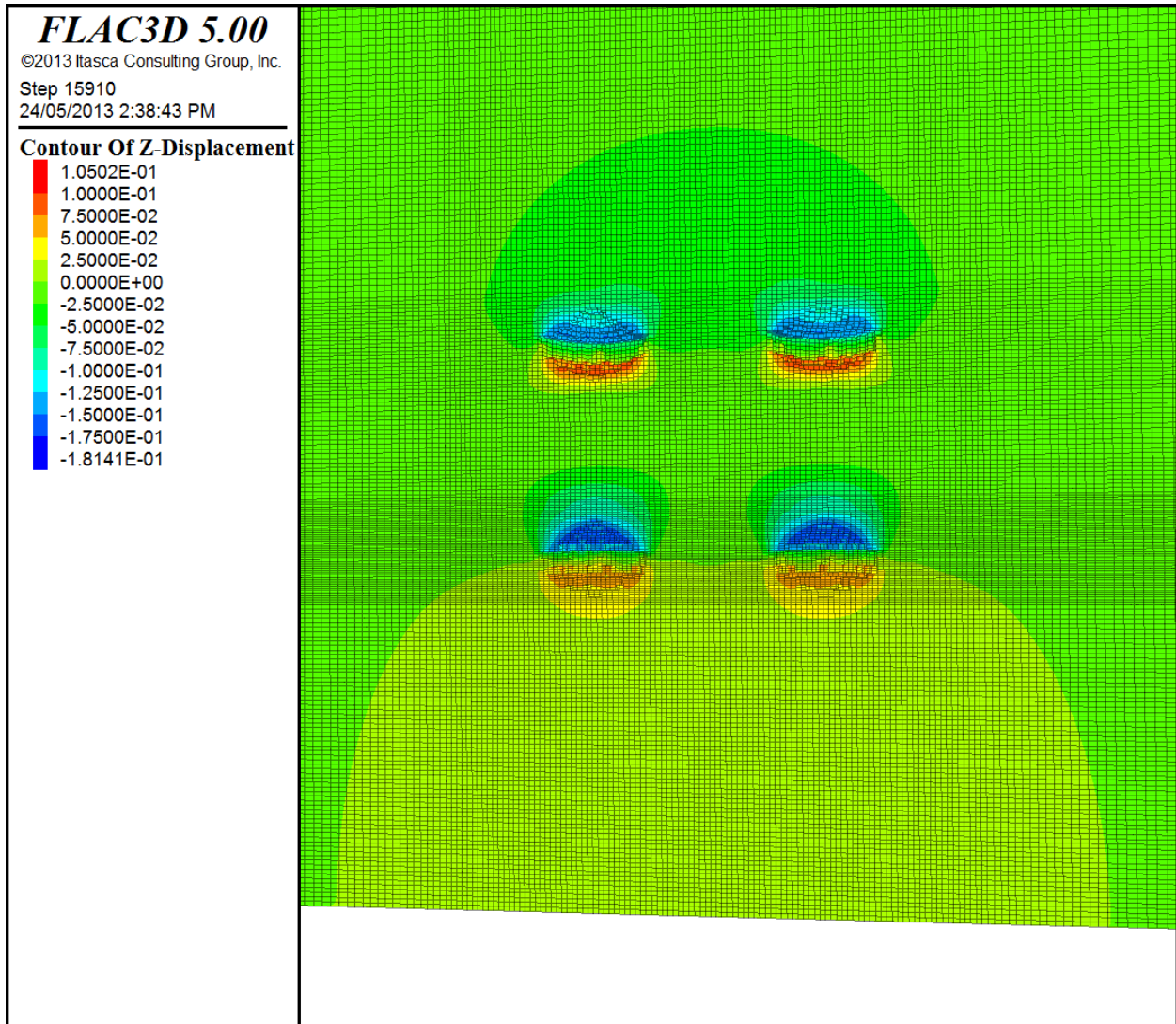
Maximum shear stress (in Pa) over a 50 year period. The caverns in the Prairie Evaporite Formation are filled with graded sands, the caverns in the Lotsberg Formation are filled with dense sands.



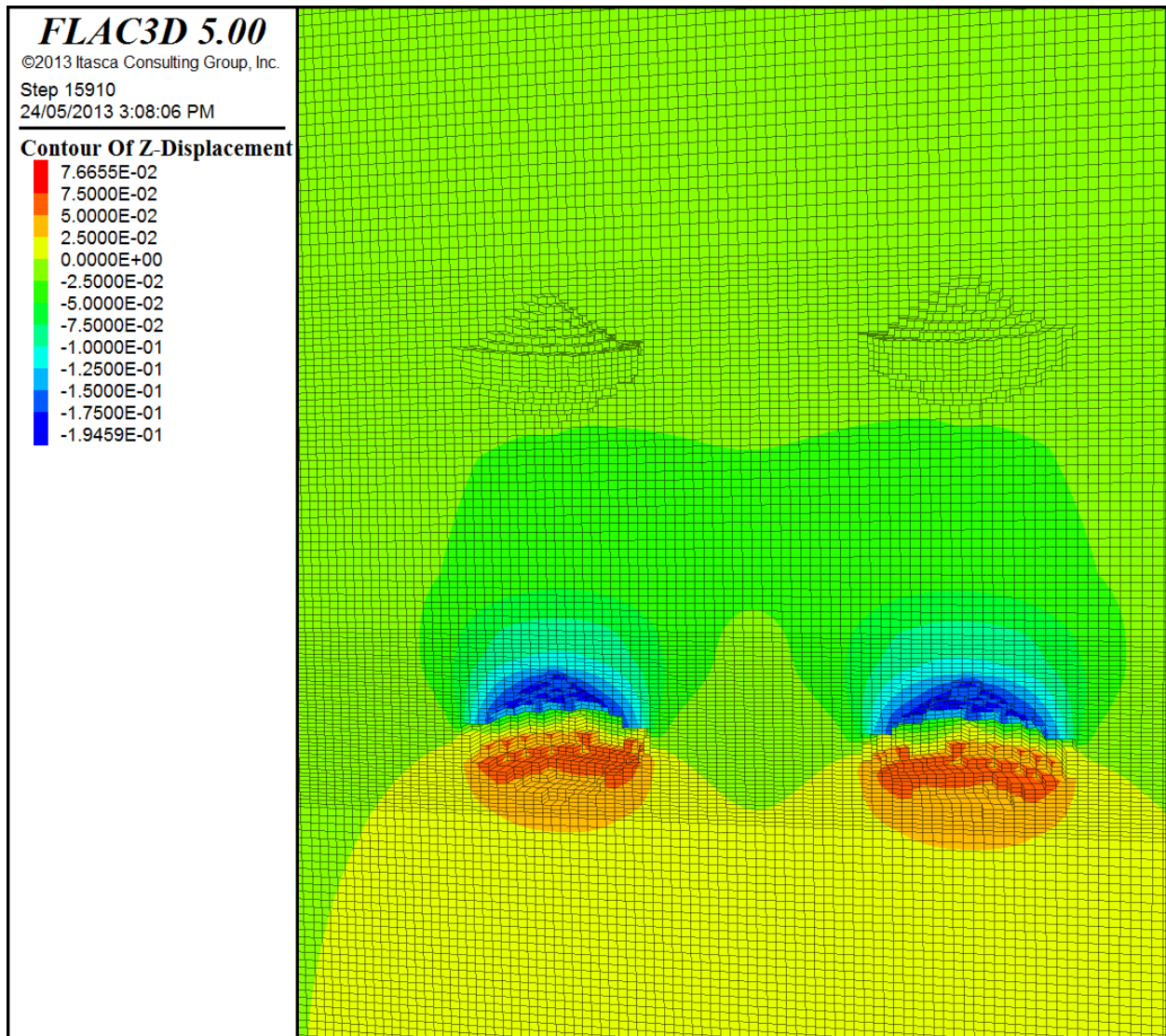
Maximum shear stress (in Pa) over a 50 year period. All caverns are filled with dense sands.



Total vertical displacement (in m) over a 50 year period. The caverns in the Prairie Evaporite Formation are filled with brine, the caverns in the Lotsberg Formation are filled with dense sands. Positive values represent upward movement.



Total vertical displacement (in m) over a 50-year period. The caverns in the Prairie Evaporite Formation are filled with graded sands; the caverns in the Lotsberg Formation are filled with dense sands. Positive values represent upward movement.



Total vertical displacement (in m) over a 50 year period. All caverns are filled with dense sands. Positive values represent upward movement.